行政院國家科學委員會專題研究計畫 成果報告

新參數超音波乳房影像技術(3/3)
研究成果報告(完整版)

計 畫 類 別 ：個別型
計 畫 編 號 ：NSC 95-2221-E-002-169-
執 行 期 間 ：95 年 08 月 01 日至 96 年 10 月 31 日
執 行 單 位 ：國立臺灣大學電機工程學系暨研究所

計 畫 主 持 人：李百祺

計畫參與人員：博士班研究生-兼任助理：廖超康、魏振瑋、張珥涵
碩士班研究生-兼任助理：李承翰、賴俊延、王慈吟、楊欣嘉
博士後研究：黃聖文

報 告 附 件 ：出席國際會議研究心得報告及發表論文

處 理 方 式 ：本計畫可公開查詢

中 華 民 國 97 年 04 月 28 日

行政院國家科學委員會補助專題研究計畫 ■ 成 果 報 告 □期中進度報告

新參數超音波乳房影像技術(3/3)

計畫類別：■ 個別型計畫　　□ 整合型計畫
計畫編號：NSC 95－2221－E－002－169
執行期間：95 年 8 月 1 日至 96 年 10 月 31 日

計畫主持人：李百祺
計畫參與人員：黃聖文、廖超康、李承翰、魏振瑋、賴俊延、王慈吟、張珵涵、楊欣嘉、

成果報告類型(依經費核定清單規定繳交)：□精簡報告　■完整報告

本成果報告包括以下應繳交之附件：
□赴國外出差或研習心得報告一份
□赴大陸地區出差或研習心得報告一份
■出席國際學術會議心得報告及發表之論文各一份
□國際合作研究計畫國外研究報告書一份

處理方式：除產學合作研究計畫、提升產業技術及人才培育研究計畫、列管計畫及下列情形者外，得立即公開查詢
■涉及專利或其他智慧財產權，□一年□二年後可公開查詢

執行單位：國立台灣大學 生醫電子與資訊學研究所
國立台灣大學 電機工程學系

中　華　民　國　96　年　11　月　1　日

中文摘要

本期計畫之研究目標為在不使用反射板的條件之下估計組織中有興趣區域的衰減係數，以達到辨別乳癌與良性組織的目的。在利用反射板的條件下，聲速與衰減係數的重建方法已於先前提出，該方法只需要使用由一個性線性陣列探頭所獲得之原始的通道信號。根據先前臨床結果，透過相對聲速之閾值，18.5 m/sec以及－28.3 m/s，可達到將惡性腫瘤從纖維腺瘤及脂肪中分隔出來的結果。然而，相對衰減係數無法與相對聲速一樣找出有效的單一閾值。由於文獻中提出惡性腫瘤的衰減係數高於一般組織，故仍以評估衰減係數為本期計畫研究目標。先前臨床實驗中，病人乳房組織可以順利被固定壓縮於實驗架構的比例很低，所以需要研究出一個不需要反射板就可以估計出組織衰減係數的方法。根據文獻，利用信號分段的方法來估計衰減係數。使用前期研究中的模擬數據評估此方法的成效，在此使用0.284，0.536以及1.136 dB/cm/MHz三種衰減係數，以通道自發自收的信號來估計衰減係數。由於有興趣區域與背景組織擁有不同的聲速，故在此利用接收聚焦的方式將經過特定點的各組發射接收信號聚集起來，如此一來，非自發自收通道之信號也可以加以利用。然而所得結果並不理想，呈現不規則性跳動。未來將針對頻譜分析改進估計的方法，盼能對於良惡性病灶的區分有所裨益。

關鍵字：聲速、衰減係數、有興趣區域、信號分段。

Abstract

The aim of this study is to estimate attenuation coefficient (AC) of a region of interest (ROI) in the tissue without a metal reflector in order to discriminate breast cancer from benign tissues. The reconstruction method with a metal reflector for sound velocity and AC distribution were previously proposed. It only used raw channel data acquired by a linear transducer array. According to previous clinical results, carcinoma could be discriminated from fibroadenoma and fat by choosing two appropriate thresholds for the relative sound velocity, 18.5 m/s and －28.3 m/s. It is reported that the AC is higher in cancerous tissue than in normal tissues, so the aim of this study is to estimate AC. In previous clinical experiment, because the proportion of patients whose breasts could be compressed in the stage was quite low, estimating these parameters without using a metal reflector would be the next step of this research. According to the literature, we use a method called signal segmentation to estimate AC. We evaluate the efficacy of this method by using simulation data created in previous study. Three kinds of attenuation coefficient used are 0.284, 0.536 and 1.136 dB/cm/MHz, respectively. We used A-line signals which were transmitted and received by the same channel to do the estimation. In fact, the sound velocities of the ROI and the background are different. Hence, we use the receiving focusing to gather the signals from all the transmit/receive combination. In this way, the signals not from transmitting and receiving by the same channel can be used. Nonetheless, the results show irregularly jittering. In the future, we will improve the estimation method based on more spectral analyses and hope this can benefit the discrimination between benign and malignant lesions.

Keywords: Attenuation Coefficient, Region of Interest, Signal Segmentation.

目錄

附錄一:

S.-W. Huang and P.-C. Li, “Computed tomography sound velocity reconstruction using incomplete data”, IEEE Transactions on Ultrasonics, Ferroelectrics and Frequency Control, Vol. 51, No. 3, pp. 329-342, March, 2004.

附錄二:

S.-W. Huang and P.-C. Li, “Experimental investigation of computed tomography sound velocity reconstruction using incomplete data”, IEEE Transactions on Ultrasonics, Ferroelectrics and Frequency Control, Vol. 51, No. 9, pp. 1072-1081, September, 2004.

附錄三:

S.-W. Huang and P.-C. Li, “Ultrasonic computed tomography reconstruction of the attenuation coefficient using a linear array”, IEEE Transactions on Ultrasonics, Ferroelectrics and Frequency

Control, Vol. 52 No. 11, pp. 2011-2022, November, 2005.

附錄四：

S.-W. Huang and P.-C. Li, “Arbitrary waveform coded excitation using bipolar square wave pulsers in medical ultrasound”, IEEE Transactions on Ultrasonics, Ferroelectrics and Frequency Control, Vol. 53 No. 1, pp. 106-116, January, 2006.

附錄五：

S.-W. Huang and P.-C. Li, “Binary Code Design for High Frequency Ultrasound”, IEEE Transactions on Ultrasonics, Ferroelectrics and Frequency Control, Vol. 54, No. 5, pp. 947-956, May, 2007.

附錄六：

S.-L. Wang, C.-H. Chang, H.-C. Yang, Y.-H. Chou and P.-C. Li, “Performance Evaluation of Coherence-Based Adaptive Imaging Using Clinical Breast Data”, IEEE Transactions on Ultrasonics, Ferroelectrics and Frequency Control, Vol. 54, No. 8, pp. 1669-1679, August, 2007.

附錄七：

C.-H. Chang, S.-W. Huang, H.-C. Yang, Y.-H. Chou and P.-C. Li, “Reconstruction of ultrasonic sound velocity and attenuation coefficient using linear arrays: clinical assessment”, Ultrasound in Medicine and Biology, Vol. 33, No.11, pp. 1681-1687, November, 2007.

行政院國家科學委員會專題研究計畫執行報告
新參數超音波乳房影像技術(3/3)

計畫編號：NSC95-2221-E-002-169
執行期限：95 年 8 月 1 日至 96 年 10 月 31 日
主持人：李百祺　執行機構及單位名稱：國立台灣大學電機工程學系
國立台灣大學生醫電子與資訊學研究所
E-mail: paichi@cc.ee.ntu.edu.tw

一、前言及文獻探討

乳癌是女性癌症中主要死因之一，早期發現早期治療則其治癒率較高。以往，乳房攝影被視為最好之非侵入式篩檢方法，因其可檢測出觸摸不到與極小的腫瘤。然而乳房攝影使用了游離輻射，而且具有較緻密的乳房年輕女性之乳房攝影片通常難以判讀[1]。相較於乳房攝影，超音波成像成為一個有效的輔助檢測方式[2]。然而，使用傳統超音波回波灰階成像來偵測乳癌通常受限於由乳房組織中聲速不均勻性所引起的影像失真[3]。使用超音波，仍然可能藉由重建聲速與衰減係數分布來偵測乳癌。舉例來說，曾有報告指出癌症組織中的聲速較脂肪來得快[4]，癌症組織中的衰減係數較囊腫來得高[5]。典型的重建需要斷層掃描式的架構，目的是從大量的投影中獲得重建所需資料，而這樣的架構鮮少用於臨床。另一種用於斷層掃描式的聲速與衰減係數重建方法是使用線性陣列之有限角度斷層掃描[6]-[8]。運用有限角度斷層掃描原理的成像設備就如同應用於傳統B-mode成像之設備，因此兩種成像方法都被考慮到了。此外，一塊金屬反射板被置於乳房下方，在資料擷取的同時，乳房是被壓縮的狀態。此方法亦需要選取一個有興趣區域(region of interest, ROI)，用以降低基於有限角度之斷層掃描式資料擷取所造成的困難。在上一期報告中，已測試臨床應用之效能。我們所使用的方法將針對組織的不均勻性來修正，而此不均勻性只存在於乳房組織而不存在於組織仿體中。在利用反射板的條件下，聲速與衰減係數的重建方法已於先前提出，該方法只需要使用由一個性線性陣列探頭所獲得之原始的通道信號。根據先前臨床結果，透過相對聲速之閾值，18.5 m/sec以及－28.3 m/s，可達到將惡性腫瘤從纖維腺瘤及脂肪中分隔出來的結果。然而，相對衰減係數無法與相對聲速一樣找出有效的單一閾值。

在計畫的第一年度，我們已完成下列工作項目：

1. 建立波傳遞模擬器，用以產生研究有限角度之超音波穿透式斷層掃描重建演算法所需的通道資料。
2. 成功發展出利用平面波入射流體圓柱的散射級數解來產生飛行時間差資料的技術。
3. 建立適用於傳統電腦斷層掃描和有限角度之超音波穿透式斷層掃描的兩個重建演算法，可解出物體的聲速分佈。
4. 以模擬檢驗第一個演算法應用於有限角度之超音波穿透式斷層掃描的效果。
5. 以模擬檢驗第二個演算法應用於有限角度之超音波穿透式斷層掃描的效果，並確認其可行性。
6. 使用模擬資料分析第二個演算法之效能。
7. 建立可使用線性陣列探頭進行有限角度之超音波穿透式斷層掃描的實驗系統。
8. 以實驗檢驗第二個演算法應用於有限角度之超音波穿透式斷層掃描的效果，並確認其可行性。
9. 使用實驗資料分析第二個演算法之效能。
10. 建立可進行傳統電腦斷層掃描之實驗系統。

在計畫的第二年度，我們已完成下列工作項目：

1.使用手動圈選之使用者介面，建立臨床資料擷取裝置，以利進行傳統電腦斷層掃描之臨床實驗系統。
2.臨床資料之取得。
3.設計一個理想的濾波器(optimal filter)來克服組織信號在傳遞中因其聲速的不均勻性所造成嚴重的失真。
4.使用理想濾波器後配合上年度之演算法二所得之實驗結果。

在計畫的第三年度，我們已完成下列工作項目：

1.臨床資料之取得。
2.利用前期與本期之臨床資料所得之實驗結果更新，包含相對聲速與相對衰減係數。
3.在沒有金屬反射板的實驗架構下建立出衰減係數估計方法。

本計畫目前為止之直接產出成果已包括七篇期刊論文,十一篇國內外研討會論文(包括兩篇邀請演講)及提出二件專利申請(一項已核准）。

二、研究目的

由於文獻中提出惡性腫瘤的聲速與衰減係數皆高於一般組織，然而在前兩年的研究裡，以反射板裝置擷取的臨床資料中，重建出聲速與衰減係數，但只能由相對聲速之雙閾值，18.5 m/sec 以及－28.3 m/s 分辨惡性腫瘤、纖維腺瘤以及脂肪，由於先前臨床實驗中,病人乳房組織可以順利被固定壓縮以取得實驗數據的比例很低,故本期計畫之研究目標為在不使用反射板的條件之下估計組織中有興趣區域的衰減係數,盼能提高可分析的樣本數，以達到辨別乳癌與良性組織的目的。

三、計畫成果

在計畫第一年度,我們已完成下列成果：

1. 建立波傳遞模擬器：

我們已在本年度建立完整的波傳遞模擬器,且用以產生研究有限角度之超音波穿透式斷層掃描重建演算法所需的通道資料(channel data)。

直接計算超音波信號在不均勻介質中傳遞時所發生的各種現象，如反射(reflection)、散射(scattering)、折射(refraction)、繞射(diffraction)及衰退(attenuation),是研究組織不均均對成像效果的衝擊及發展克服這些問題的技術最好的方式。以目前的電腦計算速度而言，直接做三維波傳遞(wave propagation)或脈衝傳遞(pulse propagation)的計算，還不實際；另一方面，現有的超音波掃描儀，仍以使用一維陣列頭探進行二維成像為主流,在這種架構下的波傳遞可算是一個二維問題。故雖然超音波信號在人體內的傳遞，是一個三維的問題，但透過計算二維的波傳遞,已經足以探討大部分的問題。

典型的超音波成像範圍涵蓋至少數百個波長。當波傳遞的距離到了這個規模時，大部分的方法，如有限元素法(finite-element method)、有限差分法(finite-difference method)，已無法維持進行成像研究時所需的精確度[9]。而 *k*-space methods 是精確度較好的一類方法。目前文獻中最準確的方法，是由 Rochester University 所發展出來，利用解藕合一階聲波傳遞方程式(coupled first-order acoustic propagation equations)來計算波傳遞的一種 *k*-space method [10]，[11]。這種 *k*-space method 在均勻介質下的計算結果是精確的，在一般弱散射介質下的計算結果也有高準確度。此外，這個方法可以直接加上 PML(完美匹配層，perfectly matched layer)無反射邊界條件(nonreflecting boundary condition)及加上 relaxation absorption 以考慮衰退。這種 *k*-space method 的低色散(dispersion)特性使 relaxation absorption 所造成的頻率相關的(frequency-dependent)衰退和相位速度(phase velocity)在做波傳遞計算時可以被準確的維持住。而當配合 smoothing 的技術時，即使在強散射的情況，這種方法也可以有很好的準確度。

以下對解藕合一階聲波傳遞方程式的 *k*-space method 做一介紹。在無損耗(lossless)的流體(fluid)介質中，藕合一階線性聲波傳遞方程式的形式為

$$-\rho(\mathbf{r})\frac{\partial u_x(\mathbf{r},t)}{\partial t}=\frac{\partial p(\mathbf{r},t)}{\partial x}\ , \tag{1}$$

$$-\rho(\mathbf{r})\frac{\partial u_y(\mathbf{r},t)}{\partial t}=\frac{\partial p(\mathbf{r},t)}{\partial y}\ , \tag{2}$$

$$-\kappa_\infty(\mathbf{r})\frac{\partial p_x(\mathbf{r},t)}{\partial t}=\frac{\partial u_x(\mathbf{r},t)}{\partial x}\ , \tag{3}$$

$$-\kappa_\infty(\mathbf{r})\frac{\partial p_y(\mathbf{r},t)}{\partial t}=\frac{\partial u_y(\mathbf{r},t)}{\partial y}\ , \tag{4}$$

其中 $\mathbf{r}=(x,y)$ 為座標，t 為時間，$p(\mathbf{r},t)=p_x(\mathbf{r},t)+p_y(\mathbf{r},t)$ 為聲壓(acoustic pressure)，u_x,u_y 為聲波粒子速度(acoustic particle velocity)$\mathbf{u}=(u_x,u_y)$ 的分量，ρ 為密度(density)，κ_∞ 為可壓縮性(compressibility)。這四個方程式可以用下面的演算法來解：

$$u_x(\mathbf{r}_1,t^+)=u_x(\mathbf{r}_1,t^-)-\frac{\Delta t}{\rho(\mathbf{r}_1)}\frac{\partial p(\mathbf{r},t)}{\partial^{(c_0\Delta t)^+}x}\ , \tag{5}$$

$$u_y(\mathbf{r}_2,t^+)=u_y(\mathbf{r}_2,t^-)-\frac{\Delta t}{\rho(\mathbf{r}_2)}\frac{\partial p(\mathbf{r},t)}{\partial^{(c_0\Delta t)^+}y}\ , \tag{6}$$

$$p_x(\mathbf{r},t+\Delta t)=p_x(\mathbf{r},t)-\frac{\Delta t}{\kappa_\infty(\mathbf{r})}\frac{\partial u_x(\mathbf{r}_1,t^+)}{\partial^{(c_0\Delta t)^-}x}\ , \tag{7}$$

$$p_y(\mathbf{r},t+\Delta t)=p_y(\mathbf{r},t)-\frac{\Delta t}{\kappa_\infty(\mathbf{r})}\frac{\partial u_y(\mathbf{r}_1,t^+)}{\partial^{(c_0\Delta t)^-}y}\ , \tag{8}$$

其中 Δt 是求解過程中每一次迭代的時間增量，Δx 和 Δy 表取樣間距，$t^+ = t + \Delta t/2$，$t^- = t - \Delta t/2$，$\mathbf{r}_1 = (x + \Delta x/2, y)$，$\mathbf{r}_2 = (x, y + \Delta y/2)$，而

$$\frac{\partial p(\mathbf{r},t)}{\partial^{(c_0\Delta t)^+}x} \equiv \mathbf{F}^{-1}\left[ik_x \exp(ik_x\Delta x/2)\cdot \sin c(c_0\Delta t k/2\pi)\mathbf{F}[p(\mathbf{r},t)]\right], \quad (9)$$

$$\frac{\partial p(\mathbf{r},t)}{\partial^{(c_0\Delta t)^+}y} \equiv \mathbf{F}^{-1}\left[ik_y \exp(ik_y\Delta y/2)\cdot \sin c(c_0\Delta t k/2\pi)\mathbf{F}[p(\mathbf{r},t)]\right], \quad (10)$$

$$\frac{\partial u_x(\mathbf{r}_1,t^+)}{\partial^{(c_0\Delta t)^-}x} \equiv \mathbf{F}^{-1}\left[ik_x \exp(-ik_x\Delta x/2)\cdot \sin c(c_0\Delta t k/2\pi)\mathbf{F}[u_x(\mathbf{r}_1,t^+)]\right], \quad (11)$$

$$\frac{\partial u_y(\mathbf{r}_1,t^+)}{\partial^{(c_0\Delta t)^-}y} \equiv \mathbf{F}^{-1}\left[ik_y \exp(-ik_y\Delta y/2)\cdot \sin c(c_0\Delta t k/2\pi)\mathbf{F}[u_y(\mathbf{r}_1,t^+)]\right], \quad (12)$$

其中 $\mathbf{F}$ 和 $\mathbf{F}^{-1}$ 分別為二維空間傅立葉轉換(Fourier Transform)及反傅立葉轉換(inverse Fourier Transform)，$k = (k_x, k_y)$ 為波數(wave number)，c_0 為均勻介質下的聲速。隨著疊代的次數增加，聲波信號便會傳遞出去。當加上 relaxation absorption 和 PML 時，演算法則修正為：

$$u_x(\mathbf{r}_1,t^+) = e^{-\alpha_x(\mathbf{r}_1)\Delta t/2}\left[e^{-\alpha_x(\mathbf{r}_1)\Delta t/2}u_x(\mathbf{r}_1,t^-) - \frac{\Delta t}{\rho(\mathbf{r}_1)}\left(\frac{\partial(p_x(\mathbf{r},t)+p_y(\mathbf{r},t))}{\partial^{(c_0\Delta t)^+}x}\right)\right], \quad (13)$$

$$u_y(\mathbf{r}_2,t^+) = e^{-\alpha_y(\mathbf{r}_2)\Delta t/2}\left[e^{-\alpha_y(\mathbf{r}_2)\Delta t/2}u_y(\mathbf{r}_2,t^-) - \frac{\Delta t}{\rho(\mathbf{r}_2)}\left(\frac{\partial(p_x(\mathbf{r},t)+p_y(\mathbf{r},t))}{\partial^{(c_0\Delta t)^+}y}\right)\right], \quad (14)$$

$$p_x(\mathbf{r},t+\Delta t) = e^{-\mu_x(\mathbf{r})\Delta t/2}\left[e^{-\mu_x(\mathbf{r})\Delta t/2}p_x(\mathbf{r},t) - \frac{\Delta t}{\kappa_\infty(\mathbf{r})}\left(\frac{\partial u_x(\mathbf{r}_1,t^+)}{\partial^{(c_0\Delta t)^-}x} - \sum_{i=1}^{N}v_i^x(\mathbf{r})S_i^x(\mathbf{r},t^+)\right)\right], \quad (15)$$

$$p_y(\mathbf{r},t+\Delta t) = e^{-\mu_y(\mathbf{r})\Delta t/2}\left[e^{-\mu_y(\mathbf{r})\Delta t/2}p_y(\mathbf{r},t) - \frac{\Delta t}{\kappa_\infty(\mathbf{r})}\left(\frac{\partial u_y(\mathbf{r}_2,t^+)}{\partial^{(c_0\Delta t)^-}y} - \sum_{i=1}^{N}v_i^y(\mathbf{r})S_i^y(\mathbf{r},t^+)\right)\right], \quad (16)$$

$$S_i^x(\mathbf{r},t^+) = e^{-\Delta t/2\tau_i(\mathbf{r})}\left[e^{-\Delta t/2\tau_i(\mathbf{r})}S_i^x(\mathbf{r},t^-) + \Delta t\frac{p_x(\mathbf{r},t)}{\tau_i(\mathbf{r})}\right], \quad (17)$$

$$S_i^y(\mathbf{r},t^+) = e^{-\Delta t/2\tau_i(\mathbf{r})}\left[e^{-\Delta t/2\tau_i(\mathbf{r})}S_i^y(\mathbf{r},t^-) + \Delta t\frac{p_y(\mathbf{r},t)}{\tau_i(\mathbf{r})}\right], \quad (18)$$

其中 α_x, α_y 是吸收參數(absorption parameter)，控制 PML 中的衰退量，N 是 relaxation absorption 所用的階(order)數，S_i^x, S_i^y 是和 relaxation absorption 有關的狀況變數(state variable)，$\mu_x, \mu_y, v_i^x, v_i^y, \tau_i$ 也和 relaxation absorption 有關。

由於組織的不均勻是直接來自於組織物理參數在空間上的變化，只要能適當地設定物體的物理參數，相位偏移和波前振幅失真的現象都能由波傳遞模擬器準確地產生。目前文獻中已有許多關於乳房、腹部、胸腔組織之物理結構的具體研究[12]，[13]，因此在使用模擬器時物體之物理參數如聲速、密度及衰減係數的設定都能有所依據，接近真正人體組織內的分佈情形。因此，由模擬器產生的資料將足以反映真實世界的情況。使用波傳遞模擬器的好處，是較實驗易於控制變因，利於找出造成影像品質不佳及改進方法的關鍵因素。以模擬器和實驗系統配合，能更有效地進行成像技術的研究，包含關於相位偏移和波前振幅失真的研究在內。

2. 建立飛行時間資料的產生器：

在發展重建聲速分佈的演算法時，必需能產生理想的飛行時間差資料，才能有效評估演算法效能。波傳遞模擬器可用以產生飛行時間差資料，但是費時太久。本年度我們發展出利用平面波入射流體圓柱(fluid cylinder)的散射級數解[14]來產生飛行時間差資料的技術，以解決這個問題。

參考圖一(a)，考慮一聲波 $w(x,y;t)$ 沿 $+y$ 方向在背景物理參數為 $(\rho_0, c_0(f))$ 的線性介質中傳播，其中 ρ 為密度，c 為聲速，f 為時域頻率，且此介質中內含半徑為 a，圓心在 (x_1, y_1) 而物理參數為 $(\rho_1, c_1(f))$ 的圓柱。因為 $w(x, y_2; t)$ 的時域傅立葉轉換 $W(x, y_2; f)$ 可由 $w(x,0;t)$ 的時域傅立葉轉換 $W(x,0;f)$ 求得，假設衰退可忽略，則若 $w(x,0;t)$ 已知，便可算出 $w(x, y_2; t)$。

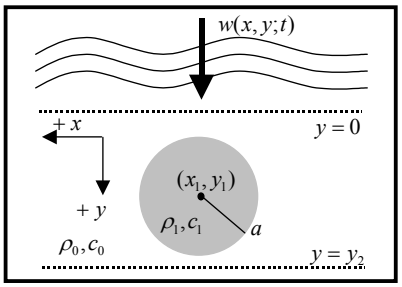

(a)

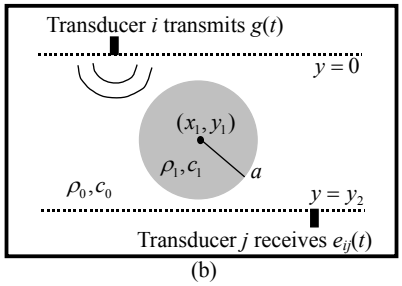

(b)

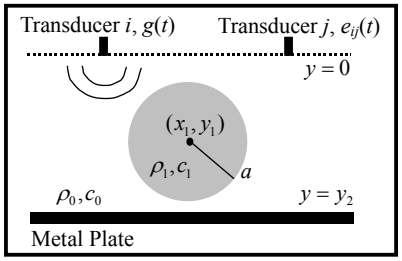

(c)

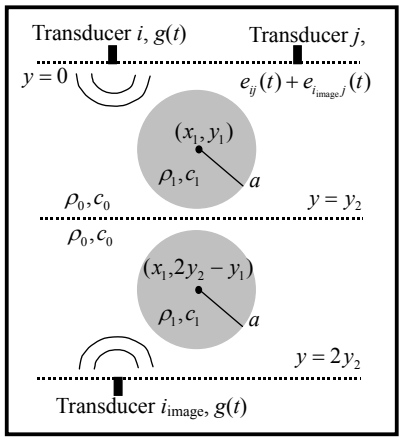

(d)

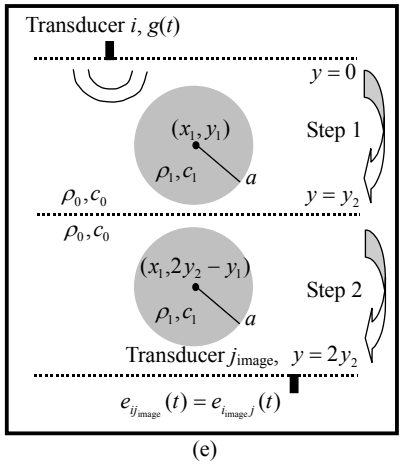

(e)

圖一 飛行時間資料的產生方式。

令$W(x,0;f)$的角頻譜為$\tilde{W}(k_x;0,f)$[15]，即

$$W(x,0;f)=\frac{1}{2\pi}\int\tilde{W}(k_x;0,f)\exp(jk_x x)dk_x \quad (19)$$

除了$|k_x|>2\pi f/c_0(f)$的複數指數函數$\exp(jk_x x)$是代表 evanescent 波之外，每個$\exp(jk_x x)$皆代表以波向量$\left(k_x,\sqrt{(2\pi f/c_0(f))^2-k_x^2}\right)$傳遞之平面波。因此

$$W(x,y_2;f)\cong\frac{1}{2\pi}\int_{-2\pi f/c_0(f)}^{2\pi f/c_0(f)}\tilde{W}'(k_x;x,y_2,f)dk_x \quad (20)$$

其中$\tilde{W}'(k_x;x,y_2,f)$為對應$\tilde{W}(k_x;0,f)\exp(jk_x x)$這個平面波入射圖一(a)中之圓柱的散射級數解。

基於以上的討論，對圖一(b)的配置而言，當上方陣列中的換能器i發射一短脈衝信號$g(t)$時，由下方陣列中的換能器j所收到的信號$e_{ij}(t)$便可以透過計算得到。假設圖一(c)中金屬板的物理參數$(\rho_{\text{m}},c_{\text{m}}(f))$滿足$\rho_{\text{m}}>>\rho_0$和$c_{\text{m}}(f)>>c_0(f)$，則透過映像法(method of images)，可知圖一(c)中的$e_{ij}(t)$等於圖一(d)中的$e_{ij}(t)+e_{i_{\text{image}}j}(t)$。此外，在$g(t)$由換能器$i$傳遞到金屬板反射，再傳遞到換能器$j$所需的飛行時間附近，換能器$j$所收到的信號主要是$e_{ij_{\text{image}}}(t)$，$e_{ij}(t)$的貢獻可忽略。因此，要產生$t_{ij}$時，我們只需考慮圖一(e)的配置。既然$e_{ij_{\text{image}}}(t)=e_{i_{\text{image}}j}(t)$，我們可分兩步驟計算出在$t_{ij}$附近的$e_{ij_{\text{image}}}(t)$：首先我們將波由平面$y=0$傳遞至平面$y=y_2$，然後再由平面$y=y_2$傳遞至平面$y=2y_2$。這個方法可直接推廣到物體內含多個圓柱的情況。

3. 建立適用於傳統電腦斷層掃描和有限角度之超音波穿透式斷層掃描的重建演算法：

我們在本年度發展出兩個演算法，可重建物體的聲速分佈。

在傳統的電腦斷層影像上，大多是使用filtered backprojection (FBP)的重建方法[16]，這種方法必須取得環繞物體至少 180 度的投影。由於我們的最終目的是以單一成像設備同時取得 B-mode 影像、聲速分佈影像和衰退係數分佈影像，因此必須捨棄 FBP，發展既適用於傳統電腦斷層掃描，又適用於使用陣列探頭來重建聲速分佈和衰退係數分佈的演算法。在不使用 FBP 的情況下，聲速的重建過程主要是解下列的一組線性方程式：

$$\mathbf{L}\Delta\mathbf{s}=\Delta\mathbf{t}\ , \quad (21)$$

其中$\mathbf{L}=\begin{bmatrix}\mathbf{l}_1 & \mathbf{l}_2 & \Lambda & \mathbf{l}_M\end{bmatrix}^{\text{T}}$為已知矩陣，由發射、接收陣元或換能器相對的幾何關係求得；$\Delta\mathbf{t}=\begin{bmatrix}\Delta t_1 & \Delta t_2 & \Lambda & \Delta t_M\end{bmatrix}^{\text{T}}$為已知向量，每個元素都代表一個飛行時間差(geometrically compensated time-of-flight)的資料，通常由量測得到；$\Delta\mathbf{s}=\begin{bmatrix}\Delta s_1 & \Delta s_2 & \Lambda & \Delta s_N\end{bmatrix}^{\text{T}}$為一待解的向量，其中每個元素都代表物體中相對應點的慢度$s_i=c_i^{-1}$(slowness，聲速的倒數)和背景慢度$s_0=c_0^{-1}$的差，即慢度差$\Delta s_i=s_i-s_0$。

為了準確解出$\Delta\mathbf{s}$，我們必須儘可能利用一些已知的資訊[17]。在軟組織中，聲速值不會超出一定的範圍，如不低於$c_{\text{lower}}=1450$ m/s、不高於$c_{\text{upper}}=1580$ m/s。定義

$$C_{\text{velocity}}=\left\{x_l\in[c_{\text{upper}}^{-1}-s_0,c_{\text{lower}}^{-1}-s_0],1\le l\le N\right\}, \quad (22)$$

則C_{velocity}表示所有合於聲速上下限的解。我們

在發展演算法時，將要求 $\Delta\mathbf{s} \in C_{\text{velocity}}$。另一方面，如果 $\mathbf{L}\Delta\mathbf{s} = \Delta\mathbf{t}$ 成立，其解 $\Delta\mathbf{s}$ 必須屬於下面所有集合的交集：

$$C_{\Delta t_i} = \left\{\mathbf{x} : \left\langle \mathbf{x}, \mathbf{l}_i \right\rangle = \Delta t_i\right\}, i = 1,2,\Lambda\ ,M \quad , \tag{23}$$

其中 $\langle \cdot,\cdot \rangle$ 表內積。由於量測的誤差和折射的效應，所有 $C_{\Delta t_i}$ 的交集通常會是空集合，即滿足所有飛行時間差的解不存在。因此，一個合理的做法是不要求 $\Delta\mathbf{s}$ 滿足所有的飛行時間差資料，而只要使總誤差最小，也就是使以下的成本函數(cost function)最小：

$$\Phi^{\text{s}}(\mathbf{x}) = \frac{1}{2}\sum_{i=1}^{M} d^2(\mathbf{x}, C_{\Delta t_i}) \quad , \tag{24}$$

其中 $d(\mathbf{x}, C_{\Delta t_i})$ 表 $\mathbf{x}$ 和 $C_{\Delta t_i}$ 的距離。我們根據下面的演算法來求得一個屬於 C_{velocity}，且又使成本函數最小的 $\Delta\mathbf{s}$ [18]：任取一 $\mathbf{x}_0 \in C_{\text{velocity}}$ 為初始值，並令

$$\mathbf{x}_{n+1} = (1-\lambda_n)\mathbf{x}_n + \lambda_n P_{C_{\text{velocity}}}\left[(1-\gamma)\mathbf{x}_n + \gamma\sum_{i=1}^{M} w_i P_{C_{\Delta t_i}}(\mathbf{x}_n)\right], n \geq 0 \quad , \tag{25}$$

其中 $\lambda_n \in [0,1]$ for all $n \geq 0$，$\sum_{n\geq 0}\lambda_n(1-\lambda_n) = \infty$，$\gamma \in (0,2]$，而 P 為投影運算子(projector)，則令 $\Delta\mathbf{s} = \lim_{n\to\infty}\mathbf{x}_n$ 即為所求。我們稱這個演算法為演算法一。

進行有限角度之超音波穿透式斷層掃描時，由於僅能在有限的角度觀察到物體，而不能取得環繞物體至少 180 度的投影，因此如果只利用飛行時間差的資訊來進行影像重建，亦即求解 $\mathbf{L}\Delta\mathbf{s} = \Delta\mathbf{t}$，不易得到準確的聲速分佈。在演算法一中，我們已加入合理的聲速上下限，以期能增進重建的準確性。為了利用到成像系統能同時取得飛行時間差和 B-mode 影像的特性，我們進一步發展出一個以 B-mode 影像提供的物體區塊資訊來幫助重建聲速分佈的演算法。如圖二所示，我們可利用 B-mode 影像找出某一軟組織和背景之間的邊界，然後令該軟組織內和背景的聲速各為一待解之未知常數，而邊界上的聲速則必須介於這兩個常數之間，這相當於要求慢度差 $\Delta\mathbf{s}$ 必須屬於

$$C_{\text{image}} = \begin{cases} \left\{\begin{array}{l}\mathbf{x} \in \mathbf{R}^{MN} : x_{b_1} = \Lambda = x_{b_{N_{\text{b}}}}, x_{r_1} = \Lambda \\ \quad = x_{r_{N_{\text{r}}}}, x_{br_i} \in [x_{b_1}, x_{r_1}] \text{ or } [x_{r_1}, x_{b_1}], 1 \leq i \leq N_{\text{br}}\end{array}\right\} \text{if } x_{b_1} \leq x_{r_1} \\ \left\{\begin{array}{l}\mathbf{x} \in \mathbf{R}^{MN} : x_{b_1} = \Lambda = x_{b_{N_{\text{b}}}}, x_{r_1} = \Lambda \\ \quad = x_{r_{N_{\text{r}}}}, x_{br_i} \in [x_{r_1}, x_{b_1}] \text{ or } [x_{b_1}, x_{r_1}], 1 \leq i \leq N_{\text{br}}\end{array}\right\} \text{otherwise} \end{cases} , \tag{26}$$

其中 $I_{\text{b}} \equiv \{b_1, b_2, \Lambda\ , b_{N_{\text{b}}}\}$ 為背景的索引集合，$I_{\text{r}} \equiv \{r_1, r_2, \Lambda\ , r_{N_{\text{r}}}\}$ 為該軟組織的索引集合，而 $I_{\text{br}} \equiv \{br_1, br_2, \Lambda\ , br_{N_{\text{br}}}\}$ 為邊界點的索引集合。當物體中所含軟組織區域不只一個時，我們可仿照上面的方面來建立 C_{image}。

我們將要求 $\Delta\mathbf{s} \in C_{\text{velocity}} \cap C_{\text{image}}$。另一方面，則不要求 $\Delta\mathbf{s}$ 滿足所有的飛行時間差資料，而只要成本函數 $\Phi^{\text{s}}(\mathbf{x}) = \frac{1}{2}\sum_{i=1}^{M} d^2(\mathbf{x}, C_{\Delta t_i})$ 最小。一個屬於 $C_{\text{velocity}} \cap C_{\text{image}}$，且又使成本函數最小的 $\Delta\mathbf{s}$ 可由以下的演算法[18]得到：任取一 $\mathbf{x}_0 \in C_{\text{velocity}} \cap C_{\text{image}}$ 為初始值，並令

$$\mathbf{x}_{n+1} = (1-\lambda_n)\mathbf{x}_n + \lambda_n P_{C_{\text{velocity}} \cap C_{\text{image}}}\left[(1-\gamma)\mathbf{x}_n + \gamma\sum_{i=1}^{M} w_i P_{C_{\Delta t_i}}(\mathbf{x}_n)\right], n \geq 0 \quad , \tag{27}$$

則 $\Delta\mathbf{s} = \lim_{n\to\infty}\mathbf{x}_n$ 即為所求。我們稱這個演算法為演算法二。

在本年度中，我們將演算法一及演算法二應用於以線性陣列探頭進行有限角度之超音波穿透式斷層掃描的聲速分佈影像重建。利用模擬所產生的飛行時間差資料，我們發現相較於演算法一，演算法二可大幅提高準確度。

4. 以模擬檢驗演算法一應用於有限角度之超音波穿透式斷層掃描的效果：

利用線性陣列進行穿射式超音波斷層掃描，可重建出物體中的聲速分佈[19]，[20]。如圖三所示，在陣列中選定發射位置及接收位置，以取得此一發射／接收組合下的金屬反射面回音信號。根據回音信號和發射信號之間的時間延遲，可取得聲波沿著由發射位置、反射面及接收位置所組成的路徑傳播所需的飛行

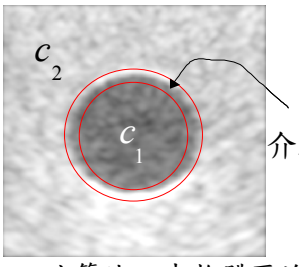

介於 c_1 和 c_2 之間

圖二 演算法二中物體區塊資訊的利用方式。

表一 電腦模擬時使用的參數。其中 c_∞ 為時間頻率 f 極大時的聲速。當 f = 5 MHz 時，在腺體組織、脂肪和腫瘤中的聲速分別為 1515.0 m/s、1468.3 m/s 和 1542.7 m/s。

Material	Sound velocity c_∞ (m/s)	Density ρ $(\mathrm{g/cm^3})$	Absorption β at 5 MHz (dB/cm)	$\tau_1 = 20$ ns $(\kappa_1/\kappa_\infty)\times 10^3$	$\tau_2 = 200$ ns $(\kappa_2/\kappa_\infty)\times 10^3$
Glandular	1521	1.05	5.68	10.76	10.34
Fat	1471	0.94	2.68	4.91	4.72
Tumor	1549	1.12	7.39	14.27	13.71

時間差。當所有發射／接收組合的信號都已量測後，便可取得一組飛行時間差資料，用以重建出物體中的聲速分佈及衰退係數分佈[6]。

我們用來檢驗演算法一的物體結構如圖一(c)所示。物體的背景為腺體組織，中心含有一個半徑為 4 mm 的脂肪圓柱，材料的參數列於表一中[4]，[21]。每一陣列通道皆具有 Gaussian 頻率響應，中心頻率為 5 MHz，雙程–12 dB 頻寬為 3 MHz。陣元間距為 0.45 mm，陣列和金屬反射面的距離為 35 mm。陣元數則分成三個案例，分別是 312 (4×)、156 (2×) 和 78 (1×)，以檢驗陣列大小和重建準確度的關係。

我們使用計畫成果第 2 項的技術來產生飛行時間資料。由 relaxation absorption 所造成的聲速對頻率的依賴關係由下式[22]決定：

$$c(f)=\sqrt{\frac{2}{\rho}}\left\{\kappa_\infty+\sum_{q=1}^{2}\frac{\kappa_q}{1+4\pi^2\tau_q^2 f^2}+\left[\left(\kappa_\infty+\sum_{q=1}^{2}\frac{\kappa_q}{1+4\pi^2\tau_q^2 f^2}\right)^2+\left(\sum_{q=1}^{2}\frac{2\pi\kappa_q\tau_q f}{1+4\pi^2\tau_q^2 f^2}\right)^2\right]^{\frac{1}{2}}\right\}^{-\frac{1}{2}}, \quad (28)$$

其中 ρ 為密度，$\kappa_\infty = 1/\rho c_\infty^2$，$c_\infty$ 為頻率 f 極大時的聲速，τ_q 和 κ_q 分別為第 q 階的 relaxation process 之 relaxation time 和 relaxation modulus。圖四所示為在案例1× 中第 39 通道發射時，不同通道接收到的包絡線資料，其中

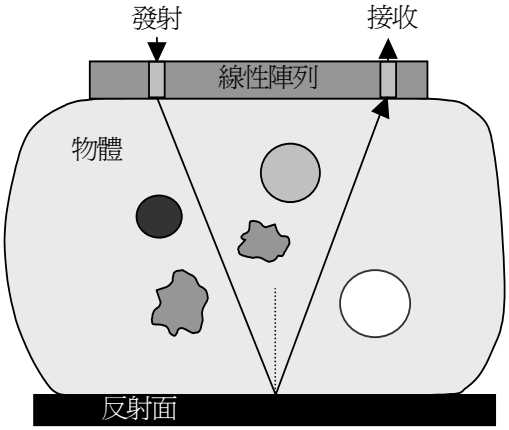

圖三 有限角度之超音波穿透式斷層掃描成像設備。

幾何延遲已經補償。我們透過計算包絡線平方後的重心位置來取得飛行時間資料。由圖四可看出脂肪圓柱造成飛行時間誤差和波形失真。在取得時間延遲後，我們使用演算法一，取 $c_{\text{lower}} = 1450$ m/s 和 $c_{\text{upper}} = 1580$ m/s 來重建中間 35 mm 寬度的聲速分佈。圖五(a)、(b)，圖五(c)、(d)及圖五(e)、(f)分別顯示案例 4×、2× 和 1× 的重建結果。左欄顯示聲速分佈，右欄顯示聲速誤差，其中聲速誤差定義為 5 MHz 時聲速重建值和真正值的差值的絕對值。由圖五可知當陣列較大時重建結果較好。為了將準確度量化，我們定義

$$|\Delta c| = \frac{1}{N_{\text{fat}}}\sum_{(m,n)\in I_{\text{f}}}\left|c(m,n)-c_{\text{f,true}}\right|, \quad (29)$$

其中 $c(m,n)$ 為聲速的重建值，$c_{\text{f,true}} = 1468.3$ m/s 為 5 MHz 時脂肪區域的真正聲速，I_{f} 是脂肪區域的索引集，N_{fat} 是 I_{f} 中的元素個數。當 $|\Delta c|$ 較小時表示準確度較高。案例 4×、2× 和 1× 的 $|\Delta c|$ 值分別為 11.8、19.9 和 28.5 m/s。

案例 4× 的結果比 2× 和 1× 好，但是使用的陣列已經太大(140.4 mm)，不適用在臨床上。因此，要靠增加陣列尺寸來改善有限角度之超音波穿透式斷層掃描的聲速影像重建品質並不實際。也就是說，使用演算法一，只用

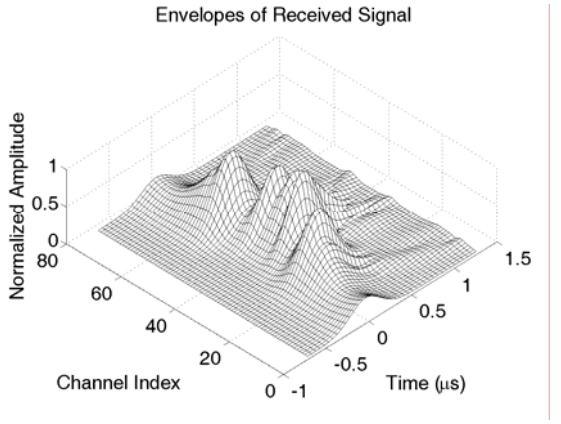

圖四 案例1× 中第 39 通道發射時，不同通道接收到的包絡線資料，其中幾何延遲已經補償。

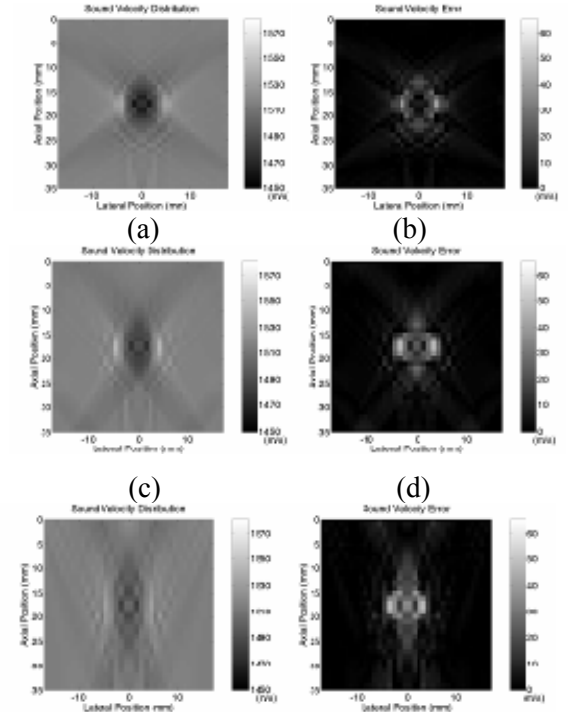

(a) (b) (c) (d) (e) (f)

圖五 (a)(b)案例4×、(c)(d)2×和(e)(f)1×的重建結果。

飛行時間資料配合聲速上下限的設定所能取得的聲速估計並不夠準確。

5. 以模擬檢驗演算法二應用於有限角度之超音波穿透式斷層掃描的效果：

本年度我們也用模擬驗證演算法二的效果。我們利用 B-mode 影像提供的物體區塊資訊來幫助重建聲速分佈，而飛行時間資料的產生方式則和驗證演算法一時所用的方式相同。

此部分的工作所考慮的所有範例，皆使用具有 234 個陣元、陣元間距為 0.15 mm 的陣列，而陣列和金屬反射板的距離是 35 mm。當產生飛行時間資料時，陣列中每三個通道只有一個被使用。另外，$c_{\text{lower}} = 1450$ m/s 而 $c_{\text{upper}} = 1580$ m/s。

我們利用計畫成果第一項所建立的波傳遞模擬器來產生所有的 B-mode 影像。為了模擬出合理的斑點(speckle)影像，我們在不同區域加上不同程度的隨機密度擾動，以造成聲阻抗不區配，進而造成散射。空間複合法(spatial compounding) [23]則被用來降低斑點強度的變異程度。我們只使用八個通道(通道 27、53、79、105、130、156、182 和 208)來發射信號以減少計算時間，且當通道 i 發射時，只有符合 $|j-i| \le 26$ 條件的接收通道 j 被使用。每次發射都產生一張子影像，而八張子影像經空間複合法產生一張複合 B-mode 影像。為了進一步降低斑點雜訊，我們將複合 B-mode 影像通過一個 $1/e$ 截止(cutoff)在 0.152 mm 的二維低通 Gaussian 濾波器以產生最後的 B-mode 影像，並施加單一的門檻(threshold)於這個影像以取得物體的區塊資訊。

我們首先考慮圖六(a)所示的物體，其背景為腺體組織，中心含有一個半徑為 4 mm 的脂肪圓柱。施加於圓柱和背景的密度隨機擾動分別為 0.5%和 2.5%。模擬所得的 B-mode 影像如圖六(b)所示，而施加門檻於此 B-mode 影像所取得的脂肪區域則如圖六(c)所示。藉由形態擴張(morphological dilation) [24]，脂肪區域和背景間的邊界可由脂肪區域直接導出，如圖六(d)所示。

重建的聲速分佈和聲速誤差的影像分別顯示在圖七(a)和(b)中。這個例子在表二中被稱為案例 i。重建的脂肪區域聲速($c_{\text{c,recon}}$)為 1465.7 m/s，和 5 MHz 時脂肪的真正聲速($c_{\text{c,true}} = 1468.3$ m/s)只差 2.6 m/s，而重建的背景聲速 $c_{\text{b,recon}}$ 和 5 MHz 時腺體組織的真正聲速($c_{\text{b,true}} = 1515.0$ m/s)相同，此處的下標 c 和 b 分別代表圓柱和背景。為了驗證演算法二的效果，我們進一步考慮具有不同幾何結構和物理參數的物體，並將這些參數和對應的重建結果列於表二中。我們也將重建結果顯示於圖七至圖九中，並以案例 i 為基準。在圖七中，我們顯示圓柱的大小所造成的影響；在圖八中，我們顯示圓柱中的聲速不同時所造成的影響；而

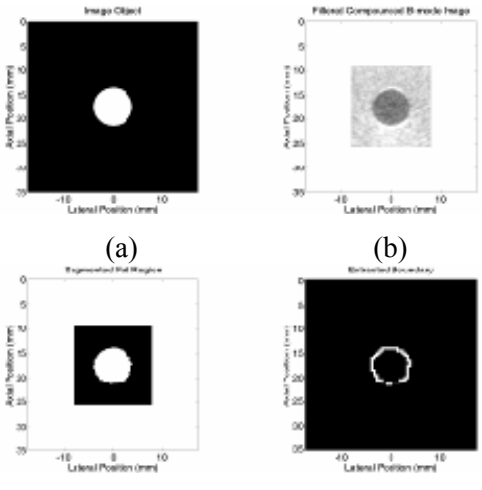

(a) (b) (c) (d)

圖六 (a)物體結構。(b)30-dB 動態範圍的 B-mode 影像。(c)脂肪區域。(d)脂肪區域和背景間的邊界。

表二 不同案例的物理參數和結果。Δc_c 和 Δc_b 是由 B-mode 影像導出邊界所得的結果，而 Δc_b^* 和 Δc_c^* 則是邊界完全匹配原始邊界時所得的結果。所有案例的 $c_{b,true}$ 值皆為 1515.0 m/s。

Case	$c_{c,true}$ (m/s)	Cylinder radius (mm)	Δc_c (m/s)	Δc_c^* (m/s)	Δc_b (m/s)	Δc_b^* (m/s)	Cylinder position
i	1468.3	4	–2.6	1.5	0.0	0.1	Center
ii	1468.3	2	–0.1	5.8	0.1	0.1	Center
iii	1468.3	6	–1.4	0.4	0.0	0.0	Center
i	1468.3	4	–2.6	1.5	0.0	0.1	Center
iv	1493.2	4	–2.8	–0.1	0.0	0.0	Center
v	1505.8	4	–2.5	–1.3	0.0	0.0	Center
vi	1568.0	4	2.0	–5.6	0.1	0.0	Center
i	1468.3	4	–2.6	1.5	0.0	0.1	Center
vii	1468.3	4	–1.2	1.9	0.0	0.1	5.5 mm above the center
viii	1468.3	4	–2.2	1.3	0.0	0.0	5.5 mm below the center

圖九考慮的是圓柱的位置。我們定義誤差為

$$\Delta c_{(\cdot)} = c_{(\cdot),\mathrm{recon}} - c_{(\cdot),\mathrm{true}} \quad , \tag{30}$$

此處 (·) 代表 b 或 c。在所有案例中，背景區域的聲速誤差幾近零，然而圓柱區域的誤差就較大。圖七(a)、(b)，圖七(c)、(d)及圖七(e)、(f)分別顯示圓柱半徑為 4 mm、2 mm 和 6 mm 時的估計結果，左欄顯示聲速分佈，右欄顯示聲

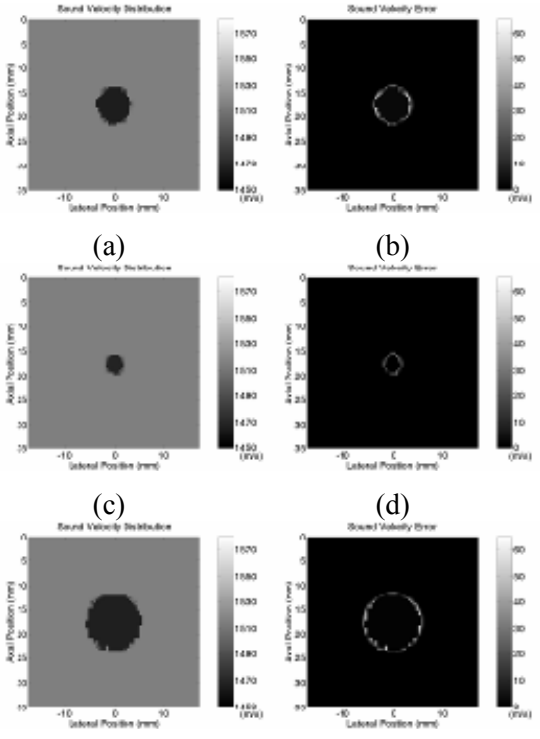

圖七 (a)(b)案例 i、(c)(d) ii 和(e)(f) iii 的重建結果。

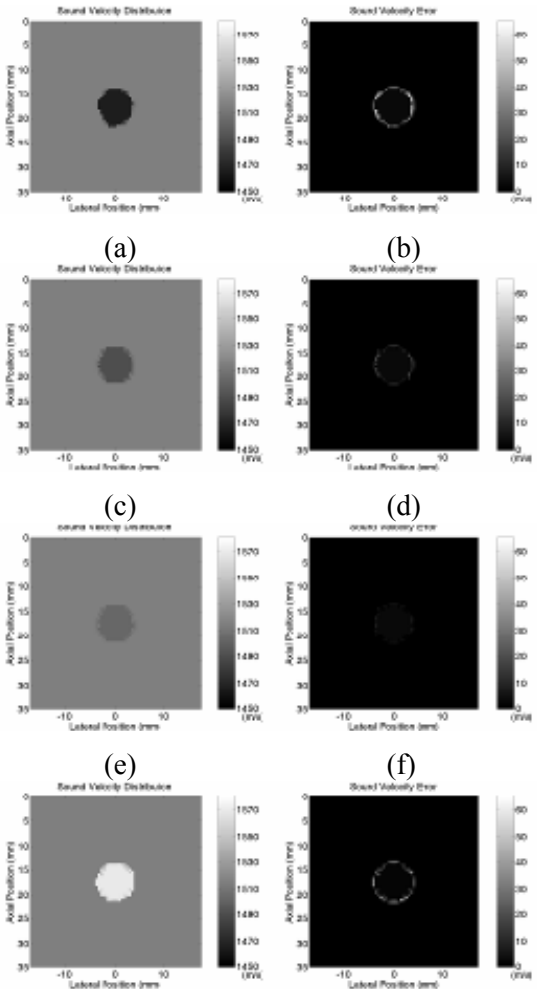

圖八 (a)(b)案例 i、(c)(d) iv、(e)(f) v 和(g)(h) vi 的重建結果。

速誤差。Δc_c 值分別為–2.6 m/s、–0.1 m/s 和–1.4 m/s，而 Δc_b 值分別為 0.0 m/s、0.1 m/s 和 0.0 m/s。圖八(a)、(b)，圖八(c)、(d)，圖八(e)、(f)及圖八(g)、(h)分別顯示圓柱聲速值($c_{c,true}$)為 1468.3 m/s、1493.2 m/s、1505.8 m/s 和 1568.0 m/s 時的估計結果。Δc_c 值分別為–2.6 m/s、–2.8 m/s、–2.5 m/s 和 2.0 m/s，而 Δc_b 值分別為 0.0 m/s、0.0 m/s、0.0 m/s 和 0.1 m/s。圖九(a)、(b)，圖九(c)、(d)及圖九(e)、(f)分別顯示圓柱在中心、較高及較低位置時的估計結果。Δc_c 值分別為–2.6 m/s、–1.2 m/s 和–2.2 m/s，而 Δc_b 值皆為零。

我們也考慮一個較複雜的物體，其結構如圖十(a)所示，背景為腺體組織，並含有三個半徑為 4 mm 的圓柱。位於左上角的第一個圓柱之物理參數除了 $c_{c,1,\infty} = 1496$ m/s 外，皆設為脂肪的物理參數，而下標 c 和 1 代表第一個圓柱，下標∞代表高頻。位於右上角的第二個圓柱設定為腫瘤，位於下方的的第三個圓柱則設定為脂肪區域。施加於三個圓柱和背景的密度隨機擾動分別為 0.5%、0.5%、0.89%和 2.5%。圖十(b)顯示 B-mode 影像，而圖十(c)為施加–14 dB 的門檻於 B-mode 影像所得的結果。在此案例中，背景中內含數個隨機分佈的小區域，它們可以藉由施加一面積門檻來移除，以得到圖十(d)所示之邊界。重建

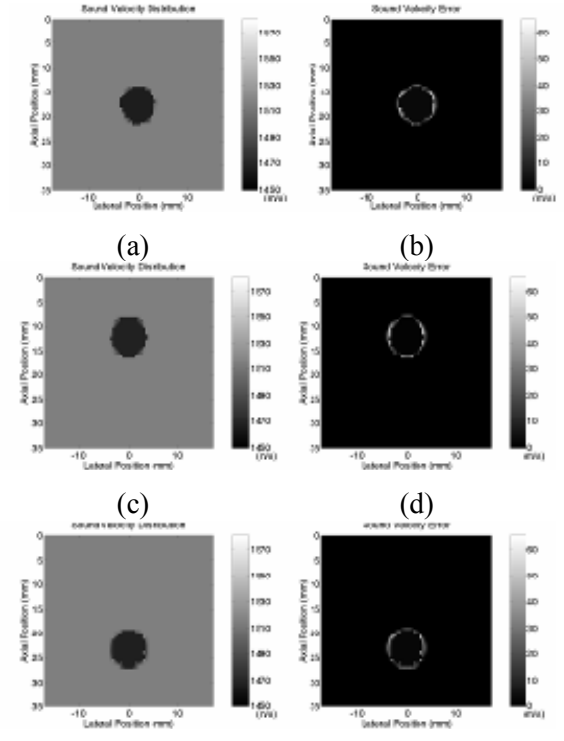

(a) (b) (c) (d) (e) (f)

圖九 (a)(b)案例 i、(c)(d) vii 和(e)(f) viii 的重建結果。

的聲速分佈和聲速誤差的影像分別顯示在圖十 (e) 和 (f) 中，而 $\Delta c_b = 0.3$ m/s、$\Delta c_{c,1} = -3.2$ m/s、$\Delta c_{c,2} = 1.2$ m/s、$\Delta c_{c,3} = 0.4$ m/s。

綜合來說，在所有考慮的案例中，使用演算法二所得的聲速誤差大致在 1–3 m/s。雖然為了減少計算時間，我們考慮的都是圓柱結構的物體，但演算法二並不受限於任何 region of interest (ROI)的形狀。因此，模擬結果顯示，使用現行的 B-mode 成像設備，以線性陣列來取得聲速分佈是可行的。

6. 使用模擬資料分析演算法二之效能：

因為演算法二使用區塊資訊來輔助聲速分佈的重建，邊界取得的準確度會直接影響到重建的準確度。我們將表二中所列的八個案例以真正的邊界取代 B-mode 影像所導出的邊界，然後重新估計聲速值，並將結果記為 Δc_c^* 和 Δc_b^* 列在表二中。一般而言，當 ROI 的面積較小時，偵測面積有誤差時的影響就會較大，這點可由比較案例 i 至 iii 的結果看出。

在邊界上重建誤差較大，主要是由於折射效應較嚴重。然而，由於在軟組織中並不會有急速變化的邊界發生，在邊界上真正的聲速

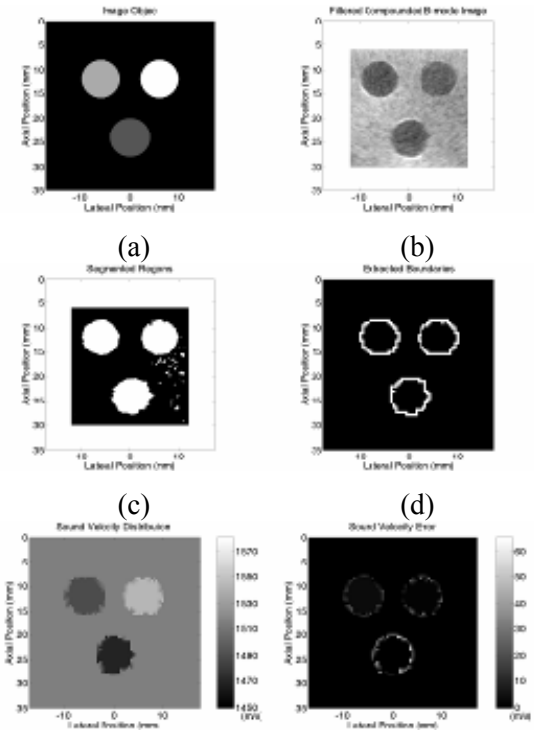

(a) (b) (c) (d) (e) (f)

圖十 (a)物體結構。(b)30-dB 動態範圍的 B-mode 影像。(c)區塊資訊。(d)邊界。(e)聲速分佈。(f)聲速誤差。

表三 重建準確度和等效陣元間距的關係。第一欄的 n 值意指陣列中每 n 個通道取一個出來用，因此等效陣元間距為 $n\times0.15$ mm。我們考慮的物體配置是前項工作成果中的案例 i(見表二)。

Effective pitch over 0.15 mm	Total number of channels	Δc in cylinder (m/s)	Δc in glandular material (m/s)
1	234	–2.6	0.0
2	117	–2.6	0.0
3	78	–2.6	0.0
4	59	–2.6	0.0
5	47	–2.7	0.0
6	39	–2.8	0.0
7	34	–2.2	0.0
8	30	–2.6	0.0
10	24	–3.7	0.0
12	20	–2.5	0.0
15	16	–3.7	0.1
20	12	–0.2	0.0

值並不具特別的意義。此外，判斷一 ROI 為何種組織是依據此 ROI 內的聲速值，和邊界上的聲速值無關，因此這對演算法二的有效性沒有影響。

我們也評估了當陣列大小固定時，所使用通道數對聲速重建準確度的影響。這部分所考慮的物體配置是前項工作成果中的案例 i，結果列於表三中。我們發現使用較多的通道並不一定得到較好的準確度。事實上，只使用 12 個通道和 3 mm 的等效陣元間距，即可得到準確的結果。使用演算法二時聲速估計的準確度對陣元間距不敏感，是因為飛行時間資料之間存在著主要由折射造成的不一致(inconsistencies)。當資料量增加時，這種不一致不一定會降低，因此準確度也就不一定提升。

在評估演算法一的效能時，我們使用的陣元間距是 0.45 mm，而表三第三列也是陣元間距為 0.45 mm 時的結果。比較後可知利用到區塊資訊的演算法二效能比演算法一好。

7. 建立可使用線性陣列探頭進行有限角度之超音波穿透式斷層掃描的實驗系統：

本年度已成功建立一個可使用線性陣列探頭進行有限角度之超音波穿透式斷層掃描的實驗系統[7]，架構如圖十一(a)所示，實體則如圖十一(b)所示。線性陣列(L6/128，STI，State College，PA)具有 128 個通道，陣元間距為 0.3 mm，elevation 寬度為 5 mm，elevation 焦距為 25 mm。陣列通道的中心頻率為 5.57 MHz，–6 dB 頻寬為 4.10 MHz。我們使用一個可由任何選定的通道發射使用者自定信號的可程式化數位陣列系統(digital array system，DiPhAS，Fraunhofer IBMT，Ingbert，Germany)[25]來擷取通道資料。所有通道資料皆透過插在電腦中的一張數位輸入輸出卡(PCI-7300A，ADLINK，台北縣，台灣)由 DiPhAS 傳送到電腦儲存並做進一步的信號處

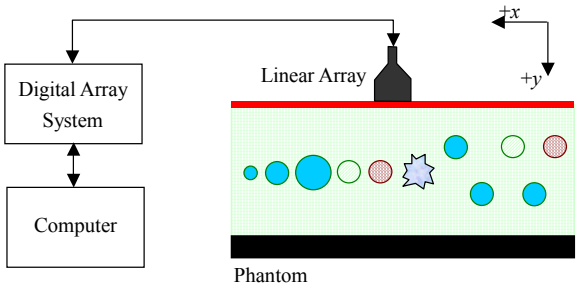

(a)

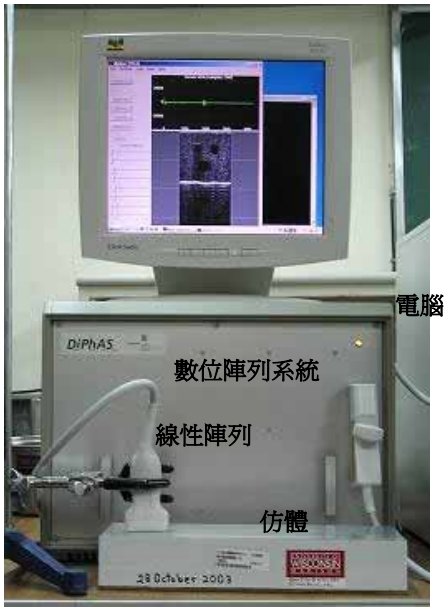

(b)

圖十一 (a)實驗系統架構圖。(b) 實驗系統照片。

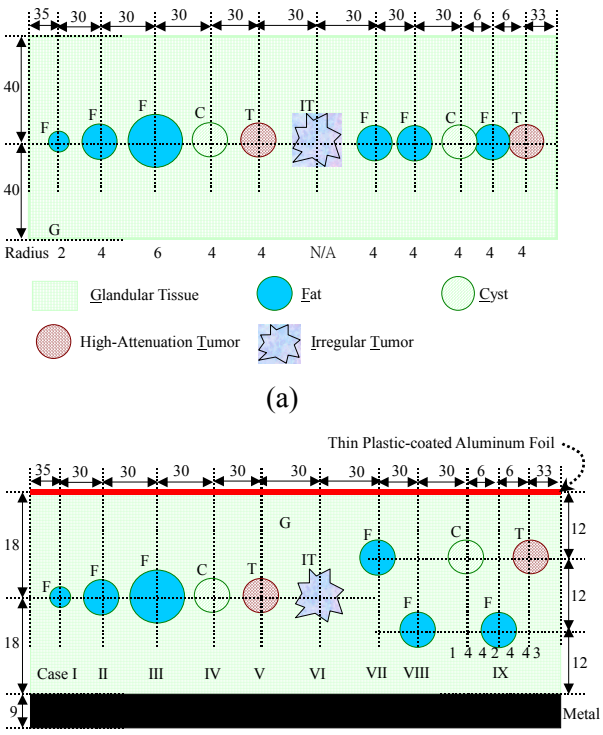

圖十二 (a)仿體的上視圖與(b)側視圖。

理。DiPhAS 原本只能支援 64 個通道，經修改後可以支援 128 個通道，但是發射通道和接收通道的編號不能相差 64，因為這些通道共用同一個多工器(multiplexer)。

8. 以實驗檢驗演算法二應用於有限角度之超音波穿透式斷層掃描的效果：

我們利用前項工作成果所建立的實驗系統配合一個仿體來檢驗演算法二應用於有限角度之超音波穿透式斷層掃描的效果。仿體委託 Dr. Ernest Madsen (Departmentof Medical Physics，University of Wisconsin-Madison，WI)製造，其上視圖和側視圖分別如圖十二(a)和圖十二(b)所示。仿體中不同材料用來模仿乳房中不同的組織，它們的參數由 Dr. Madsen 提供，列於表四中。藉由將陣列沿 x 方向移動，我們一共評估了九個案例，如表五所列。

DiPhAS 的發射波形可以任意調整，在擷取通道資料時，我們選用的波形是一週的方

表四 仿體中材料的參數。

Material	Sound velocity c at 5 MHz and 22 ℃ (m/s)	Density ρ (g/cm^3)	Attenuation coefficient α at 5 MHz (dB/cm)	B-mode contrast relative to glandular tissue (dB)
Glandular tissue	1522	1.03	2.74	—
Fat	1464	0.94	2.21	–14
Cyst	1570	1.02	0.78	<–14
High-attenuation tumor	1547	1.10	7.36	–12
Irregular tumor	1553	1.07	4.26	–10

表五 九個實驗案例的配置和估計結果。

Case	ROI	Sphere radius (mm)	ROI position	Δc_{ROI} (m/s)	Δc_{G} (m/s)
I	Fat	2	Center	2.6	0.3
II	Fat	4	Center	4.5	0.3
III	Fat	6	Center	4.3	0.2
IV	Cyst	4	Center	3.9	0.3
V	High-attenuation tumor	4	Center	10.5	–0.2
VI	Irregular tumor	N/A	Center	11.5	0.9
VII	Fat	4	6 mm above the center	4.9	0.6
VIII	Fat	4	6 mm below the center	2.5	0.0
IX-1	Cyst	4	Upper-left corner	0.6	0.6
IX-2	High-attenuation tumor	4	Upper-right corner	9.5	
IX-3	Fat	4	6 mm below the center	0.9	

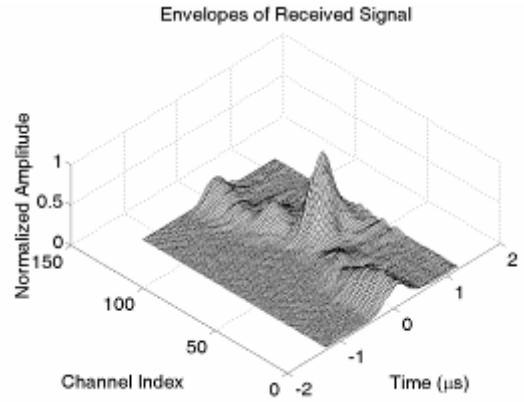

圖十三 案例 VIII 中第 64 通道發射時，不同通道接收到的包絡線資料，其中幾何延遲已經補償。

波，持續 $0.2\mu s$。所有的通道資料 $e_{ij}(t)$ (其中 i 為發射通道，j 為接收通道)皆以 40 MHz，12 位元解析度取樣。對每一發射／接收組合，們皆以 16 次平均來提高訊雜比。為了由通道資料 $e_{ij}(t)$ 取出飛行時間差 Δt_{ij}，我們先計算出成像物體為均勻介質時的飛行時間 $t_{ij,0}$，再找出以 $t_{ij,0}$ 為中心，長度為 $e_{ij}(t)$ 的包絡線峰值 e_{p}，並將飛行時間 t_{ij} 設為包絡線穿過此頂峰上升緣 $\frac{1}{2}e_{\mathrm{p}}$ 位置的時間。飛行時間差 Δt_{ij} 即為 t_{ij} 和 $t_{ij,0}$ 的差值。圖十三所示為在案例 VIII 中第 64 通道發射時，不同通道接收到的包絡線資料，其中幾何延遲已經補償。

空間複合法[23](使用五個子孔徑，中心分別在通道 22、43、65、86 和 107，每個子孔徑皆有 43 個通道)被用來降低 B-mode 影像中斑點強度的變異程度。我們使用動態聚焦和動態孔徑大小(F-number 設為 1)來成出五張子影像，所有子孔徑的 steering 角皆限制在 $\pm 45^{\circ}$。在每個畫素，所有有貢獻的子孔徑的信號平均後就得到一張 B-mode 影像。為了進一步降低斑點雜訊，我們將複合 B-mode 影像通過一個 $1/e$ 截止在 0.152 mm 的二維低通 Gaussian 濾波器以產生最後的 B-mode 影像。得到此影像後，我們施加單一的門檻以取得物體的區塊資訊，並移除面積小於 π mm^2 的小區域。

對大部分的案例(案例 I–IV、VII 和 VIII)而言，用以上的程序即可取得 ROIs。但是我們在施加門檻後會再以形態擴張和侵蝕(erosion)[24](對案例 V、VI 和 IX 屬必要)移除 ROI candidates 中的洞並使邊界更規則。最後，藉由形態擴張，ROIs 和背景間的邊界可

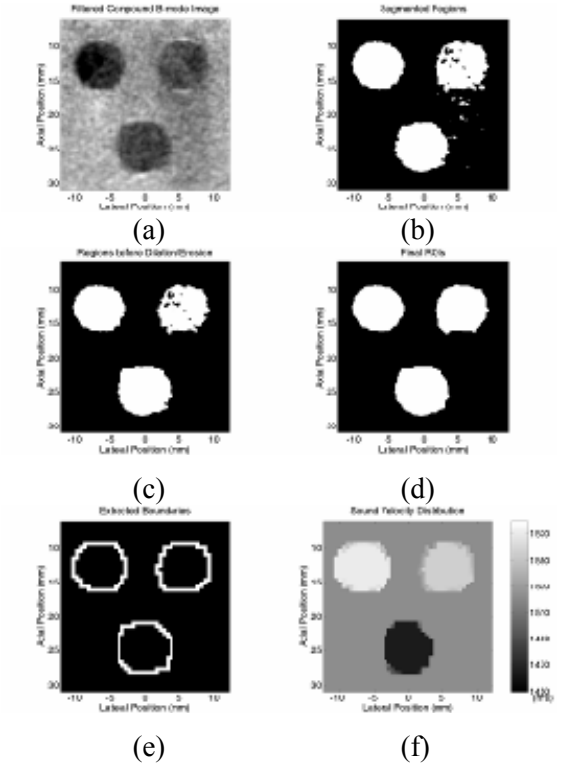

圖十四 案例 IX 的評估。(a)30-dB 動態範圍的 B-mode 影像。(b)原始的區塊資訊。(c)移除小於 π mm^2 的區域後之二元影像。(d)以形態擴張和侵蝕處理過後所得的 ROIs。(e)邊界。(f)聲速分佈。

由比較 ROIs 和它們對應的擴張版本直接導出。有了邊界，便可使用(26)式來設定 C_{image}。

圖十四(a)–(e)顯示以案例 IX 為範例時，不同步驟所得的結果。B-mode 影像以 30-dB 動態範圍顯示於圖十四(a)中；施加–16 dB 門檻後所得的二元影像如圖十四(b)所示；移除小於 π mm^2 的區域後之二元影像如圖十四(c)所示；以形態擴張和侵蝕處理過後所得的 ROIs 如圖十四(d)所示；圖十四(e)則顯示取出的邊界。

我們使用演算法二重建聲速影像，其中 $c_{\mathrm{lower}} = 1450\,\mathrm{m/s}$，$c_{\mathrm{upper}} = 1580\,\mathrm{m/s}$，結果列於表五中。案例 IX 所得的聲速分佈顯示於圖十四(f)中。定義誤差為

$$\Delta c_{(\cdot)} = c_{(\cdot),\mathrm{recon}} - c_{(\cdot),\mathrm{true}}\ , \qquad (31)$$

其中 (·) 代表 F(脂肪)、C(囊腫)、T(高衰退腫瘤)、IT(不規則腫瘤)、G (腺體組織)或 ROI。$c_{(\cdot),\mathrm{true}}$ 為表五中所示的真正聲速值，而 $c_{(\cdot),\mathrm{recon}}$ 為重建的聲速值。在案例 IX 中，$\Delta c_{\mathrm{C}} = 0.6\,\mathrm{m/s}$，$\Delta c_{\mathrm{T}} = 9.5\,\mathrm{m/s}$，$\Delta c_{\mathrm{F}} = 0.9\,\mathrm{m/s}$，$\Delta c_{\mathrm{G}} = 0.6\,\mathrm{m/s}$。

案例 I–VIII 的 B-mode 影像和重建的聲速影像顯示於圖十五至十八中。圖十五至十七分別實證 ROI 大小、ROI 內聲速及 ROI 位置

對重建準確度的影響。所有案例背景的誤差都很小。圖十五(a)、(b)，圖十五(c)、(d)及圖十五(e)、(f)分別顯示脂肪圓球半徑為 2 mm、4 mm 和 6 mm 時的估計結果，左欄顯示 B-mode 影像，右欄顯示聲速分佈。Δc_{ROI} 值分別為 2.6 m/s、4.5 m/s 和 4.3 m/s，而 Δc_{G} 值分別為 0.3 m/s、0.3 m/s 和 0.2 m/s。圖十六(a)、(b)，圖十六(c)、(d)及圖十六(e)、(f)顯示球狀區域內為不同組織(依序為囊腫、脂肪和高衰退腫瘤)時的結果。Δc_{ROI} 值分別為 3.9 m/s、4.5 m/s 和 10.5 m/s，而 Δc_{G} 值分別為 0.3 m/s、0.3 m/s 和–0.2 m/s。圖十七(a)、(b)，圖十七(c)、(d)及圖十七(e)、(f)分別顯示脂肪圓球在較高、中心及較低位置時的結果。Δc_{ROI} 值分別為 4.9 m/s、4.5 m/s 和 2.5 m/s，而 Δc_{G} 值分別為 0.6 m/s、0.3 m/s 和 0.0 m/s。最後，圖十八(a)和(b)分別顯示案例 VI 的 B-mode 影像和聲速分佈。$\Delta c_{\mathrm{IT}} = 11.5$ m/s，$\Delta c_{\mathrm{G}} = 0.9$ m/s，而不規則腫瘤和腺體組織背景間的原始聲速差是 31 m/s。由圖十八(b)可看出取出的邊界有誤差，這影響到聲速估計的準確度。

雖然我們實驗所用的仿體內所含的物體具有三維結構，使用一維線性陣列配合演算法二來估計聲速仍然得到相當好的準確度，在 11 個 ROIs 中，有八個的誤差小於 5 m/s。即

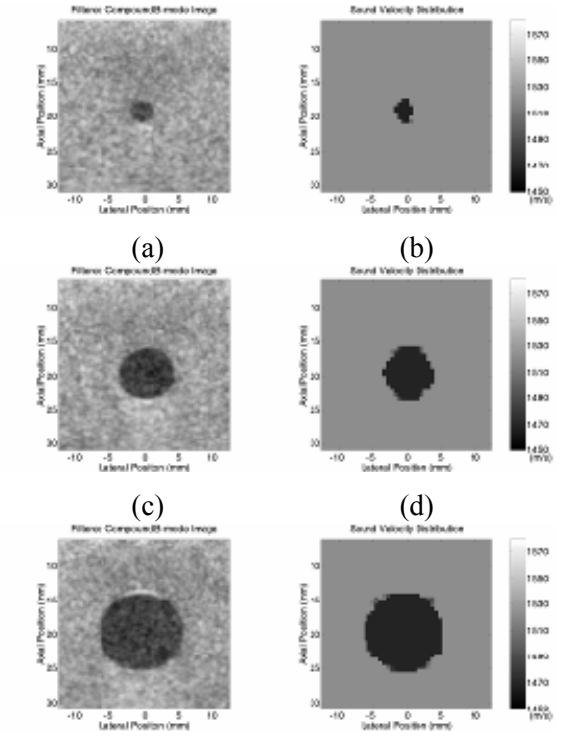

(a) (b) (c) (d) (e) (f)

圖十五 (a)(b)案例 I、(c)(d) II 和(e)(f) III 的重建結果。

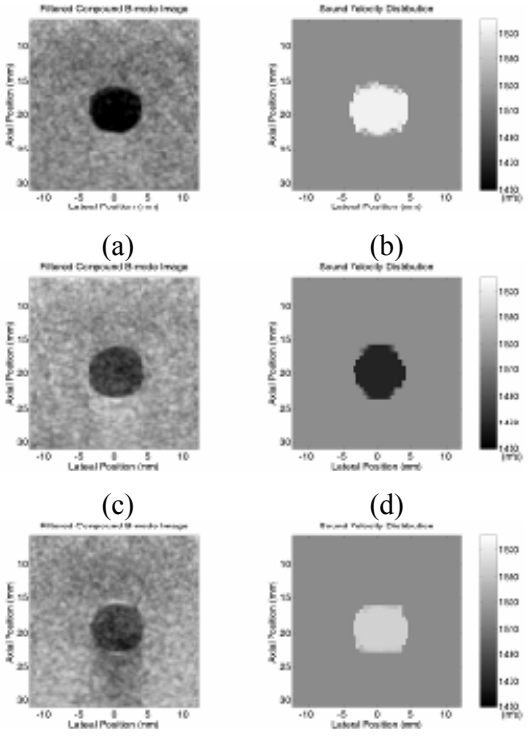

(a) (b) (c) (d) (e) (f)

圖十六 (a)(b)案例 IV、(c)(d) II 和(e)(f) V 的重建結果。

使腫瘤物體的估計值誤差較大，對這些案例而言，組織種類還是可能成功判別，因為我們知道 ROI 內的聲速比背景高，因此不可能是脂肪，而腫瘤的聲速一般而是比較高的。由仿體

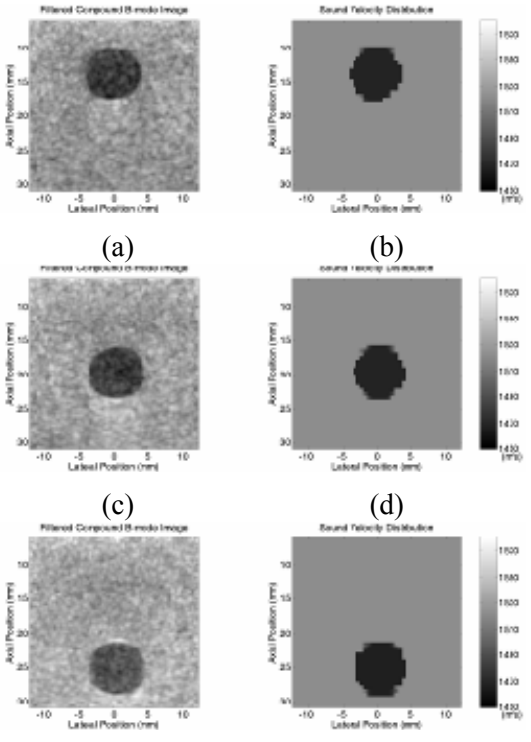

(a) (b) (c) (d) (e) (f)

圖十七 (a)(b)案例 VII、(c)(d) II 和(e)(f) VIII 的重建結果。

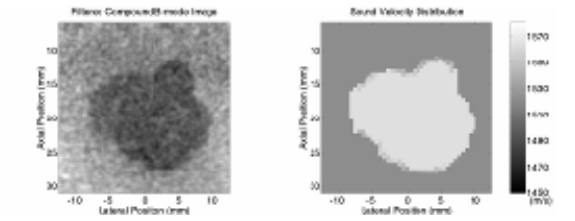

(a) (b)

圖十八 案例 VI 的(a) B-mode 影像和(b)聲速分佈。

的實驗結果，我們實證了使用現行的 B-mode 成像設備配合演算法二，以線性陣列來取得聲速分佈是可行的。

9. 使用實驗資料分析演算法二之效能：

為評估聲速誤差對 ROI 面積的敏感度，我們以人為的方式將案例 I 和 III 中的 ROI 改變，然後重新估計對應的聲速分佈。做法是將原始的 ROI 隨機在外邊界上加上畫素或在內邊界上移除畫素以產生新的 ROI，而對任一 ROI 總面積，我們皆產生十個 ROIs。圖十九(a)和(b)分別顯示案例 I 和 III 中平均聲速差(新估計值和原估計值的差)對 ROI 面積差的曲線，其中 ROI 面積差已除以實際面積(案例 I 和 III 分別是 4π mm^2 和 36π mm^2)。另外，圖十九也將代表一個標準差的 error bars 畫出，而 ROI 面積差為零時標準差也為零是因為此時沒有任何隨機產生的新 ROI。當 ROI 面積差小於±5%時平均聲速差小於±3 m/s。

實驗結果顯示 ROI 的聲速誤差傾向為正值。一個可能原因是脂肪(囊腫、高衰退腫瘤或不規則腫瘤)在 B-mode 影像中相對於原尺寸會擴張(收縮)，因為較低(較高)的聲速等效於較長(較短)的距離。由於背景的面積遠大於 ROI 面積，聲速估計值對背景聲速誤差的敏感度大於對 ROI 聲速誤差的敏感度。因此，重建出來的背景聲速只會稍微被影響，但當 ROI 面積增加時，ROI 和背景的聲速差的絕對值會傾向於降低。另一可能的誤差來源是折射效

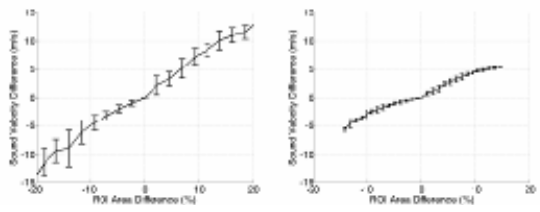

(a) (b)

圖十九 (a)案例 I 和(b)案例 III 中平均聲速差對 ROI 面積差的曲線。

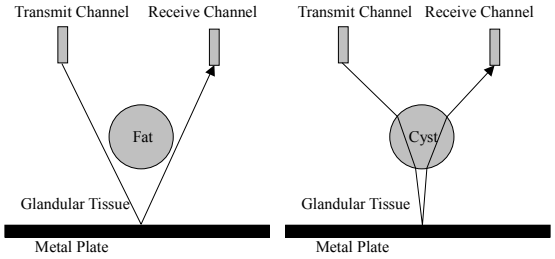

(a) (b)

圖二十 (a)案例 II 和(b)案例 IV 對應的射線軌跡圖。

應。圖二十(a)和(b)分別顯示案例 II 和 IV 對應的射線軌跡圖(ray-tracing diagrams)，由這兩個圖可看出案例 IV 被圓球影響到飛行時間的發射／接收組合數會比案例 II 多。因此，當量測飛行時間資料時，ROI 內聲速較高時有效面積就會加大，造成重建聲速分佈時相比之下 B-mode 影像中的 ROI 面積等效上被縮小了。

10. 建立可進行傳統電腦斷層掃描之實驗系統：

我們建立的實驗系統如圖二十一所示。實驗時使用者透過電腦控制整個系統，包括水槽的運動及超音波信號的發射、接收和貯存。乳房仿體固定於水槽中，位置相對於水槽不動。兩相對的超音波探頭分別置於仿體兩側，一發射一接收，位置相對於地球不動。水槽以馬達帶動，進行 x 方向的移動，並可以繞 z 軸旋轉，目的是帶著仿體移動和旋轉，以收集斷層掃描所需的投影。此外，兩探頭也可以手動的方式沿 z 軸移動，以調整高度來對不同的橫切面成像。超音波信號透過脈波產生接收器(PR5077，Panametrics，Waltham，MA)產生，再送至一中心頻率為5 MHz的發射探頭(V308

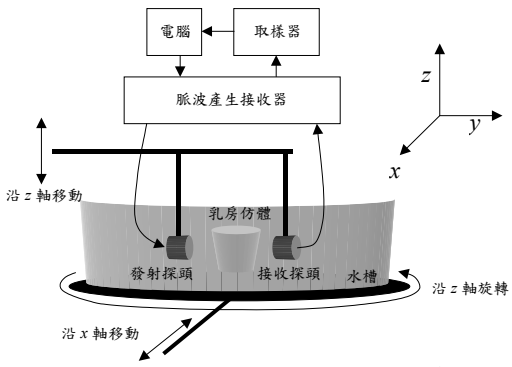

圖二十一 傳統電腦斷層掃描之實驗系統。

Panametrics)發射。信號經仿體傳遞至接收探頭(V308)，由脈波產生接收器放大再經過一個

解析度為 12 位元，取樣率為 100 MB/s 之取樣器(CompuScope 12100，Gage，Montreal，Quebec，Canada)取樣後送至電腦貯存和處理。由這個系統，可以建立仿體內部的聲速分佈。

在計畫的第二年度，我們已完成下列工作成果：

使用傳統超音波回波灰階影像來找尋乳房中的腫瘤常受限於乳房組織中聲速不均勻性[3]導致對比解析度的降低與乳癌偵測正確性的降低。然而，除了灰階影像外，聲速與衰減於乳房中的分布在診斷上是很有用的資訊，因為聲速在乳癌組織中較在脂肪中快速，衰減係數在乳癌組織中較在囊腫中大。故本研究致力於重建乳房中的聲速分佈與衰減係數分佈，以達到區分組之種類的目標，來降低陰性病理切片之比率。

在進入成果呈現以前，先來簡介一下此研究所需之演算法。

圖二十二為信號發射與接收示意圖。根據先前成果[6]-[8]以及[16]，使用水當作病人乳房信號的對照組。假設水中聲速(c_0)為1522 m/sec，其衰減係數(α_0)為0 dB/cm/MHz。若超音波信號之往返飛行時間(round-trip time-of-flight)分別為t_0於水中與t_1於乳房組織中，則：

$$t_0 = \int_L \frac{1}{c_0} dl = \int_L s_0 dl \tag{32}$$

$$t_1 = \int_L \frac{1}{c_1(x,y)} dl = \int_L s_1(x,y) dl \tag{33}$$

L為信號所經路徑，定義為慢度(slowness)。其中$s_1(x,y)$為聲速$c_1(x,y)$之倒數，則飛行時間差(Δt)為

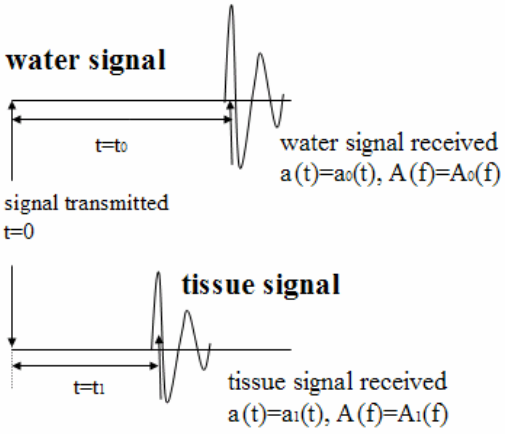

圖二十二　信號發射接收示意圖。

$$\Delta t = t_1 - t_0 = \int_L [s_1(x,y) - s_0] dl = \int_L \Delta s(x,y) dl \,. \tag{34}$$

又假設衰減在傳遞過程中與頻率成線性關係，則

$$\beta = \alpha f \quad \text{(dB/cm)} \tag{35}$$

以A_0與A_1分別代表信號在水中以及在乳房組織中之振幅，則：

$$\Delta A = -20 \log_{10} \left| \frac{A_1}{A_o} \right| \quad \text{(dB)} \tag{36}$$

$$\Delta A' = \int_L \alpha(x,y) dl \,\text{(dB/MHz)} \tag{37}$$

在此$\Delta A'$為在ΔA的頻譜中所得到的一階近似曲線(1st order polynomial curve fitting)之斜率。若將式(34)與式(37)中的積分形式寫成離散形式(discrete form)，則：

$$\Delta t_{ij} = \sum_{n=1}^{N} \sum_{m=1}^{M} \Delta s(m,n) l_{ij}(m,n) \tag{38}$$

$$\Delta A' = \sum_{n=1}^{N} \sum_{m=1}^{M} \alpha(m,n) l_{ij}(m,n) \tag{39}$$

接著在重建過程中，將灰階影像切割成N*M個像素(pixel)，且ij代表第i個陣元發射及第j個陣元接收。此外，若將式(38)與式(39)寫成矩陣的形式，則

$$L\Delta s = \Delta t \tag{40}$$

$$L\alpha = \Delta A' \tag{41}$$

圖二十三為臨床實驗系統架構圖，圖中右邊為臨床實驗擷取裝置，惟有金屬反射板才可讓整個實驗架構原理類似X光乳房攝影。系統中使用的線性陣列(L6/128，STI，State College，PA)具有128個通道，陣元間距為0.3 mm，中心頻率為5.57 MHz，–6 dB頻寬為4.10 MHz。我們使用一個可由任何選定的通道去發射使用者自訂信號的可程式化數位陣列系統(digital phased array system，DiPhAS，Fraunhofer IBMT，Ingbert，Germany)來擷取通道資料。經過一張數位I/O(input output)卡(PCI-7300A, ADLINK)後儲存於電腦，取樣頻率20 MHz。

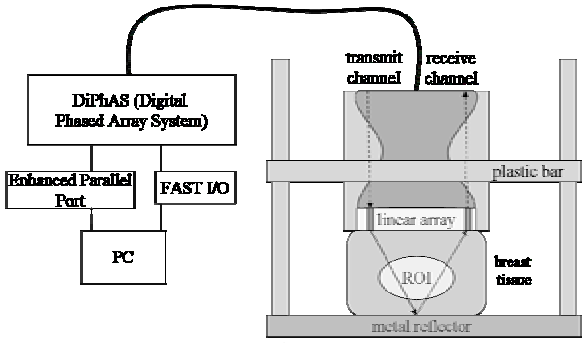

圖二十三　臨床實驗系統架構圖。

在計畫的第二年度，我們已完成下列工作成

果：

1. 利用手動圈選之使用者介面，建立臨床資料擷取裝置：

若知道乳房組織中的聲速分佈與衰減係數分佈將有助於判別病灶的種類。以先前仿體結果來說，可藉由乳房腺體聲速(約 1522 m/sec)將脂肪(約 1460 m/sec)與乳癌組織(約 1550 m/sec)、囊腫(約 1570 m/sec)區隔；再由乳房腺體組織衰減係數(約 0.50 dB/cm/MHz)將乳癌組織(約 1.10 dB/cm/MHz)與囊腫(約 0.10 dB/cm/MHz)區分。因此，在灰階影像圈選出有興趣區域後，即可計算背景(在此即指乳房腺體組織)與有興趣區域之聲速與衰減係數。

如圖二十四，在重建的灰階影像上，預先選取有興趣區域的程式，是透過 MATLAB 軟體中具使用者介面功能的指令來編寫，並使用滑鼠來控制選取。而此預先選取的另一個主要目的為給予一個重建限制，使得有興趣區域內外各自的聲速與衰減係數分佈各處相等。

如圖二十五，實線為行經有興趣區域的路徑，虛線為行經背景區域的路徑。根據上述的限制，有興趣區域內外各自的聲速與衰減係數分佈各處相等，則式(2.7)與式(2.8)可簡化為：

$$\Delta t_{ij} = \Delta s_{ROI}\sum_{n=1}^{N}\sum_{m=1}^{M} l_{ij,ROI}(m,n) + \Delta s_{back}\sum_{n=1}^{N}\sum_{m=1}^{M} l_{ij,back}(m,n)$$
$$= l_{ij,ROI}\Delta s_{ROI} + l_{ij,back}\Delta s_{back}. \quad (42)$$

$$\Delta A'_{ij} = \alpha_{ROI}\sum_{n=1}^{N}\sum_{m=1}^{M} l_{ij,ROI}(m,n) + \alpha_{back}\sum_{n=1}^{N}\sum_{m=1}^{M} l_{ij,back}(m,n)$$
$$= l_{ij,ROI}\alpha_{ROI} + l_{ij,back}\alpha_{back}. \quad (43)$$

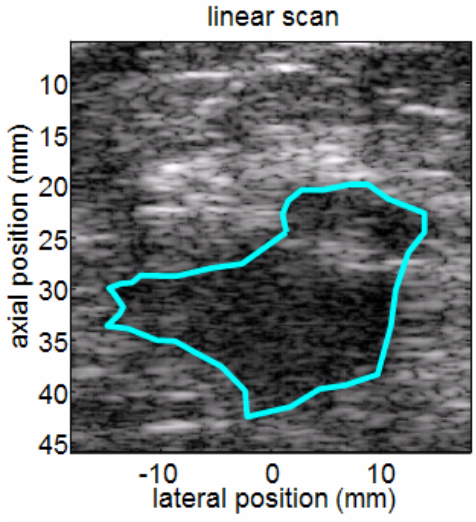

圖二十四　手動圈選的一個範例，此灰階影像為乳癌的病例。

式(42)與式(43)又可以化簡為

$$\begin{bmatrix} l_{ROI} & l_{back} \end{bmatrix}\begin{bmatrix} \Delta s_{ROI} \\ \Delta s_{back} \end{bmatrix} = \Delta t, \quad (44)$$

$$\begin{bmatrix} l_{ROI} & l_{back} \end{bmatrix}\begin{bmatrix} \alpha_{ROI} \\ \alpha_{back} \end{bmatrix} = \Delta A'. \quad (45)$$

其中，l_{ROI} 與 l_{back} 分別是在有興趣區域與背景中的總路徑長度。Δs 為兩者間的慢度差(待求得)，α 是其衰減係數(待求得)。Δt 是由接收信號估計所得之飛行時間差，$\Delta A'$ 是中心頻率 5 MHz 所對應之衰減量。

2. 臨床資料之取得：

實驗中使用一具有壓縮功能架構的裝置，如圖二十三右，調整螺絲以針對每次不同厚度的組織做壓縮，在取完乳房組織的信號後，馬上接著做水的對照組。使用一水袋內裝滿除去氣泡的水，置於探頭與金屬反射板間，取得對照組資料。臨床資料是由周宜宏醫師協助，在台北榮民總醫院超音波檢查室取得。目前總共 16 個病例，其中有興趣區域的分類如下：5 個惡性腫瘤病例，7 個纖維腺瘤病例，4 個脂肪病例，1 個油滴病例。惡性腫瘤的部分是配合追蹤病例來確認。

3. 最適化濾波器之設計：

由於聲速在乳房組織的不均勻性，造成接收信號在振幅與相位上嚴重的失真[26]-[30]，如圖二十六(a)與(b)，水的接收信號振幅與乳房組織信號振幅對照，明顯看出其振幅失真程度。因此，設計了一個最適化濾波器，使得修正後的乳房組織信號與水信號的振幅相似，來改善失真的問題。

若以 b 來代表乳房組織信號，以 w 來代表水的信號，以 f 代表欲設計出的最適化濾波

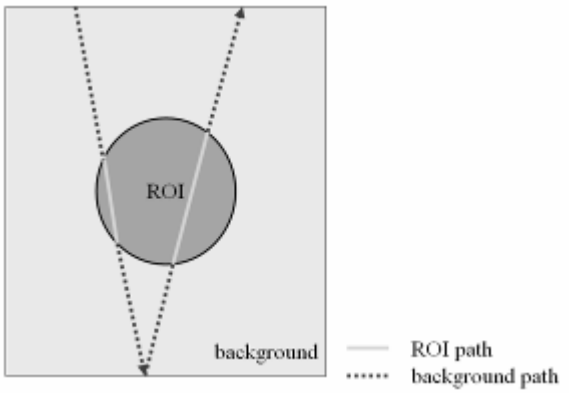

圖二十五　發射接收路徑中信號行走之示意圖。

器，最後以 d 代表理想輸出(desired output)，

則

$$b \otimes f = w \tag{46}$$

其中 w 為 b 與 f 的旋積(convolution)，若將其簡化成一個乘法，則

$$B \cdot f = w \tag{47}$$

其中 B 為 b 的旋積矩陣(convolution matrix)[31]。根據最小平方法(Least Square Method)，可由下列式子得到 f ：

$$f = (B'B)^{-1}B'w \tag{48}$$

最後我們所需要的輸出為 d ，故

$$B \cdot f' = d \tag{49}$$

其中 f' 是由 f 經下列兩步驟轉換而來：

步驟一：

讓信號頻譜頻率為零時之總能量比為 1(DC gain=1)，如此一來，衰減係數之計算才不至於失真。意即若 f 在頻譜頻率為 0 時之總能量為 k，則將其正規化(normalize)至 f /k，也就是 f'。

步驟二：

消除因信號傳遞時的延遲(delay)所造成的線性相位(linear phase)項。首先，先找到 f 的快速傅立葉轉換(fast Fourier transform, FFT)，交換(swap)FFT 左右兩邊，以及展開(unwrap)相位。接著，利用固定基頻(baseband)中固定 0 MHz 的那一點，消除線性相位項，使得新的相位分佈當作最適化濾波器的相位，也就是 f' 的相位。

圖二十六(c)與(d)分別為圖二十六(a)與(b)加窗(windowing)輸出。由圖可見，圖二十六(e)較圖二十六(b)與圖二十六(c)來得相似。圖二十七為加上最適化濾波器前與加上最適化濾波器後之相關係數的比較，加上最適化濾波器後相關係數全部有效提高至 0.75 以上，屬高度相關。

4. 使用最適化濾波器與演算法二所得之實驗結果：

使用最適化濾波器後，得到下列結果。圖二十八為相對聲速結果，發現存在著相對聲速上閾值(+50 m/sec)與下閾值(-50 m/sec)來區隔惡性腫瘤、纖維腺瘤以及脂肪。

[32]中，含有纖維腺瘤的平均背景聲速為 1529 m/sec，而含有惡性腫瘤的平均背景聲速為 1463m/sec。另外，由[33]知，惡性腫瘤的平均聲速為 1550±32 m/sec，纖維腺瘤的平均聲速為 1584±27 m/sec。由上可知，我們可以利用一個閾值(threshold)來分離惡性腫瘤與纖維腺瘤。

臨床上，脂肪與油滴(oil cyst)的灰階影像相似，但其聲速表現大不相同，油滴有較高之聲速，約 1540 m/sec，脂肪的聲速大約為 1460 m/sec [34]。圖二十八中，油滴表現出較高的相對聲速。

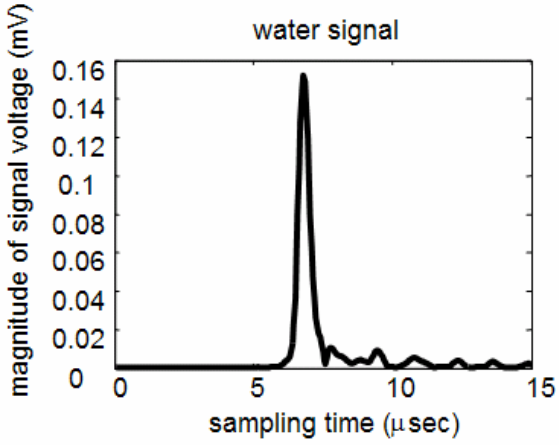

圖二十六（a） 水的信號振幅。

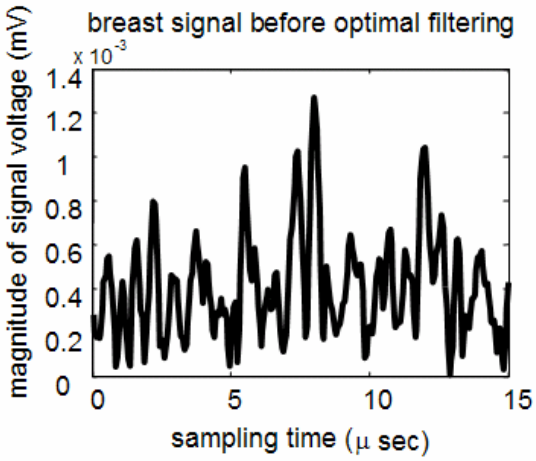

圖二十六 (b) 原始乳房組織的信號振幅，未加最適化濾波器。

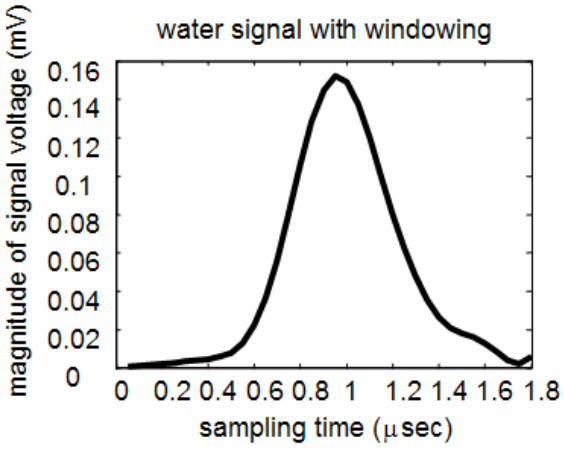

圖二十六（c） 加窗後的水信號。

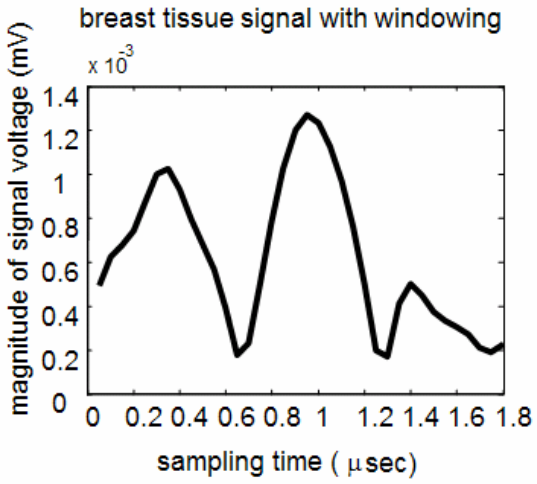

圖二十六 (d) 加窗的乳房組織信號。

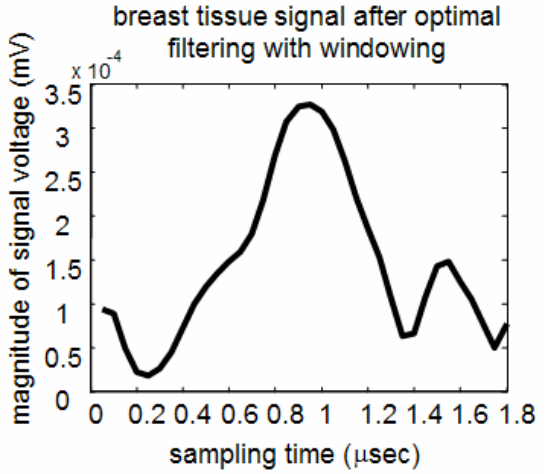

圖二十六 (e) 經過最適化濾波器處理後於加窗後的乳房組織信號。

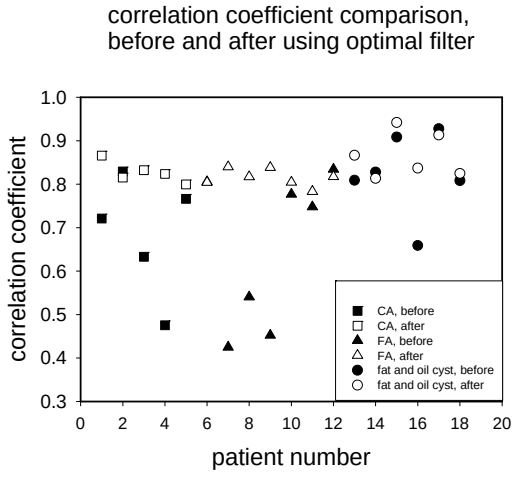

圖二十七 使用最適化濾波器前後的相關係數分佈。

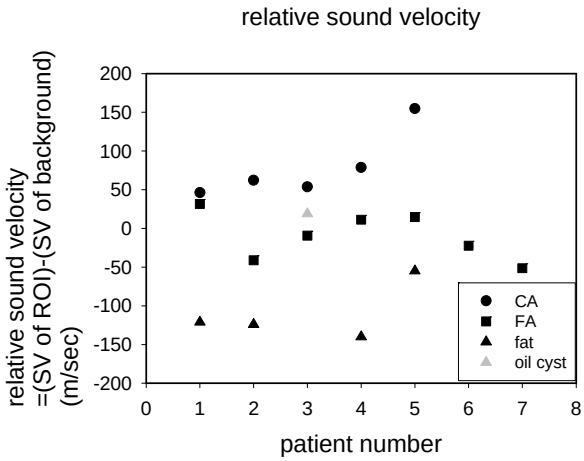

圖二十八 相對聲速結果。分類為惡性腫瘤(CA)、纖維腺瘤(FA)以及脂肪(fat) 。

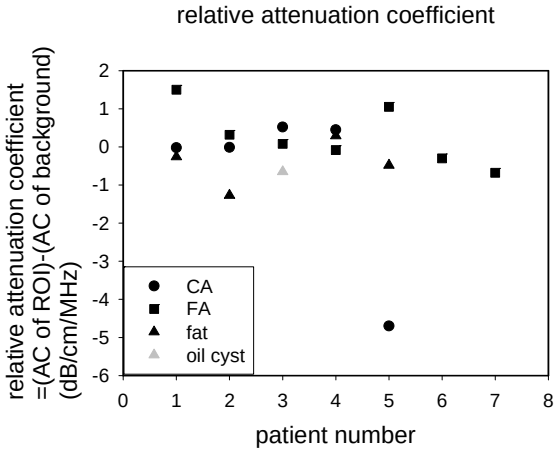

圖二十九 相對衰減係數結果。

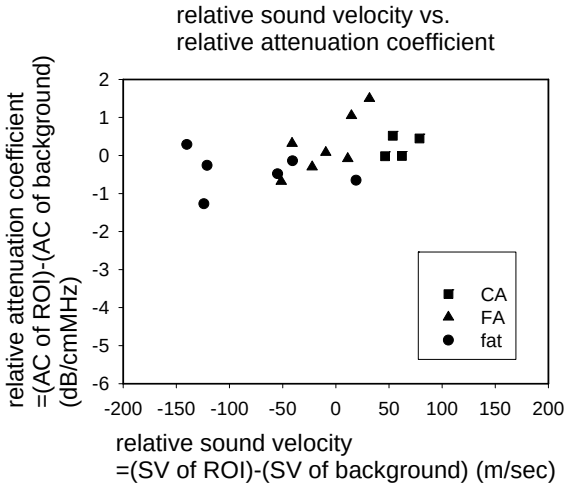

圖三十 相對聲速與相對衰減係數。

圖二十九為相對衰減係數之分佈，圖三十為相對聲速與相對衰減係數之分佈比較，發現衰減係數暫無規律。而其可能的原因為，重建過程中，強制限定有興趣區域內外各自的聲速與衰減係數為均勻，但實際上並非如此。此外，纖維腺瘤、脂肪與各式各樣的惡性腫瘤之衰減係數交錯分佈於 0.08~0.16 dB/cm/MHz [1]。故要用衰減係數將各種病灶分離並不容易。由於設計最適化濾波器是為了降低失真所

造成的影響，試比較使用最適化濾波器前後的重建結果差異。圖三十一 (a)至(e)所列為低相關係數之病人 1(CA)、3(CA)、7(FA)、9(FA) 及 16(fat)號的結果。聲速方面，圖三十一(a)與(c)中，1、3 及 9 號病人之數據在使用最適化濾波器前後的結果幾乎相同，但在此同時，7、16 號病人的有興趣區域聲速與背景聲速在使用最適化濾波器後的結果較使用最適化濾波器前分開許多。衰減係數方面，圖三十一(b)與(d)，使用最適化濾波器前之衰減係數分散於-0.4~0.7 dB/cm/MHz，使用後則落於 0~0.6 dB/cm/MHz。根據先前仿體結果，惡性腫瘤、腺體組織、脂肪的衰減係數分別為 1.10、0.55、0.44 dB/cm/MHz，故若以相對衰減係數分佈來看，可說明最適化濾波器有助於降低部分失真影響。

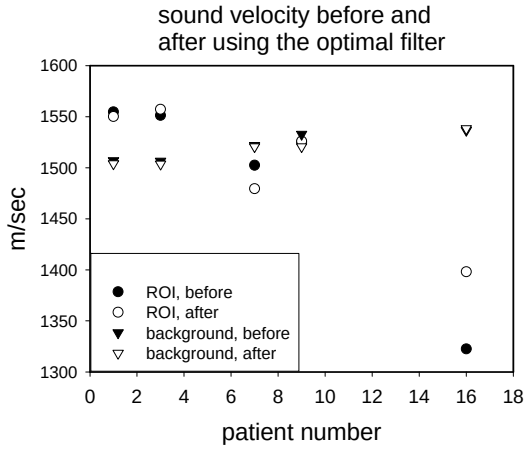

圖三十一 (a) 病人 1(CA)、3(CA)、7(FA)、9(FA)及 16(fat)號為相關係數偏低者，使用最適化濾波器前後的聲速分佈。

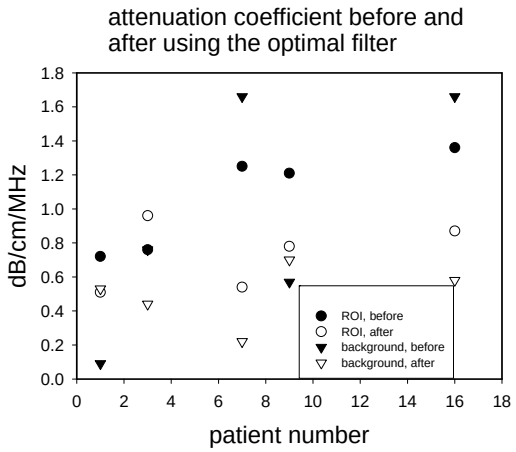

圖三十一 (b) 病人 1(CA)、3(CA)、7(FA)、9(FA)及 16(fat)號為相關係數偏低者，使用最適化濾波器前後的衰減係數分佈。其中，No.3 病人最適化濾波器前的有興趣區域衰減係數為 0.76 dB/cm/MHz。

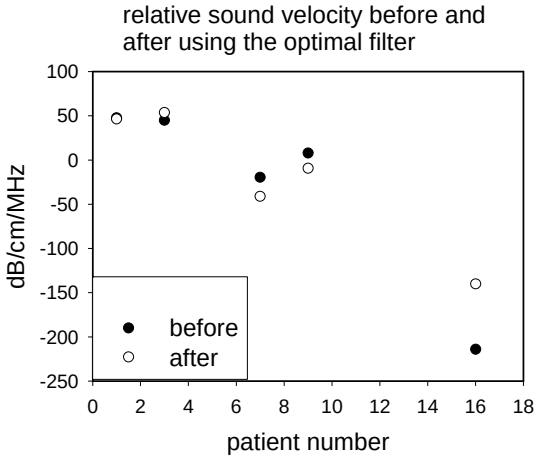

圖三十一 (c) 病人 1(CA)、3(CA)、7(FA)、9(FA)及 16(fat)號為相關係數偏低者，使用最適化濾波器前後的相對聲速分佈。

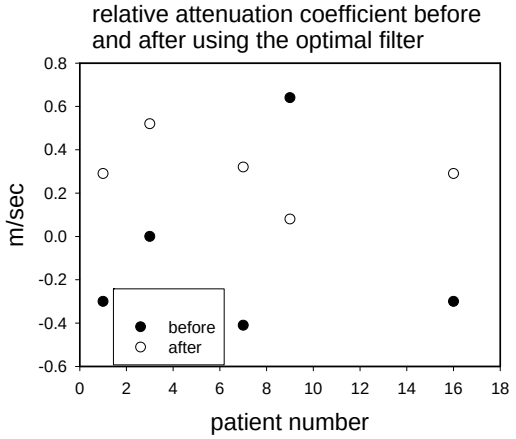

圖三十一 (d) 病人 1(CA)、3(CA)、7(FA)、9(FA)及 16(fat)號為相關係數偏低者，使用最適化濾波器前後的相對衰減係數分佈。

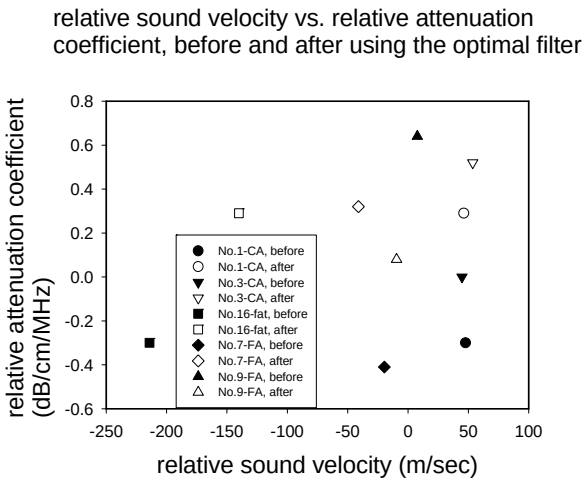

圖三十一 (e) 病人 1(CA)、3(CA)、7(FA)、9(FA)及 16(fat)號為相關係數偏低者，使用最適化濾波器前後的相對聲速與相對衰減係數之分佈。

對於有興趣區域之圈選面積的討論，可由圖三十二(a)看出，當有興趣區域所圈選面積減少時，較背景聲速快者，其聲速表現較圈選面積大時更快，反之亦然。唯一的例外為 7 號病人，推論可能的原因為該有興趣區域內非常不均勻，與先前假設其內部均勻有很大的落差所致。此例外情形在圖三十二(b)再度發生，發現在圈選面積遞減時，7 號病人的有興趣區域之衰減係數與背景衰減係數有一交錯的情形，推斷其可能原因為在圈選面積較小時，未將衰減係數較高的部分圈入，此又為 7 號病人之病灶較 1、9 號病人的病灶來得不均勻之證據。

由於灰階影像上常出先現不只單一有興趣區域，故嘗試圈選多個有興趣區域來看重建結果是否會更準確。首先，先驗證先前的仿體結果（仿體製作：Dr. Ernest Madsen, Department of Medical Physics, University of Wisconsin-Madison, MI），接著再看臨床實驗數據的部分。如圖三十三所示，在仿體之灰階影像上預先選取固定三個有興趣區域，改變第四個有興趣區域（實際上為背景的一部份）之面積（前後共討論三個相對位置–右下方、左下方及上下方的結果）。如圖三十四(a)至(f)，無論第四個有興趣區域之圈選面積大小，所得重建結果幾乎不變，此為仿體擁有均勻聲速與衰減係數背景之證據。對比之下，如圖三十五(a)至(d)，編號對照如圖二十七，發現從背景圈出的第二個有興趣區域之聲速與衰減係數都與背景有差異，至於第一個有興趣區域的部分，在第二個有興趣區域圈選前後，聲速上的表現有約 10 m/sec 的變化，在此同時，衰減係數上的表現有 0.1 dB/cm/MHz 的差異。

由以上一連串的討論可發現，仿體結果與

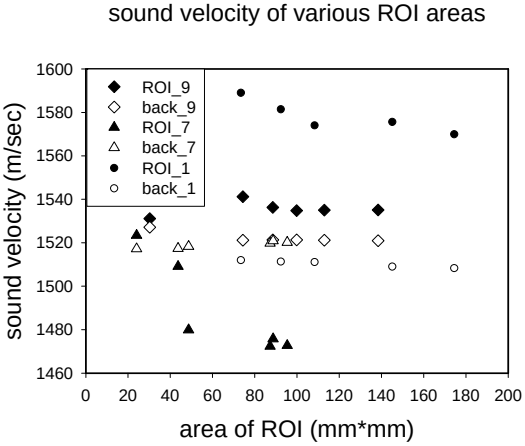

圖三十二 (a)　病人 1(CA)、7(FA)、9(FA)號為相關係數偏低者，在不同 ROI 面積下所得聲速結果。其中，1、7 及 9 號病人之灰階影像總面積各為 1622、771 及 978 mm^2。

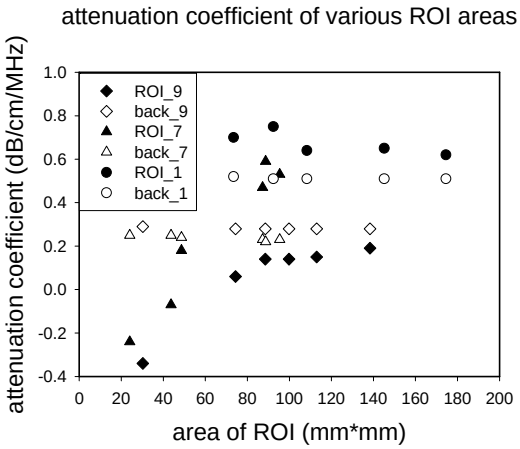

圖三十二 (b)　病人 1(CA)、7(FA)、9(FA)號為相關係數偏低者，在不同 ROI 面積下所得衰減係數結果。其中，1、7 及 9 號病人之灰階影像總面積各為 1622、771 及 978 mm^2。

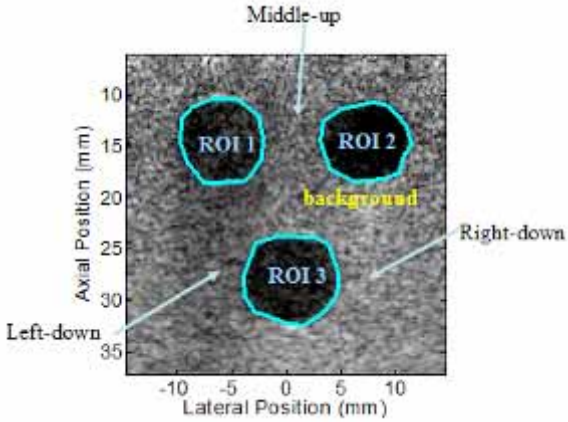

圖三十三 在仿體之灰階影像上預先選取固定三個有興趣區域，箭頭所指為第四個有興趣區域之位置。

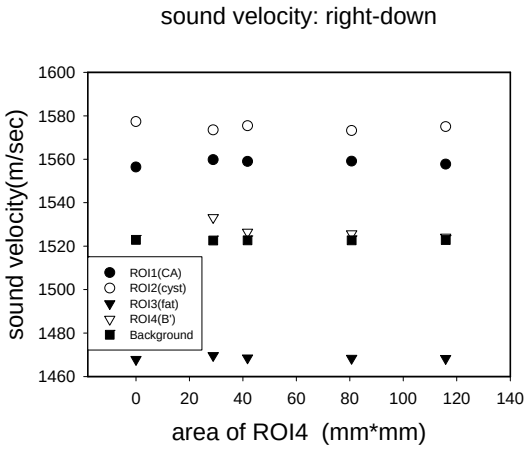

圖三十四 (a) 第四個有興趣區域位於灰階影像上之右下方，所得聲速結果。灰階影像之總面積為 1038 mm^2。

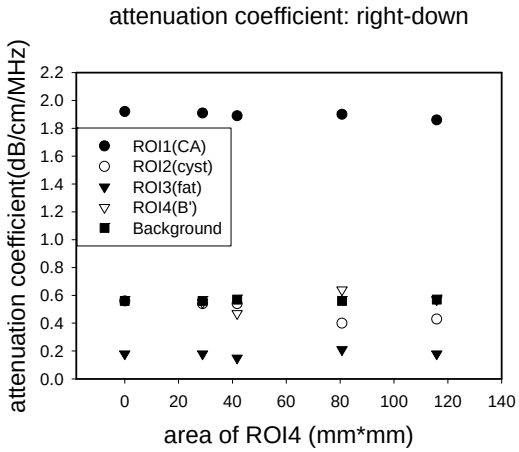

圖三十四 (b) 第四個有興趣區域位於灰階影像上之右下方，所得衰減係數結果。灰階影像之總面積為 1038 mm^2。

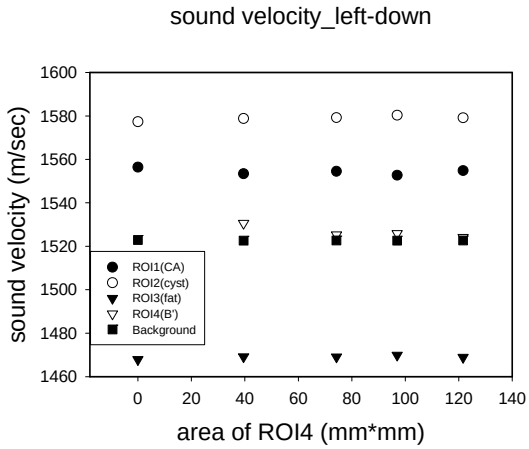

圖三十四 (c) 第四個有興趣區域位於灰階影像上之左下方，所得聲速結果。灰階影像之總面積為 1038 mm^2。

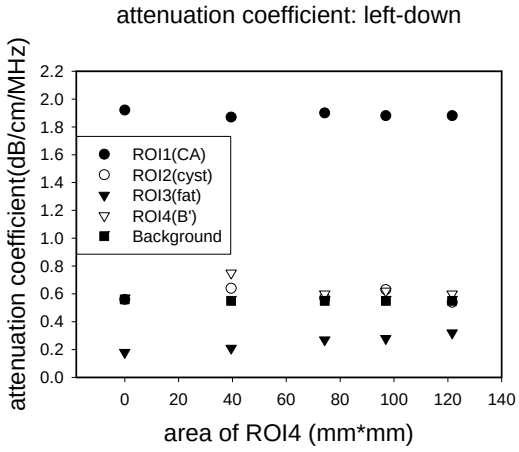

圖三十四 (d) 第四個有興趣區域位於灰階影像上之左下方，所得衰減係數結果。灰階影像之總面積為 1038 mm^2。

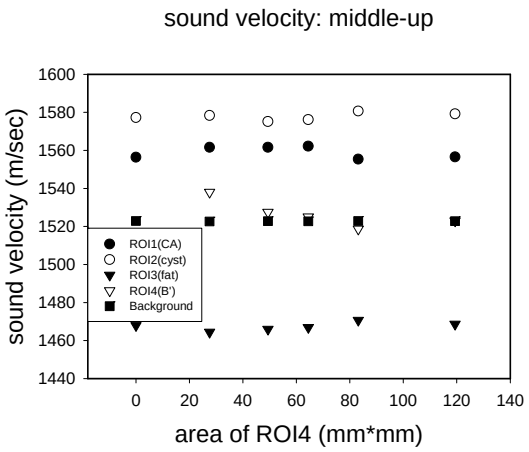

圖三十四(e) 第四個有興趣區域位於灰階影像上之正上方，所得聲速結果。灰階影像之總面積為 1038 mm^2。

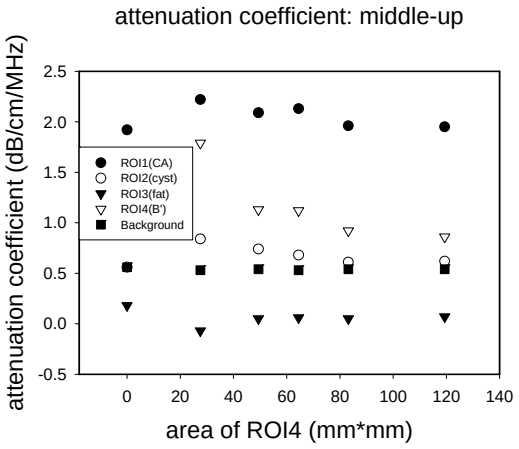

圖三十四(f) 第四個有興趣區域位於灰階影像上之正上方，所得衰減係數結果。灰階影像之總面積為 1038 mm^2。

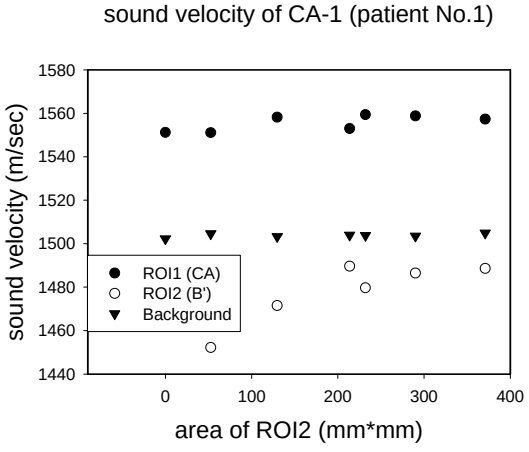

圖三十五(a) 在 1 號病人(CA)的灰階影像中，選取不同面積之第二個有興趣區域。所得聲速結果。其灰階影像之總面積為 1622 mm^2。

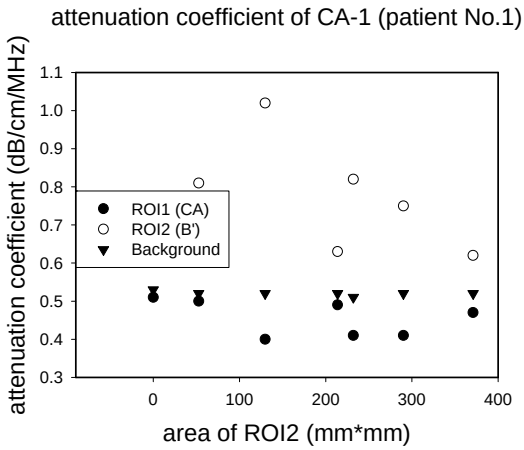

圖三十五(b)　在 1 號病人(CA)的灰階影像中，選取不同面積之第二個有興趣區域。所得衰減係數結果。其灰階影像之總面積為 1622 mm^2。

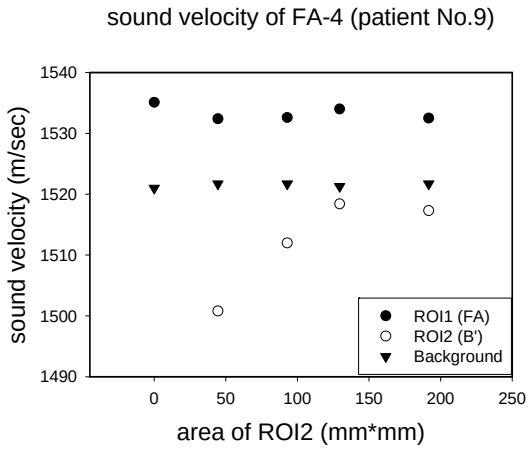

圖三十五(c)　在 9 號病人(FA)的灰階影像中，選取不同面積之第二個有興趣區域。所得聲速衰減係數結果。其灰階影像之總面積為 978 mm^2。

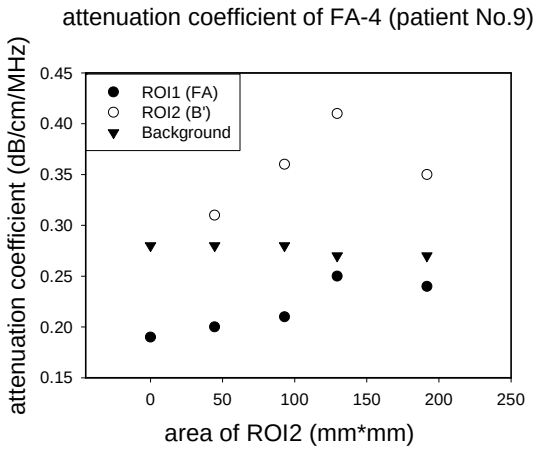

圖三十五(d)　在 9 號病人(FA)的灰階影像中，選取不同面積之第二個有興趣區域。所得聲速衰減係數結果。其灰階影像之總面積為 978 mm^2。

臨床結果的主要差別有兩點：第一，就其物理特性來看，仿體製作時在各部分幾乎為均質分佈，包含聲速與衰減係數，但人體乳房組織幾乎各處皆為不均勻分佈。第二，仿體為靜止不動的物體，但病人可能在資料擷取過程中造成移動(motion artifact)。另一方面，若探頭放置傾斜，將造成接收之訊號振幅大幅減弱，這對實驗是很不利的，故應盡量將探頭調整至可使發射信號垂直入射金屬板。

在計畫的第三年度，我們已完成下列工作成果：

1.臨床資料之取得：

延續第二年度之臨床資料之取得，實驗中使用一具壓縮功能架構的裝置，如圖二十三右，調整螺絲以針對每次不同厚度的組織做壓縮，在取完乳房組織的信號後，馬上接著做水的對照組，使用一水袋內裝滿水不含氣泡，置於探頭與金屬反射板間，以取得水的校正資料。臨床資料於台北榮民總醫院超音波檢查室取得，由周宜宏醫師協助。連同前期臨床資料，總共使用 19 個病例來做分析，其中取得有興趣區域分類如下：5 個乳癌，7 個纖維腺瘤，6 個脂肪，1 個油囊腫(oil cyst)。

2.利用前期與本期之臨床資料所得之實驗結果更新：

連同前期臨床資料總共使用 19 個病例來做分析，其中取得有興趣區域分類如下：5 個乳癌，7 個纖維腺瘤，6 個脂肪，1 個油囊腫(oil cyst)。

相對聲速為有興趣區域內之平均聲速減去背景區域之平均聲速，其結果如圖三十六所示。相對衰減係數為有興趣區域內之平均聲速減去背景聲速之平均聲速，其結果如圖三十七

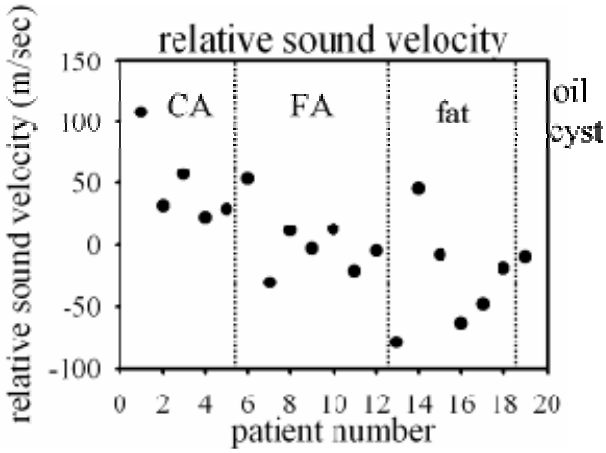

圖三十六　相對聲速結果。

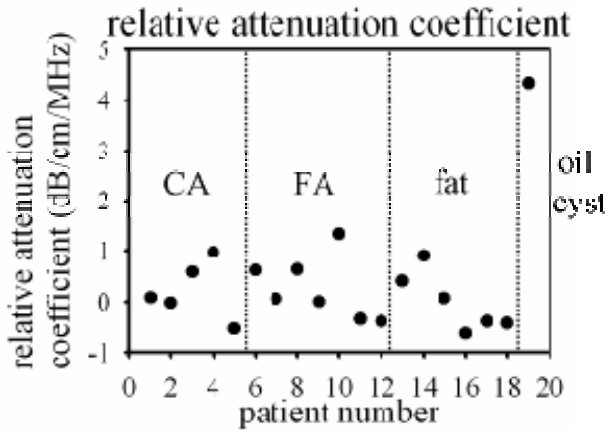

圖三十七　相對衰減係數結果。

所示。三個 ROI 種類分別之聲速與衰減係數及其標準差則列於表六，三個 ROI 種類之相對聲速與相對衰減係數則列於表七。在聲速方面，利用兩個相對聲速的閾值(threshold)：18.5 m/s 與–28.3 m/s，可有效從 18 個病例中成功區分出 14 個病例，不包含油囊腫，其相對聲速–9.4 m/s。儘管如此，在衰
減係數方面，無法找出閾值將三種不同的有興趣區域作區分。

3.在沒有金屬反射板的實驗架構下建立出衰減係數估計方法：

上述研究結果中，透過相對聲速之閾值，18.5 m/sec以及－28.3 m/s，可達到將惡性腫瘤從纖維腺瘤及脂肪中分隔出來的結果。然而，相對衰減係數無法與相對聲速一樣找出有效的單一閾值。

由於文獻中提出惡性腫瘤的衰減係數高於一般組織，故仍以評估衰減係數為本期計畫研究目標。先前臨床實驗中，病人乳房組織可以順利被固定壓縮於實驗架構(如圖二十三)的比例很低，所以需要研究出一個不需要反射板就可以估計出組織衰減係數的方法。根據文

表六　惡性腫瘤(CA)、纖維腺瘤(FA)與脂肪。(fat)之平均聲速與平均衰減係數。

	Sound Velocity (m/s)	Attenuation Coefficient (dB/cm/MHz)
CA	1530.9±36.2	0.66±0.52
FA	1499.8±26.8	0.68±0.66
Fat	1464.8±45.1	0.63±0.61

表七　惡性腫瘤(CA)、纖維腺瘤(FA)與脂肪。(fat)之平均相對聲速與平均相對衰減係數。

	Relative Sound Velocity (m/s)	Relative Attenuation Coefficient (dB/cm/MHz)
CA	49.8±35.2	0.21±0.58
FA	2.6±27.3	0.27±0.62
Fat	–25.1±44.9	–0.02±0.59

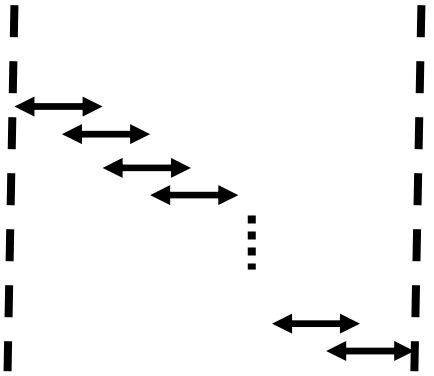

圖三十八　信號分段的示意圖。

獻[35]-[37]，利用信號分段的方法來估計衰減係數。如圖三十八，將一條 A line 信號分割成許多小段，但相鄰兩段信號之間有一半長度的重複。在組織中的，信號的衰減係數線性正比於信號的中心頻率，故可藉由中心頻率的偏移來估計出衰減係數。

以下是衰減細數估計的基本理論。

在組織中，衰減量與信號傳遞頻率呈現性關係，如式(27)。

由於衰減與頻率與行近距離皆有關，當發射波在組織中行進時，其頻率成分將受到影響而有所改變。假設一寬頻的高斯脈衝波(Gaussian pulse)其功率頻譜(power spectrum)為

$$\left|S_t(f)\right|^2 = e^{-(\frac{f-f_0}{\sigma})^2}, \qquad (50)$$

其中 f_0 為發射波的中心頻率，σ 為發射波的頻寬。若忽略後散射(backscattering)，由深度R所得信號來回(round trip)信號為

$$\left|S_r(R,f)\right|^2 = \left|S_t(f)\right|^2 e^{-4\alpha Rf} = e^{-(\frac{f-f_0}{\sigma})^2-4\alpha Rf}, \qquad (51)$$

將式(3.13)重新整理後，可得

$$\left|S_r(R,f)\right|^2 = e^{-(\frac{f-f_1}{\sigma})^2-4\alpha R(f_0-\sigma^2\alpha R)}, \qquad (52)$$

其中，f_1 為接收信號的中心頻率，

$$f_1 = f_0 - 2\sigma^2 \alpha R \,. \qquad (53)$$

由以上的推導可知，聲波的中心頻率會隨著波的行進而向下偏移。

而我們正是要利用這個偏移量來估算 α。由於兩兩分段(segment)之間的深度差固定，假設為 ΔR，則前後兩段信號偏移後的中心頻率則分別為

$$f_i = f_0 - 2\sigma^2 \alpha R \,, \qquad (54)$$

$$f_{i+1} = f_0 - 2\sigma^2 \alpha (R + \Delta R) \,. \qquad (55)$$

找出所有分段的中心頻率後，以此中心頻率分布圖求其斜率，便可找到衰減係數。注意，以上是假設各分段內衰減係數相同來計算。但今日以單一A-line信號來做分析，故距離(R)的部份只使用one-way來做計算，故式(54)與式(55)可改寫成

$$f_i = f_0 - \sigma^2 \alpha R \,, \qquad (56)$$

$$f_{i+1} = f_0 - \sigma^2 \alpha (R + \Delta R) \,. \qquad (57)$$

以下將使用前期研究中的模擬條件[6]評估此方法的成效。其中，模擬數據是使用均勻介質，衰減係數設定分別為0、0.284、0.568與1.136 dB/cm/MHz。使用8個特定通道發射(通道27、53、79、105、130、156、182以及208)，234個通道接收，取樣頻率75MHz，每條A-line共有4800個取樣點。其他模擬細節請參照[6]。

拿出8組直線發射直線接收的信號組合e根據信號分段的原理來計算，運用式(57)，算出頻率偏移後，進而計算出因聲波行進距離所造成的頻率偏移之斜率 $\frac{\Delta f}{\Delta R}$，再以此估計出衰減係數值。在此使用了三種分段長度(segment duration)，依序為0.67 μs、1.34 μs以及2.68 μs，其實就是相當於取樣點50點、100點與200點。由於取樣點在只有50、100點與200點時，頻率解析度稍嫌不足(頻率解析度依次為1.5 MHz、0.75 MHz以及0.375 MHz)，故在以上估計衰減係數的過程中，加上補零(zero padding)的步驟，以提高頻率解析度。在此使用加長信號長度31倍長，使頻率解析度提高至原本的32倍。注意在此考慮不同衰減係數下，信號所產生之最大頻率偏移量，故找尋中心頻率的範圍決定使用兩個範圍1.5-6MHz與3-6 MHz，而尋找中心頻率是使用first order moment的方法，即

$$f_c = \frac{\sum_{f_1}^{f_2} f \cdot |S(f)|}{\sum_{f_1}^{f_2} |S(f)|} \,. \qquad (58)$$

衰減係數設為0 dB/cm/MHz的部份是拿來當作對照組，確定我們的方法無誤的，圖三十九為其結果，黑色代表找尋的中心頻率範圍為1.5-6 MHz，紅色代表找尋的中心頻率範圍為3-6 MHz。其中橫軸分別代表取樣點50點，取樣點50點補零，取樣點100點，取樣點100點補零，取樣點200點以及取樣點200點補零。圖四十則為衰減係數設為0.284 dB/cm/MHz

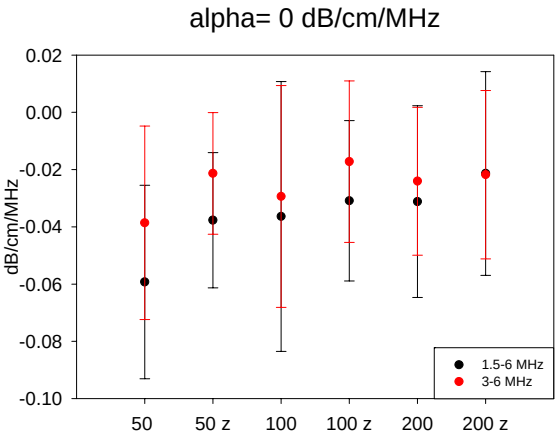

圖三十九　利用特定通道的自發自收信號所估計之衰減係數結果(平均值±標準差)，介質衰減係數0 dB/cm/MHz，中心頻率計算範圍為1.5-6 MHz(黑色圓型)與3-6 MHz(紅色圓形)。

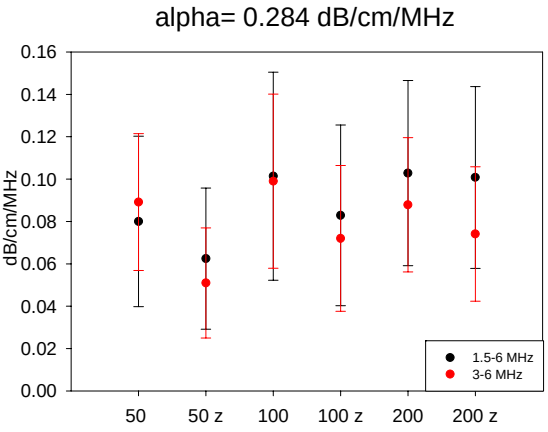

圖四十　利用特定通道的自發自收信號所估計之衰減係數結果(平均值±標準差)，介質衰減係數0.284 dB/cm/MHz，中心頻率計算範圍為1.5-6 MHz(黑色圓型)與3-6 MHz(紅色圓形)。

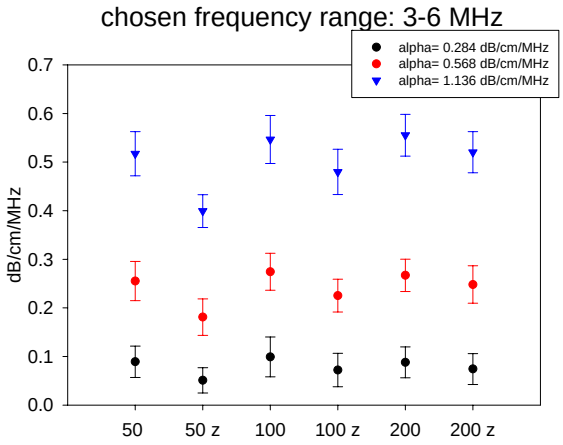

圖四十一　利用特定通道的自發自收信號所估計之衰減係數結果(平均值±標準差)。介質衰減係數0.284(黑色圓形)、0.568(紅色圓型)與1.136(藍色三角形) dB/cm/MHz，中心頻率計算範圍為3-6 MHz。

的部份。圖四十一為0.284、0.568與1.136 dB/cm/MHz三組衰減係數所得結果，找尋的中心頻率範圍為3-6 MHz。 幾乎所有情形下，補零後的結果皆變小，此情形來自於以下之可能：補零前後找到的中心頻率大小改變，造成頻率偏移變小，所以所估計出來的衰減係數值變小。

四、計畫執行進度與遭遇困難

第一年：
本計畫已如計畫書所列，如預期完成，且部分成果已有超前。

第二年：
本計畫已如計畫書所列，如預期完成。所遭遇困難主要為固定乳房組織時，可能因呼吸造成擷取信號期間有滑動的現象，所幸資料擷取時間都在數秒鐘以內，並且提醒病人閉氣，故呼吸移動的影響可忽略。另一方面，並非所有位置的有興趣區域都可以被固定，以達到擷取資料的目的。而且並非所有病人之病灶所在(即有興趣區域)都可順利被固定於實驗所設計之裝置內(具有金屬反射板)，使得現階段臨床數據之收集受到極大限制。因此，希望於未來發展出不使用金屬反射板時仍然可重建出聲速的方法，以利灰階影像之修正，進而提高影像之對比解析度。

第三年：
在現有文獻中，關於衰減係數評估的研究，幾乎都是以有反射板的實驗架構為主，由此可見，不用反射板來評估衰減係數存在許多困難。若遇到衰減係數很小的情形，信號分段的長度不足夠則造成頻率偏移量不夠，估計上所產生的誤差較大，如圖四十二所示，在衰減係數為0.284 dB/cm/MHz時，估計結果與理論值之比值在補零前後皆小於0.35，反觀衰減係數為0.568 dB/cm/MHz與1.136 dB/cm/MHz時，補零前約在0.45上下，補零後在信號分段較長的部份亦有較高的比值。以上的實驗數據結果不如預期，未來將朝超音波電腦輔助診斷中關於灰階影像值的參數分析來幫助臨床超音波診斷。

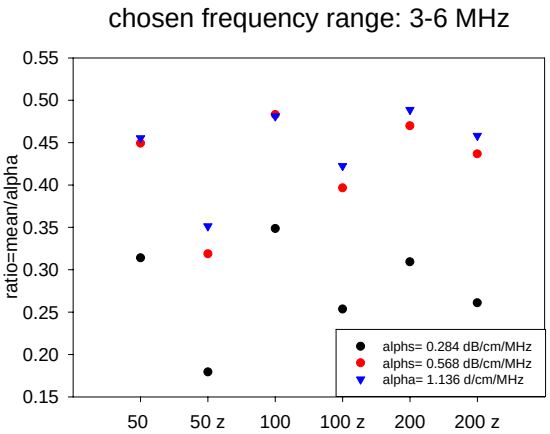

圖四十二　介質衰減係數0.284(黑色圓形)、0.568(紅色圓型)與1.136(藍色三角形) dB/cm/MHz之估計結果(平均值)與理論值之比值。

五、研究成果之重要性與卓越性

計畫第一年度完成事項的重要性如下:

本計畫成果之重要性在於針對近年來發生率及死亡率皆急遽增加之乳癌，提供了一個先進有效之診斷新技術。此技術並可和 X 光乳房攝影及其他臨床檢查相輔相成。本研究計畫之卓越性在於使用此創新之前端成像技術，可提供新的影像參數，並實現於現有之陣列成像系統架構中，且能大幅提高其臨床診斷之價值。建立在這些前端影像技術之下，亦可以進一步對相關之後端影像分析及電腦輔助診斷方法有直接之助益。

計畫第二年度完成事項的重要性如下:

本期研究中，證實此實驗系統裝置，如圖二所示，在臨床實驗中之可行性。有了此實驗裝置，如圖二右半部所示，在資料擷取過程中，可確實固定線性陣列探頭。透過最適化濾波器處理，已降低失真

所造成的影響。臨床實驗結果中，雖無法如仿體結果一樣透過聲速與衰減係數來區分出惡性腫瘤與良性病灶，但仍可透過上閾值，+50 m/sec，來區分出惡性腫瘤與纖維腺瘤。因此，本研究中所歸納出之新參數(聲速分離法)，未來仍有潛力可以減少陰性病理切片的比例。

計畫第三年度完成事項的重要性如下:

延續第二年臨床實驗的部份，儘管衰減係數能無法達到分離良惡性組織的目的，仍可以透過相對聲速之閾值，18.5 m/sec以及－28.3 m/s，可達到將惡性腫瘤從纖維腺瘤及脂肪中分隔出來的結果。不透過反射板進行衰減係數重建的部份，結果不如預期，但相信在未來更完整的實驗方法確立後 ，能有潛力幫助臨床超音波診斷。

本計畫目前為止之直接產出成果包括七篇期刊論文（皆已刊登或接受），十一篇國內外研討會論文（包括兩篇邀請演講）及提出二件專利申請（中華民國及美國申請各一件）。

六、計畫執行內容是否有修正

否。

七、參考文獻

[1] L. Landini , R. Sarnelli, and F. Squartini, "Frequency-dependent attenuation in breast tissue Characterization," *Ultrasound Med. Biol.*, vol. 11, no. 4, pp. 559－603, 1985.

[2] T. C. Telger, *Teaching Atlas of Breast Ultrasound*. New York:Thieme Medical, 1996.

[3] R. C. Gauss, M. S. Soo, and G. E. Trahey, "Wavefront distortion measurements in the human breast," *IEEE Ultrason. Symp.*, vol. 2, pp. 1547－1551, 1997.

[4] S. A. Goss, R. L. Johnston, and F. Dunn F, "Comprehensive compilation of empirical ultrasonic properties of mammalian tissues," *J. Acoust. Soc. Am.*, vol. 64, no. 2, pp. 423－457, 1978.

[5] E. L. Madsen, E. Kelly-Fry, and G. R. Frank, "Anthropomorphic phantoms for assessing systems used in ultrasound imaging of the compressed breast," *Ultrasound Med. Biol.*, No.14, suppl. 1, pp. 183－201, 1988.

[6] S.-W. Huang and P.-C. Li, "Computed tomography sound velocity reconstruction using incomplete data," *IEEE Trans. Ultrason. Ferroelec. Freq. Contr.*, vol. 51, no. 3, pp. 329－342, 2004.

[7] S.-W. Huang and P.-C. Li, "Experimental investigation of computed tomography sound velocity reconstruction using incomplete data," *IEEE Trans. Ultrason. Ferroelec. Freq. Contr.*, vol. 51, no. 9, pp. 1072－1081, 2004.

[8] S.-W. Huang and P.-C. Li, "Ultrasonic computed tomography reconstruction of the attenuation coefficient using a linear array," *IEEE Trans. Ultrason. Ferroelec. Freq. Contr.*, vol. 52, no. 11, pp. 2011－2022, 2005.

[9] T. D. Mast, L. P. Souriau, D.-L. Liu, M. Tabei, A. I. Nachman, and R. C. Waag, "A *k*-space method for large-scale models of wave propagation in tissue," *IEEE Transactions on Ultrasonics, Ferroelectrics and Frequency Control*, vol. 48, no. 2, pp. 341–354, 2001.

[10] M. Tabei, T. D. Mast, and R. C. Waag, "A *k*-space method for coupled first-order acoustic propagation equations," *J. Acoust. Soc. Amer.*, vol. 111, no. 1, pp. 53–63, 2002.

[11] M. Tabei, T. D. Mast and R. C. Waag, "Simulation of ultrasonic focus aberration and correction through human tissue," *J. Acoust. Soc. Amer.*, vol. 113, no. 2, pp. 1166–1176, 2003.

[12] Laura M. Hinkelman, Thomas L. Szabo, and Robert C. Waag, "Measurements of ultrasonic pulse distortion produced by human chest wall," *J. Acoust. Soc. Amer.*, vol. 101, no. 4, pp. 2365–2373, 1997.

[13] Laura M. Hinkelman, T. Douglas Mast, Leon A. Metlay, and Robert C. Waag, "The effect of abdominal wall morphology on ultrasonic pulse distortion. Part I. Measurements," *J. Acoust. Soc. Amer.*, vol. 104, no. 6, pp. 3635–3649, 1998.

[14] P. M. Morse and K. U. Ingard, *Theoretical Acoustics*. New York: McGraw-Hill, 1968.

[15] J. W. Goodman, *Introduction to Fourier Optics*. 2nd ed. New York: McGraw-Hill, 1996.

[16] A. C. Kak and M. Slaney, *Principles of Computerized Tomographic Imaging*. New York: Institute of Electrical and Electronics Engineers, 1988.

[17] K. C. Tam, J. W. Eberhard and K. W. Mitchell, "Incomplete-data CT image reconstructions in industrial applications," *IEEE Transactions on Nuclear Science*, vol.

37, no. 3, pp. 1490–1499, 1990.
[18] P. L. Combettes and P. Bondon, "Hard-constrained inconsistent signal feasibility problems," *IEEE Trans. Signal Processing*, vol. 47, no. 9, pp. 2460–2468, 1999.
[19] M. Krueger, A. Pesavento, and H. Ermert, "A modified time-of-flight tomography concept for ultrasonic breast imaging," in *Proc. IEEE Ultrason. Symp.*, 1996, pp. 1381–1385.
[20] M. Krueger, V. Burow, K. M. Hiltawsky, and H. Ermert, "Limited angle ultrasonic transmission tomography of the compressed female breast," in *Proc. IEEE Ultrason. Symp.*, 1998, pp. 1345–1348.
[21] E. L. Madsen, J. A. Zagzebski, G. R. Frank, J. F. Greenleaf, and P. L. Carson, "Anthropomorphic breast phantoms for assessing ultrasonic imaging system performance and for training ultrasonographers: Part I," *J. Clin. Ultrasound*, vol. 10, no. 2, pp. 67–75, 1982.
[22] A. I. Nachman, J. F. Smith, and R. C. Waag, "An equation for acoustic propagation in inhomogeneous media with relaxation losses," *J. Acoust. Soc. Amer.*, vol. 88, no. 3, pp. 1584–1595, 1990.
[23] M. O'Donnell and S. D. Silverstein, "Optimal displacement for compound image generation in medical ultrasound," *IEEE Trans. Ultrason., Ferroelect., Freq. Contr.*, vol. 35, no. 4, pp. 470–476, 1988.
[24] R. C. Gonzalez and R. E. Woods, *Digital Image Processing*. 2nd ed. Reading, MA: Addison-Wesley, 2002.
[25] R. M. Lemor, P. K. Weber, P. K. Fonfara, C. Guenther, H. J. Welsch, and M. L. Hoss, "A new combined open research platform for ultrasound radio frequency signal processing," in *Proc. IEEE Ultrason. Symp.*, 2003, pp. 33–37.
[26] Q. Zhu and B. D. Steinberg, "Large-transducer measurements of wavefront distortion in the female breasts," *Ultrason. Imaging*, vol. 14, pp. 276-299, 1992.
[27] Q. Zhu and B. D. Steinberg, "Modeling, measurement and correction of wavefront distortion produced by breast specimens," *IEEE Ultrason. Symp.*, vol.3, pp. 1613-1617, 1994.
[28] Q. Zhu and B. D. Steinberg, "A toward inverse filtering approach for ultrasonic wavefront compensation," *IEEE Ultrason. Symp.*, vol.2, pp.1357-1361, 1996.
[29] Q. Zhu and B. D. Steinberg, "Modeling and correction of incoherent wavefront distortion," *Int. J. Imag. Syst. Technol.*,vol. 8, pp. 322-335, 1997.
[30] T. Lwin and W. D. O'Brien Jr., " Tissue-induced ultrasonic wavefront distortion," *IEEE Ultrason. Symp.*, vol. 2, pp. 1415-1418, 1996.
[31] P.-C. Li, E. Ebbini, and M. O'Donnell, " A new filter design technique for coded excitation systems," *IEEE Trans. Ultrason. Ferroelec. Freq. Control*, vol. 39, no. 6, pp. 693-699, 1992.
[32] G. Kossoff, E. Kelly-Fry, and J. Jellins, "Average velocity of ultrasound in the human female breast. *J. Acoust. Soc. Am.*, vol. 53, no. 6, pp. 1730-1736, 1973.
[33] F. A. Duck, *Physical Properties of Tissue*. London:Academic Press 1990.
[34] K. R. Erikson, F. J. Fry, and J. P. Jones, "Ultrasound in medicine- a review," *IEEE Trans. Sonics. Ultrason.*, vol. 21, no. 3, pp. 144-170, 1974.
[35] R. Kuc, "Clinical application of an ultrasound attenuation coefficient estimation technique for liver pathology characterization," *IEEE Trans. Biomed. Eng.*, vol. BME-27, no. 6, pp. 312－319, 1980.
[36] R. Kuc, "Estimating acoustic attenuation from reflected ultrasound signals: comparison of spectral-shift and spectral-difference approaches," *IEEE Trans. Acoust. Speech Signal Process*, vol. 32, pp. 1–6, 1984.
[37] R. Kuc, M. Schwartz, "Estimating the Acoustic Attenuation Coefficient Slope for Liver from Reflected Ultrasound Signals," *IEEE Trans. Sonics Ultrason.,* vol. SU-26, no. 5, pp. 353–362, 1979.

附件二

可供推廣之研發成果資料表

■ 可申請專利　■ 可技術移轉　日期：96 年 4 月 24 日

國科會補助計畫	計畫名稱：新參數超音波乳房影像技術 計畫主持人：李百祺 計畫編號：NSC 95-2221-E-002-169　學門領域：醫學工程
技術/創作名稱	超音波影像方法與裝置
發明人/創作人	李百祺、黃聖文
技術說明	中文：本技術的成像設備是使用超音波陣列的成像設備，可得到超音波組織影像，另外再加上三項創新，使此設備亦可得到影像物體中的聲速和衰減係數等各影像參數。第一點是換能器陣列中所有通道都可獨立發射、接收，第二點是增加一反射面，並將陣列和此反射面置於物體的兩側，第三點是利用組織影像提供之資訊並結合新的影像重建法則，可以提高其他參數影像之準確度。利用本發明可以同時取得生物組織的超音波組織影像、聲速和衰減係數影像，並可延伸至其他參數（如彈性係數）。
	英文：The imaging setup in this disclosure is based on an ultrasound array imaging setup; therefore, tissue images can be obtained. Additionally, there are three procedures to make this setup capable of acquiring other imaging parameters such as sound velocity and attenuation. The first procedure is that every channel in the array can transmit and receive independently. The second procedure is the inclusion of a reflector, which is on the opposite side of the object. The third procedure is the use of advanced reconstruction algorithms based on the information contained in the tissue image. This invention enables obtaining the tissue image, the sound velocity image, and the attenuation image using the same setup. The apparatus can also be used to obtain other image parameters, such as tissue elasticity.

可利用之產業及可開發之產品	生物醫學超音波、乳房診斷、非破壞檢測。
技術特點	使用超音波換能器陣列進行超音波信號的發射和接收，不需旋轉陣列或物體，即可同時取得組織影像、聲速影像及衰減係數影像。此裝置亦可延伸至其他參數影像(如彈性係數)，提供更多影像資訊。
推廣及運用的價值	利用本發明同時取得生物體的超音波組織影像、聲速及衰減係數，可用以判別組織種類，如乳房腫瘤之偵測。

※ 1.每項研發成果請填寫一式二份，一份隨成果報告送繳本會，一份送　貴單位研發成果推廣單位（如技術移轉中心）。

※ **2.本項研發成果若尚未申請專利，請勿揭露可申請專利之主要內容。**

※ 3.本表若不敷使用，請自行影印使用。

Computed Tomography Sound Velocity Reconstruction Using Incomplete Data

Sheng-Wen Huang and Pai-Chi Li, *Senior Member, IEEE*

***Abstract*—An approach based on limited-angle transmission tomography for reconstruction of the sound velocity distribution in the breast is proposed. The imaging setup is similar to that of x-ray mammography. With this setup, the time-of-flight data are acquired by a linear array positioned at the top of the compressed breast that both transmits and receives, and a metal plate is placed at the bottom as a reflector. The setup allows acoustic data acquisition for simultaneous B-mode image formation and the tomographic sound velocity reconstruction. In order to improve the sound velocity estimation accuracy, a new reconstruction algorithm based on a convex programming formulation has been developed. Extensive simulations for both imaging and time-of-flight data based on a 5-MHz linear array were performed on tissues with different geometries and acoustic parameters. Results show that the sound velocity error was generally 1–3 m/s, with a maximum of 5.8 m/s. The radii of the objects under investigation varied from 2 to 6 mm, and all of them were detected successfully. Thus, the proposed approach has been shown to be both feasible and accurate. The approach can be used to complement conventional B-mode imaging to further enhance the detection of breast cancer.**

I. Introduction

The detection of breast cancer is an important task of medical ultrasound. Although B-mode imaging is commonly used, several issues need to be addressed in order to improve its effectiveness in breast cancer detection. First, severe distortions caused by sound velocity inhomogeneities (including phase aberrations and wavefront amplitude distortions [1]–[5]) may be present. Such distortions degrade the contrast resolution and, therefore, reduce cancer detectability. Furthermore, even if a region is detectable above the background, it still may be difficult to distinguish a tumor from a region of fat. This leads to a second issue, related to the fundamental contrast mechanism. In B-mode ultrasound, the image contrast is primarily determined by tissue scattering properties and acoustic impedance. In other words, if two regions in the image have similar scattering properties and acoustic impedance, they may not be distinguishable. In breast B-mode ultrasound, a fat region and a tumor may have similar characteristics on the resulting image. For example, the B-mode image of a solid homogeneous hypoechoic tumor with irregular borders may look like a fat region [6]. Alternative imaging methods can be used to form a breast image based on different acoustic parameters. One example is the elasticity imaging based on elastic modulus [7], [8]; because elastic modulus varies over a wide range in different tissues, it is possible to provide a much higher contrast among different tissues of interest.

In this paper, the physical parameter of interest is the sound velocity. One of the reasons is that the velocity of sound in cancerous tissue is higher than that in fat [9]. Although the sound velocity distribution alone may not be adequate for obtaining full diagnostic information, tumors can be detected more accurately and effectively by combining the sound velocity distribution information with the corresponding B-mode image. In other words, the B-mode image and the sound velocity distribution complement each other. The second reason for using sound velocity is that, if the sound velocity distribution can be found, it may be possible to devise an adaptive imaging scheme and to correct for the image distortion in conventional B-mode imaging due to sound velocity inhomogeneities [10]–[15].

The sound velocity distribution can be measured using ultrasonic computed tomography [16]. However, the apparatus used for computed tomography is very different from that used for B-mode imaging. It is the main purpose of this paper to develop an imaging strategy for reconstructing the sound velocity distribution using pulse-echo data from a linear array, such as that used in B-mode imaging. Note that the setup is similar to the limited-angle transmission tomography setup proposed by Krueger *et al.* [17], [18]. Nonetheless, a new reconstruction algorithm is proposed in this paper that provides a significant improvement in estimation accuracy. This improvement is mainly attributable to the proposed technique successfully incorporating information from the B-mode image of the same object. As described in Sections III and IV,B, the B-mode image is used for segmentation such that constraints can be properly defined and imposed during reconstruction. Extensive simulations were performed to test the efficacy of the proposed technique. The B-mode images were simulated using a k-space method [19], and the time-of-flight data were generated using the series solution to the scattering of a plane wave incident on a fluid cylinder [20]. Applying the proposed technique produced accurate sound velocity distributions. Note that the use of B-mode images for segmentation also has been proposed in near-infrared breast imaging [21], [22].

Manuscript received June 27, 2003; accepted October 3, 2003. Support partially supplied from the National Science Council of R.O.C. under Grant NSC 92-2213-E-002-019, and partially from National Health Research Institutes of R.O.C., is gratefully acknowledged.

The authors are with the Department of Electrical Engineering, National Taiwan University, and the Division of Medical Engineering Research, National Health Research Institutes, Taipei, Taiwan (e-mail: paichi@cc.ee.ntu.edu.tw).

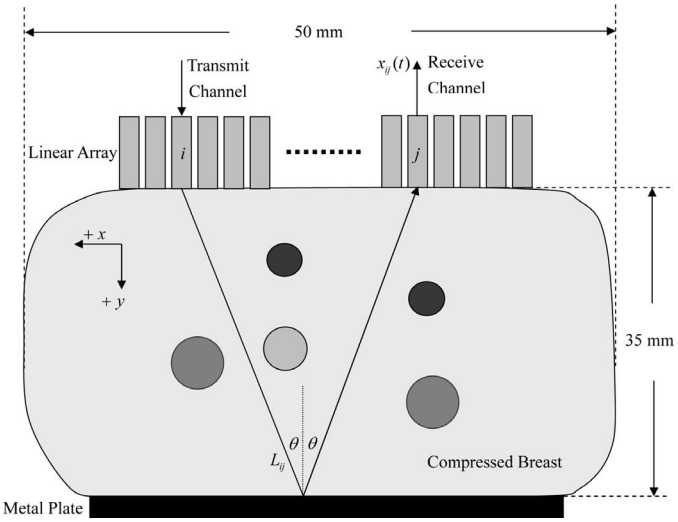

Fig. 1. Imaging setup analyzed in this paper. Each of the (N_A) channels in the array can transmit independently. A metal plate at the bottom of the compressed breast was used to reflect the signal transmitted from channel i to channel j.

The paper is organized as follows. Section II describes the methods used to generate all the required data, including the B-mode image and the time-of-flight data. Section III introduces the proposed method for reconstructing sound velocity distributions. Section IV demonstrates the efficacy of the proposed method. Section V discusses properties of the proposed method and its potential applications. The paper concludes in Section VI.

II. Data Simulations

A. Imaging Setup

The imaging setup is shown in Fig. 1. All the image objects used in this paper contain cylindrical targets along the z-axis, and t denotes the time throughout this paper. Note that the setup is similar to that of x-ray mammography [23] and the one proposed by Krueger *et al.* [17], [18] for ultrasound. Fig. 1 shows that the linear array has several (N_A) channels and that a metal plate is used for reflecting the acoustic wave. The array axis and the beam axis are defined as the x-axis and the y-axis, respectively. In addition to performing B-mode imaging, the imaging setup shown in Fig. 1 also is capable of transmitting a wideband pulse from a single channel in order to acquire a complete channel data set $\{e_{ij}(t)\}$, $1 \le i, j \le N_A$, where $e_{ij}(t)$ is the echo signal received by channel j when only channel i transmits. With $e_{ij}(t)$, the time-of-flight t_{ij} corresponding to the same transmit/receive combination for the echo reflected from the bottom metal plate can be obtained.

Let $c(x, y)$ denote the sound velocity at the center frequency of the transmitted pulse. When only soft tissues are considered and only time of flight is of interest, effects of refraction associated with sound velocity inhomogeneities can be ignored [16]. In this case:

$$t_{ij} = \int_{L_{ij}} s(x, y)dl, \tag{1}$$

where L_{ij} is the path of the line integral as shown in Fig. 1, and $s(x, y) = c^{-1}(x, y)$ is defined as the slowness. Assume the average slowness in the image object is s_0, and define:

$$t_{ij,0} = \int_{L_{ij}} s_0 dl, \tag{2}$$

as the geometrical delay, then the time of flight with geometrical delay compensated becomes:

$$\Delta t_{ij} = t_{ij} - t_{ij,0} = \int_{L_{ij}} [s(x, y) - s_0]\, dl = \int_{L_{ij}} \Delta s(x, y)dl, \tag{3}$$

where $\Delta s(x, y)$ can be discretized with spatial sampling intervals Δx_s and Δy_s in the x and y directions, respectively. In this case, (3) becomes:

$$\Delta t_{ij} = \sum_{n=1}^{N} \sum_{m=1}^{M} \Delta s(m, n) l_{ij}(m, n) = \mathbf{l}_{ij}^T \Delta \mathbf{s}, \tag{4}$$

where $\mathbf{l}_{ij}$ and $\Delta\mathbf{s}$ are $MN \times 1$ column vectors, $(\mathbf{l}_{ij})_{(m-1)N+n} \equiv l_{ij}(m, n)$ is the contribution of grid point (m, n), $1 \le m \le M$, $1 \le n \le N$ [i.e., the length of the line segment that is the intersection of the path L_{ij} and the rectangle centered at the grid point (m, n) with a size of $\Delta x_s \times \Delta y_s$], and $(\Delta\mathbf{s})_{(m-1)N+n} \equiv \Delta s(m, n)$.

There are a total of N_A^2 equations in (4). Due to the assumption of the straight-line propagation path, $\mathbf{l}_{ij} = \mathbf{l}_{ji}$, and Δt_{ij} can be set to $(\Delta t_{ij} + \Delta t_{ji})/2$ for $1 \le i \le N_A$, $1 \le j \le i$. Thus, the number of equations reduces to $N_A(N_A + 1)/2$, and they can be put into the following matrix form:

$$\mathbf{L}\Delta\mathbf{s} = \Delta\mathbf{t}, \tag{5}$$

where $\Delta\mathbf{t}$ is an $\left[N_A(N_A + 1)/2\right] \times 1$ column vector and $\mathbf{L}$ is an $\left[N_A(N_A + 1)/2\right] \times MN$ matrix. In (5), $\Delta\mathbf{t}$ is obtained from the channel data, and $\mathbf{L}$ is calculated based on the geometry. The focus of this paper is to develop a scheme for accurately solving slowness distribution $\Delta\mathbf{s}$.

B. B-mode Image Generation

All B-mode images in this paper were generated with a k-space method proposed by Tabei *et al.* [19]. This method solves the coupled first-order linear acoustic propagation equations for a fluid medium and allows inclusion of relaxation absorption and perfectly matched layers. It enables accurate calculation of scattering in soft tissues and, therefore, simulated speckle images can be formed. Furthermore, diffraction, refraction, and scattering in an inhomogeneous medium are all accounted for.

All data in this paper were generated under MATLAB (Mathworks, Natick, MA). The fast Fourier transform in the west (FFTW) routine also was adopted [24] for the fast Fourier transform in order to make the k-space method more computationally efficient. All codes were developed by the authors except for the FFTW. The hardware platform was a personal computer with a 2.4 GHz Pentium 4 CPU (Intel, Santa Clara, CA) and a total RAM of 1.5 gigabytes. It took about one day to generate the required data for each case. Obtaining a complete channel data set $\{e_{ij}(t)\}$, $1 \le i, j \le N_A$, requires N_A firings, which in general is very time consuming. In order to reduce the computation time, only eight firings were used per image, with all channels receiving to generate a B-mode image using a synthetic aperture approach.

C. Generation of the Time-of-Flight Data

The simulation time can be reduced by generating the time-of-flight data without simulating the channel data. In this case, the time-consuming k-space method is replaced by the series solution to the scattering of a plane wave incident on a fluid cylinder [20]. The details of this method are provided in Appendix A. Note that there are limitations associated with this approach: relaxation absorption cannot be fully taken into consideration, and the medium can contain only cylindrical targets with a circular cross section. Nonetheless, a case (which is the same as the 1× case in Section IV-A, except for the absence of relaxation absorption) was used for verification. The results show that the differences in time of flight between this method and the k-space method can be ignored.

III. Reconstruction of the Sound Velocity Distribution

Several approaches can be used to solve (5), of which a convex programming formulation for inconsistent problems [25] was chosen because it can incorporate the B-mode image information. Appendix B provides details of the convex programming formulation. Note that, in this paper, $C = \{\mathbf{x} \in \mathbf{X} : \text{property } P(\mathbf{x})\}$ means that C is a subset of $\mathbf{X}$ containing all $\mathbf{x}$ in $\mathbf{X}$ which have the property P [26].

To achieve good reconstruction accuracy, prior knowledge of $\Delta\mathbf{s}$ in (5) must be used. For example, the sound velocity in soft tissue and $\Delta\mathbf{s}$ are both bounded. Thus, the sound velocity is assumed to be in $[c_{\text{lower}}, c_{\text{upper}}]$ (where $c_{\text{lower}} = 1450$ m/s and $c_{\text{upper}} = 1580$ m/s throughout the paper), and this is a hard constraint (i.e., a constraint that cannot be violated). Define:

$$C_{\text{velocity}} = \Big\{\mathbf{x} \in \mathbf{R}^{MN} : x_l \in \left[c_{\text{upper}}^{-1} - s_0, c_{\text{lower}}^{-1} - s_0\right], \quad 1 \le l \le MN\Big\}, \tag{6}$$

where s_0 is the assumed background slowness; then C_{velocity} is referred to as a property set as it is relevant to the prior knowledge. Note that C_{velocity}, which contains the slowness distribution that satisfies the velocity constraints, is nonempty, bounded, closed, and convex.

If $\mathbf{L}$ in (5) is expressed as $\mathbf{L} = \left[\mathbf{l}_1\ \mathbf{l}_2\ \cdots\ \mathbf{l}_{N_A(N_A+1)/2}\right]^T$ and $\Delta\mathbf{t}$ as $\Delta\mathbf{t} = \left[\Delta t_1\ \Delta t_2\ \cdots\ \Delta t_{N_A(N_A+1)/2}\right]^T$, in order to satisfy (5), the slowness distribution $\Delta\mathbf{s}$ must belong to:

$$C_{\Delta t_i} = \left\{\mathbf{x} \in \mathbf{R}^{MN} : \langle \mathbf{x}, \mathbf{l}_i \rangle = \Delta t_i\right\}, \quad i = 1, 2, \cdots, N_A(N_A+1)/2, \tag{7}$$

where each $C_{\Delta t_i}$ is a closed and convex set in $\mathbf{R}^{MN}$ (i.e., $\Delta\mathbf{s}$ must belong to $\bigcap C_{\Delta t_i}$, the intersection of the $C_{\Delta t_i}$ sets). Each $C_{\Delta t_i}$ set in (7) is referred to as a data set as it is directly related to the known Δt_i. The $\bigcap C_{\Delta t_i}$ may be empty, and even if it is nonempty, the points in the set may not lead to reasonable sound velocities. Therefore, the $C_{\Delta t_i}$ that contains all the slowness distributions that satisfy Δt_i is a soft-constraint set. The slowness distribution $\Delta\mathbf{s}$ does not have to match all time-of-flight data. In other words, violation is allowed. Nonetheless, the distribution must minimize the total errors.

A slowness distribution $\mathbf{x} \in C_{\text{velocity}}$ minimizing the cost function (i.e., the total amount of violation of the time-of-flight data):

$$\Phi^s(\mathbf{x}) = \frac{1}{2} \sum_{i=1}^{N_A(N_A+1)/2} w_i d^2\left(\mathbf{x}, C_{\Delta t_i}\right), \tag{8}$$

where $w_i \in (0, 1]$ for all $i \in \{1, 2, \cdots, N_A(N_A+1)/2\}$, $\sum_{i=1}^{N_A(N_A+1)/2} w_i = 1$, and $d\left(\mathbf{x}, C_{\Delta t_i}\right)$ is the distance between $\mathbf{x}$ and $C_{\Delta t_i}$, can be found by taking $\mathbf{x}$ as the limit of the sequence $\{\mathbf{x}_n\}$ (i.e., $\lim_{n\to\infty} \mathbf{x}_n$). The $\mathbf{x}_0 \in C_{\text{velocity}}$ is an initial slowness distribution and:

$$\mathbf{x}_{n+1} = (1 - \lambda_n)\,\mathbf{x}_n + \lambda_n P_{C_{\text{velocity}}}\left[(1-\gamma)\mathbf{x}_n + \gamma \sum_{i=1}^{N_A(N_A+1)/2} w_i P_{C_{\Delta t_i}}(\mathbf{x}_n)\right], \quad n \ge 1, \tag{9}$$

where $\lambda_n \in [0, 1]$ for all $n \ge 0$, $\sum_{n\ge 0} \lambda_n(1 - \lambda_n) = \infty$, $\gamma \in (0, 2]$, and $P_{C_{\text{velocity}}}$ is the projector onto C_{velocity}. This algorithm is called Algorithm I. The parameters λ_n and γ determine the rate of convergence, and the weights w_i reflect the relative importance of the time-of-flight data. In each case in this paper, all weights w_i were set to be the same (i.e., each time of flight is equally important), $\lambda_n = 0.5$ for all $n \ge 0$ (satisfying $\sum_{n\ge 0} \lambda_n(1 - \lambda_n) = \infty$), and $\gamma = 1$.

As is shown in Section IV-A, using only C_{velocity} as the hard-constraint set is not sufficient to obtain an accurate sound velocity distribution; thus, other constraints are needed. A second method using the B-mode image information is proposed. Consider a B-mode image in which an object contains a region of interest surrounded by the background. Suppose that this region can be identified and segmented, then different constraints can be

$$C_{\text{image}} = \begin{cases} \left\{ \begin{array}{c} \mathbf{x} \in \mathbf{R}^{MN} : x_{b_1} = x_{b_2} = \cdots = x_{b_{N_b}}, x_{r_1} = x_{r_2} = \cdots = x_{r_{N_r}}, \\ x_{br_i} \in [x_{b_1}, x_{r_1}], 1 \le i \le N_{br} \end{array} \right\} & \text{if } x_{b_1} \le x_{r_1} \\ \left\{ \begin{array}{c} \mathbf{x} \in \mathbf{R}^{MN} : x_{b_1} = x_{b_2} = \cdots = x_{b_{N_b}}, x_{r_1} = x_{r_2} = \cdots = x_{r_{N_r}}, \\ x_{br_i} \in [x_{r_1}, x_{b_1}], 1 \le i \le N_{br} \end{array} \right\} & \text{otherwise} \end{cases}, \tag{10}$$

imposed in the region of interest and the background. In other words, the property set in (10) (see above) can be generated and used as another hard-constraint set: where $I_b \equiv \{b_1, b_2, \cdots, b_{N_b}\}$ is the background index set, $I_r \equiv \{r_1, r_2, \cdots, r_{N_r}\}$ is the region-of-interest index set, and $I_{br} \equiv \{br_1, br_2, \cdots, br_{N_{br}}\}$ is the boundary index set. All the slowness values in the background must be the same, and all the slowness values in the region of interest also must be the same. In addition, each slowness value at the boundary must be between that of the background and that of the region of interest. Note that no specific slowness value has been set in any region at this point. Also note that C_{image}, which contains all the slowness distributions that satisfy the constraint derived from the B-mode image, also is closed and convex. The C_{image} can be generated similarly when the object contains more regions of interest. A slowness distribution $\mathbf{x} \in C_{\text{velocity}} \cap C_{\text{image}}$ minimizing $\Phi^s(\mathbf{x})$ can be found by taking $\mathbf{x}$ as the limit of the sequence $\{\mathbf{x}_n\}$ (i.e., $\lim_{n\to\infty} \mathbf{x}_n$). The $\mathbf{x}_0 \in C_{\text{velocity}} \cap C_{\text{image}}$ is an initial slowness distribution and:

$$\mathbf{x}_{n+1} = (1-\lambda_n)\,\mathbf{x}_n + \lambda_n P_{C_{\text{velocity}} \cap C_{\text{image}}} \left[(1-\gamma)\mathbf{x}_n + \gamma \sum_{i=1}^{N_A(N_A+1)/2} w_i P_{C_{\Delta t_i}}(\mathbf{x}_n) \right], \; n \ge 1. \tag{11}$$

This algorithm is called Algorithm II, which differs from Algorithm I only in the projector outside the brackets (i.e., the slowness distribution must be in the hard-constraint set C_{image} in addition to being in C_{velocity} in Algorithm II). The critical issue of the proposed method is the incorporation of C_{image}, which is shown in Section IV to be crucial to the quality of the reconstructed sound velocity distribution.

A sound velocity distribution $\mathbf{c} = [c_1 \; c_2 \; \cdots \; c_{MN}]^T$ and a slowness distribution $\Delta\mathbf{s} = [\Delta s_1 \; \Delta s_2 \; \cdots \; \Delta s_{MN}]^T$ are related as follows:

$$c_l = (s_0 + \Delta s_l)^{-1}, \; l = 1, 2, \cdots, MN. \tag{12}$$

IV. Numerical Results

All the raw data generated in this paper were noise free.

A. Algorithm I: Reconstruction Without the B-mode Image

Conventional ultrasonic transmission tomography acquires complete projection data over an angular range of 180° [16], so that the reconstruction quality will be degraded if the data set does not span the full 180°. The more data are missing, the poorer the resulting reconstruction quality becomes [27]–[29].

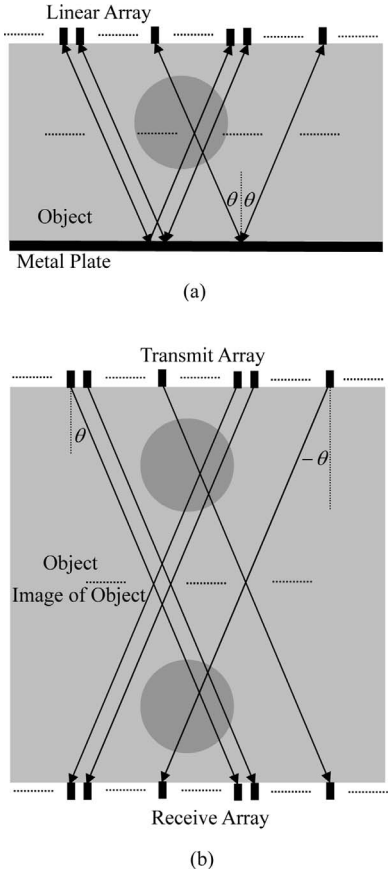

Fig. 2. (a) Collecting all the time-of-flight data with the angle of incidence of θ is equivalent to (b) inspecting the object at angle θ and angle $-\theta$ simultaneously in conventional transmission tomography.

Limited-angle transmission tomography using linear arrays does not provide a complete data set. As shown in Fig. 2(a), the incidence and reflection angles are both equal to θ. Collecting all the time-of-flight data with an angle of incidence of θ in Fig. 2(a) is effectively equal to inspecting the object at angle θ and angle $-\theta$ simultaneously in conventional transmission tomography, as shown in Fig. 2(b). To have a complete data set, the maximal available θ, denoted by $\theta_{\max}$, has to be 90°. This is impossible with a linear array. If the array has N_A transducers, a pitch of p, and a distance between the array and the metal plate of D, then it easily can be shown that:

$$\theta_{\max} = \tan^{-1}\left[\frac{(N_A - 1)\,p}{2D}\right]. \tag{13}$$

A typical $\theta_{\max}$ is 26.6° with $D = 35$ mm and $(N_A - 1)\,p = 35$ mm. Note that the data at $\theta_{\max}$ are not complete because only one time of flight can be collected at this angle. Also note that $(N_A - 1)\,p$ is close to the array width $N_A p$. Thus, in limited-angle transmission tomography, obtaining a large $\theta_{\max}$ is only possible with a large linear array; hence, the effect of the array size on reconstruction accuracy needs to be evaluated.

Consider the configuration shown in Fig. 2(a). The image object consists of a background of glandular material with a cylinder of fat with a radius of 4 mm at its center. The corresponding parameters of the different materials are listed in Table I [9], [30]. Each array channel has a Gaussian frequency response with a center frequency of 5 MHz and a two-way −12 dB fractional bandwidth of 0.6. All array elements are assumed to be a line source. The pitch is $p = 0.45$ mm and the distance is $D = 35$ mm. Sound velocity distributions were reconstructed in three cases corresponding to N_A values of 312(4×), 156(2×), and 78(1×).

The time-of-flight data were first generated using the method described in Section II-C and Appendix A. The attenuation resulting from relaxation absorption was neglected; but the dependency of sound velocity c on frequency f, also resulting from relaxation absorption, was taken into account by (14) (see next page) [31]: where ρ is the density of the medium, $\kappa_\infty = 1/\rho c_\infty^2$, c_∞ is the sound velocity of the medium when the temporal frequency f approaches infinity, τ_q is the relaxation time for the qth order relaxation process, and κ_q is the relaxation modulus for the qth order relaxation process. Fig. 3(a) shows all the receive envelope data when the 39th channel was used on transmit in the 1× case with geometrical delays compensated. The corresponding time of flight was extracted from the envelope based on the center of gravity of the square of the envelope (i.e., the center of gravity with the square of the envelope as its density distribution function) around the peak. Note that the cylinder of fat introduced both time-of-flight errors and waveform distortion. The presence of severe waveform distortion will make it difficult to determine a reliable time of flight; thus, this signal should be dropped. In this paper, all cases followed the rule below, except for the 4× case. Let E_{ij} denote the energy of the signal around the time-of-flight t_{ij} received by channel j when channel i is transmitted. Then t_{ij} (and Δt_{ij}) is dropped if:

$$E_{ij} < 0.25 \frac{1}{N_A} \sum_{q=1}^{N_A} E_{iq}. \tag{15}$$

In the 4× case, the t_{ij} data were inspected manually when $1 \le i \le 70$, $243 \le j \le 312$, or $243 \le i \le 312$, $1 \le j \le 70$, because their corresponding envelopes were not severely distorted despite the energy being low. The geometrically compensated time-of-flight data in the 1× case are shown in Fig. 3(b). Note that all the dropped Δt_{ij} data values were replaced by 0. The dropped transmit/receive combinations are shown in Fig. 3(c) in white.

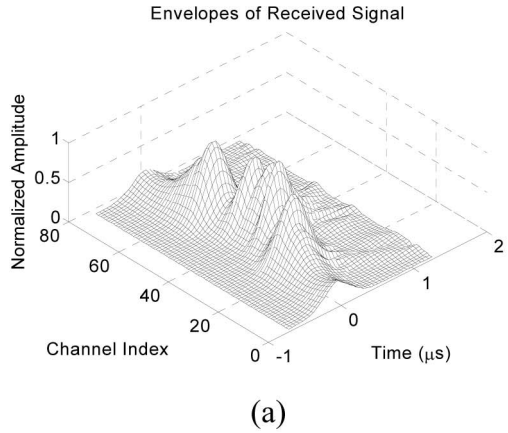

(a)

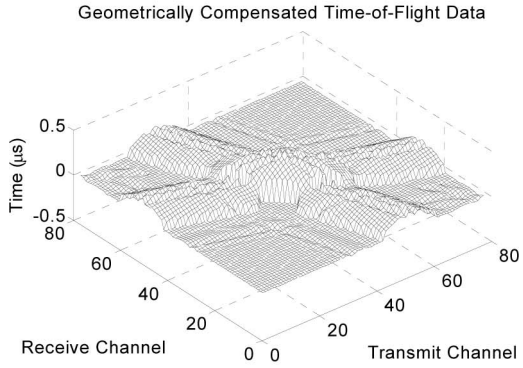

(b)

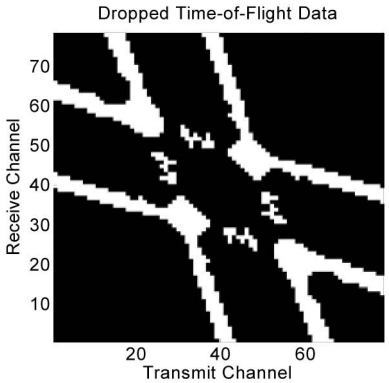

(c)

Fig. 3. (a) The envelopes of the received signals when the 39th channel is transmitted in the 1× case. Geometrical delays have been compensated. The attenuation resulting from relaxation absorption was neglected, but the dependency of sound velocity c on frequency f, also resulting from relaxation absorption, was taken into account. (b) The geometrically compensated time-of-flight data in the 1× case. Note that all the dropped Δt_{ij} data values are replaced by 0. (c) White at position (i, j) means that the associated Δt_{ij} was dropped.

TABLE I
PARAMETERS USED IN FIG. 2(A).

Material	Sound velocity c_∞ (m/s)	Density ρ (g/cm^3)	Absorption α (dB/cm/MHz)	$\tau_1 = 20$ ns $(\kappa_1/\kappa_\infty) \times 10^3$	$\tau_2 = 200$ ns $(\kappa_2/\kappa_\infty) \times 10^3$
Glandular	1521	1.05	1.136	10.76	10.34
Fat	1471	0.94	0.536	4.91	4.72
Tumor	1549	1.12	1.478	14.27	13.71

$c_\infty \equiv \lim_{f\to\infty} c(f)$. At $f = 5$ MHz the sound velocities are 1515.0 m/s, 1468.3 m/s, and 1542.7 m/s in glandular tissue, fat, and tumor, respectively. The sound velocity, density, and absorption values are in agreement with those of soft tissues as shown in [9], [30].

$$c(f) = \sqrt{\frac{2}{\rho}} \left\{ \kappa_\infty + \sum_{q=1}^{2} \frac{\kappa_q}{1 + 4\pi^2 \tau_q^2 f^2} + \left[\left(\kappa_\infty + \sum_{q=1}^{2} \frac{\kappa_q}{1 + 4\pi^2 \tau_q^2 f^2} \right)^2 + \left(\sum_{q=1}^{2} \frac{2\pi \kappa_q \tau_q f}{1 + 4\pi^2 \tau_q^2 f^2} \right)^2 \right]^{\frac{1}{2}} \right\}^{-\frac{1}{2}}, \qquad (14)$$

After the time-of-flight data were obtained, sound velocity distributions in the central 35-mm width were reconstructed using Algorithm I (Fig. 4). Here, the sampling intervals Δx_s and Δy_s of the sound velocity distribution in the x and y directions were both 1 mm. The other parameters were $c_{\text{lower}} = 1450$ m/s and $c_{\text{upper}} = 1580$ m/s. Figs. 4(a) and (b), 4(c) and (d), and 4(e) and (f) display the results for 4×, 2×, and 1×, respectively. The reconstructed sound velocity distribution is shown in the left panels over a range from 1450 m/s to 1580 m/s, and the sound velocity error is shown in the right panels over a range from 0 m/s to 65 m/s. The sound velocity error is defined as the absolute value of the difference between the reconstructed sound velocity and the true sound velocity at 5 MHz (i.e., the transmit center frequency). It is obvious that, with a larger array, the sound velocity distribution can be reconstructed more accurately. To quantify the accuracy, define:

$$|\Delta c| = \frac{1}{N_{\text{fat}}} \sum_{(m,n)\in I_{\text{f}}} |c(m,n) - c_{\text{f,true}}|, \qquad (16)$$

where $c(m,n)$ is the reconstructed sound velocity, $c_{\text{f,true}} = 1468.3$ m/s is the true sound velocity at 5 MHz in the fat region, I_{f} is the index set containing all coordinates (m,n) of a rectangle locating entirely in the fat region, and N_{fat} is the number of elements in I_{f}. A smaller $|\Delta c|$ indicates higher accuracy. The $|\Delta c|$ values in the 4×, 2×, and 1× cases were 11.8, 19.9, and 28.5 m/s, respectively.

The 4× case outperformed the 2× and 1× cases, but the array used in that case is too large ($N_A p = 140.4$mm) and may not be clinically useful. However, the value of $\theta_{\max}$ in the 4× case is only 63.4°. In other words, the time-of-flight data for the 4× case is far from a complete data set. Therefore, increasing the array size to enhance the quality of sound velocity distribution is impractical in limited-angle transmission tomography.

B. Algorithm II: Reconstruction with the B-mode Image Information

With only the time-of-flight data and the general constraints on the sound velocity, Section IV-A shows that the accuracy of the sound velocity estimation is insufficient. This subsection uses Algorithm II, introduced in Section III, in order to improve this. In this case, constraints are derived from the B-mode image, and these are incorporated in the algorithm. The time-of-flight data were generated in the same way as described in Section IV-A.

Consider again the configuration shown in Fig. 2(a). In all cases shown below, an array with $N_A = 234$ and $p = 0.15$ mm (giving an array width of $N_A p = 35.1$ mm) was used. When generating the time-of-flight data, only every third channel both on transmit and receive in the array was used. The distance D between the array and the metal plate was 35 mm. The other parameters were $c_{\text{lower}} = 1450$ m/s, $c_{\text{upper}} = 1580$ m/s, $\Delta x_s = 0.5$ mm, and $\Delta y_s = 0.5$ mm.

The k-space method introduced in Section II-B was used to generate all the B-mode images in this paper. The pixel sizes used in the k-space method and the B-mode images are both 0.04 mm by 0.04 mm throughout the paper. Random perturbations to densities in different regions were introduced to produce speckle images because they can introduce acoustic impedance mismatches and, therefore, cause scattering. Spatial compounding [32] then was applied to reduce the speckle intensity variations before segmentation was subsequently applied. To reduce the computation time, only eight channels (channels 27, 53, 79, 105, 130, 156, 182, and 208) were used on transmit, and only receive channels with j values obeying $|j-i| \le 26$ were used on receive when channel i was fired. One subimage per transmit was reconstructed, and all eight subimages were compounded into a single image. To further reduce the speckle noise, the compound B-mode image was low-pass filtered using a two-dimensional Gaussian filter with

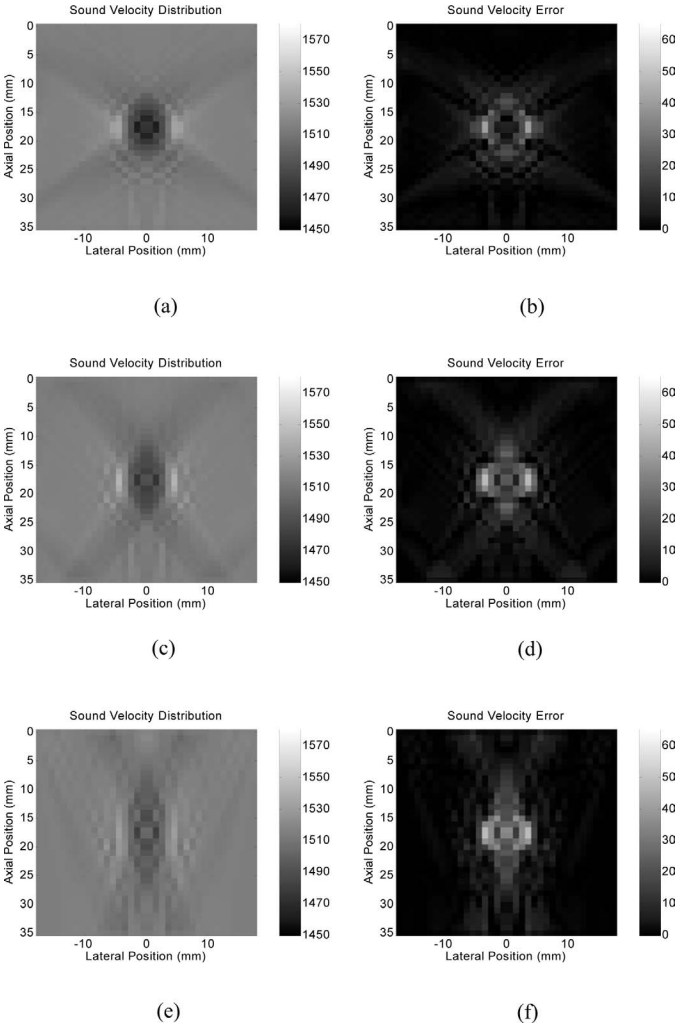

Fig. 4. (a), (c), (e) Sound velocity distributions in the central 35-mm width in the 4×, 2×, and 1× cases, respectively. (b), (d), (f) Reconstruction errors in the central 35-mm width in the 4×, 2×, and 1× cases, respectively. Algorithm I was used; therefore, no B-mode image information was used. Note that absolute values of the errors are displayed. Also note that these results using Algorithm I are inferior to those of Algorithm II, as shown in the following figures.

a $1/e$ cutoff at 0.152 mm to generate the final B-mode image. Once the filtered B-mode image was obtained, a single threshold was applied for segmentation.

An object shown in Fig. 5(a) was considered first. It comprised a background of glandular material with a cylinder of fat with a radius of 4 mm at its center. The random perturbations added to the densities were 0.5% and 2.5% (root-mean-squared amplitude) for the cylinder and the background, respectively. The corresponding B-mode image is shown in Fig. 5(b). After applying a threshold to the processed B-mode image, the fat region was extracted as shown in Fig. 5(c). The boundary between the fat region and the background was directly derived from the segmented fat region by morphological dilation [33] (according to the disparity between the segmented fat region and its dilated version) as shown in Fig. 5(d).

The reconstructed sound velocity distribution and the image of sound velocity error are shown in Figs. 6(a) and

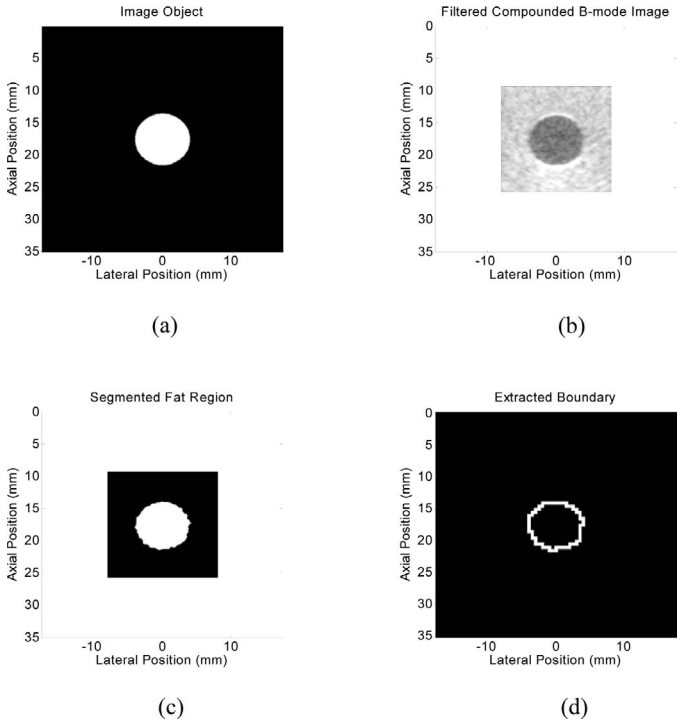

Fig. 5. (a) Image object comprising a background of glandular material with a cylinder of fat with a radius of 4 mm at its center. (b) B-mode image displayed with a 30-dB dynamic range. (c) Segmented fat region. (d) Boundary between the fat region and the background derived from the segmented fat region.

(b), respectively. This example is referred to as Case I in Table II. The reconstructed sound velocity in the segmented fat region ($c_{\mathrm{c,recon}}$) is 1465.7 m/s, which is only 2.6 m/s slower than the true sound velocity of fat at 5 MHz ($c_{\mathrm{c,true}} = 1468.3$ m/s). Moreover, the reconstructed sound velocity in the background region, $c_{\mathrm{b,recon}}$, is the same as the true sound velocity of glandular material at 5 MHz ($c_{\mathrm{b,true}} = 1515.0$ m/s). Note that the subscripts c and b here stand for cylinder and background, respectively. Objects with different geometries and acoustic parameters also were evaluated. The parameters are summarized in Table II, and the reconstructed results are shown in Figs. 6–8 using Case I as the reference. In Fig. 6, effects of the size of the cylinder on the reconstruction accuracy are shown. In Fig. 7, the results correspond to different sound velocity in the cylinder. In Fig. 8, effects of the position of the cylinder in the axial dimension are demonstrated. Define errors as:

$$\Delta c_{(\cdot)} = c_{(\cdot),\mathrm{recon}} - c_{(\cdot),\mathrm{true}}, \tag{17}$$

where $(\cdot)$ denotes b or c. In all cases, the errors in the background region were almost zero. However, the errors in the fat region were more significant. Also note that, in all cases, larger errors occurred at boundaries. Figs. 6(a) and (b), 6(c) and (d), and 6(e) and (f) show the estimation results corresponding to cylinders with radii of 4 mm, 2 mm, and 6 mm, respectively. The left panels [Figs. 6(a), (c), and (e)] are the sound velocity distributions; the right panels [Figs. 6(b), (d), and (f)] are the sound velocity errors. The

TABLE II
PARAMETERS USED IN THE CASES SHOWN IN FIGS. 6–8 AND THE ESTIMATION RESULTS.

Case	$c_{c,true}$ (m/s)	Cylinder radius (mm)	Δc_c (m/s)	Δc_c^* (m/s)	Δc_b (m/s)	Δc_b^* (m/s)	Cylinder position
I	1468.3	4	−2.6	1.5	0.0	0.1	Center
II	1468.3	2	−0.1	5.8	0.1	0.1	Center
III	1468.3	6	−1.4	0.4	0.0	0.0	Center
I	1468.3	4	−2.6	1.5	0.0	0.1	Center
IV	1493.2	4	−2.8	−0.1	0.0	0.0	Center
V	1505.8	4	−2.5	−1.3	0.0	0.0	Center
VI	1568.0	4	2.0	−5.6	0.1	0.0	Center
I	1468.3	4	−2.6	1.5	0.0	0.1	Center
VII	1468.3	4	−1.2	1.9	0.0	0.1	5.5 mm up from the center
VIII	1468.3	4	−2.2	1.3	0.0	0.0	5.5 mm down from the center

Δc_c and Δc_b were obtained with the boundary derived from the B-mode images. Δc_b^* and Δc_c^* were obtained with the boundary set to perfectly match the original boundary. $c_{b,true} = 1515.0$ m/s in all cases.

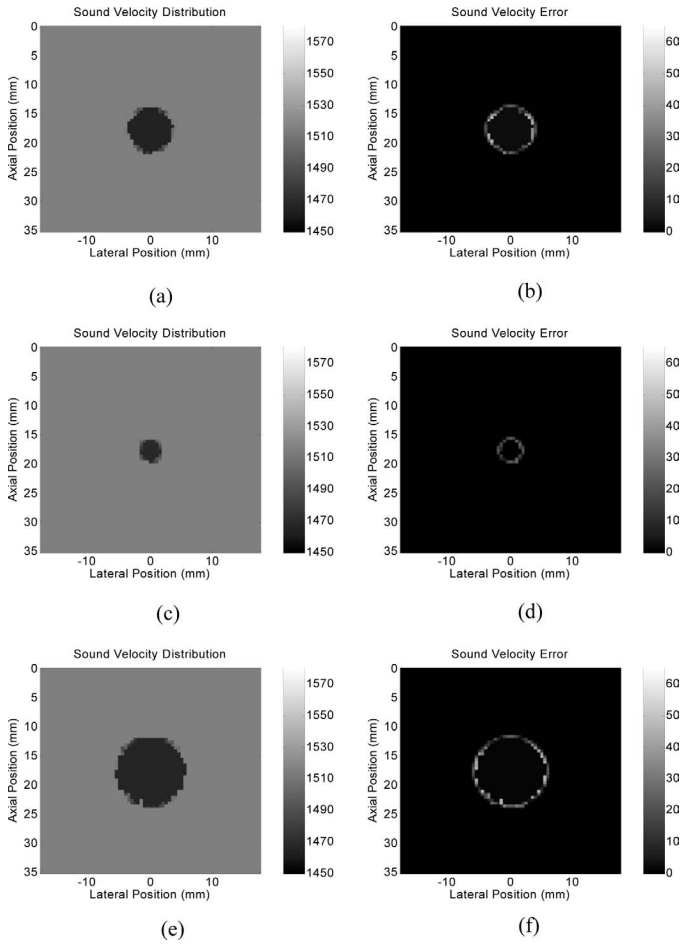

Fig. 6. Reconstructed sound velocity distributions and reconstruction errors. (a) and (b) Case I (cylinder radius = 4 mm, $c_{c,true}$ = 1468.3 m/s, and $c_{b,true} = 1515.0$ m/s). (c) and (d) Case II (cylinder radius = 2 mm, $c_{c,true} = 1468.3$ m/s, and $c_{b,true} = 1515.0$ m/s). (e) and (f) Case III (cylinder radius = 6 mm, $c_{c,true} = 1468.3$ m/s, and $c_{b,true}$ = 1515.0 m/s). Algorithm II was used, hence, the B-mode segmentation information was used. The simulation parameters also are listed in Table II.

Δc_c values are −2.6 m/s, −0.1 m/s, and −1.4 m/s, respectively, and those of Δc_b are 0.0 m/s, 0.1 m/s, and 0.0 m/s, respectively. Figs. 7(a) and (b), 7(c) and (d), 7(e) and (f), and 7(g) and (h) show the sound velocity distributions and sound velocity errors corresponding to cylinders with sound velocities ($c_{c,true}$) of 1468.3 m/s, 1493.2 m/s, 1505.8 m/s, and 1568.0 m/s, respectively. The Δc_c values are −2.6 m/s, −2.8 m/s, −2.5 m/s, and 2.0 m/s, respectively; those of Δc_b are 0.0 m/s, 0.0 m/s, 0.0 m/s, and 0.1 m/s, respectively. Figs. 8(a) and (b), 8(c) and (d), and 8(e) and (f) show the sound velocity distributions and sound velocity errors corresponding to cylinders at different positions (center, upper, and lower, respectively). The Δc_c values are −2.6 m/s, −1.2 m/s, and −2.2 m/s, respectively; those of Δc_b are all zero.

All the above cases considered only a single target in the object. A more complicated object comprising a background of glandular material with three cylinders, all with a radius of 4 mm, also was used to test Algorithm II. The geometry of the object is shown in Fig. 9(a). The first cylinder, located in the upper-left corner, was assigned the physical parameters of fat except for the sound velocity, which was set to $c_{c,1,\infty} = 1496$ m/s; the subscripts c and 1 denote the first cylinder, and the subscript ∞ indicates an infinitely high frequency. The second cylinder, located in the upper-right corner, was assigned the parameters of a tumor, and the third cylinder, located in the lower region, was assigned those of fat. All parameters are listed in Table I. The random perturbations added to the densities of the first, second, and third cylinder, and the backgrounds were 0.5%, 0.5%, 0.89%, and 2.5% (root-mean-squared amplitude), respectively. The B-mode image is shown in Fig. 9(b). Fig. 9(c) shows the segmentation result after a −14 dB (with respect to the maximal intensity) threshold is applied. In this case, several smaller regions randomly distributed in the background also were present. For each pixel of a size of $\Delta x_s \cdot \Delta y_s$, if the above-threshold area is lower than $0.96 \cdot \Delta x_s \cdot \Delta y_s$, then this pixel will

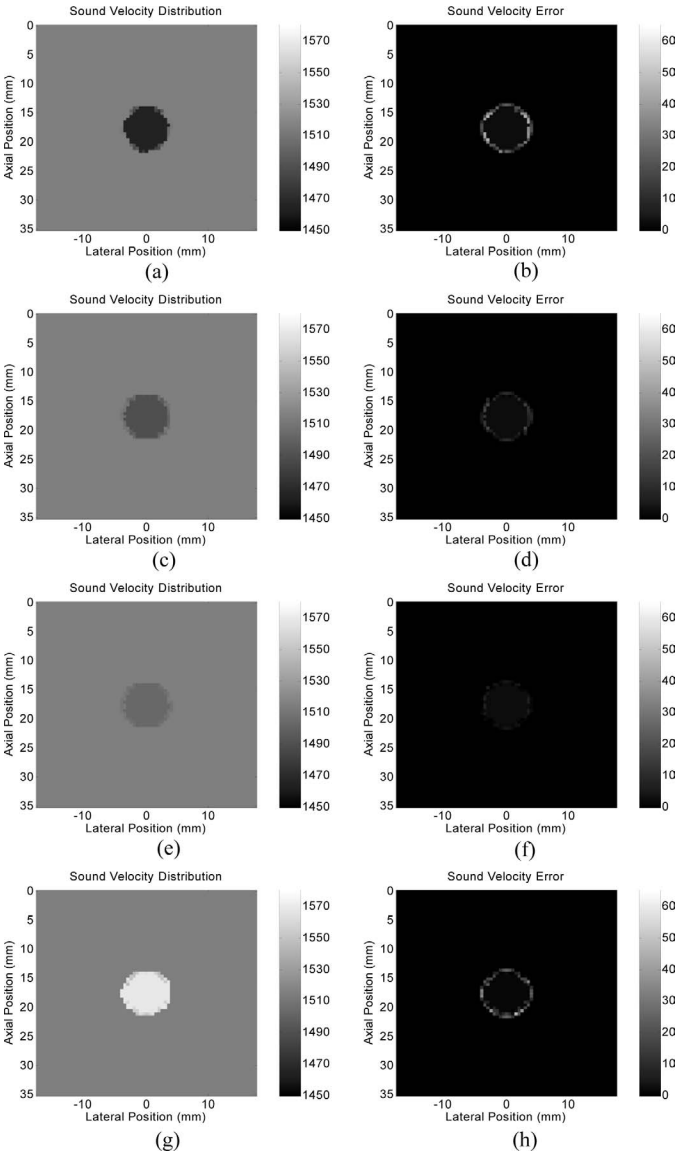

Fig. 7. Reconstructed sound velocity distributions and reconstruction errors. (a) and (b) Case I (cylinder radius = 4 mm, $c_{\mathrm{c,true}} = 1468.3$ m/s, and $c_{\mathrm{b,true}} = 1515.0$ m/s). (c) and (d) Case IV (cylinder radius = 4 mm, $c_{\mathrm{c,true}} = 1493.2$ m/s, and $c_{\mathrm{b,true}} = 1515.0$ m/s). (e) and (f) Case V (cylinder radius = 4 mm, $c_{\mathrm{c,true}} = 1505.8$ m/s, and $c_{\mathrm{b,true}} = 1515.0$ m/s). (g) and (h) Case VI (cylinder radius = 4 mm, $c_{\mathrm{c,true}} = 1568.0$ m/s, and $c_{\mathrm{b,true}} = 1515.0$ m/s). The simulation parameters also are listed in Table II.

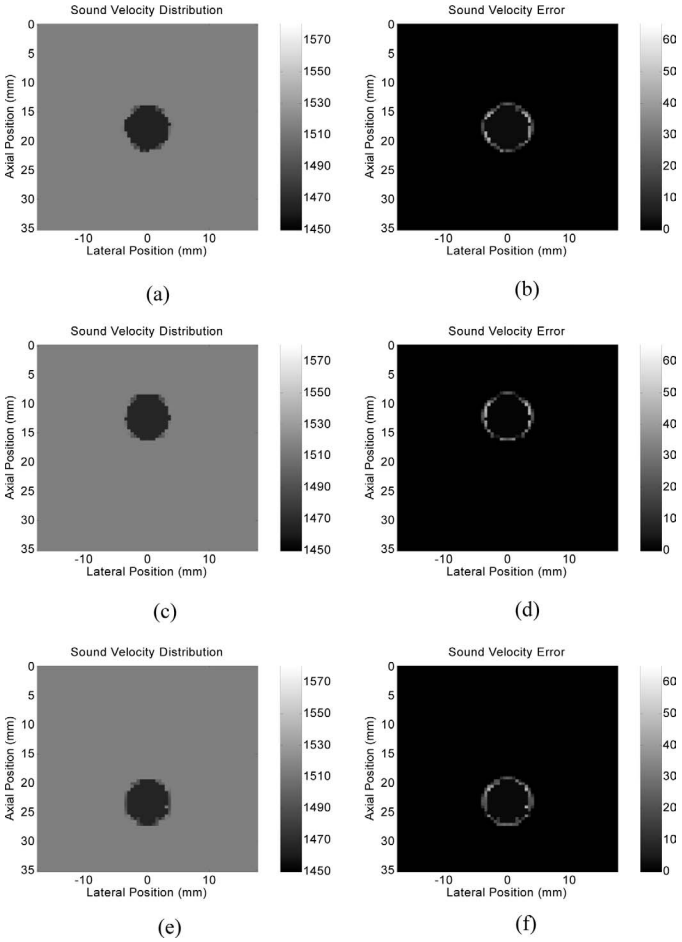

Fig. 8. Reconstructed sound velocity distributions and reconstruction errors. (a) and (b) Case I (the cylinder is at the center). (c) and (d) Case VII (the cylinder is at an upper position). (e) and (f) Case VIII (the cylinder is at a lower position). In all cases cylinder radius = 4 mm, $c_{\mathrm{c,true}} = 1468.3$ m/s, and $c_{\mathrm{b,true}} = 1515.0$ m/s. The simulation parameters also are listed in Table II.

be regarded as being outside the region of interest. That is, an area ratio threshold of 0.96 was applied to the segmentation results shown in Fig. 9(c) before morphological dilation was applied. Therefore, these small regions were automatically removed during boundary extraction due to their smaller size; the boundaries are shown in Fig. 9(d). Note that removal of the smaller regions depends on the sampling intervals (Δx_{s} and Δy_{s}), and additional image processing techniques may be applied to improve boundary detection. The reconstructed sound velocity distribution is shown in Fig. 9(e), and the reconstruction error is shown in Fig. 9(f). In this case, $\Delta c_{\mathrm{b}} = 0.3$ m/s, $\Delta c_{\mathrm{c},1} = -3.2$ m/s, $\Delta c_{\mathrm{c},2} = 1.2$ m/s, and $\Delta c_{\mathrm{c},3} = 0.4$ m/s.

V. Discussion

A. Accuracy of Sound Velocity Reconstruction

The derivation of (5) assumed straight-line propagation, whereas the time-of-flight data were generated with the effects of refraction. Nonetheless, sound velocity reconstruction generally still was accurate due to the use of hard constraints derived from the B-mode image. Besides, the time of flight was used only to derive soft constraints that were allowed to be violated, which reduced the impact of refraction.

Note that the segmentation method used in this paper produced a detected area smaller than the original area. The accuracy of boundary extraction also affects the reconstruction results. All of the eight cases described in Section IV-B were repeated using the true boundaries instead of boundaries derived from the segmented B-mode images. The results are denoted as $\Delta c_{\mathrm{c}}^{*}$ and $\Delta c_{\mathrm{b}}^{*}$, and are listed in Table II. In general, the reduction in the detected area has a bigger impact on smaller targets because the relative error of detected area (error of area over true area) is larger

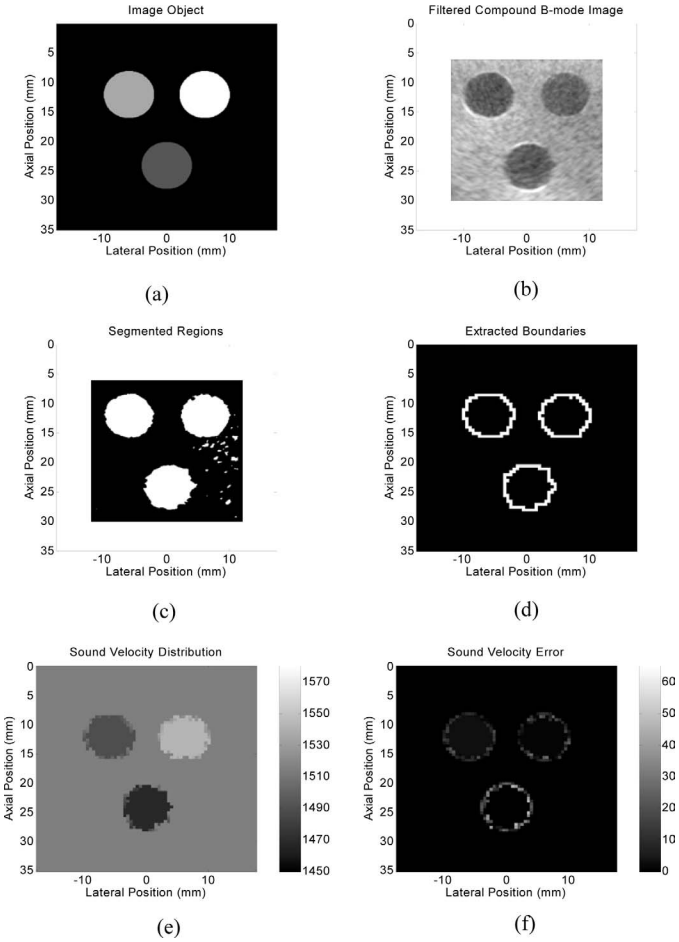

Fig. 9. (a) Image object comprising a background of glandular material ($c_{\mathrm{b},\infty} = 1521$ m/s, $\rho_{\mathrm{b}} = 1.05$ g/cm^3, and $\alpha_{\mathrm{b}} = 1.136$ dB/cm/MHz) with three cylinders of the same radius of 4 mm ($c_{\mathrm{c},1,\infty} = 1496$ m/s, $\rho_{\mathrm{c},1} = 0.94$ g/cm^3 and $\alpha_{\mathrm{c},1} = 0.536$ dB/cm/MHz in the upper-left cylinder, $c_{\mathrm{c},2,\infty} = 1549$ m/s, $\rho_{\mathrm{c},2} = 1.12$ g/cm^3 and $\alpha_{\mathrm{c},2} = 1.478$ dB/cm/MHz in the upper-right cylinder and $c_{\mathrm{c},3,\infty} = 1471$ m/s, $\rho_{\mathrm{c},3} = 0.94$ g/cm^3, and $\alpha_{\mathrm{c},3} = 0.536$ dB/cm/MHz in the lower cylinder). (b) B-mode image displayed with a 30-dB dynamic range. (c) Segmented regions. (d) Boundaries between the three cylinders and the background. (e) Reconstructed sound velocity distribution. (f) Sound velocity reconstruction error.

for smaller targets, and a larger relative error of detected area will result in a larger sound velocity estimation error. Further investigation is required to better understand the distribution of the estimation errors and its relation to the accuracy of boundary detection.

Large reconstruction errors occurred at the boundary, which is primarily due to refraction effects being much more significant there. Thus, either a significant portion of the time-of-flight data is discarded [as shown in Fig. 3(c)], or the remaining time-of-flight data have larger errors. Nonetheless, note that the "true" sound velocity at the boundary is not very meaningful because a sharp discontinuity in sound velocity is not expected in soft tissue.

B. Effect of Pitch on Sound Velocity Reconstruction

In the above simulations, only every third channel was used to obtain the time-of-flight data in order to save computation time. The effect of the number of channels on the accuracy of the reconstructed sound velocity was assessed, and the results are summarized in Table III. The spatial sampling interval of the sound velocity distribution in the x and y directions were both 0.5 mm in all cases. The results show that the reconstruction accuracy does not necessarily improve when more channels are used. In fact, good accuracy was achieved even when using only 12 channels with an effective pitch of 3 mm, which is much larger than the spatial sampling interval of the sound velocity distribution.

TABLE III
RELATION BETWEEN RECONSTRUCTION ACCURACY AND EFFECTIVE PITCH.

Effective pitch over 0.15 mm	Total number of channels	Δc in cylinder (m/s)	Δc in glandular material (m/s)
1	234	−2.6	0.0
2	117	−2.6	0.0
3	78	−2.6	0.0
4	59	−2.6	0.0
5	47	−2.7	0.0
6	39	−2.8	0.0
7	34	−2.2	0.0
8	30	−2.6	0.0
10	24	−3.7	0.0
12	20	−2.5	0.0
15	16	−3.7	0.1
20	12	−0.2	0.0

The n value in the first column means that only every nth channel in the array was used; the effective pitch was $n \times 0.15$ mm. Case I in Table II was evaluated. The spatial sampling intervals of sound velocity distribution in the x and y directions were both 0.5 mm.

The reason for the relative insensitivity of the accuracy to the pitch is that the time-of-flight constraints were only soft constraints and that there may be inconsistencies among them. Although more soft constraints may make the solution more reliable, the degree of inconsistency will not necessarily decrease as the number of soft constraints increases. Therefore, more time-of-flight data do not necessarily lead to a more accurate solution. However, these observations may be attributable to the objects under consideration having a simple geometry; hence, more studies are needed to better understand the performance of the algorithm with complex structures and the application of time-of-flight constraints.

In Section IV-A, a pitch of $p = 0.45$ mm (instead of 0.15 mm used in Section IV-B) was used in the simulations for testing Algorithm I in order to reduce the computation time for the 4× case. Despite the difference, the reconstruction results shown in Table III support the conclusion that Algorithm II outperforms Algorithm I.

C. Signal-to-Noise Ratio

To acquire the time-of-flight data, only one channel transmits at each firing. In this paper, in the simulations

no noise is added. In practice, however, the signal-to-noise ratio may be insufficient due to attenuation, thus affecting the accuracy of time-of-flight estimation. To address this problem, coded excitation techniques [34] can be used to increase the transmitted power while maintaining good temporal resolution. Note that a signal-to-noise ratio increase of more than 20 dB is achievable in this case because the code length is limited only by the depth of region of interest when only one channel is fired. Furthermore, because only the time of flight is of interest, the range sidelobe after pulse compression may not be as critical as in B-mode imaging.

D. Miscellaneous Issues

Accurate reconstruction of the sound velocity distribution would allow it to be used to correct for waveform distortion resulting from sound velocity inhomogeneities and, therefore, enhancement of the B-mode image quality. The results shown in this paper serve as a promising first step toward achieving this long-term research objective. However, it might not be possible to accurately reconstruct the sound velocity distribution without a good B-mode image. A possible approach to this circular problem is to iteratively solve the sound velocity distribution and use this to correct for the distortion in B-mode imaging. Note that, in addition to the sound velocity distribution being used to correct for the waveform distortion, it also can be used as an independent image to complement the B-mode image.

Although image segmentation was not a main subject of this study, it certainly is crucial to the accuracy of the reconstructed sound velocity. Both the proposed reconstruction technique and the segmentation method will be tested in the future using experimental data.

Although circular objects were used throughout this paper, there is no fundamental restriction on the shape of region of interest detectable by the proposed technique. The circular shape was chosen only for computation simplicity.

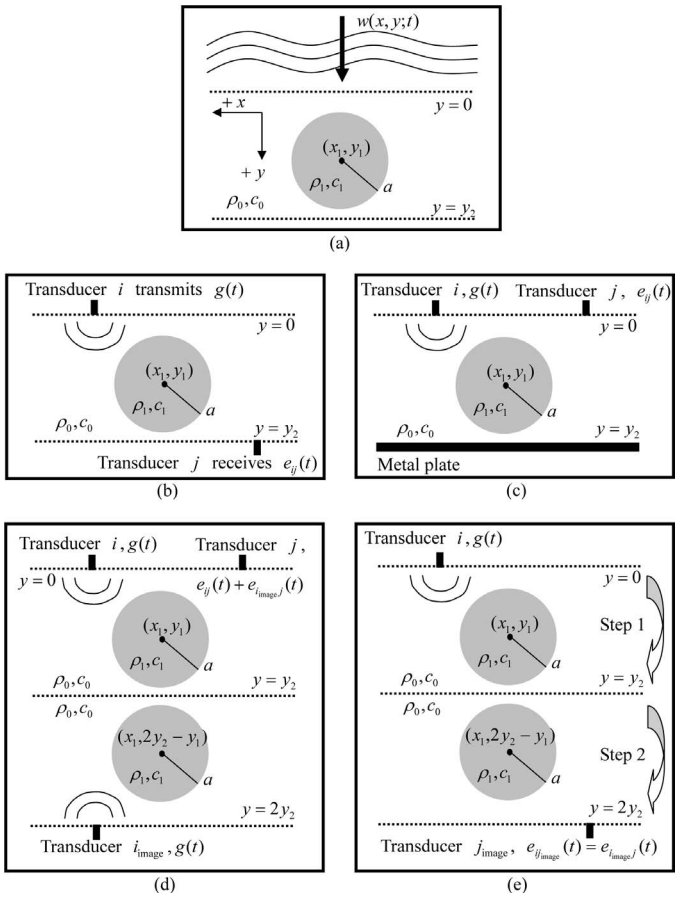

Fig. 10. Illustration of time-of-flight data generation (see text for details).

VI. Conclusions

Here we have proposed a method for incorporating the segmentation information of a B-mode image into the process of sound velocity reconstruction with limited-angle transmission tomography. A k-space method was used to simulate the B-mode images, and the series solution to the scattering of a plane wave incident on a fluid cylinder was used to generate the required time-of-flight data. Effects of wave propagation, such as refraction and diffraction, were included in the generated data. In the cases considered in this paper, the reconstructed sound velocities are accurate except at the boundaries. Simulation results based on a 5-MHz linear array show that the sound velocity error was generally 1–3 m/s, with a maximum of 5.8 m/s. The radius of the object under investigation was 2–6 mm, and all the objects were detected successfully. With this method, obtaining the sound velocity distribution is feasible with the current B-mode imaging setup using linear arrays. Moreover, it is expected that an accurate sound velocity distribution can be used to correct phase aberrations and wavefront amplitude distortion and, hence, improve the B-mode image quality. More studies are needed, particularly with objects having more complex geometries; and experiments will be conducted in order to further evaluate the proposed method.

Appendix A
Generation of Channel Data with the Series Solution in [20]

With reference to Fig. 10(a), consider the following problem: An acoustic wave $w(x, y; t)$ propagates along the $+y$ direction in a linear fluid medium that has background physical parameters $(\rho_0, c_0(f))$—where ρ is the density, c is the sound velocity, and f is the temporal frequency—and contains a cylinder with physical parameters $(\rho_1, c_1(f))$, radius a, and centered at (x_1, y_1). Assuming that attenuation can be ignored and that $w(x, 0; t)$ is known, find $w(x, y_2; t)$.

Because the medium is linear, the above problem is equivalent to the following: find $W(x, y_2; f)$ assuming that

$W(x,0;f)$ is known, where $W(x,0;f)$ and $W(x,y_2;f)$ are the temporal Fourier transforms of $w(x,0;t)$ and $w(x,y_2;t)$, respectively. It has been shown that, if $W(x,y;f)$ represents an incident plane wave, then there exists an exact series solution for $W(x,y_2;f)$ [20].

Let the angular spectrum of $W(x,0;f)$ be $A(k_x;0,f)$ [35], i.e.:

$$W(x,0;f)=\frac{1}{2\pi}\int A(k_x;0,f)\exp(jk_xx)dk_x. \tag{A1}$$

Except for those complex-exponential functions $\exp(jk_xx)$ with $|k_x|>2\pi f/c_0(f)$, which represent evanescent waves, each $\exp(jk_xx)$ represents a plane wave propagating with the wave vector $\left(k_x,\sqrt{(2\pi f/c_0(f))^2-k_x^2}\right)$. Thus:

$$W(x,y_2;f)\cong\frac{1}{2\pi}\int_{-2\pi f/c_0(f)}^{2\pi f/c_0(f)}A'\left(k_x;x,y_2,f\right)dk_x, \tag{A2}$$

where $A'(k_x;x,y_2,f)$ is the series solution corresponding to the term $A(k_x;0,f)\exp(jk_xx)$.

For the configuration in Fig. 10(b), the method for calculating the signal, $e_{ij}(t)$, received by transducer j in the lower array when transducer i in the upper array transmits a short pulse $g(t)$ can be obtained based on the above discussion. To treat the case shown in Fig. 10(c), let the metal plate have physical parameters $(\rho_{\rm m},c_{\rm m}(f))$ and assume that $\rho_{\rm m}\gg\rho_0$ and $c_{\rm m}(f)\gg c_0(f)$ so that the method of images can be adopted. If the plate is sufficiently thick such that the echoes from its upper and lower surfaces are well separated, the plate then can be treated as infinitely thick and $e_{ij}(t)$ in Fig. 10(c) is equal to $e_{ij}(t)+e_{i_{\rm image}j}(t)$ in Fig. 10(d). Furthermore, $e_{ij}(t)$ in Fig. 10(d) is negligible around $t=t_{ij}$ in Fig. 10(c) [t_{ij} is the time of flight and is the time needed for $g(t)$ to travel from transducer i to the metal plate, then to transducer j in Fig. 10(c)]. That is, when only t_{ij} is of interest, there is no need to calculate $e_{ij}(t)$ as $e_{ij}(t)$ can at most contain scattered waves relevant to transducer i around t_{ij}, thus neglecting transducer i does not alter the estimate of t_{ij}. Therefore, to obtain t_{ij} one only needs to consider the configuration in Fig. 10(e). Note that $e_{ij_{\rm image}}(t)=e_{i_{\rm image}j}(t)$. Obtaining $e_{ij_{\rm image}}(t)$ around t_{ij} is a two-step process: the wave first propagates from plane $y=0$ to plane $y=y_2$, then propagates from plane $y=y_2$ to plane $y=2y_2$. This method still can be applied when the object contains more cylinders with a circular cross section.

Appendix B
A Brief Introduction to the Convex Programming Formulation [25], [26], [36]

A complete inner product space is called a Hilbert space. On the finite-dimensional Euclidean space $\mathbf{R}^{MN}$, if for all $\mathbf{x}=(x_1,x_2,\cdots,x_{MN})^{\rm T}$ in $\mathbf{R}^{MN}$ and all $\mathbf{y}=(y_1,y_2,\cdots,y_{MN})^{\rm T}$ in $\mathbf{R}^{MN}$, their inner product is defined as the Euclidean inner product:

$$\langle\mathbf{x},\mathbf{y}\rangle=\sum_{l=1}^{MN}x_ly_l=\mathbf{y}^{\rm T}\mathbf{x}, \tag{B1}$$

and $\mathbf{R}^{MN}$ is a Hilbert space [36]. Each slowness distribution $\Delta\mathbf{s}$ is an element in $\mathbf{R}^{MN}$.

Let C be a closed convex set in a Hilbert space $\mathbf{H}$. Then for each u in $\mathbf{H}$, there exists a unique u^* in C that is closest to u. That is:

$$\|u-u^*\|=\min_{v\in C}\|u-v\|, \tag{B2}$$

where $\|\cdot\|$ is the norm induced by the inner product. This unique nearest neighbor u^* in C of u is called the projection of u onto C, and the operator assigning $u^*=P_cu$ to each u is called the projector onto C and is denoted by P_C. For example, if the closed convex set C represents a set of distributions satisfying a given condition and u is any initial guess, then a distribution in C that is closest to distribution u can be found. Assume that, for a real problem, one tries to find a solution u in $\mathbf{H}$ satisfying a given constraint, and the associated constraint set:

$$C=\{u\in\mathbf{H}\mid u\text{ satisfies the given constraint}\} \tag{B3}$$

is nonempty, closed, and convex, then a solution $u\in C$ is $u^*=P_Cu_0$, where u_0 is any given initial condition. If there are k constraints in a problem and each:

$$C_i=\{u\in\mathbf{H}\mid u\text{ satisfies the }i\text{th constraint}\},\quad i=1,2,\cdots,k, \tag{B4}$$

is closed and convex, then all the solutions form a set $C_0=\bigcap_{i=1}^kC_i$ which is also closed and convex. Thus, $P_{C_0}u_0$ is a solution provided that C_0 is nonempty.

In the presence of inconsistent constraints, which may arise from inaccurate measurements such as estimation errors in the pulse arrival time, C_0 is empty and there is no solution. One way to solve this problem is to divide all of the constraints into two classes: one class contains the hard constraints the solution must satisfy, and the other class contains the soft constraints for which the total amount of violation must be minimized. Let $I^{\rm c}=I^{\rm h}\bigcup I^{\rm s}$ be the finite constraint index set, where $I^{\rm h}$ denotes the possibly empty hard-constraint index set, $I^{\rm s}$ denotes the nonempty soft-constraint index set, and $I^{\rm h}\bigcap I^{\rm s}$ is empty. Define:

$$\Phi^{\rm s}(u)=\frac{1}{2}\sum_{i\in I^{\rm s}}w_id^2(u,C_i), \tag{B5}$$

where $w_i\in(0,1]$ for all $i\in I^{\rm s}$, $\sum_{i\in I^{\rm s}}w_i=1$, and $d(u,C_i)=\inf\{\|u-v\|\mid v\in C_i\}$ is the distance between u and C_i, where inf stands for the greatest lower bound. Suppose that $\mathbf{H}$ is finite dimensional, C_i is bounded for some $i\in I$, $C^{\rm h}=\mathbf{H}\bigcap\left(\bigcap_{i\in I^{\rm h}}C_i\right)$ is nonempty, and

take $u_0 \in C^{\mathrm{h}}$, $\lambda_n \in [0,1]$ for all $n \geq 0$ such that $\sum_{n\geq 0} \lambda_n(1-\lambda_n) = \infty$, and $\gamma \in (0,2]$. Let:

$$u_{n+1} = (1-\lambda_n)u_n + \lambda_n P_{C^{\mathrm{h}}}\left[(1-\gamma)u_n + \gamma \sum_{i\in I^{\mathrm{s}}} w_i P_{C_i}(u_n)\right], \quad n \geq 1. \quad \text{(B6)}$$

The sequence $\{u_n\}$ then converges to a point u with $\Phi^{\mathrm{s}}(u) = \min_{v\in C^{\mathrm{h}}} \Phi^{\mathrm{s}}(v)$. That is, (B6) can be used to find a solution that satisfies all the hard constraints and minimizes the objective function Φ^{s}, which is the total amount of violation of the soft constraints. Note that such a problem is in a convex programming formulation because Φ^{s} is a convex function on a convex set C^{h}.

Acknowledgments

The authors thank the reviewers for insightful comments.

References

[1] Q. Zhu and B. D. Steinberg, "Wavefront amplitude distortion and image sidelobe levels: Part I—Theory and computer simulations," *IEEE Trans. Ultrason., Ferroelect., Freq. Contr.*, vol. 40, no. 6, pp. 747–753, 1993.

[2] Q. Zhu, B. D. Steinberg, and R. L. Arenson, "Wavefront amplitude distortion and image sidelobe levels: Part II—*In vivo* experiments," *IEEE Trans. Ultrason., Ferroelect., Freq. Contr.*, vol. 40, no. 6, pp. 754–762, 1993.

[3] Q. Zhu and B. D. Steinberg, "Wavefront amplitude distribution in the female breast," *J. Acoust. Soc. Amer.*, vol. 96, no. 1, pp. 1–9, 1994.

[4] L. M. Hinkelman, D.-L. Liu, R. C. Waag, Q. Zhu, and B. D. Steinberg, "Measurements and correction of ultrasonic pulse distortion produced by the human breast," *J. Acoust. Soc. Amer.*, vol. 97, no. 3, pp. 1958–1969, 1995.

[5] R. C. Gauss, M. S. Soo, and G. E. Trahey, "Wavefront distortion measurements in the human breast," in *Proc. IEEE Ultrason. Symp.*, 1997, pp. 1547–1551.

[6] M. E. Lanfranchi, *Breast Ultrasound*. 2nd ed. New York: Marban Books, 2000.

[7] W.-C. Yeh, P.-C. Li, Y.-M. Jeng, H.-C. Hsu, P.-L. Kuo, M.-L. Li, P.-M. Yang, and P.-H. Lee, "Elastic modulus measurements of human liver and correlation with pathology," *Ultrasound Med. Biol.*, vol. 28, no. 4, pp. 467–474, 2002.

[8] B. S. Garra, E. I. Céspedes, J. Ophir, S. R. Spratt, R. A. Zuurbier, C. M. Magnant, and M. F. Pennanen, "Elastography of breast lesions: Initial clinical results," *Radiology*, vol. 202, no. 1, pp. 79–86, 1997.

[9] S. A. Goss, R. L. Johnston, and F. Dunn, "Comprehensive compilation of empirical ultrasonic properties of mammalian tissues," *J. Acoust. Soc. Amer.*, vol. 64, no. 2, pp. 423–457, 1978.

[10] S. W. Flax and M. O'Donnell, "Phase-aberration correction using signals from point reflectors and diffuse scatterers: Basic principles," *IEEE Trans. Ultrason., Ferroelect., Freq. Contr.*, vol. 35, no. 6, pp. 758–767, 1988.

[11] M. O'Donnell and S. W. Flax, "Phase-aberration correction using signals from point reflectors and diffuse scatterers: Measurements," *IEEE Trans. Ultrason., Ferroelect., Freq. Contr.*, vol. 35, no. 6, pp. 768–774, 1988.

[12] D.-L. Liu and R. C. Waag, "Correction of ultrasonic wavefront distortion using backpropagation and a reference waveform method for time-shift compensation," *J. Acoust. Soc. Amer.*, vol. 96, no. 2, pp. 649–660, 1994.

[13] G. C. Ng, S. S. Worrell, P. D. Freiburger, and G. E. Trahey, "A comparative evaluation of several algorithms for phase aberration correction," *IEEE Trans. Ultrason., Ferroelect., Freq. Contr.*, vol. 41, no. 5, pp. 631–643, 1994.

[14] G. C. Ng, P. D. Freiburger, W. F. Walker, and G. E. Trahey, "A speckle target adaptive imaging technique in the presence of distributed aberrations," *IEEE Trans. Ultrason., Ferroelect., Freq. Contr.*, vol. 44, no. 1, pp. 140–151, 1997.

[15] R. C. Gauss, G. E. Trahey, and M. S. Soo, "Adaptive imaging in the breast," in *Proc. IEEE Ultrason. Symp.*, 1999, pp. 1563–1569.

[16] A. C. Kak and M. Slaney, *Principles of Computerized Tomographic Imaging*. New York: Institute of Electrical and Electronics Engineers, 1988.

[17] M. Krueger, A. Pesavento, and H. Ermert, "A modified time-of-flight tomography concept for ultrasonic breast imaging," in *Proc. IEEE Ultrason. Symp.*, 1996, pp. 1381–1385.

[18] M. Krueger, V. Burow, K. M. Hiltawsky, and H. Ermert, "Limited angle ultrasonic transmission tomography of the compressed female breast," in *Proc. IEEE Ultrason. Symp.*, 1998, pp. 1345–1348.

[19] M. Tabei, T. D. Mast, and R. C. Waag, "A k-space method for coupled first-order acoustic propagation equations," *J. Acoust. Soc. Amer.*, vol. 111, no. 1, pp. 53–63, 2002.

[20] P. M. Morse and K. U. Ingard, *Theoretical Acoustics*. New York: McGraw-Hill, 1968.

[21] N. G. Chen, P. Y. Guo, S. K. Yan, D. Q. Piao, and Q. Zhu, "Simultaneous near-infrared diffusive light and ultrasound imaging," *Appl. Opt.*, vol. 40, no. 34, pp. 6367–6680, 2001.

[22] M. Huang, T. Xie, N. G. Chen, and Q. Zhu, "Simultaneous reconstruction of absorption and scattering maps with ultrasound localization: Feasibility study using transmission geometry," *Appl. Opt.*, vol. 42, no. 19, pp. 4102–4114, 2003.

[23] J. D. Bronzino, *The Biomedical Engineering HandBook*. 2nd ed. vol. 1, Boca Raton, FL: CRC Press, 2000.

[24] M. Frigo and S. G. Johnson, "FFTW: An adaptive software architecture for the FFT," in *Proc. ICASSP*, 1998, pp. 1381–1384.

[25] P. L. Combettes and P. Bondon, "Hard-constrained inconsistent signal feasibility problems," *IEEE Trans. Signal Processing*, vol. 47, no. 9, pp. 2460–2468, 1999.

[26] H. L. Royden, *Real Analysis*. 3rd ed. Englewood Cliffs, NJ: Prentice-Hall, 1988.

[27] P. Oskoui and H. Stark, "A comparative study of three reconstruction methods for a limited-view computer tomography problem," *IEEE Trans. Med. Imag.*, vol. 8, no. 1, pp. 43–49, 1989.

[28] K. C. Tam, J. W. Eberhard, and K. W. Mitchell, "Incomplete-data CT image reconstructions in industrial applications," *IEEE Trans. Nucl. Sci.*, vol. 37, no. 3, pp. 1490–1499, 1990.

[29] H. Stark, *Image Recovery: Theory and Application*. London: Academic, 1987.

[30] E. L. Madsen, J. A. Zagzebski, G. R. Frank, J. F. Greenleaf, and P. L. Carson, "Anthropomorphic breast phantoms for assessing ultrasonic imaging system performance and for training ultrasonographers: Part I," *J. Clin. Ultrasound*, vol. 10, no. 2, pp. 67–75, 1982.

[31] A. I. Nachman, J. F. Smith, and R. C. Waag, "An equation for acoustic propagation in inhomogeneous media with relaxation losses," *J. Acoust. Soc. Amer.*, vol. 88, no. 3, pp. 1584–1595, 1990.

[32] M. O'Donnell and S. D. Silverstein, "Optimal displacement for compound image generation in medical ultrasound," *IEEE Trans. Ultrason., Ferroelect., Freq. Contr.*, vol. 35, no. 4, pp. 470–476, 1988.

[33] R. C. Gonzalez and R. E. Woods, *Digital Image Processing*. 2nd ed. Reading, MA: Addison-Wesley, 2002.

[34] M. O'Donnell, "Coded excitation system for improving the penetration of real-time phased-array imaging systems," *IEEE Trans. Ultrason., Ferroelect., Freq. Contr.*, vol. 39, no. 3, pp. 341–351, 1992.

[35] J. W. Goodman, *Introduction to Fourier Optics*. 2nd ed. New York: McGraw-Hill, 1996.

[36] H. Stark and Y. Yang, *Vector Space Projections: A Numerical Approach to Signal and Image Processing, Neural Nets, and Optics*. New York: Wiley, 1998.

Sheng-Wen Huang was born in 1971 in Changhua, Taiwan, R.O.C. He received the B.S. degree in electrical engineering from National Taiwan University, Taipei, Taiwan, R.O.C. in 1993. He is currently a research assistant with the Division of Medical Engineering Research at National Health Research Institutes and a Ph.D. student at the Department of Electrical Engineering, National Taiwan University. His current research interests include ultrasonic tomography and behaviors of ultrasound contrast agents.

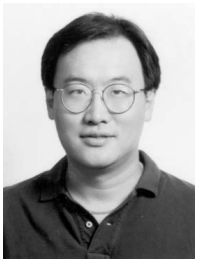

Pai-Chi Li (S'93–M'95–SM'01) received the B.S. degree in electrical engineering from National Taiwan University, Taipei, Taiwan, R.O.C., in 1987, and the M.S. and Ph.D. degrees from the University of Michigan, Ann Arbor, in 1990 and 1994, respectively, both in electrical engineering: systems.

He was a research assistant with the Department of Electrical Engineering and Computer Science at the University of Michigan from 1990 to 1994. He joined Acuson Corporation, Mountain View, CA, as a member of the technical staff in June 1994. His work in Acuson was primarily in the areas of medical ultrasonic imaging system design for both cardiology and general imaging applications. In August 1997, he went back to the Department of Electrical Engineering at National Taiwan University where he is currently a full professor. His current research interests include biomedical ultrasonic imaging and signal processing.

Dr. Li is a senior member of IEEE and Associate Editor of *IEEE Transactions on Ultrasonics, Ferroelectrics, and Frequency Control*. He received the 2003 Distinguished Research Achievement Award from National Taiwan University, the 2002 Dr. Wu Dayou Research Award from the National Science Council, the 2002 Outstanding Young Electrical Engineer Award from the Chinese Institute of Electrical Engineering and the Distinguished Industrial Collaboration Award of Ministry of Education. He also was the recipient of the Distinguished Achievement Award in Electrical Engineering: Systems in 1994 for his outstanding academic achievement at the University of Michigan.

Experimental Investigation of Computed Tomography Sound Velocity Reconstruction Using Incomplete Data

Sheng-Wen Huang and Pai-Chi Li, *Senior Member, IEEE*

***Abstract*—An approach for reconstructing the sound velocity distribution in the breast was previously proposed and verified by simulations, and the present study investigated the approach experimentally. The experimental setup comprised a 5-MHz, 128-channel linear array, a programmable digital array system, a phantom containing objects with differing physical properties, and a computer. The array system was used to collect channel data for simultaneous B-mode image formation and limited-angle tomographic sound velocity reconstruction. The phantom was constructed from materials mimicking the following tissues in the breast: glandular tissue, fat, cysts, high-attenuation tumors, and irregular tumors. The sound velocities in these materials matched those in the corresponding real tissues. The imaging setup is similar to that of x-ray mammography, in which a linear array is placed at the top of the breast and a metal plate is placed at the bottom for reflecting sound waves. Thus, both B-mode images and the sound velocity distribution can be acquired using the same setup. An algorithm based on a convex programming formulation was used to reconstruct the sound velocity images. By scanning the phantom at different positions, nine cases were evaluated. In each of the nine cases, the image object comprised a background (glandular tissue) and one or three regions of interest (fat, tumor, or cyst). The sound velocity was accurately estimated in the nine cases evaluated, with sound velocity errors being less than 5 m/s in 8 of 11 regions of interest. Thus, obtaining the sound velocity distribution is feasible with a B-mode imaging setup using linear arrays. Knowledge of the sound velocity distribution in the breast can be used to complement B-mode imaging and to enhance the detection of breast cancer.**

I. Introduction

The detection of breast cancer using B-mode ultrasound is of clinical importance [1]–[4]. Although x-ray mammography is also a popular modality for breast cancer detection, ultrasound is more effective in cases such as the differential diagnosis of pathologies in the radiologically dense breast [1]. Furthermore, B-mode ultrasound is an effective adjunct to mammography in reducing the number of negative biopsy results [4]. However, in B-mode imaging, the wavefronts can be severely distorted by sound velocity inhomogeneities [5]–[7], which degrade contrast resolution and, therefore, reduce cancer detectability. Furthermore, even if a region of interest (ROI) is detectable in B-mode imaging, a tumor still may be indistinguishable from a fat region due to similar image contrast [1]. Thus, additional information is needed to enhance breast cancer detection by ultrasound.

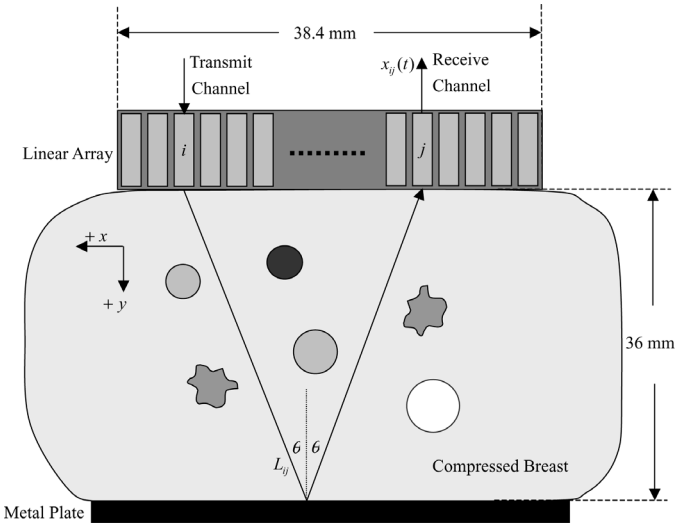

Fig. 1. Tomographic imaging setup allowing the acquisition of both B-mode images and sound velocity distributions. Each of the (N_A) channels in the array can transmit independently. A metal plate at the bottom of the compressed breast reflects the acoustic signal.

The sound velocity distribution in the breast can offer additional diagnostic information because the velocity of sound is higher in cancerous tissue than in fat [8]. By combining the sound velocity distribution information with the corresponding B-mode image, tumors can be detected more accurately and effectively. Although ultrasonic computed tomography can be used to measure the sound velocity distribution [9], tomography equipment is very different from that used for B-mode imaging. Hence, we [10] adopted the tomographic imaging setup shown in Fig. 1 that allowed the acquisition of both B-mode images and sound velocity distributions using a single setup. This setup is similar to both that of x-ray mammography and the limited-angle transmission tomography setup proposed by Krueger *et al.* [11], [12]. Fig. 1 shows that a linear array is placed at the top of the image object, and a metal plate at the bottom reflects the acoustic wave. In addition to performing B-mode imaging, the imaging setup also is capable of transmitting a wideband pulse from a

Manuscript received March 26, 2004; accepted June 8, 2004. Partial financial support from NSC (grant no. NSC 93-2213-E-002-119) is appreciated.

The authors are with the Department of Electrical Engineering, National Taiwan University, and also with the Division of Medical Engineering Research, National Health Research Institutes, Taipei, Taiwan (e-mail: paichi@cc.ee.ntu.edu.tw).

single channel in order to acquire a complete channel data set and a corresponding time-of-flight data set, which contains information on the sound velocity distribution of the image object.

A complete time-of-flight data set spanning an angular range of 180° is necessary for accurate sound velocity reconstruction in conventional ultrasonic transmission tomography [13]–[15]. The setup in Fig. 1 yields an incomplete time-of-flight data set. Hence, as shown in [10], the sound velocity distribution cannot be accurately reconstructed using the time-of-flight data alone. A reconstruction algorithm based on a convex programming formulation was proposed in [10]. It also was demonstrated that a significant improvement in estimation accuracy can be achieved if the ROIs in the B-mode image of the same object can be identified and segmented such that proper constraints can be defined and imposed during reconstruction. Extensive simulations were performed in [10] to test the efficacy of the proposed technique. The effects of wave propagation such as refraction and diffraction were included in the simulated data. In the cases considered in that paper, the reconstructed sound velocities are accurate except at the boundaries. Simulation results based on a 5-MHz linear array showed that the sound velocity error was generally 1–3 m/s, with a maximum of 5.8 m/s. The objects under investigation had radii of 2–6 mm, and all of them were detected successfully. Therefore, it was concluded in [10] that obtaining the sound velocity distribution is feasible with the current B-mode imaging setup using linear arrays.

In this paper, a custom-made phantom containing a variety of image objects with differing physical properties was used to experimentally investigate the performance of the approach proposed and evaluated by simulations in [10].

This paper is organized as follows. Section II reviews the method for reconstructing the sound velocity distribution. Section III introduces the experimental setup and presents the experimental results. A discussion is provided in Section IV, and the paper concludes in Section V.

II. Reconstruction Algorithm

In this section, the method for reconstructing the sound velocity distribution is briefly reviewed. Details can be found in [10].

A. Imaging Setup

Consider the imaging setup shown in Fig. 1. Assume that the linear array has N_{A} channels. The imaging setup is capable of acquiring a complete channel data set $\{e_{ij}(t)\}$, $1 \le i, j \le N_{\mathrm{A}}$, where $e_{ij}(t)$ is the echo signal received by channel j when only channel i transmits. With $e_{ij}(t)$, the time-of-flight t_{ij} corresponding to the same transmit/receive combination for the echo reflected from the bottom metal plate can be obtained.

The effects of refraction associated with sound velocity inhomogeneities on the time of flight can be ignored if only soft tissues are considered [9], which is an acceptable approximation for breast tissue. Let $c(x, y)$ denote the sound velocity at the center frequency of the transmitted pulse, $s(x, y) = c^{-1}(x, y)$ be the slowness, and $s_0 = c_0^{-1}$ be the average slowness in the image object. Then the time of flight after geometrical delay compensation is:

$$\begin{aligned}\Delta t_{ij} = t_{ij} - t_{ij,0} &= \int_{L_{ij}} s(x,y)dl - \int_{L_{ij}} s_0 dl \\ &= \int_{L_{ij}} \left[s(x,y) - s_0\right] dl = \int_{L_{ij}} \Delta s(x,y) dl, \quad (1)\end{aligned}$$

where L_{ij} is the path of the line integral as shown in Fig. 1. Discretizing $\Delta s(x, y)$ with spatial sampling intervals Δx_{s} and Δy_{s} in the x and y directions, respectively, changes (1) to:

$$\Delta t_{ij} = \sum_{n=1}^{N} \sum_{m=1}^{M} \Delta s(m,n) l_{ij}(m,n) = \mathbf{l}_{ij}^{\mathrm{T}} \Delta \mathbf{s}, \quad (2)$$

where $\mathbf{l}_{ij}$ and $\Delta\mathbf{s}$ are $MN \times 1$ column vectors, $(\mathbf{l}_{ij})_{(m-1)N+n} \equiv l_{ij}(m, n)$ is the contribution of grid point (m, n), $1 \le m \le M$, $1 \le n \le N$, and $(\Delta\mathbf{s})_{(m-1)N+n} \equiv \Delta s(m, n)$.

Due to the assumption of straight-line propagation, $\mathbf{l}_{ij} = \mathbf{l}_{ji}$, and Δt_{ij} can be set to $(\Delta t_{ij} + \Delta t_{ji})/2$ for $1 \le i \le N_{\mathrm{A}}$, $1 \le j \le i$. Thus, the number of equations in (2) is $N_{\mathrm{A}}(N_{\mathrm{A}} + 1)/2$, and they can be expressed in the following matrix form:

$$\mathbf{L}\Delta\mathbf{s} = \Delta\mathbf{t}, \quad (3)$$

where $\Delta\mathbf{t}$ is an $[N_{\mathrm{A}}(N_{\mathrm{A}} + 1)/2] \times 1$ column vector and $\mathbf{L}$ is an $[N_{\mathrm{A}}(N_{\mathrm{A}} + 1)/2] \times MN$ matrix. In (3), $\Delta\mathbf{t}$ is obtained from the channel data, and $\mathbf{L}$ is calculated from geometry.

B. Algorithm for Reconstructing the Sound Velocity Distribution

In [10], a convex programming formulation for inconsistent problems [16] was used to solve (3) due to its ability to incorporate the B-mode image information. In this paper, $C = \{\mathbf{x} \in \mathbf{X} : \text{property } P(\mathbf{x})\}$ means that C is a subset of $\mathbf{X}$ containing all $\mathbf{x}$ in $\mathbf{X}$ which have the property P [17]. For any $\mathbf{x} = (x_1, x_2, \ldots, x_{MN})^{\mathrm{T}}$ and $\mathbf{y} = (y_1, y_2, \ldots, y_{MN})^{\mathrm{T}}$ in $\mathbf{R}^{MN}$, their inner product is defined as the Euclidean inner product:

$$\langle \mathbf{x}, \mathbf{y} \rangle = \sum_{l=1}^{MN} x_l y_l = \mathbf{y}^{\mathrm{T}}\mathbf{x}. \quad (4)$$

Let $\mathbf{L}$ in (3) be expressed as $\mathbf{L} = \begin{bmatrix}\mathbf{l}_1 & \mathbf{l}_2 & \cdots \mathbf{l}_{N_{\mathrm{A}}(N_{\mathrm{A}}+1)/2}\end{bmatrix}^{\mathrm{T}}$ and $\Delta\mathbf{t}$ as $\Delta\mathbf{t} = \begin{bmatrix}\Delta t_1 & \Delta t_2 & \cdots & \Delta t_{N_{\mathrm{A}}(N_{\mathrm{A}}+1)/2}\end{bmatrix}^{\mathrm{T}}$, and define:

$$\begin{aligned}&C_{\Delta t_i} = \left\{\mathbf{x} \in \mathbf{R}^{MN} : \langle \mathbf{x}, \mathbf{l}_i \rangle = \Delta t_i\right\}, \\ &i = 1, 2, \cdots, N_{\mathrm{A}}(N_{\mathrm{A}} + 1)/2,\end{aligned} \quad (5)$$

then a slowness distribution minimizing the following cost function (i.e., the total amount of violation of the time-of-flight data) is used:

$$\Phi^{\mathrm{s}}(\mathbf{x}) = \frac{1}{2} \sum_{i=1}^{N_{\mathrm{A}}(N_{\mathrm{A}}+1)/2} w_i d^2\left(\mathbf{x}, C_{\Delta t_i}\right), \tag{6}$$

where $w_i \in (0,1]$ for all $i \in \{1,2,\cdots,N_{\mathrm{A}}\left(N_{\mathrm{A}}+1\right)/2\}$, $\sum_{i=1}^{N_{\mathrm{A}}(N_{\mathrm{A}}+1)/2} w_i = 1$, and $d\left(\mathbf{x}, C_{\Delta t_i}\right) = \inf\left\{\sqrt{\langle \mathbf{x}-\mathbf{y}, \mathbf{x}-\mathbf{y}\rangle} : \mathbf{y} \in C_{\Delta t_i}\right\}$ is the distance between $\mathbf{x}$ and $C_{\Delta t_i}$, where inf stands for the greatest lower bound.

To achieve good reconstruction accuracy, in addition to determining $\Delta\mathbf{s}$ so as to minimize the cost function, two kinds of a priori knowledge of $\Delta\mathbf{s}$ are used. First, the sound velocity is assumed to be in $[c_{\mathrm{lower}}, c_{\mathrm{upper}}]$ (where $c_{\mathrm{lower}} = 1450$ m/s and $c_{\mathrm{upper}} = 1580$ m/s throughout the paper); therefore, $\Delta\mathbf{s}$ must belong to:

$$C_{\mathrm{velocity}} = \left\{\mathbf{x} \in \mathbf{R}^{MN} : x_l \in \left[c_{\mathrm{upper}}^{-1} - s_0, c_{\mathrm{lower}}^{-1} - s_0\right], \; 1 \le l \le MN\right\}. \tag{7}$$

Second, the B-mode image information is used. Consider a B-mode image in which an object contains an ROI surrounded by the background, and this ROI can be identified and segmented. $\Delta\mathbf{s}$ must belong to the following set:

$$C_{\mathrm{image}} = \left\{ \begin{array}{l} \left\{ \begin{array}{c} \mathbf{x} \in \mathbf{R}^{MN} : \\ x_{b_1} = x_{b_2} = \cdots = x_{b_{N_b}}, \\ x_{r_1} = x_{r_2} = \cdots = x_{r_{N_r}}, \\ x_{br_i} \in \left[x_{b_1}, x_{r_1}\right], \\ 1 \le i \le N_{\mathrm{br}} \end{array} \right\} \quad \text{if } x_{b_1} \le x_{r_1} \\ \left\{ \begin{array}{c} \mathbf{x} \in \mathbf{R}^{MN} : \\ x_{b_1} = x_{b_2} = \cdots = x_{b_{N_b}}, \\ x_{r_1} = x_{r_2} = \cdots = x_{r_{N_r}}, \\ x_{br_i} \in \left[x_{r_1}, x_{b_1}\right], \\ 1 \le i \le N_{\mathrm{br}} \end{array} \right\} \quad \text{otherwise} \end{array} \right., \tag{8}$$

where $I_{\mathrm{b}} \equiv \{b_1, b_2, \ldots, b_{N_b}\}$ is the background index set, $I_{\mathrm{r}} \equiv \{r_1, r_2, \ldots, r_{N_r}\}$ is the ROI index set, and $I_{\mathrm{br}} \equiv \{br_1, br_2, \ldots, br_{N_{\mathrm{br}}}\}$ is the boundary index set. Eq. (8) means that all the slowness values in the background must be the same, and all the slowness values in the ROI also must be the same. In addition, each slowness value at the boundary must be between that of the background and that of the ROI. The C_{image} can be defined similarly when the object contains more ROIs.

According to [16], a slowness distribution $\mathbf{x} \in C_{\mathrm{velocity}} \cap C_{\mathrm{image}}$ minimizing $\Phi^{\mathrm{s}}(\mathbf{x})$ can be found by taking $\mathbf{x}$ as the limit of the sequence $\{\mathbf{x}_n\}$ (i.e., $\lim_{n\to\infty} \mathbf{x}_n$). $\mathbf{x}_0 \in C_{\mathrm{velocity}} \cap C_{\mathrm{image}}$ is an initial slowness distribution and $\mathbf{x}_{n+1}$ is given in (9) (see next page), where $\lambda_n \in [0,1]$ for all $n \ge 0$, $\sum_{n\ge 0} \lambda_n(1-\lambda_n) = \infty$, $\gamma \in (0,2]$, and $P_{C_{(\cdot)}}$ is the projector onto $C_{(\cdot)}$ [i.e., $P_{C_{(\cdot)}}(\mathbf{x}) = \arg\min_{\mathbf{y}\in C_{(\cdot)}} \langle \mathbf{x}-\mathbf{y}, \mathbf{x}-\mathbf{y}\rangle$, which means $\left\langle \mathbf{x} - P_{C_{(\cdot)}}(\mathbf{x}), \mathbf{x} - P_{C_{(\cdot)}}(\mathbf{x})\right\rangle = \min_{\mathbf{y}\in C_{(\cdot)}} \langle \mathbf{x}-\mathbf{y}, \mathbf{x}-\mathbf{y}\rangle$]. Each case in this paper used uniform weighting (i.e., each time of flight is equally important), $\lambda_n = 0.5$ for all $n \ge 0$ (satisfying $\sum_{n\ge 0} \lambda_n(1-\lambda_n) = \infty$), and $\gamma = 1$.

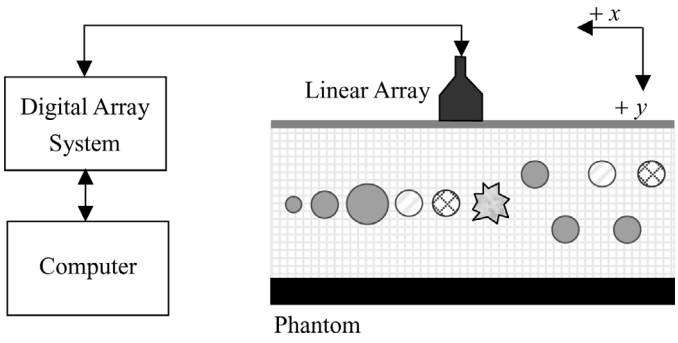

Fig. 2. Schematic of the data-acquisition setup.

III. Experimental Results

A. Experimental Setup and Methods

A schematic of the experimental setup is shown in Fig. 2. The linear array (L6/128, STI, State College, PA) has $N_{\mathrm{A}} = 128$ channels, an element pitch p of 0.3 mm, an elevation width of 5 mm, and an elevation focus of 25 mm. The array channels have a center frequency of 5.57 MHz and a −6 dB bandwidth of 4.10 MHz. A programmable digital array system (DiPhAS, Fraunhofer IBMT, Ingbert, Germany) [18] capable of transmitting a short pulse from any selected channel is used to acquire the channel data. All channel data were transferred from the array system to the computer for storage and further processing via a digital input/output (I/O) card (PCI-7300A, ADLINK, Taipei, Taiwan) on the computer. When channel i transmits, all channels, except for channel j with $|j-i| = 64$, can receive (channel i and channel j with $|j-i| = 64$ share the same multiplexer and thus cannot be turned on simultaneously). That is, a channel data set $\{e_{ij}(t)\}$, $1 \le i, j \le N_{\mathrm{A}}$, $|j-i| \ne 64$, can be collected by the array system. The transmitted pulse is a one-cycle square wave with a duration of 0.2 μs, and all $e_{ij}(t)$ were sampled at 40 MHz with a vertical resolution of 12 bits. For each transmit/receive combination, data corresponding to 16 consecutive firings were averaged off-line to enhance the signal-to-noise ratio. The cross sections of the custom-made phantom[1] are shown in Figs. 3(a) and (b) (top and side views, respectively). The corresponding parameters of the different materials (mimicking different tissues in the breast), which were supplied by Dr. Madsen, are listed in Table I. The nine cases listed in Table II were generated by moving the array along the x-axis.

[1]By Dr. Ernest Madsen, Department of Medical Physics, University of Wisconsin-Madison, WI.

$$\mathbf{x}_{n+1} = (1-\lambda_n)\,\mathbf{x}_n + \lambda_n P_{C_{\text{velocity}} \cap C_{\text{image}}} \left[(1-\gamma)\mathbf{x}_n + \gamma \sum_{i=1}^{N_{\text{A}}(N_{\text{A}}+1)/2} w_i P_{C_{\Delta t_i}}(\mathbf{x}_n) \right],\ n \geq 0, \tag{9}$$

TABLE I
PARAMETERS OF THE MATERIALS USED IN THE PHANTOM.[1]

Material	Sound velocity c at 5 MHz and 22°C (m/s)	Density ρ (g/cm^3)	Attenuation coefficient α at 5 MHz (dB/cm)	B-mode contrast relative to glandular tissue (dB)
Glandular tissue	1522	1.03	2.74	—
Fat	1464	0.94	2.21	−14
Cyst	1570	1.02	0.78	< −14
High-attenuation tumor	1547	1.10	7.36	−12
Irregular tumor	1553	1.07	4.26	−10

[1]Note that the materials are mimicked.

TABLE II
OBJECTS INCLUDED IN DIFFERENT CASES AND THE ESTIMATION RESULTS.[1]

Case	ROI	Sphere radius (mm)	ROI position	Δc_{ROI} (m/s)	Δc_{G} (m/s)
I	Fat	2	Center	2.6	0.3
II	Fat	4	Center	4.5	0.3
III	Fat	6	Center	4.3	0.2
IV	Cyst	4	Center	3.9	0.3
V	High-attenuation tumor	4	Center	10.5	−0.2
VI	Irregular tumor	N/A	Center	11.5	0.9
VII	Fat	4	6 mm above center	4.9	0.6
VIII	Fat	4	6 mm below center	2.5	0.0
IX-1	Cyst	4	Upper-left corner	0.6	0.6
IX-2	High-attenuation tumor	4	Upper-right corner	9.5	—
IX-3	Fat	4	6 mm below center	0.9	—

[1]The material in the background was glandular tissue in all cases.

B. Extraction of Time-of-Flight Data

To extract Δt_{ij} (the time of flight after geometrical delay compensation), the peak value e_{p} of the envelope of $e_{ij}(t)$ about $t_{ij,0}$ (with a time window of 10 μs) was found, then t_{ij} (the time of flight) was set to be the time when the envelope crossed $\frac{1}{2}e_{\text{p}}$ at the rising edge of the peak. The following two rules were applied to remove the t_{ij} associated with severely distorted $e_{ij}(t)$ around $t_{ij,0}$. First, t_{ij} and Δt_{ij} were ignored if:

$$E_{ij} < 0.15 \frac{1}{N_{\text{A}}} \sum_{q=1}^{N_{\text{A}}} E_{iq}, \tag{10}$$

where E_{ij} denotes the energy of the envelope of $e_{ij}(t)$ about $t_{ij,0}$ with element factor compensation. Element factors for all transmit/receive combinations were estimated using a channel data set collected with only water between the array and the metal plate. After the first step, Δt_{u} and Δt_{l} were found, where Δt_{u} (Δt_{l}) is a time value such that 95% of the Δt_{ij} is smaller (larger) than it and the other is larger (smaller) than it. Second, t_{ij} was dropped if:

$$\left| \Delta t_{ij} - \frac{\Delta t_{\text{u}} + \Delta t_{\text{l}}}{2} \right| > 2\left(\Delta t_{\text{u}} - \Delta t_{\text{l}}\right). \tag{11}$$

Fig. 4(a) shows all the receive envelope data around $\Delta t_{ij,0}$ when the 64th channel was used on transmit in Case VIII with the element factor compensated. The geometrically compensated time-of-flight data in Case VIII are shown in Fig. 4(b). Note that all the removed and unavailable Δt_{ij} data values are replaced by 0. The removed and unavailable transmit/receive combinations are shown in Fig. 4(c) in white, in which the two vertical lines and the two horizontal lines were due to two dead elements of the array. The two lines at 45° were due to the multiplexer setup.

C. Generation of C_{image}

Spatial compounding [19] (with five subapertures all having 43 channels and centered at channels 22, 43, 65,

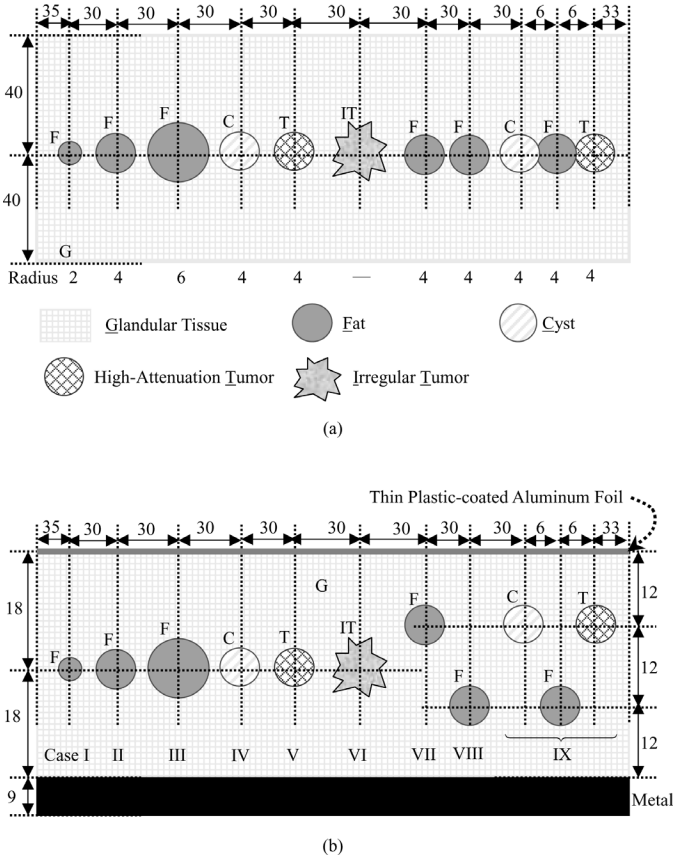

Fig. 3. Cross sections of the phantom used in this paper. (a) Top view. (b) Side view. All the dimensions are in millimeters.

86, and 107) was performed to generate B-mode images with reduced speckle intensity variations. The pixel size was 0.038 mm (x-axis) by 0.037 mm (y-axis). Dynamic focusing was performed and dynamic aperture size was used with the lower limit of the F-number being 1 on both transmit and receive when forming a subimage. The steering angle of all subapertures was limited to within $\pm 45°$. At each pixel, the signals of all contributing subapertures were averaged. In Case I, the speckle signal-to-noise ratio, defined as the mean pixel intensity over the standard deviation of the pixel intensity, in the ROI was raised from 0.90 to 1.86 by spatial compounding. To further reduce the speckle variations, the compound B-mode image was low-pass filtered using a two-dimensional Gaussian filter with a $1/e$ cutoff at 0.152 mm to generate the final B-mode image. Once the filtered B-mode image was obtained, a single threshold was applied for segmentation, and the regions in the thresholded binary image with an area smaller than π mm^2 were removed.

For most cases (Cases I–IV, VII, and VIII) the ROIs could be extracted successfully by the above procedures, but morphological dilation and erosion [20] (which were necessary for Cases V, VI, and IX) were applied to all cases after thresholding in order to remove the holes in ROI candidates and make the boundaries more regular. The morphological structuring element was disk shaped with a radius of 40 pixels for both dilation and erosion.

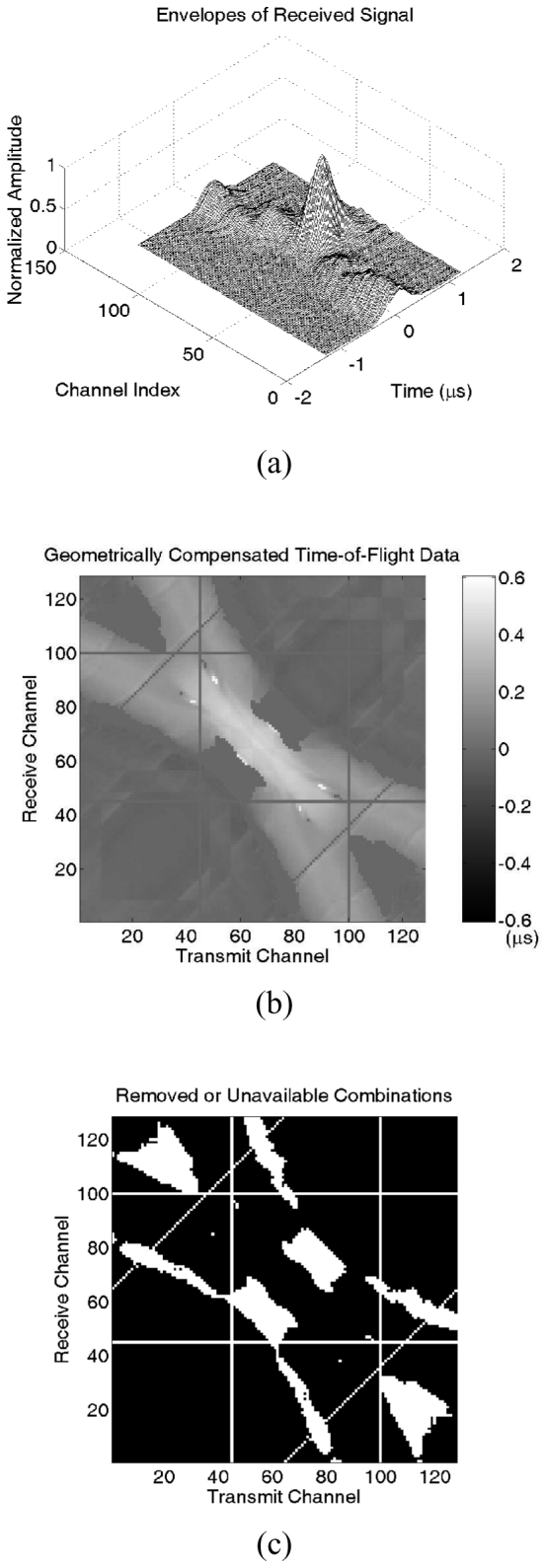

Fig. 4. (a) Envelopes of the received signals when the 64th channel transmits in Case VIII. Geometrical delays and element factors have been compensated. (b) The geometrically compensated time-of-flight data. Note that all the removed and unavailable Δt_{ij} data values are replaced by 0. (c) A white pixel at position (i, j) means that the associated Δt_{ij} value was removed or unavailable.

The sampling intervals Δx_s and Δy_s of the sound velocity distribution in the x and y directions were 0.55 mm and 0.53 mm, respectively, which were different from those of the B-mode image. Therefore, after finding the ROIs, the resultant binary images were resampled by applying an area ratio threshold of 0.96. For each pixel of size $\Delta x_s \cdot \Delta y_s$ in the resampled binary image, if the above-threshold area was lower than $0.96 \cdot \Delta x_s \cdot \Delta y_s$, then this pixel was regarded as being outside the ROI. The boundaries were derived from the resampled ROIs by morphological dilation (according to the disparity between the ROIs and their dilated versions), and with these boundaries C_{image} was generated using (8).

Figs. 5(a)–(e) show the results corresponding to different steps using Case IX as an example. The filtered compound B-mode image is displayed in Fig. 5(a) with a 30-dB dynamic range. Fig. 5(b) shows the segmentation result after a −16 dB threshold (with respect to the maximum intensity) was applied. The binary image after removing regions smaller than π mm^2 is shown in Fig. 5(c). Morphologically dilating the ROI candidates, then eroding the resultant binary image extracted the ROIs [see Fig. 5(d)]. Fig. 5(e) shows the extracted boundaries.

D. Reconstructed Sound Velocity Images

The sound velocity images were reconstructed using the algorithm introduced in Section II-B, using $c_{\text{lower}} = 1450$ m/s and $c_{\text{upper}} = 1580$ m/s. All the reconstruction results are listed in Table II. The reconstructed sound velocity distribution for Case IX is shown in Fig. 5(f) over the range 1450 m/s to 1580 m/s. Define errors as:

$$\Delta c_{(\cdot)} = c_{(\cdot),\text{recon}} - c_{(\cdot),\text{true}}, \tag{12}$$

where $(\cdot)$ denotes F (fat), C (cyst), T (high-attenuation tumor), IT (irregular tumor), G (glandular tissue), or ROI, $c_{(\cdot),\text{true}}$ is the true sound velocity listed in Table I, and $c_{(\cdot),\text{recon}}$ is the reconstructed sound velocity. In Case IX, $\Delta c_C = 0.6$ m/s, $\Delta c_T = 9.5$ m/s, $\Delta c_F = 0.9$ m/s, and $\Delta c_G = 0.6$ m/s.

The filtered compound B-mode images and reconstructed sound velocity images for Cases I–VIII are shown in Figs. 6–9. Figs. 6–8 demonstrate the effects on the reconstruction accuracy of the size of the spherical objects, different sound velocities in the objects, and the depth of the objects, respectively. In all cases, the errors in the background region are small. Figs. 6(a) and (b), (c) and (d), and (e) and (f) show the estimation results corresponding to fat spheres with a radius of 2 mm, 4 mm, and 6 mm, respectively. The left panels [Figs. 6(a), (c), and (e)] are the filtered compound B-mode images, and the right panels [Figs. 6(b), (d), and (f)] are the estimated sound velocity distributions. The Δc_{ROI} values are 2.6 m/s, 4.5 m/s, and 4.3 m/s, respectively; and those of Δc_G are 0.3 m/s, 0.3 m/s, and 0.2 m/s, respectively. Figs. 7(a) and (b), (c) and (d), and (e) and (f) show the filtered compound B-mode images and the sound velocity distributions corresponding to spheres consisting of different tissues (cyst, fat, and tumor, respectively). The Δc_{ROI} values are 3.9 m/s, 4.5 m/s, and 10.5 m/s, respectively; and those of Δc_G are 0.3 m/s, 0.3 m/s, and −0.2 m/s, respectively. Figs. 8(a) and (b), (c) and (d), and (e) and (f) show the filtered compound B-mode images and the sound velocity distributions corresponding to fat spheres at different positions (upper, center, and lower, respectively). The Δc_{ROI} values are 4.9 m/s, 4.5 m/s, and 2.5 m/s, respectively; and those of Δc_G are 0.6 m/s, 0.3 m/s, and 0.0 m/s, respectively. Figs. 9(a) and (b) show the filtered compound B-mode image and the sound velocity distribution for Case VI, respectively. In this case $\Delta c_{\text{IT}} = 11.5$ m/s,

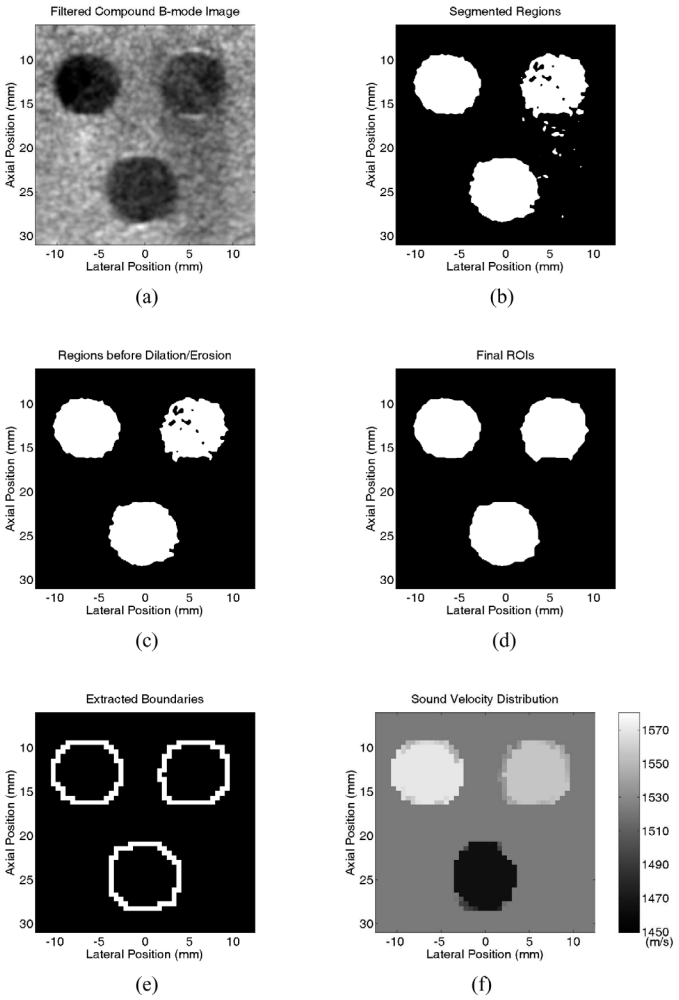

Fig. 5. Evaluation of Case IX. The image object comprises a background of glandular material ($c_G = 1522$ m/s, $\rho_G = 1.03$ g/cm^3, and $\alpha_G = 2.74$ dB/cm) with three spheres, all with a radius of 4 mm ($c_C = 1570$ m/s, $\rho_C = 1.02$ g/cm^3, and $\alpha_C = 0.78$ dB/cm in the upper-left cyst sphere; $c_T = 1547$ m/s, $\rho_T = 1.10$ g/cm^3, and $\alpha_T = 7.36$ dB/cm in the upper-right high-attenuation tumor sphere; and $c_F = 1464$ m/s, $\rho_F = 0.94$ g/cm^3, and $\alpha_F = 2.21$ dB/cm in the lower fat sphere). (a) Filtered compound B-mode image displayed with a 30-dB dynamic range. (b) Segmented regions. (c) Binary image after removing smaller regions. (d) ROIs extracted by dilation and erosion based on the binary image in (c). (e) Boundaries between the three spheres and the background. (f) Reconstructed sound velocity distribution.

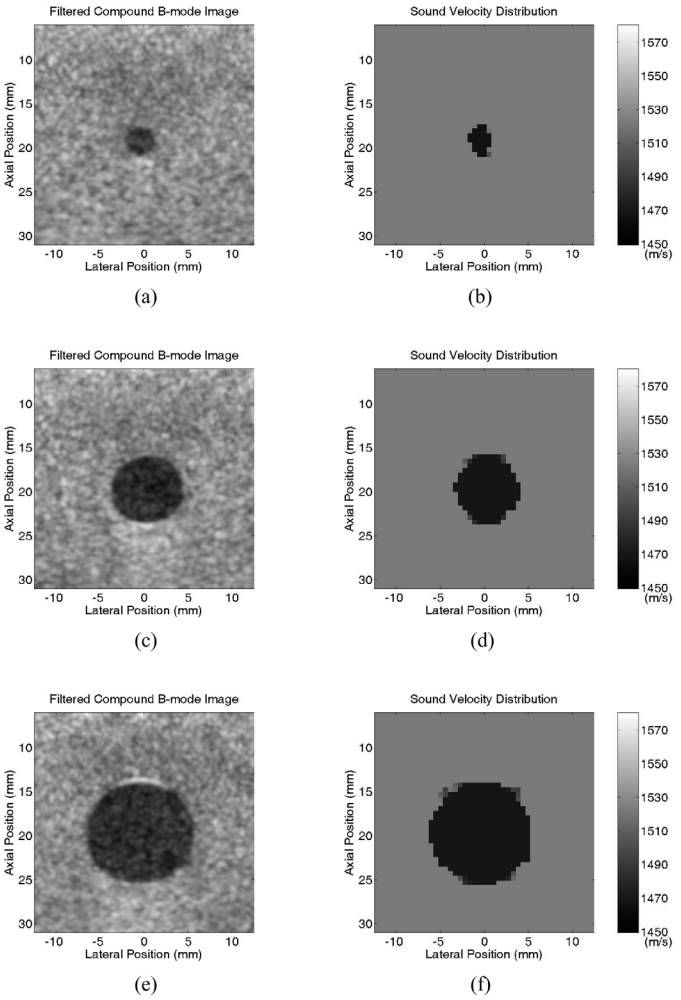

Fig. 6. Filtered compound B-mode images (displayed with a 30-dB dynamic range) and reconstructed sound velocity distributions of objects containing fat spheres (c_F = 1464 m/s, ρ_F = 0.94 g/cm^3, and α_F = 2.21 dB/cm) with different radii. (a) and (b) Case I (radius = 2 mm). (c) and (d) Case II (radius = 4 mm). (e) and (f) Case III (radius = 6 mm).

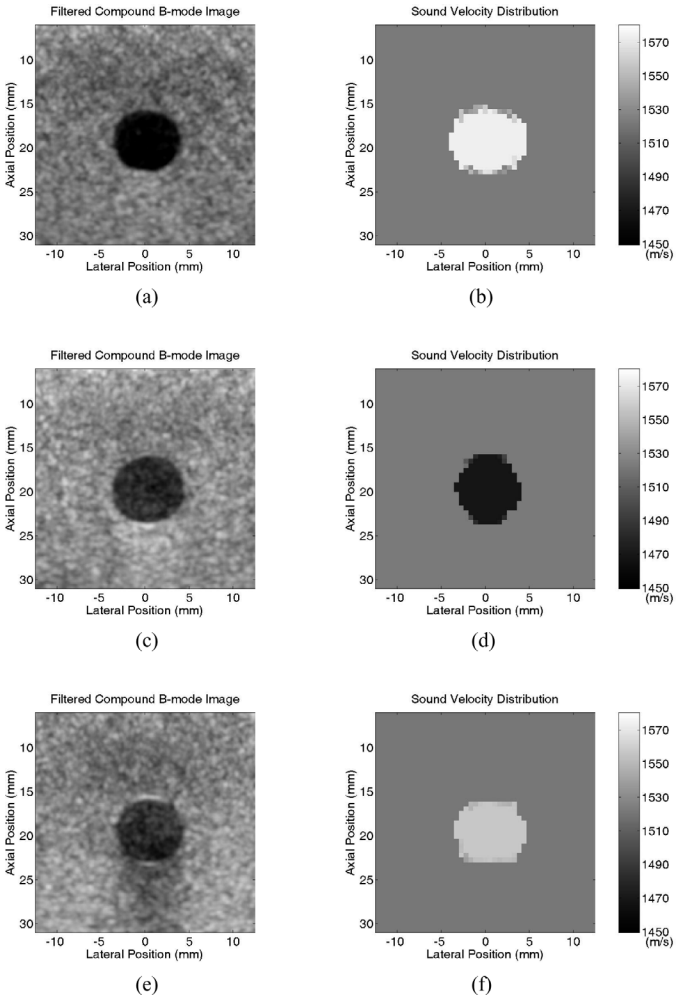

Fig. 7. Filtered compound B-mode images (displayed with a 30-dB dynamic range) and reconstructed sound velocity distributions of objects containing spheres all with a radius of 4 mm but representing different tissue types. (a) and (b) Case IV (cyst; c_C = 1570 m/s, ρ_C = 1.02 g/cm^3, and α_C = 0.78 dB/cm). (c) and (d) Case II (fat; c_F = 1464 m/s, ρ_F = 0.94 g/cm^3, and α_F = 2.21 dB/cm). (e) and (f) Case V (tumor; c_T = 1547 m/s, ρ_T = 1.10 g/cm^3, and α_T = 7.36 dB/cm).

$\Delta c_G = 0.9$ m/s, and the original sound velocity difference between the irregular tumor and the glandular background is 31 m/s, as shown in Table I. Fig. 9(b) exhibits large errors in boundary extraction that affect the accuracy of sound velocity estimation.

IV. Discussion

To evaluate the sensitivity of the sound velocity error to the area of the segmented ROI, the ROIs in Case I and III were artificially changed and the corresponding sound velocity distributions then were estimated. Every new ROI was generated from the original ROI by adding pixels on the outer boundary or removing pixels on the inner boundary. Ten different ROIs were randomly generated given a total ROI area. Figs. 10(a) and (b) show the curves of mean sound velocity difference (between the new estimated sound velocity and the original one in the ROI) versus ROI area difference for Case I and III, respectively. The ROI area difference was normalized with respect to the nominal area (i.e., 4π mm^2 and 36π mm^2 for Case I and III, respectively). Also shown in Fig. 10 are the error bars specifying ± 1 standard deviation. Note that the standard deviation corresponding to the zero ROI area difference was zero since the ROI was fixed at this point and no randomly generated ROIs were generated. It was found that the sound velocity error is less than ± 3 m/s when the ROI area difference is within $\pm 5\%$ in these cases.

The algorithm introduced in Section II-B treats image objects as two-dimensional. Although the image objects in this paper were three-dimensional, generally good sound velocity estimation accuracy was achieved. The reconstruction errors are larger for the high-attenuation and irregular tumors. A new phantom is required in order to experimentally investigate whether or not the higher attenuations

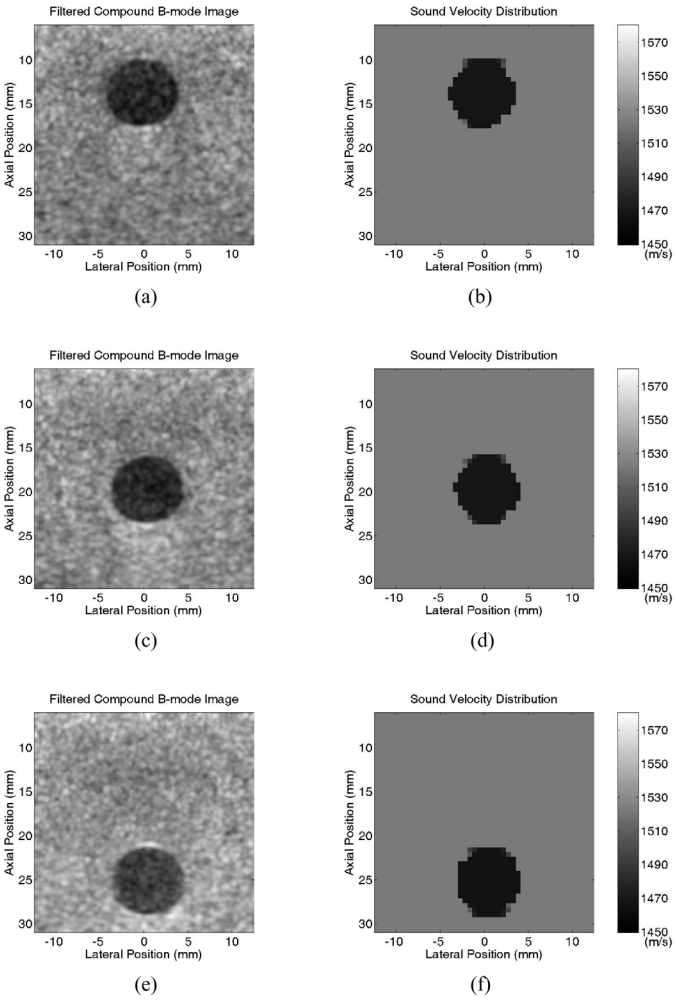

Fig. 8. Filtered compound B-mode images (displayed with a 30-dB dynamic range) and reconstructed sound velocity distributions of objects containing fat spheres ($c_{\mathrm{F}} = 1464$ m/s, $\rho_{\mathrm{F}} = 0.94$ g/cm^3, and $\alpha_{\mathrm{F}} = 2.21$ dB/cm) all with a radius of 4 mm but at different positions. (a) and (b) Case VII (the sphere is above center). (c) and (d) Case II (the sphere is at the center). (e) and (f) Case VIII (the sphere is below center).

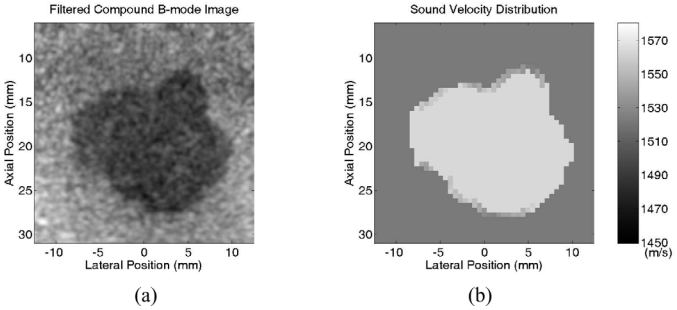

Fig. 9. (a) Filtered compound B-mode image (displayed with a 30-dB dynamic range) and (b) reconstructed sound velocity distribution of an object containing an irregular tumor. $c_{\mathrm{IT}} = 1553$ m/s, $\rho_{\mathrm{IT}} = 1.07$ g/cm^3, and $\alpha_{\mathrm{IT}} = 4.26$ dB/cm.

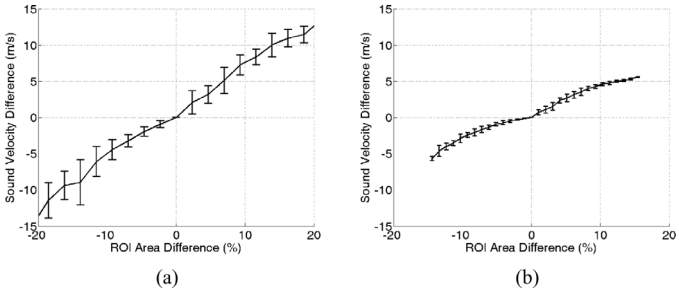

Fig. 10. The curves of mean sound velocity difference (between the new estimated sound velocity and the original one in the ROI) versus ROI area difference in percentage for (a) Case I and (b) Case III. Ten different ROIs were randomly generated given an ROI area. The error bars specify ±1 standard deviation. Note that the standard deviation corresponding to the zero ROI area difference was zero as the ROI was fixed at this point and no randomly generated ROIs were generated.

result in larger errors. The large error in the boundary extraction for Case VI partially contributes to the sound velocity estimation error in that case. More studies are needed to verify the efficacy of this algorithm on general objects in clinical situations.

The sound velocity error in ROI tends to be positive in this paper (this phenomenon did not occur in [10]). One possible reason is the expansion (contraction) of the fat (cyst, high-attenuation tumor, or irregular tumor) region in the B-mode image with respect to its original size—a lower (higher) sound velocity is equivalent to a longer (shorter) distance. Because the area of the background is much larger than that of the ROI, the sound velocity estimation is more sensitive to the sound velocity error in the background than that in the ROI. Therefore, the reconstructed sound velocity in the background will be only slightly affected, and the absolute value of the difference of the reconstructed sound velocities between the ROI and the background tends to decrease as the area of ROI increases. Another potential source of error is a refraction artifact. The ray-tracing diagrams shown in Figs. 11(a) and (b) for Cases II and IV, respectively, illustrate that the number of transmit/receive combinations with times of flight affected by the sphere is larger in Case IV than in Case II. This point is further demonstrated by Figs. 11(c) and (d), which show the geometrically compensated time-of-flight data for Cases II and IV, respectively (note that the colormap for Case IV has been reversed for display purposes). Thus, a higher sound velocity in the ROI will increase its effective area when measuring the time-of-flight data. However, the area of the ROI is relatively less affected by the sound velocity in B-mode. Consequently, the area is effectively contracted during reconstruction.

In a few cases there were multiple reflections between the array and the top surface of the phantom, which made finding the peak of the echo from the metal plate difficult. This explains why we used the rising edge rather than the peak to estimate the time of flight.

The shadows of the high-attenuation and irregular tumors are clearly seen in B-mode images for Cases V,

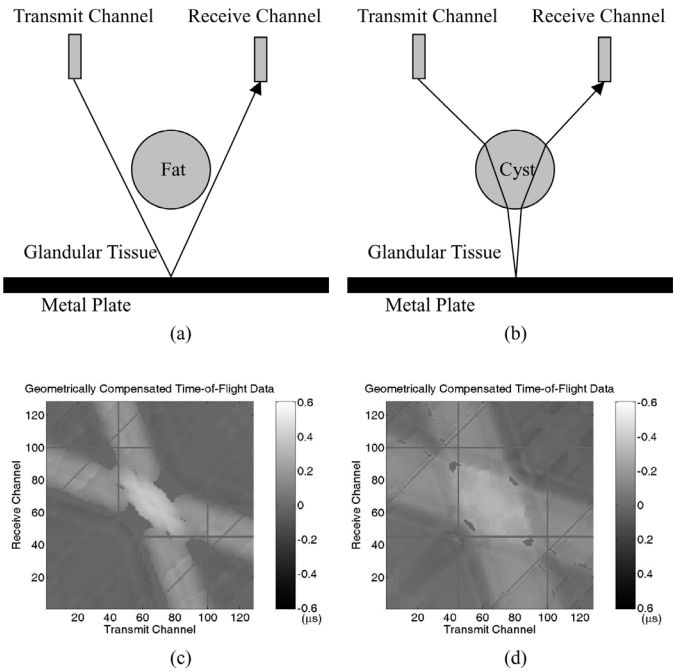

Fig. 11. The ray-tracing diagrams for (a) Case II and (b) Case IV, and the geometrically compensated time-of-flight data in (c) Case II and (d) Case IV. Note that the colormap in (d) for Case IV has been reversed for display purposes.

VI, and IX. These shadows complicated the extraction of ROIs. If only the tissue type is important, then sound velocity images are not necessary in these simple cases. However, if the image contains more complicated objects, B-mode image alone may be insufficient for identifying different tissue types. In this case, the algorithm proposed in [10] can be used to complement conventional B-mode ultrasound and to enhance breast cancer detection in the situations in which a fat region may be incorrectly diagnosed as a tumor, because the fat region typically has a sound velocity lower than the glandular tissue. Based on the result of Case I, a tumor with a diameter as small as 4 mm may be distinguishable using B-mode ultrasound with the help of the sound velocity information.

V. Conclusions

In the study described in this paper, we experimentally investigated the method proposed in [10] for reconstructing the sound velocity distribution in the breast. The experimental setup—which consisted of a 128-channel array, a digital array system, a phantom, and a computer—allowed acoustic data acquisition for simultaneous B-mode image formation and limited-angle tomographic sound velocity reconstruction. The reconstruction algorithm incorporates the segmentation information from the B-mode image of the same object. Nine cases were evaluated by scanning the phantom at different positions. Although the image objects were three-dimensional, good sound velocity estimation results were obtained using the one-dimensional array, with sound velocity errors being less than 5 m/s in 8 of 11 ROIs. Although the errors associated with tumor objects were larger, successful tissue classification was still possible using the information that the sound velocity should be higher in the ROI than in the background for those cases. Therefore, this method makes obtaining the sound velocity distribution feasible with the current B-mode imaging setup using linear arrays. Our future work will focus on an efficient implementation of the algorithm, application of the sound velocity information to phase aberration correction, and performance evaluation of the method in clinical situations.

Acknowledgments

The authors thank Computed Ultrasound Global, Inc., Taipei, Taiwan, for providing the digital array system.

References

[1] M. E. Lanfranchi, *Breast Ultrasound*. 2nd ed. New York: Marban Books, 2000.
[2] T. C. Telger, *Teaching Atlas of Breast Ultrasound*. New York: Thieme Medical Publ., 1996.
[3] C.-M. Chen, Y.-H. Chou, K.-C. Han, G.-S. Hung, C.-M. Tiu, H.-J. Chiou, and S.-Y. Chiou, "Breast lesions on sonograms: Computer-aided diagnosis with nearly setting-independent features and artificial neural networks," *Radiology*, vol. 226, no. 2, pp. 504–514, 2003.
[4] A. T. Stavros, D. Thickman, C. L. Rapp, M. A. Dennis, S. H. Parker, and G. A. Sisney, "Solid breast nodules: Use of sonography to distinguish between benign and malignant lesions," *Radiology*, vol. 196, no. 1, pp. 123–134, 1995.
[5] Q. Zhu, B. D. Steinberg, and R. L. Arenson, "Wavefront amplitude distortion and image sidelobe levels: Part II–In vivo experiments," *IEEE Trans. Ultrason., Ferroelect., Freq. Contr.*, vol. 40, no. 6, pp. 754–762, 1993.
[6] L. M. Hinkelman, D.-L. Liu, R. C. Waag, Q. Zhu, and B. D. Steinberg, "Measurements and correction of ultrasonic pulse distortion produced by the human breast," *J. Acoust. Soc. Amer.*, vol. 97, no. 3, pp. 1958–1969, 1995.
[7] R. C. Gauss, M. S. Soo, and G. E. Trahey, "Wavefront distortion measurements in the human breast," in *Proc. IEEE Ultrason. Symp.*, 1997, pp. 1547–1551.
[8] S. A. Goss, R. L. Johnston, and F. Dunn, "Comprehensive compilation of empirical ultrasonic properties of mammalian tissues," *J. Acoust. Soc. Amer.*, vol. 64, no. 2, pp. 423–457, 1978.
[9] A. C. Kak and M. Slaney, *Principles of Computerized Tomographic Imaging*. New York: Institute of Electrical and Electronics Engineers, 1988.
[10] S.-W. Huang and P.-C. Li, "Computed tomography sound velocity reconstruction using incomplete data," *IEEE Trans. Ultrason., Ferroelect., Freq. Contr.*, vol. 51, no. 3, pp. 329–342, 2004.
[11] M. Krueger, A. Pesavento, and H. Ermert, "A modified time-of-flight tomography concept for ultrasonic breast imaging," in *Proc. IEEE Ultrason. Symp.*, 1996, pp. 1381–1385.
[12] M. Krueger, V. Burow, K. M. Hiltawsky, and H. Ermert, "Limited angle ultrasonic transmission tomography of the compressed female breast," in *Proc. IEEE Ultrason. Symp.*, 1998, pp. 1345–1348.
[13] P. Oskoui and H. Stark, "A comparative study of three reconstruction methods for a limited-view computer tomography problem," *IEEE Trans. Med. Imag.*, vol. 8, no. 1, pp. 43–49, 1989.
[14] K. C. Tam, J. W. Eberhard, and K. W. Mitchell, "Incomplete-data CT image reconstructions in industrial applications," *IEEE Trans. Nucl. Sci.*, vol. 37, no. 3, pp. 1490–1499, 1990.
[15] H. Stark, *Image Recovery: Theory and Application*. London: Academic, 1987.

[16] P. L. Combettes and P. Bondon, "Hard-constrained inconsistent signal feasibility problems," *IEEE Trans. Signal Processing*, vol. 47, no. 9, pp. 2460–2468, 1999.
[17] H. L. Royden, *Real Analysis*. 3rd ed. Englewood Cliffs, NJ: Prentice-Hall, 1988.
[18] R. M. Lemor, P. K. Weber, P. K. Fonfara, C. Guenther, H. J. Welsch, and M. L. Hoss, "A new combined open research platform for ultrasound radio frequency signal processing," in *Proc. IEEE Ultrason. Symp.*, 2003, pp. 33–37.
[19] M. O'Donnell and S. D. Silverstein, "Optimal displacement for compound image generation in medical ultrasound," *IEEE Trans. Ultrason., Ferroelect., Freq. Contr.*, vol. 35, no. 4, pp. 470–476, 1988.
[20] R. C. Gonzalez and R. E. Woods, *Digital Image Processing*. 2nd ed. Reading, MA: Addison-Wesley, 2002.

Sheng-Wen Huang was born in 1971 in Changhua, Taiwan, R.O.C. He received the B.S. and Ph.D. degrees from National Taiwan University, Taipei, Taiwan, R.O.C. in 1993 and 2004, respectively, both in electrical engineering. He is currently a research assistant with the Division of Medical Engineering Research at National Health Research Institutes. His current research interests include ultrasonic tomography, coded excitation, and behaviors of ultrasound contrast agents.

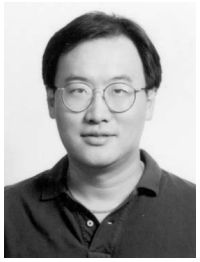

Pai-Chi Li (S'93–M'95–SM'01) received the B.S. degree in electrical engineering from National Taiwan University, Taipei, Taiwan, R.O.C., in 1987, and the M.S. and Ph.D. degrees from the University of Michigan, Ann Arbor, in 1990 and 1994, respectively, both in electrical engineering: systems.

He was a research assistant with the Department of Electrical Engineering and Computer Science at the University of Michigan from 1990 to 1994. He joined Acuson Corporation, Mountain View, CA, as a member of the technical staff in June 1994. His work in Acuson was primarily in the areas of medical ultrasonic imaging system design for both cardiology and general imaging applications. In August 1997, he went back to the Department of Electrical Engineering at National Taiwan University where he is currently a full professor. His current research interests include biomedical ultrasonic imaging and signal processing.

Dr. Li is a senior member of IEEE and Associate Editor of *IEEE Transactions on Ultrasonics, Ferroelectrics, and Frequency Control*. He received the 2003 Distinguished Research Achievement Award from National Taiwan University, the 2002 Dr. Wu Dayou Research Award from the National Science Council, the 2002 Outstanding Young Electrical Engineer Award from the Chinese Institute of Electrical Engineering and the Distinguished Industrial Collaboration Award of Ministry of Education. He also was the recipient of the Distinguished Achievement Award in Electrical Engineering: Systems in 1994 for his outstanding academic achievement at the University of Michigan.

Ultrasonic Computed Tomography Reconstruction of the Attenuation Coefficient Using a Linear Array

Sheng-Wen Huang and Pai-Chi Li,

***Abstract*—The attenuation coefficient distribution and sound velocity distribution in the breast can be used to complement B-mode ultrasound imaging in the detection of breast cancer. This study investigated an approach for reconstructing the attenuation coefficient distribution in the breast using a linear array. The imaging setup was identical to that for conventional B-mode breast imaging, and the same setup has been used for reconstruction of sound velocity distributions in previous studies. In this study, we further developed a reconstruction method for the attenuation coefficient distribution. In particular, the proposed method incorporates the segmentation information from B-mode images and uses the sound velocity distribution to compensate for refraction effects. Experiments were conducted with a setup consisting of a 5-MHz, 128-channel linear array, a programmable digital array system, a phantom, and a computer. The constructed phantom contained materials mimicking the following breast tissues: glandular tissue, fat, cysts, high-attenuation tumors, and irregular tumors. Application of the proposed technique resulted in all the cysts and tumors (including high-attenuation and irregular tumors) being distinguished by thresholding the reconstructed attenuation coefficients. We have demonstrated that it is possible to use the same imaging setup to acquire data for B-mode image, sound velocity distribution, and attenuation coefficient distribution simultaneously. Moreover, the experimental data indicate its potential in improving the detection of breast cancer.**

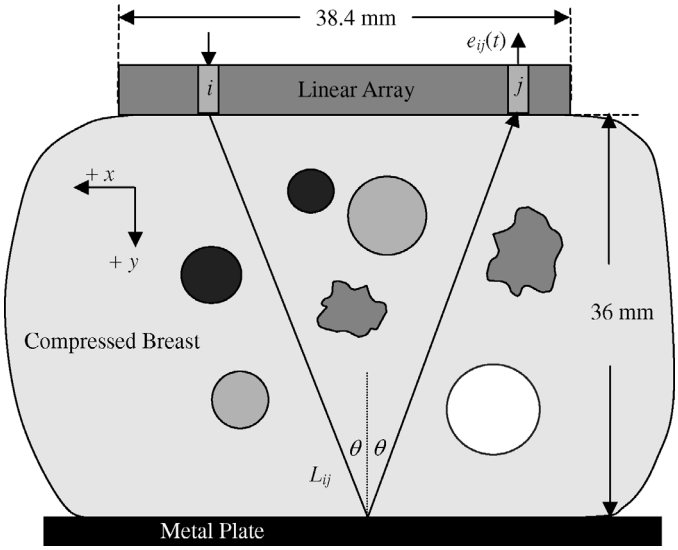

Fig. 1. Tomographic imaging setup allowing the acquisition of B-mode images, sound velocity distributions, and attenuation coefficient distributions. Each of the (N_A) channels in the array can transmit independently. The metal plate at the bottom of the compressed breast reflects the acoustic signal.

I. Introduction

B-mode ultrasound is commonly used to distinguish between solid tumors and fluid-filled cysts in breast tissue. It also is used to evaluate lumps that are difficult to visualize on a mammogram [1]–[4]. However, ultrasound is not used for routine breast cancer screening because it does not consistently detect certain early signs of cancer (e.g., microcalcifications) and its ability in distinguishing malignant tumors from benign tumors is often limited. In addition to conventional B-mode ultrasound, knowledge of the sound velocity distribution and the attenuation coefficient distribution in the breast can be used in diagnoses because the sound velocity is higher in cancerous tissue than in fat, and the attenuation coefficient is higher in cancerous tissue than in a cyst [5]–[8]. Thus, combining the information in the sound velocity distribution and the attenuation coefficient distribution with the corresponding B-mode image improves the accuracy and effectiveness of tumor detection.

Ultrasonic computed tomography has long been proposed for imaging the sound velocity and attenuation coefficient of the breast [9], but this has been hampered by the required imaging setup differing greatly from that used for B-mode imaging. In the present study, the single imaging setup shown in Fig. 1 was adopted for B-mode ultrasound imaging and determining the sound velocity distribution and attenuation coefficient distribution [10], [11]. This setup is similar to both that of mammography [12] and the limited-angle transmission tomography setup proposed by Krueger [13], [14]. Note that the setup in Fig. 1 yields an incomplete time-of-flight data set, which generally leads to inaccurate sound velocity estimation [15]–[17]. To improve the estimation accuracy, we used a reconstruction algorithm based on a convex programming formulation [18] that has been demonstrated to significantly improve the estimation accuracy using both simulations [10] and experimental data from a breast phantom

Manuscript received December 28, 2004; accepted May 12, 2005. Partial financial support from NSC (grant no. 94-2213-E-002-031 and 94-2120-M-002-004.) is appreciated.

The authors are with the Department of Electrical Engineering, National Taiwan University, and the Division of Medical Engineering Research, National Health Research Institutes, Taipei, Taiwan (e-mail: paichi@cc.ee.ntu.edu.tw).

[11]. In those simulations, results based on a 5-MHz linear array showed that the sound velocity error was generally 1–3 m/s, with a maximum of 5.8 m/s. The objects under investigation had radii of 2–6 mm, and all of them were detected successfully [10]. In the phantom experiments, nine cases were evaluated by scanning a custom-made phantom containing a variety of image objects with differing physical properties at different positions [11]. The image objects were three-dimensional, and good sound-velocity estimations were obtained even when using a one-dimensional array: the sound velocity errors were less than 5 m/s in 8 of 11 regions of interest (ROIs). This demonstrates that it is feasible to obtain the sound velocity distribution with current B-mode imaging setups using linear arrays.

The tomographic imaging setup shown in Fig. 1 also can be used to measure attenuation coefficient distributions, enabling B-mode images, sound velocity distributions, and attenuation coefficient distributions to be acquired using a single setup. As is shown in Section II-A, the mathematical formulation for solving the attenuation coefficient distribution is similar to that for the sound velocity distribution. However, refraction due to sound velocity inhomogeneities may cause redistribution of the acoustic energy and distort the attenuation data. Therefore, given the reconstructed sound velocity distribution, we proposed a technique based on the angular spectrum method that compensates for the refraction effects [19]. In this study, we experimentally investigated this approach using the same phantom as used in [11].

This paper is organized as follows. Section II introduces the methods for reconstructing the attenuation coefficient distribution. Section III introduces the experimental setup and presents the experimental results. A discussion is provided in Section IV, and the paper concludes in Section V.

II. Reconstruction Algorithm

In this paper, t and f denote time and temporal frequency, respectively, and x and y denote spatial coordinates.

When a single-frequency (f) acoustic plane wave propagates in a homogeneous soft tissue, its amplitude A decays exponentially with the propagation distance d_{p}:

$$A = A_0 \exp\left(-\alpha_{\mathrm{neper}} d_{\mathrm{p}}\right), \tag{1}$$

where A_0 is the original amplitude and α_{neper} is the attenuation coefficient of the tissue at frequency f. Defining $\alpha_{\mathrm{dB}} = 20\log_{10}(e)\cdot\alpha_{\mathrm{neper}} = 8.69\cdot\alpha_{\mathrm{neper}}$, the amplitude reduction in decibels is:

$$-20\log_{10}\left(\frac{A}{A_0}\right) = \alpha_{\mathrm{dB}} d_{\mathrm{p}}. \tag{2}$$

Eq. (2) assumes straight-line propagation, even in the presence of velocity variations [9]. On the other hand, the line integral of the attenuation coefficient distribution $\alpha_{\mathrm{dB,O}}(x, y; f)$ of an object along a particular path is regarded to be the difference between the received signal amplitude at f in decibels with water replacing the original image object and the signal amplitude with the real image object [9]. Such an approach accounts for effects of transducers based on the assumption of negligible attenuation in water and neglects the effects of refraction and reflection resulting from sound velocity inhomogeneities and impedance inhomogeneities. This assumption also is adopted in this paper.

Consider the imaging setup shown in Fig. 1. In addition to performing B-mode imaging, the setup is capable of transmitting a pulse from a single channel in order to acquire a complete data set $\{e_{ij}(t)\}$, $1 \le i, j \le N_{\mathrm{A}}$, where N_{A} is the number of channels in the array and $e_{ij}(t)$ are the data received by channel j when only channel i transmits. Let $\{e_{\mathrm{O},ij}(t)\}$ be the complete channel data set with the object positioned between the array and the metal plate, and $\{e_{\mathrm{W},ij}(t)\}$ be the complete channel data set with the object replaced by water. Note that $\{e_{\mathrm{O},ij}(t)\}$ and $\{e_{\mathrm{W},ij}(t)\}$ are the echo signals covering the entire propagation path from the transmit channel i to the reflection plate, then received by channel j. With each $e_{(\circ),ij}(t)$, where $(\circ)$ denotes "O" (object) or "W" (water), a signal $a_{(\circ),ij}(t)$ corresponding specifically to the echo reflected from the bottom plate can be extracted. Let $A_{(\circ),ij}(f)$ denote the temporal spectrum of $a_{(\circ),ij}(t)$ and define:

$$\Delta A_{ij}(f) = 20\log_{10}\left(\left|A_{\mathrm{W},ij}(f)\right|\right) - 20\log_{10}\left(\left|A_{\mathrm{O},ij}(f)\right|\right), \tag{3}$$

then:

$$\Delta A_{ij}(f) = \int_{L_{ij}} \alpha_{\mathrm{dB,O}}(x, y; f)\, dl, \tag{4}$$

where L_{ij} is the path of the line integral as shown in Fig. 1. Note that the introduction of $|A_{\mathrm{W},ij}(f)|$ in (3) is to compensate for effects relevant to the geometry and other properties of the transducer and the metal plate (e.g., finite-element width).

In soft tissues, the attenuation coefficient is approximately a linear function of frequency over the frequency range considered here [9], [20]. That is:

$$\alpha_{\mathrm{dB,O}}(x, y; f) \cong \alpha_{\mathrm{dB,O}}(x, y; f_0)\left|f/f_0\right|, \tag{5}$$

where f_0 is the frequency of interest. Define:

$$\Delta\overline{A}_{ij}(f_0, \Delta f) = \frac{1}{\Delta f}\int_{f_0-\Delta f/2}^{f_0+\Delta f/2} \frac{f_0}{f}\Delta A_{ij}(f)\, df, \tag{6}$$

then:

$$\Delta\overline{A}_{ij}(f_0, \Delta f) \cong \int_{L_{ij}} \alpha_{\mathrm{dB,O}}(x, y; f_0)\, dl. \tag{7}$$

Applying a procedure similar to that in Section II-A of [10], (7) becomes:

$$\Delta\overline{A}_{ij}\left(f_0, \Delta f\right) = \mathbf{l}_{ij}^{\mathrm{T}}\boldsymbol{\alpha}, \tag{8}$$

where $\mathbf{l}_{ij}$ and the attenuation coefficient distribution $\boldsymbol{\alpha}$ are $MN \times 1$ column vectors, and M and N are the numbers of grid points along the x-axis and y-axis, respectively. The number of equations in (8) is $N_{\mathrm{A}}\left(N_{\mathrm{A}}+1\right)/2$, and they can be expressed in the following matrix form:

$$\mathbf{L}\boldsymbol{\alpha} = \Delta\mathbf{a}, \tag{9}$$

where the attenuation data $\Delta\mathbf{a}$ is a $\left[N_{\mathrm{A}}\left(N_{\mathrm{A}}+1\right)/2\right] \times 1$ column vector consisting of $\Delta\overline{A}_{ij}\left(f_0, \Delta f\right)$, and $\mathbf{L}$ is a $\left[N_{\mathrm{A}}\left(N_{\mathrm{A}}+1\right)/2\right] \times MN$ matrix [10].

An acoustic wave propagating in an image object with sound velocity inhomogeneities (such as the breast) experiences both phase and amplitude distortion [21], [22]. Wavefront amplitude distortion affects $A_{\mathrm{O},ij}(f)$ and consequently also the estimation accuracy of the attenuation coefficient distribution. Here we developed a technique to compensate for such errors by using the reconstructed sound velocity distribution to estimate the refraction effects (resulting from sound velocity inhomogeneities) on $a_{\mathrm{O},ij}(t)$. We used the angular spectrum method, and the attenuation data after correction is denoted here as $\Delta\mathbf{a}'$. As is shown in Section III, using $\Delta\mathbf{a}'$ instead of $\Delta\mathbf{a}$ to estimate the attenuation coefficient distribution results in higher accuracy in most cases.

As illustrated in Fig. 2(a), consider an acoustic wave $W(x,\, y;\, f)$ propagating in the $+y$ direction in a linear fluid medium with a sound velocity distribution of $c(x,\, y;\, f)$, a sound velocity of $c_0(f)$ in the background, and an attenuation coefficient of $\alpha_{0,\mathrm{dB}}(f)$ that is independent of the position. The problem is defined as to find $W(x,\, y_1;\, f)$ assuming that $W(x,\, 0;\, f)$ is known.

$W(x,\, y_1;\, f)$ can be found by calculating $W(x,\, \mathrm{d}y;\, f)$, $W(x,\, 2\mathrm{d}y;\, f), \ldots,$ and $W(x,\, N_y\mathrm{d}y;\, f)$ sequentially with $N_y\mathrm{d}y = y_1$. Assume that $W(x,\, q\mathrm{d}y;\, f)$ has been found. Let the angular spectrum of $W(x,\, y;\, f)$ be $\widetilde{W}\left(k_x;\, y,\, f\right)$ [19], i.e.:

$$W(x,\, y;\, f) = \frac{1}{2\pi}\int \widetilde{W}\left(k_x;\, y,\, f\right)\exp\left(jk_x x\right)dk_x, \tag{10}$$

then:

$$W(x,\, q\mathrm{d}y + \mathrm{d}y;\, f) \cong \frac{h_q(x;\, f)}{2\pi}\int_{-2\pi f/c_0(f)}^{2\pi f/c_0(f)} H\left(k_x;\, \mathrm{d}y,\, f\right)\widetilde{W}\left(k_x;\, q\mathrm{d}y,\, f\right) \times \exp\left(jk_x x\right)dk_x, \tag{11}$$

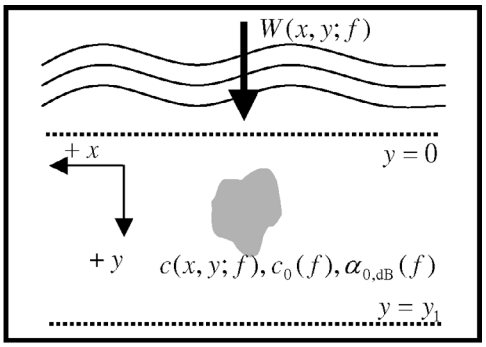

(a)

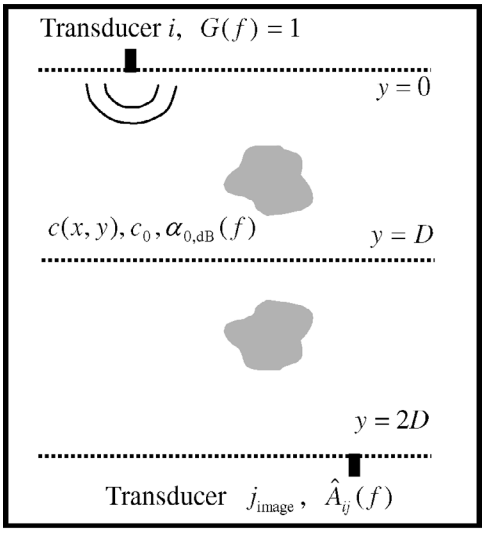

(b)

Fig. 2. Illustration of the technique for finding an estimate of $\hat{A}_{\mathrm{O},ij}(f)$ of $A_{\mathrm{O},ij}(f)$. (a) Basic form of the problem. (b) Configuration used to find $\hat{A}_{\mathrm{O},ij}(f)$.

where:

$$h_q(x;\, f) = \exp\left\{j2\pi f\int_{q\mathrm{d}y}^{(q+1)\mathrm{d}y}\left[c^{-1}(x,\, y;\, f) - c_0^{-1}\right]dy\right\}, \tag{12}$$

and:

$$H\left(k_x;\, \mathrm{d}y,\, f\right) = \exp\left[j\mathrm{d}y\sqrt{\left(2\pi f/c_0\right)^2 - k_x^2}\right] \times 10^{-\frac{\alpha_{0,\mathrm{dB}}(f)\mathrm{d}y}{20}\left\{\cos\left[\sin^{-1}\left(k_x c_0/f\right)\right]\right\}^{-1}}. \tag{13}$$

Based on the above discussion, an estimate of $\hat{A}_{\mathrm{O},ij}(f)$ of $A_{\mathrm{O},ij}(f)$—taking the sound velocity inhomogeneities into account but not inhomogeneities in the attenuation coefficient and density—can be obtained by considering the configuration in Fig. 2(b) [10]. $G(f)$ is the temporal spectrum of the transmitted signal that can be assigned arbitrarily, D is the distance between the array and the metal plate, $c(x,\, y)$ (with $0 \le y \le D$) is the

reconstructed sound velocity distribution that is independent of f, c_0 is the sound velocity in the background, and $\alpha_{0,\mathrm{dB}}(f) = 0.5f$ dB/cm, with f in megahertz. Note that $c(x, y) = c(x, 2D - y)$ for $D \leq y \leq 2D$. An estimate of $A_{\mathrm{W},ij}(f)$, $\hat{A}_{\mathrm{W},ij}(f)$, can be similarly obtained with $c(x, y) = c_0$ (e.g., 1480 m/s) and zero attenuation. Define:

$$\Delta\hat{A}_{ij}(f) = 20\log_{10}\left(\left|\hat{A}_{\mathrm{W},ij}(f)\right|\right) - 20\log_{10}\left(\left|\hat{A}_{\mathrm{O},ij}(f)\right|\right), \quad (14)$$

then a vector $\Delta\mathbf{a}'' = \mathbf{a} - \hat{\mathbf{a}}$, where $\hat{\mathbf{a}}$ consists of:

$$\Delta\overline{\hat{A}}_{ij}(f_0, \Delta f) = \frac{1}{\Delta f}\int_{f_0-\Delta f/2}^{f_0+\Delta f/2}\frac{f_0}{f}\Delta\hat{A}_{ij}(f)df, \quad (15)$$

can be constructed, and the equation to be solved becomes $\mathbf{L}(\boldsymbol{\alpha} - \alpha_{0,\mathrm{dB}}(f_0)\mathbf{i}) = \Delta\mathbf{a}''$, i.e.:

$$\mathbf{L}\boldsymbol{\alpha} = \Delta\mathbf{a}' \equiv (\Delta\mathbf{a}'' + \alpha_{0,\mathrm{dB}}(f_0)\mathbf{L}\mathbf{i}), \quad (16)$$

where $\mathbf{i}$ is an $MN \times 1$ vector whose elements all equal 1. $\Delta\mathbf{a}'$ is called the corrected attenuation data in this paper because the refraction effects have been partially removed.

A convex programming formulation [18] used to reconstruct the sound velocity distributions in [10], [11] is used to solve (16). Two kinds of a priori knowledge of $\boldsymbol{\alpha}$ are used. First, the attenuation coefficient is assumed to be in $[\alpha_{\mathrm{dB,lower}}, \alpha_{\mathrm{dB,upper}}]$ (where $\alpha_{\mathrm{dB,lower}} = 0$ dB/cm and $\alpha_{\mathrm{dB,upper}} = 2f_0$ dB/cm with f_0 in megahertz in this paper); therefore, $\boldsymbol{\alpha}$ must belong to:

$$C_{\mathrm{attenuation}} = \left\{\mathbf{x} \in \mathbf{R}^{MN} : x_l \in [\alpha_{\mathrm{dB,lower}}, \alpha_{\mathrm{dB,upper}}],\ 1 \leq l \leq MN\right\}. \quad (17)$$

Second, segmentation information from the corresponding B-mode image is used. Consider a B-mode image in which an object contains an identified and segmented ROI surrounded by the background. $\boldsymbol{\alpha}$ must belong to the set shown in (18) (see next page), where $I_{\mathrm{b}} \equiv \{b_1, b_2, \ldots, b_{N_{\mathrm{b}}}\}$ is the background index set, $I_{\mathrm{r}} \equiv \{r_1, r_2, \ldots, r_{N_r}\}$ is the ROI index set, and $I_{\mathrm{br}} \equiv \{br_1, br_2, \ldots, br_{N_{\mathrm{br}}}\}$ is the boundary index set. Eq. (18) means that all the attenuation coefficients in the background must be the same, and all the attenuation coefficients in the ROI also must be the same. In addition, the attenuation coefficients at the boundaries must fall between those of the background and the ROI. C_{image} can be defined similarly when the object contains more than one ROI.

Define $\mathbf{L}$ as $\mathbf{L} = \left[\mathbf{l}_1\ \mathbf{l}_2\ \ldots\ \mathbf{l}_{N_{\mathrm{A}}(N_{\mathrm{A}}+1)/2}\right]^{\mathrm{T}}$, $\Delta\mathbf{a}'$ as $\Delta\mathbf{a}' = \left[\Delta\overline{A}'_1\ \Delta\overline{A}'_2\ \ldots\ \Delta\overline{A}'_{N_{\mathrm{A}}(N_{\mathrm{A}}+1)/2}\right]^{\mathrm{T}}$, and

$$C_{\Delta A_i} = \left\{\mathbf{x} \in \mathbf{R}^{MN} : \mathbf{l}_i^{\mathrm{T}}\mathbf{x} = \Delta\overline{A}'_i(f_0, \Delta f)\right\}, \quad i = 1, 2, \ldots, N_{\mathrm{A}}(N_{\mathrm{A}}+1)/2, \quad (19)$$

then an attenuation coefficient distribution $\mathbf{x} \in C_{\mathrm{attenuation}} \cap C_{\mathrm{image}}$ minimizing the total amount of violation of the attenuation data in the mean-squared-error sense can be found by taking $\mathbf{x}$ as the limit of the sequence $\{\mathbf{x}_n\}$. $\mathbf{x}_0 \in C_{\mathrm{attenuation}} \cap C_{\mathrm{image}}$ is an initial attenuation coefficient distribution, and

$$\mathbf{x}_{n+1} = \frac{1}{2}\mathbf{x}_n + \frac{1}{2}P_{C_{\mathrm{attenuation}} \cap C_{\mathrm{image}}}\left[\frac{1}{N_{\mathrm{A}}(N_{\mathrm{A}}+1)/2}\sum_{i=1}^{N_{\mathrm{A}}(N_{\mathrm{A}}+1)/2}P_{C_{\Delta A_i}}(\mathbf{x}_n)\right], \quad n \geq 0, \quad (20)$$

where $P_{C_{(-)}}$ is the projector onto $C_{(-)}$ [23].

III. Experimental Results

A schematic of the experimental setup is shown in Fig. 3(a). The linear array (L6/128, Sound Technology Inc., State College, PA) has $N_{\mathrm{A}} = 128$ channels, an element pitch p of 0.3 mm, an elevation width of 5 mm, and an elevation focus of 25 mm. The array channels have a center frequency of 5.57 MHz and a -6 dB bandwidth of 4.10 MHz. A programmable digital array system (DiPhAS, Fraunhofer IBMT, St. Ingbert, Germany) [24] capable of transmitting a short pulse from any selected channel is used to acquire a channel data set $\{e_{ij}(t)\}$, $1 \leq i, j \leq N_{\mathrm{A}}$, $|j - i| \neq 64$ (because the array data acquisition system has 64 system channels, channel i and channel j with $|j - i| = 64$ share the same multiplexer and thus cannot be turned on simultaneously). All channel data were transferred from the array system to the computer for storage and further processing via a digital input/output card (PCI-7300A, Adlink, Taipei County, Taiwan) on the computer. The transmitted pulse is a one-cycle square wave with a duration of 0.2 μs, and all $e_{ij}(t)$ were sampled at 40 MHz with a vertical resolution of 12 bits. For each transmit/receive combination, data corresponding to 16 consecutive firings were averaged off-line to increase the signal-to-noise ratio. Fig. 3(b) shows a side view of the phantom, which was custom-made by Dr. Ernest Madsen (Department of Medical Physics, University of Wisconsin-Madison, WI). The parameters of the different materials (mimicking different tissues in the breast) are listed in Table I. The nine cases listed in Table II were generated by moving the array along the x-axis.

$$C_{\text{image}} = \begin{cases} \left\{ \begin{array}{c} \mathbf{x} \in \mathbf{R}^{MN} : x_{b_1} = x_{b_2} = \cdots = x_{b_{N_b}},\, x_{r_1} = x_{r_2} = \cdots = x_{r_{N_r}}, \\ x_{br_i} \in [x_{b_1},\, x_{r_1}],\, 1 \le i \le N_{\text{br}} \end{array} \right\} & \text{if } x_{b_1} \le x_{r_1} \\ \left\{ \begin{array}{c} \mathbf{x} \in \mathbf{R}^{MN} : x_{b_1} = x_{b_2} = \cdots = x_{b_{N_b}},\, x_{r_1} = x_{r_2} = \cdots = x_{r_{N_r}}, \\ x_{br_i} \in [x_{r_1},\, x_{b_1}],\, 1 \le i \le N_{\text{br}} \end{array} \right\} & \text{otherwise} \end{cases}, \tag{18}$$

TABLE I
PARAMETERS OF THE MATERIALS USED IN THE PHANTOM (AT 22°C).[1]

Material	Sound velocity c at $f_0 = 5$ MHz (m/s)	Density ρ (g/cm^3)	Attenuation coefficient α_{dB} at f_0 (dB/cm)	B-mode contrast relative to glandular tissue (dB)
Glandular tissue	1522	1.03	2.74	—
Fat	1464	0.94	2.21	−14
Cyst	1570	1.02	0.78	< −14
High-attenuation tumor	1547	1.10	7.36	−12
Irregular tumor	1553	1.07	4.26	−10

[1]Note that the materials were designed to mimic the listed tissues.

TABLE II
OBJECTS INCLUDED IN THE DIFFERENT CASES, AND THE ESTIMATION RESULTS.[1]

Case	ROI	Sphere radius (mm)	ROI position	Δc_{ROI}[2] (m/s)	$\Delta\alpha_{\text{ROI}}/\Delta\alpha'_{\text{ROI}}/\Delta\alpha^*_{\text{ROI}}$[3] (dB/cm)	$\Delta\alpha_{\text{G}}/\Delta\alpha'_{\text{G}}/\Delta\alpha^*_{\text{G}}$[3] (dB/cm)
I	Fat	2	Center	2.6	−2.21/−1.50/5.83	0.02/−0.08/−0.13
II	Fat	4	Center	4.5	−1.22/−0.39/1.74	0.06/−0.07/−0.14
III	Fat	6	Center	4.3	−0.78/−0.14/0.27	0.04/−0.08/−0.14
IV	Cyst	4	Center	3.9	3.64/0.87/0.26	−0.17/−0.17/−0.09
V	High-attenuation tumor	4	Center	10.5	2.64/1.76/2.32	−0.09/−0.09/−0.08
VI	Irregular tumor	N/A	Center	11.5	1.45/0.87/0.78	0.26/0.29/0.36
VII	Fat	4	High	4.9	−0.24/1.69/2.76	0.02/−0.14/−0.18
VIII	Fat	4	Low	2.5	−1.19/−1.30/0.26	0.11/−0.02/−0.06
IX-1	Cyst	4	Upper-left	0.6	2.82/−0.07/−0.36	0.02/0.00/0.00
IX-2	High-attenuation tumor	4	Upper-right	9.5	2.53/1.78/1.82	—
IX-3	Fat	4	Low	0.9	−2.05/−1.73/−0.66	—

[1]The material in the background was glandular tissue in all cases.
[2]The Δc_{ROI} values were the sound velocity errors listed in Table II of [11].
[3]The $\Delta\alpha_{\text{ROI}}$ and $\Delta\alpha_{\text{G}}$ values were obtained using the original attenuation data, the $\Delta\alpha'_{\text{ROI}}$ and $\Delta\alpha'_{\text{G}}$ values were obtained using the corrected attenuation data, and the $\Delta\alpha^*_{\text{ROI}}$ and $\Delta\alpha^*_{\text{G}}$ values were obtained using the corrected attenuation data with the sound velocities in the ROI and the background set to those listed in Table I, and all the sound velocities at the boundary set to their mean values.

$$a_{(\circ),ij}(t) \equiv \begin{cases} w_{\text{T}}\left(t - t_{(\circ),ij,\text{p}} + T/2;\, r\right) e_{(\circ),ij}(t) & t_{(\circ),ij,\text{p}} - T/2 \le t < t_{(\circ),ij,\text{p}} + T/2 \\ 0 & \text{otherwise} \end{cases}, \tag{21}$$

Details of the generation of C_{image}, the extraction of time-of-flight data, and the reconstruction of the sound velocity distribution can be found in [11]. With the reconstructed sound velocity distribution, $\Delta\hat{A}_{ij}(f)$ was calculated according to (14). Let $t_{(\circ),ij,0}$ be the time of flight according to a nominally constant sound velocity. The peak position $t_{(\circ),ij,\text{p}}$ of the envelope of $e_{(\circ),ij}(t)$ around $t_{(\circ),ij,0}$ (with a time window of 10 μs) was found, then $a_{(\circ),ij}(t)$ is

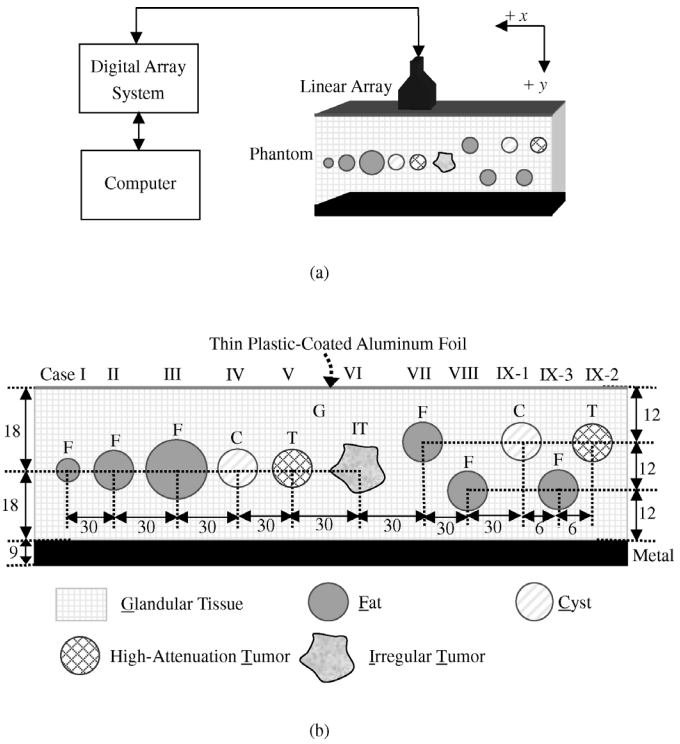

Fig. 3. (a) Schematic of the data-acquisition setup. (b) Side view of the phantom. All the dimensions are in millimeters and all the centers of the ROIs (fats, cysts, and tumors) are in the same plane.

given by (21) (see previous page), where T is the duration of w_{T}, and:

$$w_{\mathrm{T}}(t;\, r) = \begin{cases} \sin^2\left(\dfrac{\pi t}{rT}\right) & 0 \le t < \dfrac{rT}{2} \\ 1 & \dfrac{rT}{2} \le t \le T - \dfrac{rT}{2} \\ \sin^2\left[\dfrac{\pi(T-t)}{rT}\right] & T - \dfrac{rT}{2} < t \le T \\ 0 & \text{elsewhere} \end{cases} \tag{22}$$

is a Tukey window with a taper ratio of r [25]. By taking fast Fourier transforms of $a_{\mathrm{W},ij}(t)$ and $a_{\mathrm{O},ij}(t)$, $\Delta A_{ij}(f)$ was extracted according to (3), and the corrected attenuation data $\Delta\mathbf{a}'$ was obtained subsequently according to (6), (15), and (16). With $\Delta\mathbf{a}'$, $C_{\Delta A_i}$ was established according to (19).

The parameters used in this study were $f_0 = 5$ MHz (close to 5.57 MHz, the center frequency of the array), $\Delta f = 4$ MHz, $T = 4$ μs, and $r = 0.4$. The attenuation data corresponding to the discarded time-of-flight data were also discarded [11] due to the invalidity of the assumption of straight-line propagation. Figs. 4(a) and (b) show the raw attenuation data and the attenuation data corrected with the technique introduced in Section II-B, respectively, for Case II. In Fig. 4(a), energy redistribution caused by refraction is evident as variation in the attenuation data is large. In contrast, the corrected attenuation data shown in Fig. 4(b) are more consistent with the fact that the attenuation coefficients in fat and glandular tissue listed in Table I are close.

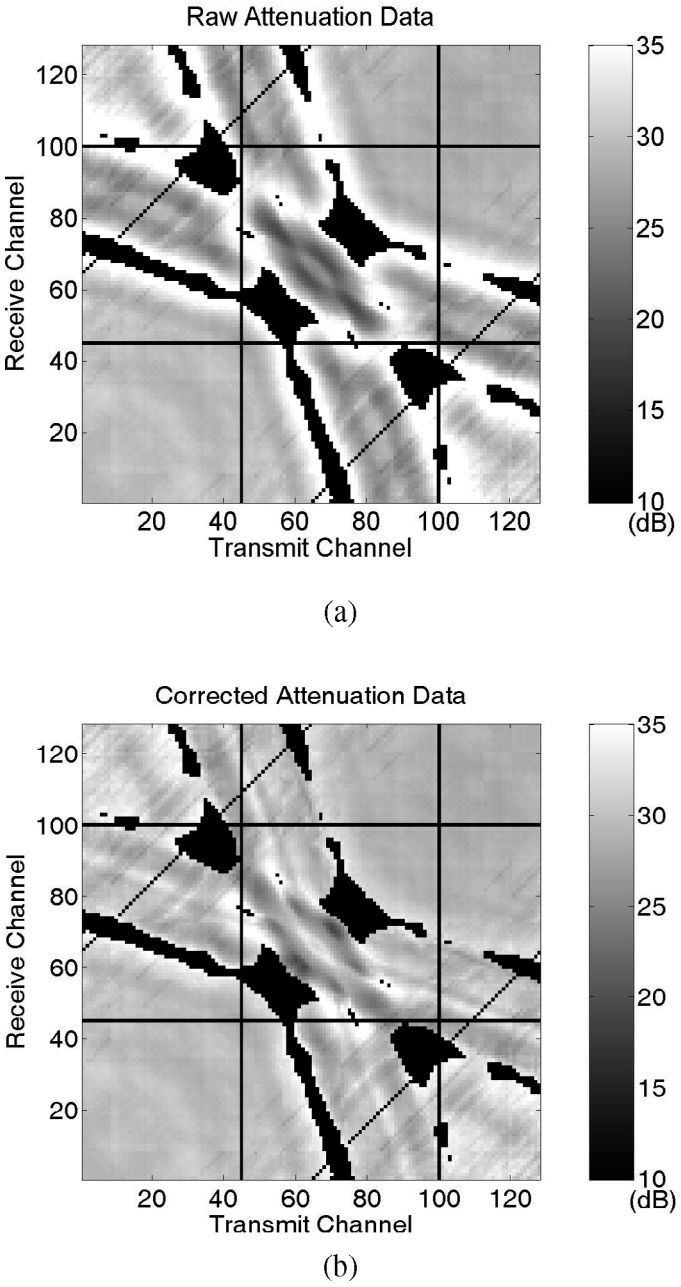

Fig. 4. (a) The raw attenuation data and (b) the attenuation data corrected using the technique described in Section II-B for Case II. Note that all the discarded and unavailable data values are replaced by 0, and thus are displayed in black.

The attenuation coefficient images were reconstructed using the algorithm described in Section II-C [i.e., by iteratively calculating $\mathbf{x}_{n+1}$ in (20)] for the nine cases listed in Table II and illustrated in Fig. 3(b). All the reconstruction results are listed in Table II, and the estimation errors

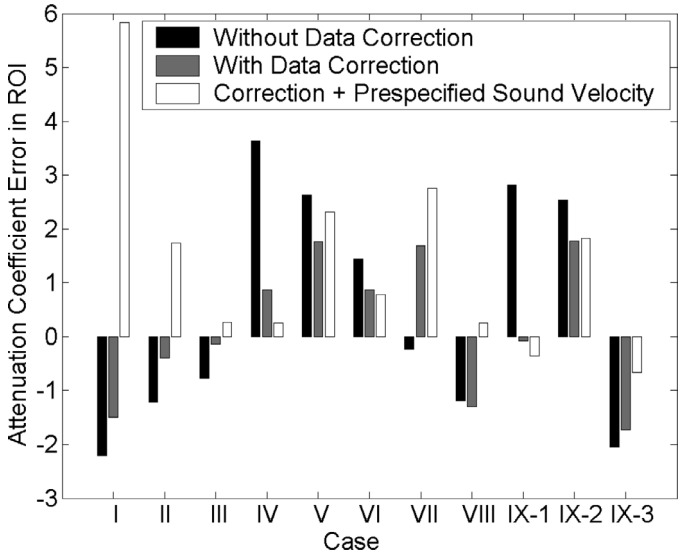

Fig. 5. Reconstructed attenuation coefficient errors without data correction (shown as black bars), with data correction using the estimated sound velocities (shown as gray bars), and with data correction using the sound velocities listed in Table I (shown as white bars).

in the ROIs also are plotted in Fig. 5. The errors are defined as:

$$\Delta\alpha_{(\cdot)} = \alpha_{\mathrm{dB},(\cdot),\mathrm{recon}}(f_0) - \alpha_{\mathrm{dB},(\cdot),\mathrm{true}}(f_0) \text{ and}$$
$$\Delta\alpha'_{(\cdot)} = \alpha'_{\mathrm{dB},(\cdot),\mathrm{recon}}(f_0) - \alpha_{\mathrm{dB},(\cdot),\mathrm{true}}(f_0), \quad (23)$$

where $(\cdot)$ is "F" (fat), "C" (cyst), "T" (high-attenuation tumor), "IT" (irregular tumor), "G" (glandular tissue), or "ROI"; $\alpha_{\mathrm{dB},(\cdot),\mathrm{true}}(f_0)$ is the attenuation coefficient listed in Table I; and $\alpha_{\mathrm{dB},(\cdot),\mathrm{recon}}(f_0)$ and $\alpha'_{\mathrm{dB},(\cdot),\mathrm{recon}}(f_0)$ are the attenuation coefficients reconstructed without and with data correction, respectively. In all cases the errors in the background region are small, and the errors in the ROIs are larger. Also listed in Table II are the estimation errors for sound velocity defined as:

$$\Delta c_{(\cdot)} = c_{(\cdot),\mathrm{recon}} - c_{(\cdot),\mathrm{true}}, \quad (24)$$

where $c_{(\cdot),\mathrm{true}}$ is the true sound velocity listed in Table I, and $c_{(\cdot),\mathrm{recon}}$ is the reconstructed sound velocity [11].

Fig. 6 shows the results using Case IX as an example. The B-mode image (with filtering and compounding [11]) is displayed in Fig. 6(a) with a 30-dB dynamic range. Fig. 6(b) shows the extracted boundaries that are used to generate C_{image}. The reconstructed sound velocity distribution for Case IX is shown in Fig. 6(c) over the range 1450 m/s to 1580 m/s, which is required for the correction of attenuation data. Figs. 6(d) and (e) show the reconstructed attenuation coefficient distributions without and with data correction, respectively. In this case, $\Delta\alpha'_{\mathrm{C}} = -0.07$ dB/cm ($\Delta\alpha_{\mathrm{C}} = 2.82$ dB/cm), $\Delta\alpha'_{\mathrm{T}} = 1.78$ dB/cm ($\Delta\alpha_{\mathrm{T}} = 2.53$ dB/cm), $\Delta\alpha'_{\mathrm{F}} = -1.73$ dB/cm ($\Delta\alpha_{\mathrm{F}} = -2.05$ dB/cm), and $\Delta\alpha'_{\mathrm{G}} = 0.00$ dB/cm ($\Delta\alpha_{\mathrm{G}} = 0.02$ dB/cm). Thus, the corrected attenuation data improves the accuracy of estimation of the attenuation coefficients.

Figs. 7(a) and (b), (c) and (d), (e) and (f), and (g) and (h) show the reconstructed attenuation coefficient distributions of objects containing ROIs representing different tissues: Cases II, IV, V, and VI for the fat, cyst, tumor, and irregular tumor, respectively. The left panels [Figs. 7(a), (c), (e), and (g)] are the results without data correction, and the right panels [Figs. 7(b), (d), (f), and (h)] are those with data correction. For Cases IV and IX, the estimated attenuation coefficients are higher in the cyst than in the background without data correction [Figs. 6(d) and 7(c)]; such contradictions were eliminated by correcting the attenuation data, as shown in Figs. 6(e) and 7(d), respectively.

IV. Discussion

Because of the finite elevational width of the one-dimensional linear array used in this study (5 mm), integration effects were present in the reconstruction results. Nonetheless, such effects are inherent in all tomographic imaging setups and accurate estimation of the attenuation coefficients was still achieved in this paper. Effects of the integration effects need to be evaluated further when breast ultrasound channel data are available.

The accuracy of the estimation of the attenuation coefficient is dependent on the area of the segmented ROI. To evaluate the sensitivity of the attenuation coefficient error to the ROI area, the sound velocity distributions and the attenuation coefficient distributions were estimated after the ROIs in Cases I and III had been changed artificially. Every new ROI was generated from the original ROI by adding pixels on the outer boundary or removing pixels on the inner boundary, and 10 different ROIs were randomly generated given a prespecified ROI area. Figs. 8(a) and (b) show the relations between the attenuation coefficient differences (between the new estimated attenuation coefficient and the original one in the ROI) and the ROI area difference for Cases I and III, respectively. The ROI area difference was normalized to the reference area (i.e., 4 π mm^2 and 36 π mm^2 for Cases I and III, respectively). Note that the standard deviation corresponding to the zero ROI area difference was zero because the ROI was fixed at this point and no random ROIs were generated. The results show that the estimated attenuation coefficient is more affected by the ROI area when the original ROI area is smaller. Furthermore, using the corrected attenuation data to estimate the attenuation coefficient is more sensitive to the ROI area than using the original attenuation data, which is attributable to the sound velocity error propagating to the corrected attenuation data.

The reconstructed attenuation coefficient depends on the sound velocity distribution of the same object used to estimate the refraction effects. The $\Delta\alpha^*_{\mathrm{ROI}}$ and $\Delta\alpha^*_{\mathrm{G}}$ values listed in Table II were obtained using the corrected attenuation data with the sound velocities in the ROI and the background set to those listed in Table I, and with all

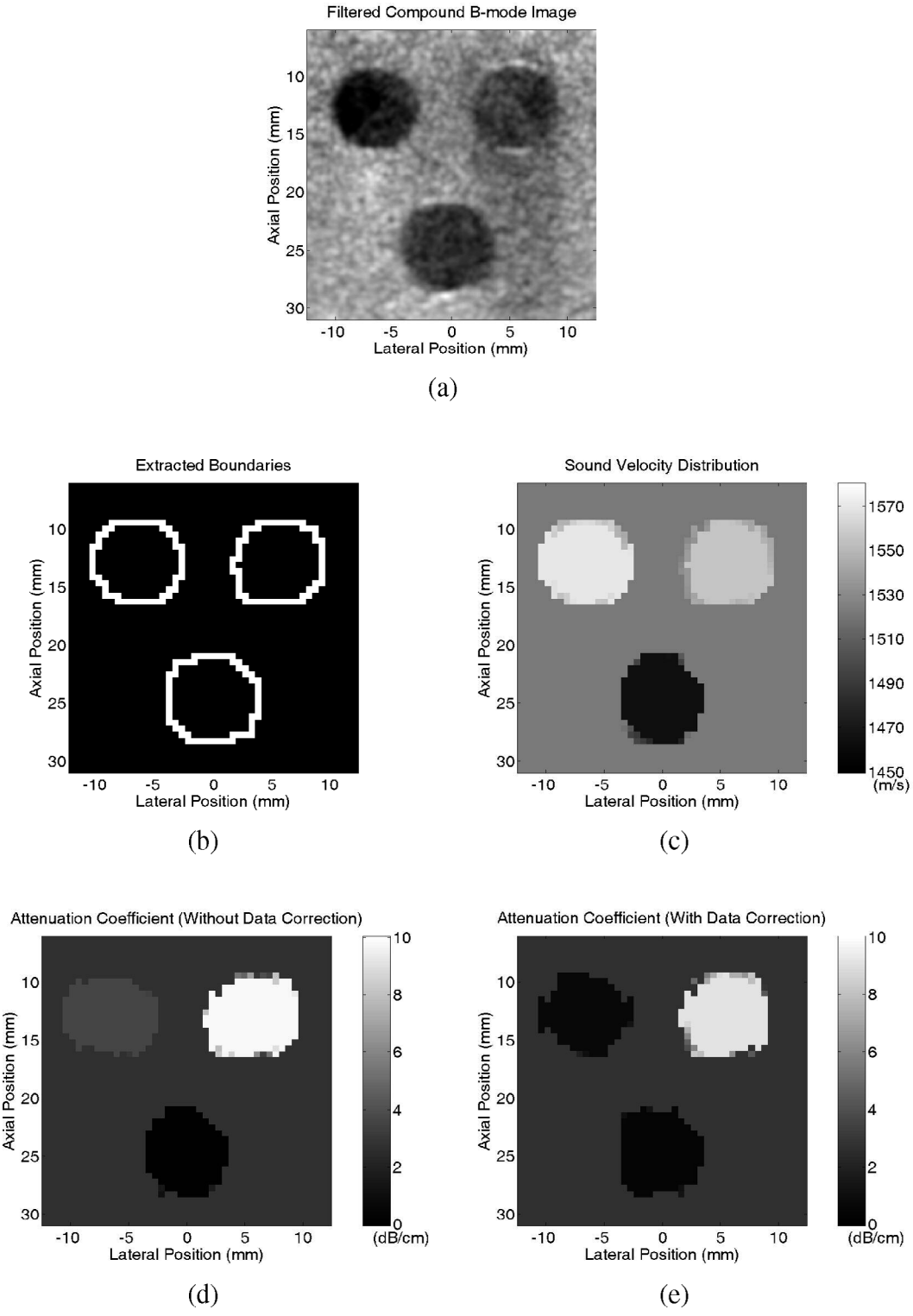

Fig. 6. Evaluation of Case IX. The image object comprises a background of glandular material ($c_{\mathrm{G}} = 1522$ m/s, $\rho_{\mathrm{G}} = 1.03$ g/cm^3, and $\alpha_{\mathrm{dB,G}} = 2.74$ dB/cm) with three spheres, all with a radius of 4 mm ($c_{\mathrm{C}} = 1570$ m/s, $\rho_{\mathrm{C}} = 1.02$ g/cm^3, and $\alpha_{\mathrm{dB,C}} = 0.78$ dB/cm in the upper-left cyst sphere; $c_{\mathrm{T}} = 1547$ m/s, $\rho_{\mathrm{T}} = 1.10$ g/cm^3, and $\alpha_{\mathrm{dB,T}} = 7.36$ dB/cm in the upper-right, high-attenuation tumor sphere; and $c_{\mathrm{F}} = 1464$ m/s, $\rho_{\mathrm{F}} = 0.94$ g/cm^3, and $\alpha_{\mathrm{dB,F}} = 2.21$ dB/cm in the lower fat sphere). (a) Filtered compound B-mode image displayed with a 30-dB dynamic range. (b) Boundaries between the three spheres and the background. (c) Reconstructed sound velocity distribution. (d) Reconstructed attenuation coefficient distribution without data correction. (e) Reconstructed attenuation coefficient distribution with data correction.

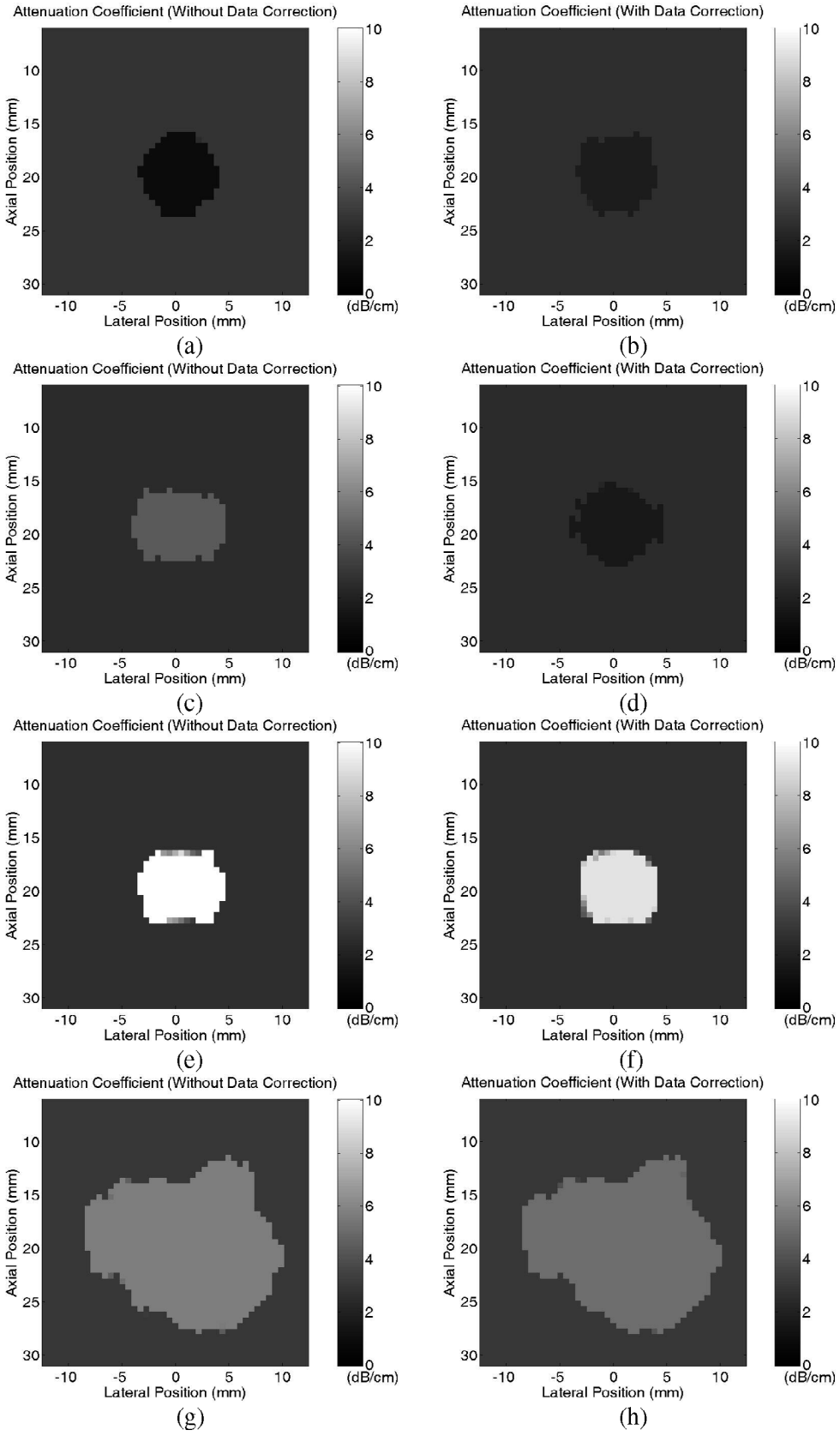

Fig. 7. Reconstructed attenuation coefficient distributions of objects containing ROIs representing different tissue types without and with data correction. (a) and (b) Case II (fat sphere with a radius of 4 mm; $c_{\mathrm{F}} = 1464$ m/s, $\rho_{\mathrm{F}} = 0.94$ g/cm^3, and $\alpha_{\mathrm{dB,F}} = 2.21$ dB/cm). (c) and (d) Case IV (cyst sphere with a radius of 4 mm; $c_{\mathrm{C}} = 1570$ m/s, $\rho_{\mathrm{C}} = 1.02$ g/cm^3, and $\alpha_{\mathrm{dB,C}} = 0.78$ dB/cm). (e) and (f) Case V (tumor sphere with a radius of 4 mm; $c_{\mathrm{T}} = 1547$ m/s, $\rho_{\mathrm{T}} = 1.10$ g/cm^3, and $\alpha_{\mathrm{dB,T}} = 7.36$ dB/cm). (g) and (h) Case VI (irregular tumor; $c_{\mathrm{IT}} = 1553$ m/s, $\rho_{\mathrm{IT}} = 1.07$ g/cm^3, and $\alpha_{\mathrm{dB,IT}} = 4.26$ dB/cm).

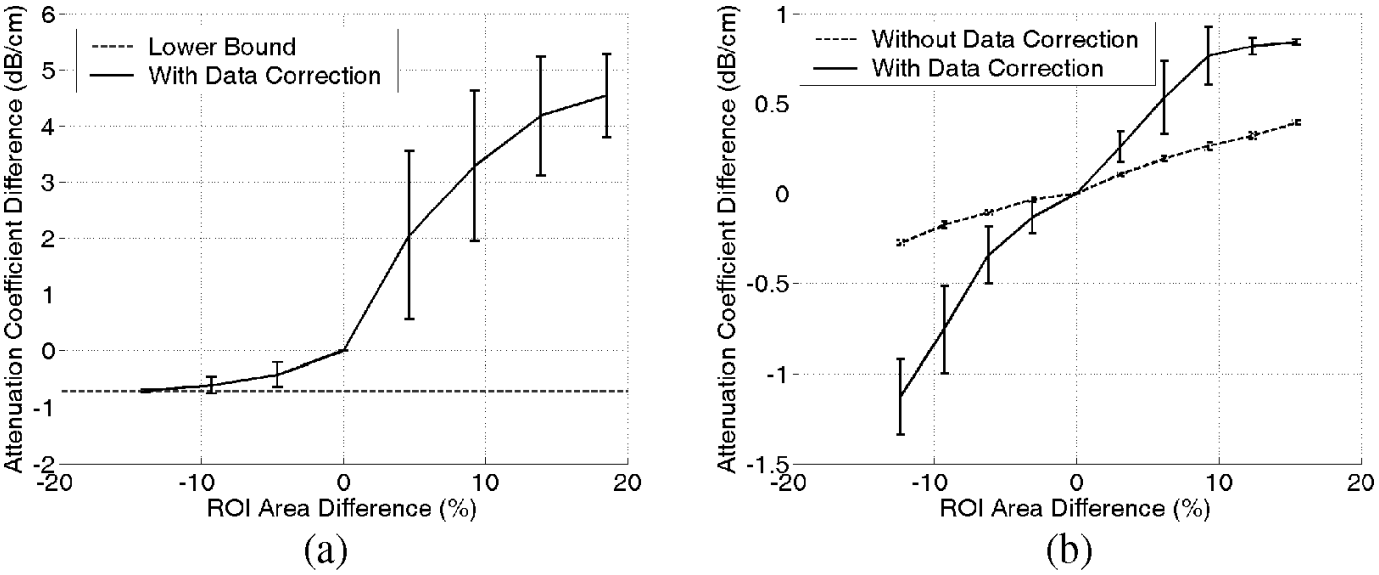

Fig. 8. The relations between the attenuation coefficient differences (between the new estimated attenuation coefficient and the original one in the ROI) and the ROI area difference in percentage. (a) Case I. (b) Case III. Ten different ROIs were randomly generated given a prespecified ROI area. The error bars denote ± one standard deviation. The horizontal dashed line shown in (a) corresponds to $\alpha_{\mathrm{dB,lower}} = 0$ dB/cm.

the sound velocities at the boundary set to their mean values. In general, using prespecified sound velocities instead of reconstructed ones to estimate the artifacts associated with refraction did not improve the results. Together with the results shown in Fig. 8, it is possible that the effectiveness of the proposed approach is closely related to the accuracy of the ROI area. Nonetheless, further studies are needed to examine this aspect.

According to Table II and Fig. 5, the reconstruction accuracy in the ROI was improved by applying the correction technique, except in Cases VII and VIII. Additional experiments on a new phantom with confirmed acoustic parameters may be required to investigate why the correction technique fails in some cases.

The results show that all $\Delta\alpha_{\mathrm{F}}$ values are negative and that all $\Delta\alpha_{\mathrm{C}}$, $\Delta\alpha_{\mathrm{T}}$, and $\Delta\alpha_{\mathrm{IT}}$ values are positive. Furthermore, $\alpha_{\mathrm{dB,F,recon}}(f_0) = 0$ dB/cm in Case I and $\alpha_{\mathrm{dB,T,recon}}(f_0) = 10$ dB/cm in Case V reached the lower bound and the upper bound for the attenuation coefficient, respectively. This is mainly attributable to refraction causing energy redistribution. The fat sphere, in which the sound velocity is lower than that in the background, tends to distribute more energy to the transmit/receive combinations with a path across the ROI; and the cyst sphere, high-attenuation tumor sphere, and the irregular tumor region produce the opposite effect because in them the sound velocity is higher than that in the background.

In the phantom study, according to the results in [11], fat regions and tumors (including high-attenuation and irregular tumors) can be successfully discriminated by applying a threshold (e.g., 1500 m/s) to the sound velocities estimated in all relevant cases. Furthermore, the approach proposed here enables discrimination of cysts and tumors by applying another threshold (e.g., 3 dB/cm in this study) to the estimated attenuation coefficients. Therefore, to improve the detection of breast cancer, B-mode image, sound velocity distribution, and attenuation coefficient distribution can be applied sequentially. When a region cannot be identified using the B-mode image, this region can be rejected as a tumor if its sound velocity is lower than a threshold; if the sound velocity in this region is higher than this threshold, the attenuation coefficient then can be used to distinguish a tumor from a cyst by setting another threshold. Note that, although it is straightforward to select thresholds in the phantom study, training data may be required for deriving the thresholds relative to those of the background in clinical situations [26].

For image objects with inhomogeneous acoustic properties such as the breast, automatic image segmentation for separating the ROIs from the background may be difficult. In this case, the reconstruction algorithm still can be applied, and the estimation result in each region is simply the average for that region. Furthermore, the automatic segmentation may be replaced with manual or semiautomatic segmentation to reduce such potential errors.

Convex programming was used to solve (16). Although several other approaches may be used—including the algebraic reconstruction techniques (ARTs) [9] and the pseudoinverse approach [13], [14]—only those capable of incorporating a priori knowledge of the image object are preferred. This is because the time-of-flight data set and the attenuation data set are incomplete [15]–[17]. Furthermore, because the data are generally inconsistent due to sound velocity inhomogeneities and measurement errors, a solution that can minimize the total violation of the data is desirable. Note that, according to the above discussion, there are two classes of constraints for the problem encountered in this study: one class contains the hard constraints associated with the a priori knowledge that should not be violated, and the other class contains the soft constraints

associated with the measurement data for which the total violation should be minimized [10], [18]. The convex programming formulation proposed in [18] is a direct approach to solving this kind of problem, and thus it was used to solve (16). Finding the projection onto a convex set is essential for convex programming, and details can be found in [23].

V. Conclusions

In this study, we experimentally evaluated an approach to estimating attenuation coefficient distributions in the breast using the tomographic imaging setup studied in [10], [11] for sound velocity reconstruction. The experimental setup comprising a 128-channel linear array, a digital array system, a phantom, and a computer allowed acoustic data acquisition for simultaneous B-mode image formation, and limited-angle tomographic sound velocity and attenuation coefficient reconstructions. Nine cases were evaluated by scanning the phantom at different positions. Application of a data-correction technique based on the angular spectrum method and the reconstructed sound velocity distribution improved the estimation accuracy in 9 of 11 ROIs. Furthermore, cysts and tumors (including high-attenuation and irregular tumors) were successfully discriminated by applying a threshold to the estimated attenuation coefficients. These results demonstrate the feasibility of using a linear-array setup compatible with a B-mode imaging setup to estimate attenuation coefficients. . . . . experiments are underway to investigate the performance of this approach in clinical situations.

Acknowledgment

The authors thank Computed Ultrasound Global, Inc., Taipei, Taiwan, for providing the digital array system.

References

[1] M. E. Lanfranchi, *Breast Ultrasound*. 2nd ed. New York: Marban Books, 2000.
[2] T. C. Telger, *Teaching Atlas of Breast Ultrasound*. New York: Thieme Medical, 1996.
[3] C.-M. Chen, Y.-H. Chou, K.-C. Han, G.-S. Hung, C.-M. Tiu, H.-J. Chiou, and S.-Y. Chiou, "Breast lesions on sonograms: Computer-aided diagnosis with nearly setting-independent features and artificial neural networks," *Radiology*, vol. 226, no. 2, pp. 504–514, 2003.
[4] A. T. Stavros, D. Thickman, C. L. Rapp, M. A. Dennis, S. H. Parker, and G. A. Sisney, "Solid breast nodules: Use of sonography to distinguish between benign and malignant lesions," *Radiology*, vol. 196, no. 1, pp. 123–134, 1995.
[5] S. A. Goss, R. L. Johnston, and F. Dunn, "Comprehensive compilation of empirical ultrasonic properties of mammalian tissues," *J. Acoust. Soc. Amer.*, vol. 64, no. 2, pp. 423–457, 1978.
[6] S. A. Goss, R. L. Johnston, and F. Dunn, "Compilation of empirical ultrasonic properties of mammalian tissues. II," *J. Acoust. Soc. Amer.*, vol. 68, no. 1, pp. 93–108, 1980.
[7] E. L. Madsen, J. A. Zagzebski, G. R. Frank, J. F. Greenleaf, and P. L. Carson, "Anthropomorphic breast phantoms for assessing ultrasonic imaging system performance and for training ultrasonographers: Part I," *J. Clin. Ultrasound*, vol. 10, no. 2, pp. 67–75, 1982.
[8] E. L. Madsen, E. Kelly-Fry, and G. R. Frank, "Anthropomorphic phantoms for assessing systems used in ultrasound imaging of the compressed breast," *Ultrasound Med. Biol.*, vol. 14, suppl. 1, pp. 183–201, 1988.
[9] A. C. Kak and M. Slaney, *Principles of Computerized Tomographic Imaging*. New York: Institute of Electrical and Electronics Engineers, 1988.
[10] S.-W. Huang and P.-C. Li, "Computed tomography sound velocity reconstruction using incomplete data," *IEEE Trans. Ultrason., Ferroelect., Freq. Contr.*, vol. 51, no. 3, pp. 329–342, 2004.
[11] S.-W. Huang and P.-C. Li, "Experimental investigation of computed tomography sound velocity reconstruction using incomplete data," *IEEE Trans. Ultrason., Ferroelect., Freq. Contr.*, vol. 51, no. 9, pp. 1072–1081, 2004.
[12] J. D. Bronzino, *The Biomedical Engineering Handbook*. 2nd ed. vol. 1, Boca Raton, FL: CRC Press, 2000.
[13] M. Krueger, A. Pesavento, and H. Ermert, "A modified time-of-flight tomography concept for ultrasonic breast imaging," in *Proc. IEEE Ultrason. Symp.*, 1996, pp. 1381–1385.
[14] M. Krueger, V. Burow, K. M. Hiltawsky, and H. Ermert, "Limited angle ultrasonic transmission tomography of the compressed female breast," in *Proc. IEEE Ultrason. Symp.*, 1998, pp. 1345–1348.
[15] P. Oskoui and H. Stark, "A comparative study of three reconstruction methods for a limited-view computer tomography problem," *IEEE Trans. Med. Imag.*, vol. 8, no. 1, pp. 43–49, 1989.
[16] K. C. Tam, J. W. Eberhard, and K. W. Mitchell, "Incomplete-data CT image reconstructions in industrial applications," *IEEE Trans. Nucl. Sci.*, vol. 37, no. 3, pp. 1490–1499, 1990.
[17] H. Stark, *Image Recovery: Theory and Application*. London: Academic, 1987.
[18] P. L. Combettes and P. Bondon, "Hard-constrained inconsistent signal feasibility problems," *IEEE Trans. Signal Processing*, vol. 47, no. 9, pp. 2460–2468, 1999.
[19] J. W. Goodman, *Introduction to Fourier Optics*. 2nd ed. New York: McGraw-Hill, 1996.
[20] M. E. Lyons and K. J. Parker, "Absorption and attenuation in soft tissues II—Experimental results," *IEEE Trans. Ultrason., Ferroelect., Freq. Contr.*, vol. 35, no. 4, pp. 511–521, 1988.
[21] Q. Zhu and B. D. Steinberg, "Wavefront amplitude distortion and image sidelobe levels: Part I—Theory and computer simulations," *IEEE Trans. Ultrason., Ferroelect., Freq. Contr.*, vol. 40, no. 6, pp. 747–753, 1993.
[22] Q. Zhu, B. D. Steinberg, and R. L. Arenson, "Wavefront amplitude distortion and image sidelobe levels: Part II—In vivo experiments," *IEEE Trans. Ultrason., Ferroelect., Freq. Contr.*, vol. 40, no. 6, pp. 754–762, 1993.
[23] H. Stark and Y. Yang, *Vector Space Projections: A Numerical Approach to Signal and Image Processing, Neural Nets, and Optics*. New York: Wiley, 1998.
[24] R. M. Lemor, P. K. Weber, P. K. Fonfara, C. Guenther, H. J. Welsch, and M. L. Hoss, "A new combined open research platform for ultrasound radio frequency signal processing," in *Proc. IEEE Ultrason. Symp.*, 2003, pp. 33–37.
[25] F. J. Harris, "On the use of windows for harmonic analysis with the discrete Fourier transform," *Proc. IEEE*, vol. 66, no. 1, pp. 51–83, 1978.
[26] J. S. Schreiman, J. J. Gisvold, J. F. Greenleaf, and R. C. Bahn, "Ultrasound transmission computed tomography of the breast," *Radiology*, vol. 150, no. 2, pp. 523–530, 1984.

Sheng-Wen Huang was born in 1971 in Changhua, Taiwan, R.O.C. He received the B.S. and Ph.D. degrees from National Taiwan University, Taipei, Taiwan, R.O.C., in 1993 and 2004, respectively, both in electrical engineering. He worked as a postdoctoral researcher at National Taiwan University from 2004 to 2005, and is currently a postdoctoral researcher with the Department of Biomedical Engineering at the University of Michigan. His current research interests include thermal strain imaging, coded excitation, and optoacoustic imaging.

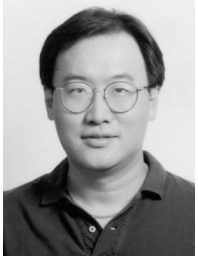

Pai-Chi Li (S'93–M'95–SM'01) received the B.S. degree in electrical engineering from National Taiwan University, Taipei, Taiwan, R.O.C., in 1987, and the M.S. and Ph.D. degrees from the University of Michigan, Ann Arbor, MI, in 1990 and 1994, respectively, both in electrical engineering: systems.

He was a research assistant with the Department of Electrical Engineering and Computer Science of the University of Michigan from 1990 to 1994. He joined Acuson Corporation, Mountain View, CA, as a member of the Technical Staff in June 1994. His work with Acuson was primarily in the areas of medical ultrasonic imaging system design for both cardiology and general imaging applications. In August 1997, he went back to the Department of Electrical Engineering at National Taiwan University, where he is currently a full professor. His current research interests include biomedical ultrasonic imaging and signal processing.

Dr. Li is a senior member of IEEE and Associate Editor of *IEEE Transactions on Ultrasonics, Ferroelectrics, and Frequency Control*. He is also on the Editorial Board of *Ultrasonic Imaging*. He received the 2004 Distinguished Research Award, National Science Council, the 2004 Distinguished Research Achievement Award, National Taiwan University, the 2003 Outstanding Researcher Award, National Taiwan University, the 2002 Dr. Wu Dayou Research Award from National Science Council, the 2002 Outstanding Young Electrical Engineer Award from Chinese Institute of Electrical Engineering and the Distinguished Industrial Collaboration Award of Ministry of Education. He was also the recipient of the Distinguished Achievement Award in Electrical Engineering: Systems in 1994 for his outstanding academic achievement at the University of Michigan.

Arbitrary Waveform Coded Excitation Using Bipolar Square Wave Pulsers in Medical Ultrasound

Sheng-Wen Huang and Pai-Chi Li, *Senior Member, IEEE*

***Abstract*—This paper presents a new coded excitation scheme that efficiently synthesizes codes for arbitrary waveforms using a bipolar square wave pulser. In a coded excitation system, pulse compression is performed to restore the axial resolution. In order to maintain low range sidelobes, the system needs to transmit signals that have smooth spectra. However, such a transmitter requires the generation of arbitrary waveforms and, therefore, is more expensive. In other words, a trade-off is necessary between the compression performance and the transmitter cost. Here we propose a method that preserves the low-cost advantage of a bipolar pulser while achieving approximately the same compression performance as an arbitrary waveform generator. The key idea of the proposed method is the conversion of a nonbinary code (i.e., requiring an arbitrary waveform generator) with good compression performance into a binary code (i.e., requiring only a bipolar pulser) by code translation and code tuning. The code translation is implemented by sending the nonbinary code into a virtual one-bit, sigma-delta modulator, and the code tuning involves minimizing the root-mean-square error between the resultant binary code and the original nonbinary code by sequential and iterative tuning while taking the transducer response into account. Tukey-windowed chirps are known to have good compression performance. Such chirps of different durations (16, 20, and 24 μs), all with a taper ratio of 0.15, a center frequency of 2.5 MHz, and an equivalent bandwidth of 1.5 MHz, were converted into binary Tukey-windowed chirps that were compared with pseudochirps (i.e., direct binary approximations of the original chirp) over the same spectral band. The bit rate was 40 MHz. Simulation results show that the use of binary Tukey-windowed chirps can reduce the code duration by 20.6% or the peak sidelobe level by 6 dB compared to the commonly used pseudochirps. Experimental results obtained under the same settings were in agreement with the simulations. Our results demonstrate that arbitrary waveform coded excitation can be realized using bipolar square wave pulsers for applications in medical ultrasound.**

I. Introduction

Coded excitation has been studied for many years in medical ultrasound [1]–[15]. It is primarily used to either improve the signal-to-noise ratio (SNR) without increasing the excitation voltage or lower the excitation voltage without sacrificing the SNR [1]–[4]. Other applications of coded excitation include increasing the frame rate and improving resolution [5], enhancing the detection of contrast agent [6], increasing the depth of field [7], improving the SNR in finite amplitude distortion based harmonic imaging [8], enhancing the generation of harmonics by contrast agent microbubbles [9], [10], and suppressing selected harmonic components in nonlinear imaging [11].

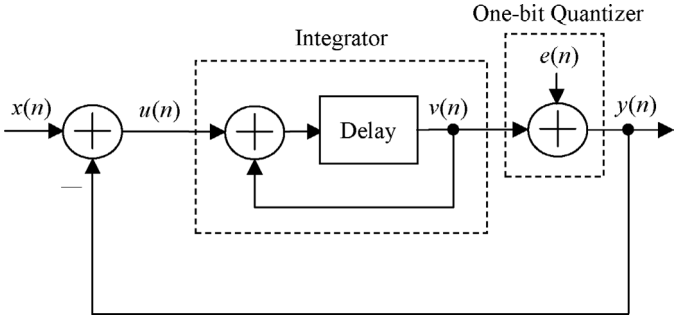

Fig. 1. Block diagram of the first-order, one-bit, sigma-delta modulator.

In this paper, coded excitation is treated as an approach to improving the SNR under the condition of a fixed peak acoustic power. In a coded excitation system, a wide transmit bandwidth is maintained while the transmit pulse length is increased. Thus, the axial resolution can be restored at the receiver by means of pulse compression. If multiple firings along the same direction are allowed, the use of (orthogonal) Golay coded excitation [3] makes pulse compression straightforward, in which case the axial sidelobes after pulse compression are eliminated by filtering and by cancellation in the coherent sum of the received signals corresponding to different firings. However, pulse compression becomes more challenging when only single firing is allowed for each beam direction because only filtering can be used to restore the axial resolution. In this paper, we only consider the single-firing case.

The performance of pulse compression generally is characterized by the mainlobe width (related to the axial resolution), the sidelobe level (related to the dynamic range and contrast resolution), and the SNR improvement. Given a code, once the filter length is fixed, the more stringent the constraints [such as the mainlobe width or the peak sidelobe level (PSL)] imposed on the compression results, the lower the output SNR is. Furthermore, the filter

Manuscript received June 1, 2004; accepted June 24, 2005. Partial support from the National Science Council of R.O.C. under Grant NSC 94-2213-E-002-031 and from National Health Research Institutes of R.O.C. is gratefully acknowledged.

The authors are with the Department of Electrical Engineering, National Taiwan University, and the Division of Medical Engineering Research, National Health Research Institutes, Taipei, Taiwan (e-mail: paichi@cc.ee.ntu.edu.tw).

must be extended when the constraints cannot be satisfied. Therefore, the code must be properly designed to meet the system requirements.

Achieving optimal pulse compression performance requires the ability to generate an arbitrary transmit waveform in order to realize the desired spectral characteristics. However, an arbitrary waveform generator is expensive. Here we propose a method that preserves the low-cost advantage of a bipolar pulser while achieving compression performance similar to that of an arbitrary waveform generator. The key idea of the proposed method is the conversion of a nonbinary code into a binary code by code translation and code tuning. The code translation is implemented by sending the nonbinary code into a virtual one-bit sigma-delta modulator, and the code tuning involves minimizing the root-mean-square error between the resultant binary code and the original nonbinary code by sequential and iterative tuning using the output of the sigma-delta modulator as the initial condition while taking the transducer response into account. It is shown that good compression performance can be achieved by using the converted binary code instead of the original code. Hence, the proposed method can be used to effectively realize arbitrary waveform coded excitation with bipolar pulsers.

This paper is organized as follows. Section II describes the method used to translate an arbitrary code into a binary code, and the method used to tune the binary code. Section III introduces the formulas for designing the compression filter. Section IV demonstrates the efficacy of the proposed method using simulations and experimental data. Section V discusses characteristics, applications, and extensions of the proposed method, and the paper concludes in Section VI.

II. Code Conversion

The overall goal of code conversion is to convert a nonbinary code into a binary code that exhibits similar compression performance. A two-step method was developed to achieve this goal. The first step uses a sigma-delta modulator to translate the nonbinary code into a temporary binary code. Section II-C shows that this temporary code only exhibits acceptable compression performance when the bit rate is excessively high; hence, a second step is needed. The algorithm introduced in Section II-D is used as the second step to tune the temporary code into a new code that has improved compression performance.

A. Sigma-Delta Modulation

Let $x(t)$ be a band-limited, continuous time signal and $x(n)$ be its corresponding discrete time signal uniformly sampled at f_s:

$$x(n) = x(t)\big|_{t=n/f_s}. \tag{1}$$

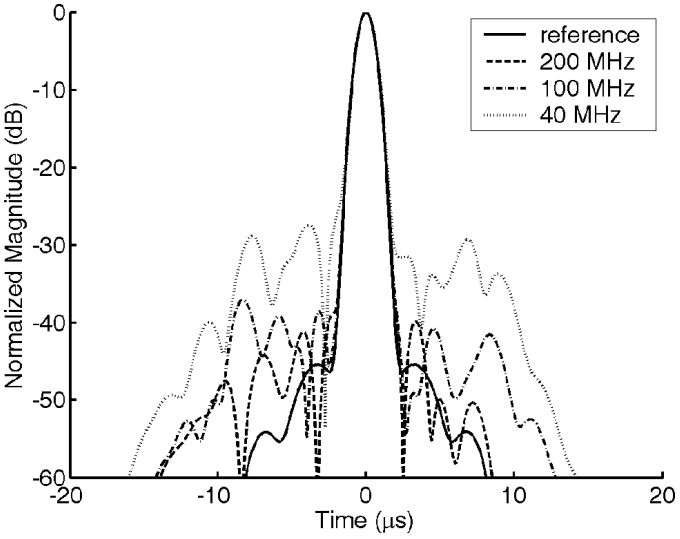

Fig. 2. Normalized envelopes of $x_c(t)$, and $y_c(t; f_s)$ for $f_s = 40$, 100, and 200 MHz.

In this paper, t denotes the time, and the letters n, k, p, q, and l within parentheses denote discrete time indices.

Fig. 1 shows a block diagram of a first-order, one-bit sigma-delta modulator [16], where $e(n)$ is the quantization error. Note that the entire system is in the discrete domain because the modulator is used only for discrete code translation (and not analog-to-digital conversion). Without loss of generality, assume that the input signal $x(n)$ is bounded by $\pm V$ and that the output signal $y(n)$ is within $\{+1, -1\}$. The quantizer will not be overloaded if $V = 1$ and $|v(0)| \le 2$, (i.e., $|e(n)| \le 1$ for all $n \ge 0$). Based on Fig. 1:

$$v(n) = y(n) - e(n), \tag{2}$$

$$\begin{aligned} v(n) &= u(n-1) + v(n-1) \\ &= [x(n-1) - y(n-1)] + [y(n-1) - e(n-1)] \\ &= x(n-1) - e(n-1). \end{aligned} \tag{3}$$

Thus:

$$y(n) = x(n-1) + e(n) - e(n-1). \tag{4}$$

If f_s is much higher than the bandwidth of $x(n)$, $x(n)$ can be efficiently reconstructed by appropriately filtering $y(n)$.

B. Code Translation

Let $x(t)$ be the desired band-limited waveform for coded excitation. The goal is to build a binary version of the original code such that, after being filtered by the transducer, the filtered binary waveform is similar to the filtered version of the original code. In other words, the transducer's frequency response is used as the reconstruction filter in a sigma-delta modulator. We first choose a sampling frequency f_s and discretize $x(t)$ into $x(n)$, then send the sequence $x(n)$ into the sigma-delta modulator shown in Fig. 1. The output signal $y(n)$ of the modulator is the

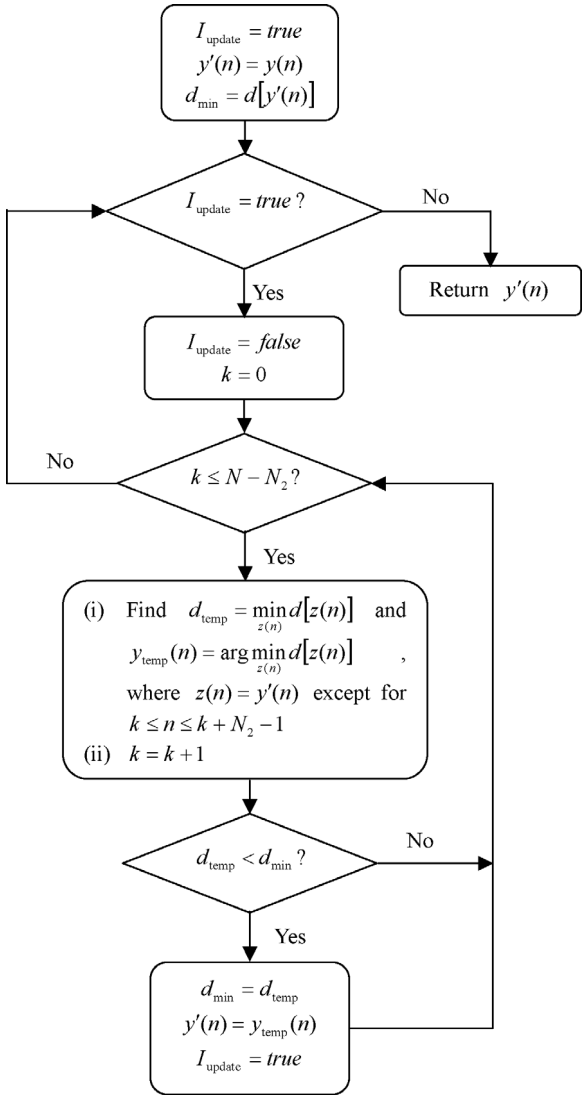

Fig. 3. Flow diagram for code tuning.

corresponding binary code of $x(t)$ with a bit rate of f_s, and the actual transmitted signal is:

$$y(t;\, f_s) = \sum_n y(n+1)\Pi(f_s t - n), \tag{5}$$

where:

$$\Pi(t) = \begin{cases} 1 & \text{if } 0 \le t \le 1 \\ 0 & \text{otherwise} \end{cases}. \tag{6}$$

C. Preliminary Evaluation

Let $h_t(t)$ be the impulse response of the transducer and $\otimes$ denote convolution. Because $h_t(t)$ can be viewed as the reconstruction filter for the sigma-delta modulator, a higher f_s is desired such that $y(t;\, f_s) \otimes h_t(t)$ is approximately the same as $x(t) \otimes h_t(t)$. However, f_s is also the bit rate of the binary code and must be within a certain range due to hardware limitations of the bipolar pulser.

The effects of the bit rate on pulse compression are illustrated using a Tukey-windowed chirp [12] as an example. Specifically:

$$x(t) = w_T(t;r)\sin\left\{2\pi\left[\left(f_0 - \frac{\Delta f}{2}\right)t + \frac{\alpha}{2}t^2\right]\right\},\ 0 \le t \le T, \tag{7}$$

where f_0 is the carrier frequency, Δf is the bandwidth of the linear chirp, T is the pulse duration, α is the slope of the linear chirp (i.e., $\alpha = \Delta f/T$), and:

$$w_T(t;r) = \begin{cases} \sin^2\left(\dfrac{\pi t}{rT}\right) & 0 \le t < \dfrac{rT}{2} \\ 1 & \dfrac{rT}{2} \le t \le T - \dfrac{rT}{2} \\ \sin^2\left[\dfrac{\pi(T-t)}{rT}\right] & T - \dfrac{rT}{2} < t \le T \\ 0 & \text{elsewhere} \end{cases}, \tag{8}$$

is a Tukey window with a taper ratio of r. The compression filter $h_c(t)$ is chosen to be a windowed matched filter:

$$h_c(t) = w_C(t) \cdot \sin\left\{2\pi\left[\left(f_0 - \frac{\Delta f}{2}\right)(T-t) + \frac{\alpha}{2}(T-t)^2\right]\right\},\ 0 \le t \le T, \tag{9}$$

where $w_C(t)$ is a Chebyshev window with a sidelobe attenuation of -90 dB. The signal:

$$x_c(t) = x(t) \otimes h_t(t) \otimes h_t(t) \otimes h_c(t), \tag{10}$$

is the ideal pulse-echo compressed signal and is used as a reference to evaluate the pulse-echo compression results at different bit rates:

$$y_c(t;\, f_s) = y(t;\, f_s) \otimes h_t(t) \otimes h_t(t) \otimes h_c(t). \tag{11}$$

Let $f_0 = 2.5$ MHz, $\Delta f = 1.85$ MHz, $T = 20\ \mu$s, $r = 0.3$, and the transducer have a Gaussian frequency response with a center frequency of f_0 and a -6 dB bandwidth of 1.5 MHz. Fig. 2 shows the normalized envelopes of $x_c(t)$ (solid line) and $y_c(t;\, f_s)$ for $f_s = 40$, 100, and 200 MHz (dotted line, dash-dotted line, and dashed line, respectively). Fig. 2 demonstrates that $y(t;\, f_s)$ with a higher f_s has lower axial sidelobes after compression.

D. Code Tuning

Fig. 2 shows that the PSL exceeds -30 dB with a bit rate of 40 MHz, and that a rate of 200 MHz is needed to suppress the PSL to the -40 dB level. Such a high bit rate is not acceptable in most systems. In addition to the filtering approach commonly used in the literature [1], [13], tuning of the output code $y(n)$ of the sigma-delta modulator is performed in this study to further improve the compression results.

The algorithm for tuning an N-bit code $y(n)$, $0 \le n \le N-1$, into a new code $y'(n)$ is illustrated using the flow diagram shown in Fig. 3. We define:

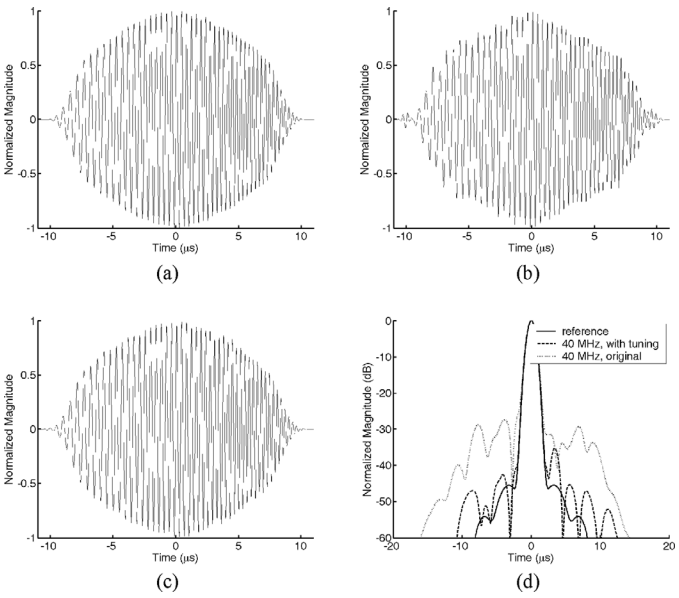

Fig. 4. (a) $x(t) \otimes h_{\mathrm{t}}(t)$. (b) $y(t;\ 40\ \mathrm{MHz}) \otimes h_{\mathrm{t}}(t)$. (c) $y'(t;\ 40\ \mathrm{MHz}) \otimes h_{\mathrm{t}}(t)$. (d) Normalized envelopes of $x_{\mathrm{c}}(t)$ (solid line), $y_{\mathrm{c}}(t;\ 40\ \mathrm{MHz})$ (dotted line), and $y'_{\mathrm{c}}(t;\ 40\ \mathrm{MHz})$ (dashed line).

$$d[y(n)] = \|[y\,(t;\ f_{\mathrm{s}}) - x(t)] \otimes h_{\mathrm{t}}(t)\|\,, \tag{12}$$

where $\|\cdot\|$ denotes the L^2 norm; then $d[y(n)]$ is a measure of the similarity between $y\,(t;\ f_{\mathrm{s}})$ and $x(t)$. If $y(n)$ is tuned into a code $y_{\mathrm{temp},1}(n)$ such that $d\,[y_{\mathrm{temp},1}(n)] < d\,[y(n)]$, $y_{\mathrm{temp},1}(n)$ is considered better than $y(n)$ and will be the current candidate for the final code $y'(n)$. If a code $y_{\mathrm{temp},2}(n)$ generated by tuning $y_{\mathrm{temp},1}(n)$ satisfies $d\,[y_{\mathrm{temp},2}(n)] < d\,[y_{\mathrm{temp},1}(n)]$, $y_{\mathrm{temp},2}(n)$ will become the new candidate for $y'(n)$. The process continues until the candidate code cannot be further updated. In this algorithm, any new candidate for $y'(n)$ is different from the current candidate in at most N_2 ($N_2 = 16$ in this paper) consecutive bits, and the start index of the 16 bits is shifted sequentially and iteratively until the similarity to $x(n)$ cannot be further improved.

Figs. 4(a)–(c) show $x(t) \otimes h_{\mathrm{t}}(t)$, $y(t;\ 40\ \mathrm{MHz}) \otimes h_{\mathrm{t}}(t)$, and $y'(t;\ 40\ \mathrm{MHz}) \otimes h_{\mathrm{t}}(t)$, respectively. The parameters are the same as those used in Section II-C. Fig. 4(d) shows the normalized envelopes of $x_{\mathrm{c}}(t)$ (solid line), $y_{\mathrm{c}}(t;\ 40\ \mathrm{MHz})$ (dotted line), and $y'_{\mathrm{c}}(t;\ 40\ \mathrm{MHz})$ (dashed line). Fig. 4 demonstrates that tuning a code can significantly improve the compression performance.

III. Design of the Compression Filter

This section presents the design principles of the compression filter. In this paper, pulse compression is realized at baseband. Assume that the digitized echo signal is:

$$y'_{\mathrm{rf}}(n) = \left[y'\,(t;\ f_{\mathrm{s}}) \otimes h_{\mathrm{t}}(t) \otimes h_{\mathrm{t}}(t)\right]_{t=n/f_{\mathrm{s,ADC}}}\,, \tag{13}$$

where $f_{\mathrm{s,ADC}}$ is the sampling rate of the analog-to-digital converter (ADC) at the receiver. The $y'_{\mathrm{rf}}(n)$ is demodulated into a baseband signal:

$$y'_{\mathrm{bb}}(n) = h_{\mathrm{K}}(n) \otimes \left[y'_{\mathrm{rf}}(n) \cdot \exp\left(-j2\pi f_0 n/f_{\mathrm{s,ADC}}\right)\right], \tag{14}$$

where $h_{\mathrm{K}}(n)$ is a Kaiser-windowed, finite impulse response low-pass filter [17], i.e.:

$$h_{\mathrm{K}}(n) = \frac{\sin 2\pi f_{\mathrm{c}}(n - M/2)}{\pi(n - M/2)} \cdot \frac{I_0\left[\beta\left(1 - \left[(n - M/2)/(M/2)\right]^2\right)^{1/2}\right]}{I_0(\beta)},\ 0 \le n \le M, \tag{15}$$

where $I_0(\cdot)$ represents the zeroth-order modified Bessel function of the first kind, f_{c} is the -6 dB cutoff frequency, $(M+1)$ is the filter length, and β is a shape parameter. The $y'_{\mathrm{bb}}[n]$ is then D times downsampled to obtain:

$$y'_{\mathrm{d}}(n) = y'_{\mathrm{bb}}(Dn). \tag{16}$$

Given a compression filter $h_{\mathrm{d,c}}(n)$, the compressed signal is:

$$y'_{\mathrm{d,c}}(n) = y'_{\mathrm{d}}(n) \otimes h_{\mathrm{d,c}}(n). \tag{17}$$

Let $n_{\mathrm{d}}(n)$ and $n_{\mathrm{d,c}}(n)$ denote the noise after downsampling and compression, respectively, and define the autocorrelation function of a random process $s(n)$ as:

$$R_s(k) = E\left\{s(n)s^*(n-k)\right\}, \tag{18}$$

where the asterisk denotes complex conjugation and E denotes the statistical expectation operator; then [18]:

$$R_{n_{\mathrm{d,c}}}(k) = R_{n_{\mathrm{d}}}(k) \otimes h_{\mathrm{d,c}}(k) \otimes h^*_{\mathrm{d,c}}(-k), \tag{19}$$

and the ensemble-averaged noise power after pulse compression is $R_{n_{\mathrm{d,c}}}(0)$. If the peak of the compressed signal is normalized to unity by scaling the filter coefficients, the inverse of $R_{n_{\mathrm{d,c}}}(0)$ is the output SNR.

Let m denote the index of the peak position of $y'_{\mathrm{d,c}}(n)$, I_{sl} denote the index set of the sidelobes, s specifies the predetermined allowable PSL, and $s_{\mathrm{dB}} = 20\log s$. The goal is to find a compression filter $h'_{\mathrm{o}}(n)$ such that $R_{n_{\mathrm{d,c}}}(0)$ is minimized under the constraints of $y'_{\mathrm{d,c}}(m) = 1$ and $\left|y'_{\mathrm{d,c}}(n)\right| \le s$ for $n \in I_{\mathrm{sl}}$ [i.e., $h'_{\mathrm{o}}(n)$ maximizes the output SNR while maintaining the axial resolution and dynamic range specified by I_{sl} and s, respectively]. Unfortunately, this problem cannot be solved systematically, so the above formulation is slightly modified to the following: find the optimal compression filter $h_{\mathrm{o}}(n)$ resulting in the minimal $R_{n_{\mathrm{d,c}}}(0)$ under the constraints of $y'_{\mathrm{d,c}}(m) = 1$, and $\left|\mathrm{Re}\left\{y'_{\mathrm{d,c}}(n)\right\}\right|$, $\left|\mathrm{Im}\left\{y'_{\mathrm{d,c}}(n)\right\}\right| \le s/\sqrt{2}$ for $n \in I_{\mathrm{sl}}$, where

$\mathrm{Re}\{\cdot\}$ and $\mathrm{Im}\{\cdot\}$ denote the real part and the imaginary part, respectively. That is:

$$h_{\mathrm{o}}(n) = \arg\min_{h_{\mathrm{d,c}}} R_{n_{\mathrm{d,c}}}(0) \text{ subject to}$$
$$\begin{cases} y'_{\mathrm{d,c}}(m) = 1 \\ \left|\mathrm{Re}\left\{y'_{\mathrm{d,c}}(n)\right\}\right| \le s/\sqrt{2} & \text{for } n \in I_{\mathrm{sl}} \\ \left|\mathrm{Im}\left\{y'_{\mathrm{d,c}}(n)\right\}\right| \le s/\sqrt{2} & \text{for } n \in I_{\mathrm{sl}} \end{cases}. \quad (20)$$

The solution of (20) (given a filter length N_{f}) is provided in the Appendix, where it is shown that this is a quadratic programming problem. Furthermore, it can be shown that, if the constraints can be satisfied using a filter length of N_{f}, the optimal compression filter is unique and can be found.

IV. Performance of the Proposed Method

In this section, the method introduced in Section II is applied and compared with the pseudochirp approach proposed in [1]. The pseudochirp is the binary version of the original chirp signal that also can be implemented using a bipolar square wave pulser. All codes operate at a sampling frequency (or bit rate) of 40 MHz. The mainlobe is defined as the central nine points of the compressed signal, with the rest of the signal being defined as the sidelobe region.

A. Simulation Results

In the simulations, the additive noise sampled by the ADC was assumed to be a white noise $n_{\mathrm{w}}(n)$ with a variance of σ_{w}^2. Therefore:

$$n_{\mathrm{d}}(n) = \{h_{\mathrm{K}}(l) \otimes [n_{\mathrm{w}}(l) \cdot \exp(-j2\pi f_0 l/f_{\mathrm{s,ADC}})]\}\big|_{l=Dn}, \quad (21)$$

and (22) (see next page). Note that $R_{n_{\mathrm{w}}}(k) = \sigma_{\mathrm{w}}^2\delta(k)$, where $\delta(k)$ is a discrete-time impulse [17].

A chirp $x_{\mathrm{cp}}(n)$ with a duration of T and a sampling frequency of f_{s} can be defined as:

$$x_{\mathrm{cp}}(n) = \sin\left\{2\pi\left[\left(f_0 - \frac{\Delta f}{2}\right)\frac{n}{f_{\mathrm{s}}} + \frac{\alpha}{2}\left(\frac{n}{f_{\mathrm{s}}}\right)^2\right]\right\}, \quad 0 \le n \le N-1, \quad (23)$$

where $N = f_{\mathrm{s}}T$, and its corresponding pseudochirp $z_{\mathrm{pc}}(n)$ is defined by:

$$z_{\mathrm{pc}}(n) = \begin{cases} 1 & \text{if } x_{\mathrm{cp}}(n) \ge 0 \\ -1 & \text{otherwise} \end{cases}. \quad (24)$$

The following pseudochirp signal was used to evaluate its performance in SNR enhancement:

$$z_{\mathrm{pc}}(t;\, f_{\mathrm{s}}) = \sum_n z_{\mathrm{pc}}(n)\Pi(f_{\mathrm{s}}t - n). \quad (25)$$

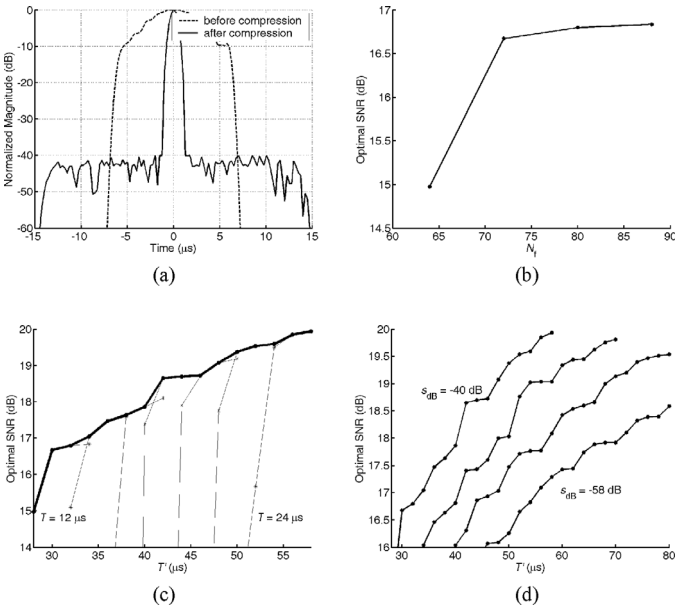

Fig. 5. (a) The demodulated and downsampled pseudochirp with $T = 12$ μs (dashed line) and the compressed signal corresponding to $N_{\mathrm{f}} = 64$ and $s_{\mathrm{dB}} = -40$ dB (solid line). (b) The curve of optimal SNR versus N_{f} corresponding to $s_{\mathrm{dB}} = -40$ dB for the pseudochirp with $T = 12$ μs. (c) The curves of optimal SNR versus T' corresponding to $s_{\mathrm{dB}} = -40$ dB for the pseudochirps with $T = 12$ μs to 24 μs with a step of 2 μs. The characteristic curve of the pseudochirp corresponding to $s_{\mathrm{dB}} = -40$ dB also is shown here as a thick solid line. (d) The characteristic curves of pseudochirps corresponding to $s_{\mathrm{dB}} = -40$ dB to -58 dB with a step of -6 dB.

The transducer was assumed to have a Gaussian frequency response with a center frequency of 2.5 MHz and a -6 dB bandwidth of 1.5 MHz. The other parameters were $f_{\mathrm{s,ADC}} = 20$ MHz, $M = 18$, $\beta = 3.7$, $f_{\mathrm{c}} = 0.1125$, $D = 5$ (i.e., corresponding to a sampling rate after downsampling, $f_{\mathrm{s,d}}$, of 4 MHz), $\sigma_{\mathrm{w}}^2 = 1$, $f_0 = 2.5$ MHz, and $\Delta f = 1.5$ MHz. Fig. 5(a) shows the downsampled baseband signal $z_{\mathrm{pc,d}}(n)$ for $T = 12$ μs (dashed line) and the compressed signal $z_{\mathrm{pc,d,c}}(n)$ corresponding to $N_{\mathrm{f}} = 64$ and $s_{\mathrm{dB}} = -40$ dB (solid line). The optimal SNR, which corresponds to the minimal $R_{n_{\mathrm{d,c}}}(0)$ in (20), is 15.0 dB. Fig. 5(b) is a plot of the optimal SNR versus N_{f} corresponding to $s_{\mathrm{dB}} = -40$ dB and $T = 12$ μs. Fig. 5(b) shows that the optimal SNR increases with N_{f}.

Define $T' = (T + N_{\mathrm{f}}/f_{\mathrm{s,d}})$ as the total temporal duration of the compressed signal. The performance of a code is determined by the optimal SNR, assuming T' and s_{dB} are fixed. Plots of the optimal SNR versus T' corresponding to $s_{\mathrm{dB}} = -40$ dB and $T = 12$ μs to 24 μs with a step of 2 μs are shown in Fig. 5(c) for the pseudochirps. At a given T', the maximum of the optimal SNRs corresponding to various T values are found. A curve connecting such points also is shown in Fig. 5(c) as a thick solid line. This curve is called the characteristic curve of the pseudochirp at $s_{\mathrm{dB}} = -40$ dB. In this format, a code with a (vertically) higher curve outperforms a code with a lower curve. Four characteristic curves of pseudochirps corresponding to $s_{\mathrm{dB}} = -40$ dB to -58 dB with a step of -6 dB are

$$
\begin{aligned}
R_{n_{\mathrm{d}}}(k) &= E\Bigg\{ \sum_{p} h_{\mathrm{K}}(p) n_{\mathrm{w}}(Dn-p) \exp\left[-j2\pi f_0 (Dn-p)/f_{\mathrm{s,ADC}}\right] \cdot \\
&\qquad \sum_{q} h_{\mathrm{K}}^{*}(q) n_{\mathrm{w}}^{*}(Dn-Dk-q) \exp\left[j2\pi f_0 (Dn-Dk-q)/f_{\mathrm{s,ADC}}\right] \Bigg\} \\
&= \sum_{p,q} h_{\mathrm{K}}(p) h_{\mathrm{K}}^{*}(q) \exp\left[-j2\pi f_0 (Dk-p+q)/f_{\mathrm{s,ADC}}\right] \cdot \\
&\quad E\left\{ n_{\mathrm{w}}(Dn-p) n_{\mathrm{w}}^{*}(Dn-Dk-q) \right\} \\
&= \sum_{p,q} h_{\mathrm{K}}(p) h_{\mathrm{K}}^{*}(q) \exp\left[-j2\pi f_0 (Dk-p+q)/f_{\mathrm{s,ADC}}\right] R_{n_{\mathrm{w}}}(Dk-p+q) \\
&= \sigma_{\mathrm{w}}^{2} \sum_{q} h_K(Dk+q) h_{\mathrm{K}}^{*}(q) = \sigma_{\mathrm{w}}^{2} \cdot \left[h_{\mathrm{K}}(l) \otimes h_{\mathrm{K}}^{*}(-l) \right]_{l=Dk} .
\end{aligned}
\tag{22}
$$

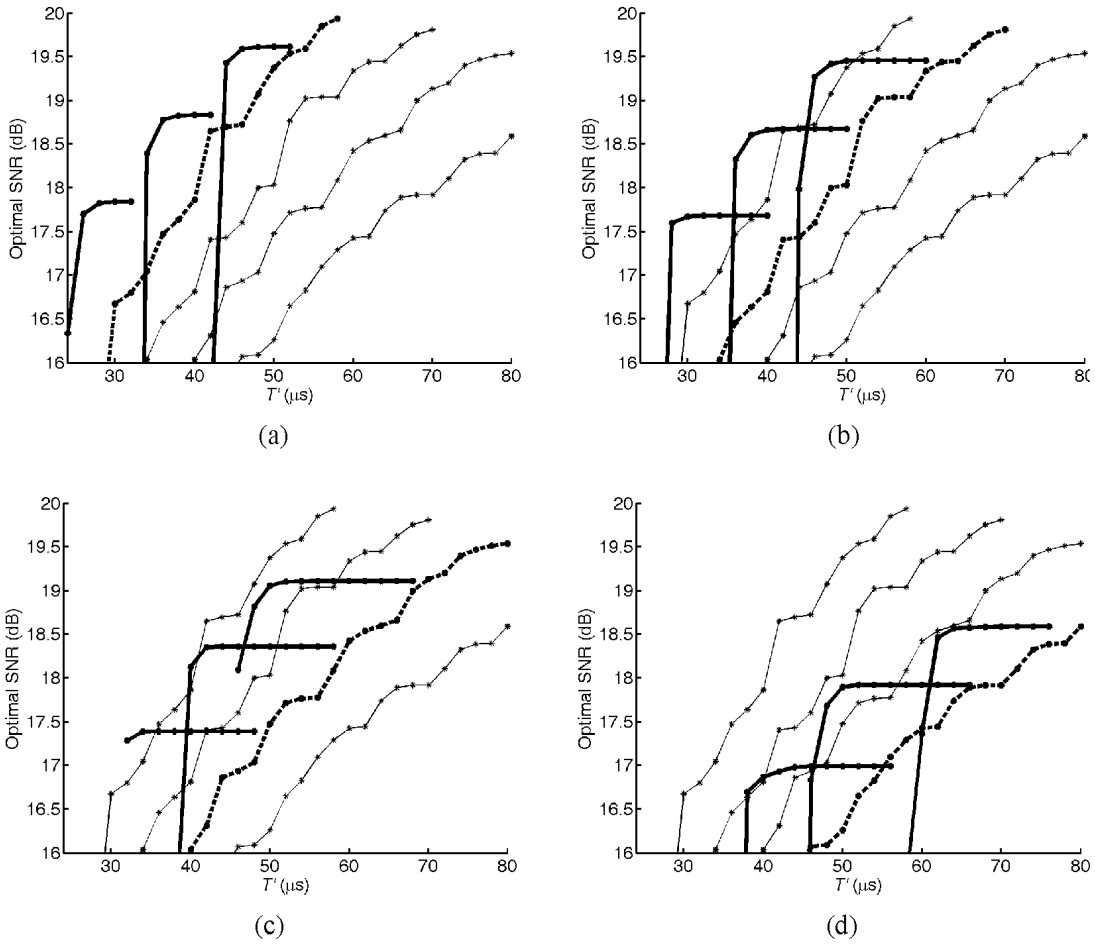

Fig. 6. The curves of optimal SNR versus T' for binary Tukey-windowed chirps generated by simulations. (a) $s_{\mathrm{dB}} = -40$ dB. (b) $s_{\mathrm{dB}} = -46$ dB. (c) $s_{dB} = -52$ dB. (d) $s_{\mathrm{dB}} = -58$ dB. In each panel, the curves corresponding to three binary Tukey-windowed chirps are shown from top to bottom as thick solid lines: $y'_{\mathrm{bTc}}(n;\ 24\ \mu\mathrm{s})$, $y'_{\mathrm{bTc}}(n;\ 20\ \mu\mathrm{s})$, and $y'_{\mathrm{bTc}}(n;\ 16\ \mu\mathrm{s})$. Also shown in each panel are the characteristic curves of pseudochirps for comparison. The characteristic curve corresponding to the same PSL is shown as a thick dashed line; the others are shown as thin solid lines.

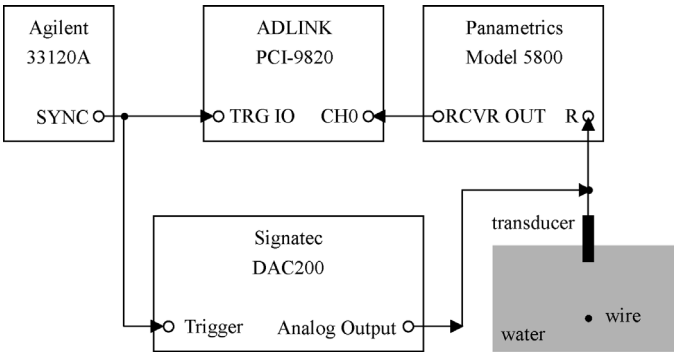

Fig. 7. Block diagram of the experimental setup.

shown in Fig. 5(d). These curves were subsequently used to evaluate the performance of the binary Tukey-windowed chirps.

Tukey-windowed chirps [defined in (7) and denoted by $x_{\mathrm{Tc}}(t;\, T)$] were converted into binary Tukey-windowed chirps [denoted by $y'_{\mathrm{bTc}}(n;\, T)$] using the method presented in Section II. All Tukey-windowed chirps had $f_0 = 2.5$ MHz, $\Delta f = 1.625$ MHz, and $r = 0.15$. With these settings, the -12 dB bandwidths of a Tukey-windowed chirp and a pseudochirp with $f_0 = 2.5$ MHz and $\Delta f = 1.5$ MHz are the same. Because $|x_{\mathrm{Tc}}(t;\, T)| \leq 1$, overloading did not occur in the sigma-delta modulator. To make the spatial-peak-pulse-average intensity [1] associated with the binary Tukey-windowed chirp the same as that associated with the pseudochirp, the transmitted signal was scaled according to:

$$y''_{\mathrm{bTc}}(t;\, T) = \frac{4}{\pi} y'_{\mathrm{bTc}}(t;\, T). \tag{26}$$

The factor $4/\pi$ is the magnitude of the fundamental frequency of a periodic square wave with an amplitude of 1. Other parameters were $f_{\mathrm{s,ADC}} = 20$ MHz, $M = 18$, $\beta = 3.7$, $f_{\mathrm{c}} = 0.1125$, $D = 5$, and $\sigma_{\mathrm{w}}^2 = 1$.

Figs. 6(a)–(d) are plots of the optimal SNR versus T' for binary Tukey-windowed chirps corresponding to $s_{\mathrm{dB}} = -40$ dB to -58 dB with a step of -6 dB, respectively. In each figure panel, the curves corresponding to three binary Tukey-windowed chirps are shown as thick solid lines from top to bottom: $y'_{\mathrm{bTc}}(n;\, 24\ \mu\mathrm{s})$, $y'_{\mathrm{bTc}}(n;\, 20\ \mu\mathrm{s})$, and $y'_{\mathrm{bTc}}(n;\, 16\ \mu\mathrm{s})$. Each panel of Fig. 6 includes the characteristic curves of pseudochirps for comparison. The characteristic curve corresponding to the same PSL is shown as a thick dashed line, and the others are shown as thin solid lines. Fig. 6 shows that using a binary Tukey-windowed chirp improves the SNR by up to 2 dB relative to using a pseudochirp given an s_{dB} and a T' since, given an s_{dB}, the turning-point positions (which represent more efficient code/filter combinations) in the curves for binary Tukey-windowed chirps are generally 1–2 dB higher than the characteristic curves of pseudochirps. Taking a 1 dB SNR improvement as an example, this means that using a binary Tukey-windowed chirp instead of a pseudochirp results in a $\left(1 - 10^{-1/10}\right) \cdot 100\% = 20.6\%$ reduction in code duration and dead zone because the SNR improvement is approximately proportional to the code duration. Moreover, comparing the turning-point positions in the curves for binary Tukey-windowed chirps with respect to the characteristic curves of pseudochirps shows that using a binary Tukey-windowed chirp in general results in a PSL that is 6 dB lower than that when using a pseudochirp.

B. Experimental Results

Fig. 7 shows the experimental setup. A transducer with a diameter of 25.4 mm and a focal length of 71.1 mm (V304, Panametrics, Waltham, MA) was used to transmit and receive the ultrasonic signal. The image target was a nylon wire with a diameter of 0.2 mm placed 68.7 mm from the transducer. The pulse-echo signal from the wire and its spectrum obtained by using a pulser/receiver (PR5800, Panametrics) to transmit and receive are shown in Figs. 8(a) and (b), respectively. The estimated center frequency and one-way -6 dB bandwidth were 2.56 MHz and 1.45 MHz, respectively, according to the measurements. A waveform generator (DAC200, Signatec, Corona, CA) was used to generate the coded signal at a sampling rate of 200 MHz (i.e., there are five samples per bit) with an amplitude resolution of 12 bits. The pulser/receiver was used to provide a 60 dB gain to the echo signal. The amplified echo then was digitized by an ADC (PCI-9820, ADLINK, Taipei, Taiwan) at a sampling rate of 60 MHz (i.e., $f_{\mathrm{s,ADC}} = 60$ MHz) with an amplitude resolution of 14 bits. The transmit and receive timing was controlled by a function/arbitrary waveform generator (33120A, Agilent, Palo Alto, CA), which generated a 1-kHz trigger signal for the waveform generator and the ADC.

Because the noise was not white in this setup, a dummy experiment was conducted in order to estimate $R_{n_{\mathrm{d}}}(k)$. A total of 4000 records were acquired at 16,000 samples per record in the absence of a transmit signal. The parameters were $M = 54$, $\beta = 3.7$, $f_{\mathrm{c}} = 0.0375$, and $D = 15$ (i.e., $f_{\mathrm{s,d}} = 4$ MHz). The $R_{n_{\mathrm{d}}}(k)$ was estimated from $n_{\mathrm{d}}(n)$ using the following equation [18]:

$$R_{n_{\mathrm{d}}}(k) = \frac{\sum\limits_{n \in I_n} n_{\mathrm{d}}(n) n_{\mathrm{d}}^*(n-k)}{\sum\limits_{n \in I_n} 1}, \tag{27}$$

where I_n is an index set. The power spectral density of $n_{\mathrm{d}}(n)$, obtained by taking the Fourier transform of $R_{n_{\mathrm{d}}}(k)$, is shown in Fig. 9. Electromagnetic interference manifested as several spikes in the power spectral density in this setup. An experiment also was conducted using a one-cycle square wave with a duration of 0.4 μs and an amplitude of $\pi/4$ V as the transmitted signal. The SNR at baseband was 14.8 dB, and this value was used as a reference in the subsequent experiments.

The codes (seven pseudochirps and three binary Tukey-windowed chirps) evaluated in Section IV-A were evaluated experimentally here. The transmitted signal levels were $\pm\pi/4$ V and ± 1 V for the pseudochirp and the binary Tukey-windowed chirp, respectively, in order to maintain a

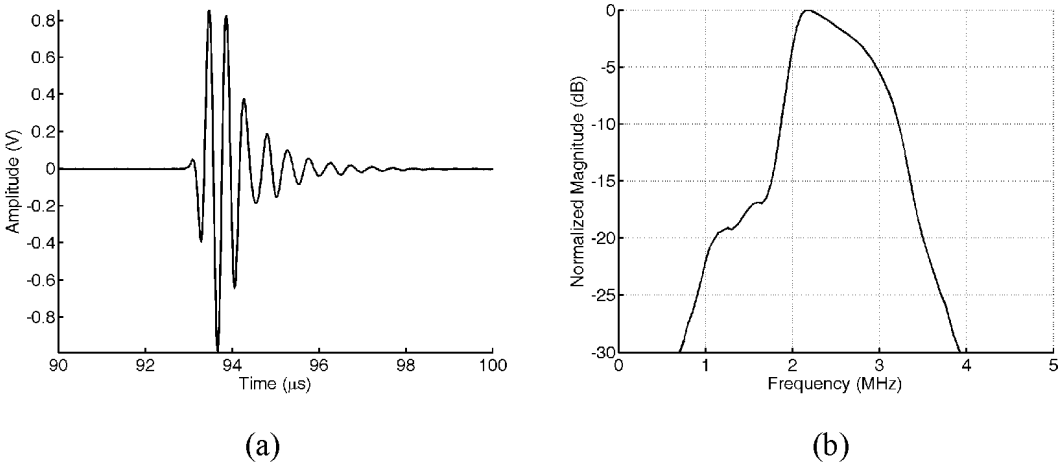

Fig. 8. (a) The pulse-echo signal and (b) the corresponding spectrum of the signal obtained from the wire using a pulser/receiver to transmit and receive.

constant peak acoustic power for all cases. The echo signal ($y'_{\mathrm{bTc,d}}$ or $z_{\mathrm{pc,d}}$) from the wire was estimated using 16,000 records to reduce noise and to design the compression filter. The output SNR corresponding to each compression filter was estimated using $n_{\mathrm{d}}(n)$. The SNR improvement using coded excitation is defined as the output SNR using coded excitation minus 14.8 dB (i.e., the SNR reference). The thick solid lines in Figs. 10(a)–(d) show the optimal improved SNR versus T' for binary Tukey-windowed chirps corresponding to $s_{\mathrm{dB}} = -40$ dB to -58 dB with a step of -6 dB, respectively.

In each panel of Fig. 10, the curves corresponding to the three binary Tukey-windowed chirps, $y'_{\mathrm{bTc}}(n;\ 24\ \mu\mathrm{s})$, $y'_{\mathrm{bTc}}(n;\ 20\ \mu\mathrm{s})$, and $y'_{\mathrm{bTc}}(n;\ 16\ \mu\mathrm{s})$, are shown from top to bottom. Each figure panel also contains the characteristic curves of pseudochirps corresponding to $s_{\mathrm{dB}} = -40$ dB to -58 dB with a step of -6 dB for comparison. The characteristic curve corresponding to the same PSL is shown as a thick dashed line, and the others are shown as thin solid lines. The experimental results again show that using a binary Tukey-windowed chirp instead of a pseudochirp reduces the code duration by at least 20.6% or the PSL by 6 dB.

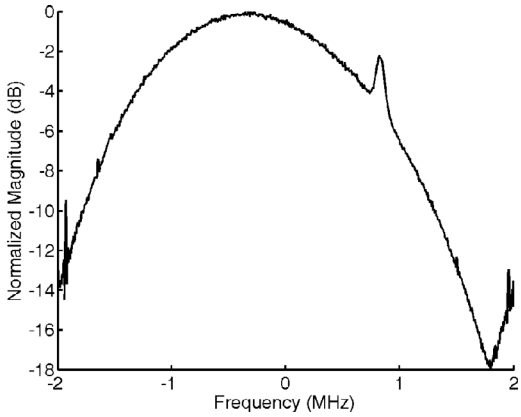

Fig. 9. The measured power spectral density of $n_{\mathrm{d}}(n)$.

V. Discussion

The code-tuning algorithm introduced in Section II-D does not guarantee the smallest $\|[y'\ (t;\ f_{\mathrm{s}}) - x(t)] \otimes h_{\mathrm{t}}(t)\|$ because the compression performance could be improved by using other algorithms such as a genetic algorithm [19]. Furthermore, other metrics could be adopted for the error between the original nonbinary code and its corresponding binary code.

Let the bit duration be the inverse of the bit rate, the shortest time between any two consecutive transitions in the code is equal to the bit duration using the proposed method. One inherent restriction in this paper is that a transition always occurs at an instant equal to an integral multiple of the bit duration. This restriction is not necessary and can be removed. For example, assume that the shortest switching time of the pulser is limited to 25 ns and that the clock rate of the system is 200 MHz, then the bit rate of the code can be set to 200 MHz instead of 40 MHz, but the time between any two consecutive transitions is limited to be larger than or equal to five clock cycles in order not to violate the minimal switching time (25 ns). With this scheme, similarity between the original nonbinary code and its corresponding binary code will increase without the necessity of reducing the shortest switching time, or the compression performance can be maintained when the shortest switching time is kept at a higher value. This subject is currently under investigation.

If the quantizer is not overloaded, a second-order sigma-delta modulator is more capable of shaping the quantization noise than a first-order, sigma-delta modulator. However, the code-tuning algorithm dominates the similarity between the converted binary code and the original code and, consequently, the required switching time. In other words, the output of the sigma-delta modulator is used only as its initial condition. Furthermore, to avoid the quantizer overload and the relevant nonlinear distortion, the modulator input level must be lower than the quantization level if a second-order, sigma-delta modulator is used as the code translator instead of the original first-order,

sigma-delta modulator [16]. Therefore, only the first-order, sigma-delta modulator was considered in this study.

The application of the proposed method for code conversion is not limited to SNR improvement. In [6], [7], the codes are used for special purposes (as mentioned in Section I), nonbinary, and inflexible; the proposed method for code conversion can be applied to those cases to eliminate the need for arbitrary waveform generators. The selected error metric results in the fundamental component in the binary code dominating its similarity to the corresponding nonbinary code, and the signal integrity of higher harmonics is not controlled. Therefore, for cases in which the higher harmonics are desired [8]–[11], the applicability of the method must be further investigated.

VI. Conclusions

This paper proposes a method for exciting nonbinary codes using bipolar square wave pulsers. A nonbinary code is converted into a binary code by code translation and code tuning such that the desired waveform can be transmitted using a bipolar pulser. Tukey-windowed chirps were converted with different durations (16, 20, and 24 μs), all with a taper ratio of 0.15, a center frequency of 2.5 MHz, and an equivalent bandwidth of 1.5 MHz, into binary Tukey-windowed chirps that were compared with pseudochirps over the same spectral band. The bit rate was 40 MHz. Simulation results showed that using a binary Tukey-windowed chirp instead of a pseudochirp reduces the code duration by 20.6% when the constraints on PSL and the SNR improvement are fixed. Moreover, using a binary Tukey-windowed chirp can in general lower the PSL by 6 dB relative to that when using a pseudochirp if the total duration and the SNR improvement are fixed. Experimental results under the same settings were in agreement with the simulations. Although the converted binary code is only an approximation of the original code after convolving with the impulse response of the transducer, the proposed method is successful at improving the SNR. With our method, the low-cost advantage of bipolar pulsers is preserved while the compression performance of the coded excitation system is enhanced in medical ultrasound. The proposed method for code conversion also can be used to eliminate the need for an arbitrary waveform generator in other applications, such as pulse inversion imaging [6] and dynamic transmit focusing [7].

Appendix A
Formulation for Finding the Optimal Compression Filter Defined in (20)

Given a filter length of N_f [i.e., $h_{\mathrm{d,c}}(n)$ is nonzero only for $0 \le n \le N_\mathrm{f}-1$], then:

$$\begin{aligned} R_{n_{\mathrm{d,c}}}(0) &= \sum_{q=0}^{N_\mathrm{f}-1}\sum_{p=0}^{N_\mathrm{f}-1} R_{n_\mathrm{d}}(-p+q)h_{\mathrm{d,c}}(p)h^*_{\mathrm{d,c}}(q), \\ &= \mathbf{h}^\mathrm{H}\mathbf{H}\mathbf{h} \end{aligned} \tag{A1}$$

where:

$$\mathbf{h} \equiv \left[h_{\mathrm{d,c}}(0)\ h_{\mathrm{d,c}}(1)\cdots\ h_{\mathrm{d,c}}\left(N_\mathrm{f}-1\right)\right]^T, \tag{A2}$$

$\mathbf{H}$ is an $N_\mathrm{f}\times N_\mathrm{f}$ Hermitian matrix (i.e., $\mathbf{H}=\mathbf{H}^\mathrm{H}$) and

$$(\mathbf{H})_{pq} \equiv R_{n_\mathrm{d}}(p-q), \tag{A3}$$

T denotes transpose, and H denotes the Hermitian (i.e., conjugate transpose). Because

$$\mathbf{h}^\mathrm{H}\mathbf{H}\mathbf{h} = \left(\mathbf{h}^\mathrm{H}\mathbf{H}\mathbf{h}\right)^\mathrm{H} = \left(\mathbf{h}^\mathrm{H}\mathbf{H}\mathbf{h}\right)^*, \tag{A4}$$

$\mathrm{Im}\left\{\mathbf{h}^\mathrm{H}\mathbf{H}\mathbf{h}\right\}=0$ and:

$$\mathbf{h}^\mathrm{H}\mathbf{H}\mathbf{h} = \left(\mathbf{h}^\mathrm{H}\mathbf{H}\mathbf{h}\right)^\mathrm{T}. \tag{A5}$$

Let $\mathrm{Re}\{\mathbf{H}\}\equiv\mathbf{H}_\mathrm{r}$, $\mathrm{Im}\{\mathbf{H}\}\equiv\mathbf{H}_\mathrm{i}$, $\mathrm{Re}\{\mathbf{h}\}\equiv\mathbf{h}_\mathrm{r}$, $\mathrm{Im}\{\mathbf{h}\}\equiv\mathbf{h}_\mathrm{i}$, $\mathrm{Re}\{y'_\mathrm{d}(k)\}\equiv y_\mathrm{r}(k)$, $\mathrm{Im}\{y'_\mathrm{d}(k)\}\equiv y_\mathrm{i}(k)$, and $j\equiv\sqrt{-1}$, then:

$$\begin{aligned} \mathbf{h}^\mathrm{H}\mathbf{H}\mathbf{h} &= \mathbf{h}_\mathrm{r}^\mathrm{T}\mathbf{H}\mathbf{h}_\mathrm{r} + \mathbf{h}_\mathrm{i}^\mathrm{T}\left(-j\mathbf{H}\right)\mathbf{h}_\mathrm{r} + \mathbf{h}_\mathrm{r}^\mathrm{T}\left(j\mathbf{H}\right)\mathbf{h}_\mathrm{i} + \mathbf{h}_\mathrm{i}^\mathrm{T}\mathbf{H}\mathbf{h}_\mathrm{i} \\ &= \begin{bmatrix}\mathbf{h}_\mathrm{r}\\ \mathbf{h}_\mathrm{i}\end{bmatrix}^\mathrm{T}\begin{bmatrix}\mathbf{H} & j\mathbf{H}\\ -j\mathbf{H} & \mathbf{H}\end{bmatrix}\begin{bmatrix}\mathbf{h}_\mathrm{r}\\ \mathbf{h}_\mathrm{i}\end{bmatrix} = \left(\begin{bmatrix}\mathbf{h}_\mathrm{r}\\ \mathbf{h}_\mathrm{i}\end{bmatrix}^\mathrm{T}\begin{bmatrix}\mathbf{H} & j\mathbf{H}\\ -j\mathbf{H} & \mathbf{H}\end{bmatrix}\begin{bmatrix}\mathbf{h}_\mathrm{r}\\ \mathbf{h}_\mathrm{i}\end{bmatrix}\right)^\mathrm{T} \\ &= \begin{bmatrix}\mathbf{h}_\mathrm{r}\\ \mathbf{h}_\mathrm{i}\end{bmatrix}^\mathrm{T}\begin{bmatrix}\mathbf{H}^\mathrm{T} & -j\mathbf{H}^\mathrm{T}\\ j\mathbf{H}^\mathrm{T} & \mathbf{H}^\mathrm{T}\end{bmatrix}\begin{bmatrix}\mathbf{h}_\mathrm{r}\\ \mathbf{h}_\mathrm{i}\end{bmatrix} \\ &= \begin{bmatrix}\mathbf{h}_\mathrm{r}\\ \mathbf{h}_\mathrm{i}\end{bmatrix}^\mathrm{T}\begin{bmatrix}\left(\mathbf{H}+\mathbf{H}^\mathrm{T}\right)/2 & j\left(\mathbf{H}-\mathbf{H}^\mathrm{T}\right)/2\\ -j\left(\mathbf{H}-\mathbf{H}^\mathrm{T}\right)/2 & \left(\mathbf{H}+\mathbf{H}^\mathrm{T}\right)/2\end{bmatrix}\begin{bmatrix}\mathbf{h}_\mathrm{r}\\ \mathbf{h}_\mathrm{i}\end{bmatrix} \\ &= \begin{bmatrix}\mathbf{h}_\mathrm{r}\\ \mathbf{h}_\mathrm{i}\end{bmatrix}^\mathrm{T}\begin{bmatrix}\mathbf{H}_\mathrm{r} & -\mathbf{H}_\mathrm{i}\\ \mathbf{H}_\mathrm{i} & \mathbf{H}_\mathrm{r}\end{bmatrix}\begin{bmatrix}\mathbf{h}_\mathrm{r}\\ \mathbf{h}_\mathrm{i}\end{bmatrix} \\ &\equiv \mathbf{g}^\mathrm{T}\mathbf{G}\mathbf{g}, \end{aligned} \tag{A6}$$

and:

$$y'_{\mathrm{d,c}}(n) = \sum_{p=0}^{N_\mathrm{f}-1} h_{\mathrm{d,c}}(p)y'_\mathrm{d}(n-p) = \mathbf{y}_{n,\mathrm{r}}^\mathrm{T}\mathbf{g} + j\mathbf{y}_{n,\mathrm{i}}^\mathrm{T}\mathbf{g}, \tag{A7}$$

where:

$$\mathbf{g} = \begin{bmatrix}\mathbf{h}_\mathrm{r}\\ \mathbf{h}_\mathrm{i}\end{bmatrix}, \tag{A8}$$

$$\mathbf{G} = \begin{bmatrix}\mathbf{H}_\mathrm{r} & -\mathbf{H}_\mathrm{i}\\ \mathbf{H}_\mathrm{i} & \mathbf{H}_\mathrm{r}\end{bmatrix}, \tag{A9}$$

$$\begin{aligned} \mathbf{y}_{n,\mathrm{r}} = [&y_\mathrm{r}(n)\quad y_\mathrm{r}(n-1)\cdots \\ &y_\mathrm{r}\left(n-N_\mathrm{f}+1\right)\quad -y_\mathrm{i}(n)\quad -y_\mathrm{i}(n-1)\cdots \\ &-y_\mathrm{i}\left(n-N_\mathrm{f}+1\right)]^\mathrm{T}, \end{aligned} \tag{A10}$$

and:

$$\begin{aligned} \mathbf{y}_{n,\mathrm{i}} = [&y_\mathrm{i}(n)\quad y_\mathrm{i}(n-1)\cdots \\ &y_\mathrm{i}\left(n-N_\mathrm{f}+1\right)y_\mathrm{r}(n)\quad y_\mathrm{r}(n-1)\cdots \\ &y_\mathrm{r}\left(n-N_\mathrm{f}+1\right)]^\mathrm{T}. \end{aligned} \tag{A11}$$

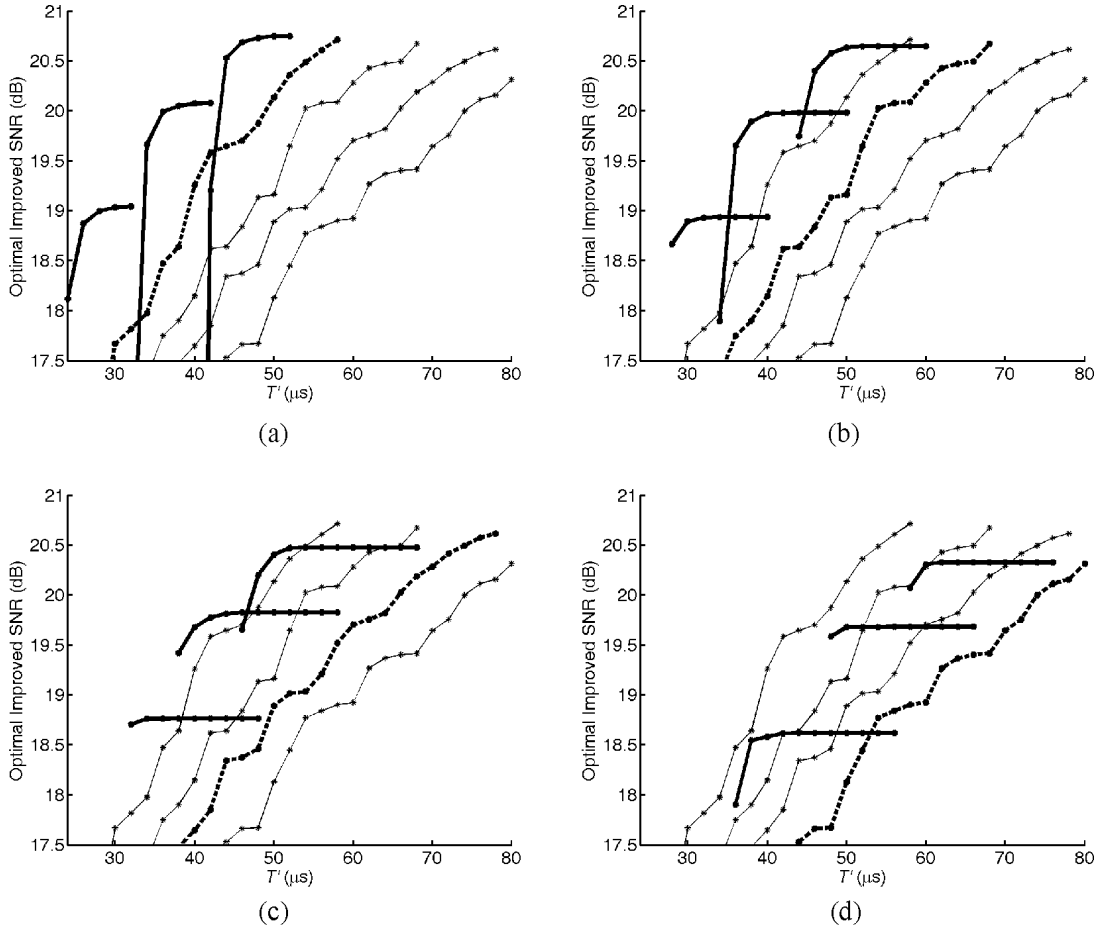

Fig. 10. The curves of optimal SNR versus T' for binary Tukey-windowed chirps obtained from experiments. (a) $s_{\mathrm{dB}} = -40$ dB. (b) $s_{\mathrm{dB}} = -46$ dB. (c) $s_{\mathrm{dB}} = -52$ dB. (d) $s_{\mathrm{dB}} = -58$ dB. In each panel, the curves corresponding to three binary Tukey-windowed chirps are shown from top to bottom as thick solid lines: $y'_{\mathrm{bTc}}(n;\ 24\ \mu\mathrm{s})$, $y'_{\mathrm{bTc}}(n;\ 20\ \mu\mathrm{s})$, and $y'_{\mathrm{bTc}}(n;\ 16\ \mu\mathrm{s})$. Also shown in each panel are the characteristic curves of pseudochirp corresponding to $s_{\mathrm{dB}} = -40$ dB to -58 dB with a step of -6 dB for comparison. The characteristic curve corresponding to the same PSL is shown as a thick dashed line; the others are shown as thin solid lines.

Thus the constraint $y'_{\mathrm{d,c}}(m) = 1$ can be formulated as:

$$\mathbf{y}_{m,\mathrm{r}}^{\mathrm{T}}\mathbf{g} = 1 \text{ and } \mathbf{y}_{m,\mathrm{i}}^{\mathrm{T}}\mathbf{g} = 0, \tag{A12}$$

and $\left|\mathrm{Re}\left\{y'_{\mathrm{d,c}}(n)\right\}\right| \le s/\sqrt{2}$ and $\left|\mathrm{Im}\left\{y'_{\mathrm{d,c}}(n)\right\}\right| \le s/\sqrt{2}$ can be formulated as:

$$\mathbf{y}_{n,\mathrm{r}}^{\mathrm{T}}\mathbf{g} \le \frac{s}{\sqrt{2}},\ \left(-\mathbf{y}_{n,\mathrm{r}}\right)^{\mathrm{T}}\mathbf{g} \le \frac{s}{\sqrt{2}},\ \mathbf{y}_{n,\mathrm{i}}^{\mathrm{T}}\mathbf{g} \le \frac{s}{\sqrt{2}},$$
$$\text{and } \left(-\mathbf{y}_{n,\mathrm{i}}\right)^{\mathrm{T}}\mathbf{g} \le \frac{s}{\sqrt{2}}. \tag{A13}$$

Eq. (A1), (A6), (A12), and (A13) show that (20) is a quadratic programming problem with a convex feasible set [20]. Furthermore, $\mathbf{G}$ is positive definite (i.e., $\mathbf{g}^{\mathrm{T}}\mathbf{G}\mathbf{g} > 0$ for all $\mathbf{g}$ nonzero) as $\mathbf{g}^{\mathrm{T}}\mathbf{G}\mathbf{g} = R_{n_{\mathrm{d,c}}}(0)$. Therefore, if the constraints can be satisfied using a filter length of N_{f}, the optimal compression filter $h_{\mathrm{o}}(n)$ of this length exists, is unique, and can be found [20].

References

[1] M. O'Donnell, "Coded excitation system for improving the penetration of real-time phased-array imaging systems," *IEEE Trans. Ultrason., Ferroelect., Freq. Contr.*, vol. 39, no. 3, pp. 341–351, 1992.

[2] B. Haider, P. A. Lewin, and K. E. Thomenius, "Pulse elongation and deconvolution filtering for medical ultrasonic imaging," *IEEE Trans. Ultrason., Ferroelect., Freq. Contr.*, vol. 45, no. 1, pp. 98–113, 1998.

[3] R. Y. Chiao and L. J. Thomas, "Synthetic transmit aperture imaging using orthogonal Golay coded excitation," in *Proc. IEEE Ultrason. Symp.*, 2000, pp. 1677–1680.

[4] Y. Wang, K. Metzger, D. N. Stephens, G. Williams, S. Brownlie, and M. O'Donnell, "Coded excitation with spectrum inversion (CEXSI) for ultrasound array imaging," *IEEE Trans. Ultrason., Ferroelect., Freq. Contr.*, vol. 50, no. 7, pp. 805–823, 2003.

[5] J. Shen and E. S. Ebbini, "A new coded-excitation ultrasound imaging system—Part I: Basic principles," *IEEE Trans. Ultrason., Ferroelect., Freq. Contr.*, vol. 43, no. 1, pp. 131–140, 1996.

[6] C.-C. Shen and P.-C. Li, "Pulse-inversion-based fundamental imaging for contrast detection," *IEEE Trans. Ultrason., Ferroelect., Freq. Contr.*, vol. 50, no. 9, pp. 1124–1133, 2003.

[7] S. Zhou and J. A. Hossack, "Dynamic-transmit focusing using time-dependent focal zone and center frequency," *IEEE Trans. Ultrason., Ferroelect., Freq. Contr.*, vol. 50, no. 2, pp. 142–152, 2003.

[8] P.-C. Li, "Pulse compression for finite amplitude distortion based harmonic imaging using coded waveforms," *Ultrason. Imag.*, vol. 21, no. 1, pp. 1–16, 1999.

[9] Y. Takeuchi, "Coded excitation for harmonics imaging," in *Proc. IEEE Ultrason. Symp.*, 1996, pp. 1433–1436.

[10] J. Borsboom, C. T. Chin, and N. de Jong, "Experimental valida-

tion of a nonlinear coded excitation method for contrast imaging," in *Proc. IEEE Ultrason. Symp.*, 2002, pp. 1933–1936.
[11] W. Wilkening, M. Krueger, and H. Ermert, "Phase-coded pulse sequence for non-linear imaging," in *Proc. IEEE Ultrason. Symp.*, 2000, pp. 1559–1562.
[12] T. X. Misaridis and J. A. Jensen, "An effective coded excitation scheme based on a Tukey-windowed FM signal and an optimized digital filter," in *Proc. IEEE Ultrason. Symp.*, 1999, pp. 1589–1593.
[13] P.-C. Li, E. Ebbini, and M. O'Donnell, "A new filter design technique for coded excitation systems," *IEEE Trans. Ultrason., Ferroelect., Freq. Contr.*, vol. 39, no. 6, pp. 693–699, 1992.
[14] T. X. Misaridis, M. H. Pedersen, and J. A. Jensen, "Clinical use and evaluation of coded excitation in B-mode images," in *Proc. IEEE Ultrason. Symp.*, 2000, pp. 1689–1693.
[15] T. Azuma, Y. Miwa, and S. Umemura, "Subaperture decoding to enhance performance of coded excitation," in *Proc. IEEE Ultrason. Symp.*, 2002, pp. 1669–1672.
[16] P. M. Aziz, H. V. Sorensen, and J. van der Spiegel, "An overview of sigma-delta converters," *IEEE Signal Process. Mag.*, vol. 13, no. 1, pp. 61–84, 1996.
[17] A. V. Oppenheim and R. W. Schafer, *Discrete-Time Signal Processing*. Englewood Cliffs, NJ: Prentice-Hall, 1989.
[18] S. Haykin, *Adaptive Filter Theory*. 4th ed. Upper Saddle River, NJ: Prentice-Hall, 2002.
[19] R. L. Haupt and S. E. Haupt, *Practical Genetic Algorithms*. New York: Wiley, 1998.
[20] S. G. Nash and A. Sofer, *Linear and Nonlinear Programming*. New York: McGraw-Hill, 1996.

Sheng-Wen Huang was born in 1971 in Changhua, Taiwan, R.O.C. He received the B.S. and Ph.D. degrees from National Taiwan University, Taipei, Taiwan, R.O.C., in 1993 and 2004, respectively, both in electrical engineering. He worked as a postdoctoral researcher at National Taiwan University from 2004 to 2005, and is currently a postdoctoral researcher with the Department of Biomedical Engineering at the University of Michigan. His current research interests include thermal strain imaging, coded excitation, and optoacoustic imaging.

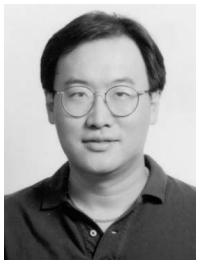

Pai-Chi Li (S'93–M'95–SM'01) received the B.S. degree in electrical engineering from National Taiwan University, Taipei, Taiwan, R.O.C., in 1987, and the M.S. and Ph.D. degrees from the University of Michigan, Ann Arbor, MI, in 1990 and 1994, respectively, both in electrical engineering: systems.

He was a research assistant with the Department of Electrical Engineering and Computer Science of the University of Michigan from 1990 to 1994. He joined Acuson Corporation, Mountain View, CA, as a member of the Technical Staff in June 1994. His work with Acuson was primarily in the areas of medical ultrasonic imaging system design for both cardiology and general imaging applications. In August 1997, he went back to the Department of Electrical Engineering at National Taiwan University, where he is currently a full professor. His current research interests include biomedical ultrasonic imaging and signal processing.

Dr. Li is a senior member of IEEE and Associate Editor of *IEEE Transactions on Ultrasonics, Ferroelectrics, and Frequency Control*. He is also on the Editorial Board of *Ultrasonic Imaging*. He received the 2004 Distinguished Research Award, National Science Council, the 2004 Distinguished Research Achievement Award, National Taiwan University, the 2003 Outstanding Researcher Award, National Taiwan University, the 2002 Dr. Wu Dayou Research Award from National Science Council, the 2002 Outstanding Young Electrical Engineer Award from Chinese Institute of Electrical Engineering and the Distinguished Industrial Collaboration Award of Ministry of Education. He was also the recipient of the Distinguished Achievement Award in Electrical Engineering: Systems in 1994 for his outstanding academic achievement at the University of Michigan.

Binary Code Design for High-Frequency Ultrasound

Sheng-Wen Huang and Pai-Chi Li, *Senior Member, IEEE*

***Abstract*—This paper proposes an approach to designing binary codes suitable for high-frequency applications of coded excitation in medical ultrasound. For a high-frequency ultrasound system, transmitting well-designed binary codes with a low sampling ratio (i.e., the bit rate divided by the transducer center frequency) is a practical way to improve the signal-to-noise ratio (SNR) because the challenge of implementing arbitrary-waveform generators for transmitting nonbinary codes increases with the frequency and the switching speed of square-wave pulsers are limited. One conventional approach designs codes using a base sequence that modulates wideband sequences up to the transducer passband. Because a major portion of codes is excluded as a candidate, codes designed using this approach typically need long compression filters for restoring the axial resolution, and they do not improve the SNR efficiently. In contrast, the approach proposed here searches all the codes that match the transducer passband; hence, the resultant codes exhibit better performance. The technique was tested using a bit rate of 50 MHz and a sampling ratio of 2. For a transducer with an ideal Gaussian frequency response with a center frequency of 25 MHz and a −6 dB bandwidth of 15 MHz, the SNR for the same sidelobe extent was 1 to 6 dB higher for the codes designed using the proposed approach compared with those designed using the conventional approach. When a real transducer response with a center frequency of 26.4 MHz and a one-way −6 dB bandwidth of 20.7 MHz was considered, the codes designed using the proposed approach were superior by 0.5 to 5 dB. Therefore, our approach is better than the conventional approach for designing binary codes for high-frequency ultrasound, with the results indicating that the moderate bit rate of 50 MHz will suffice when the ultrasonic center frequency is 25 MHz.**

I. Introduction

A primary application of coded excitation in medical ultrasound is improving the signal-to-noise ratio (SNR) without increasing the peak acoustic power [1], and the papers on coded waveforms (e.g., [2], [3]) published in this journal describe some of the recent progress and offer extensive references to previous studies in diverse applications. Fig. 1 shows a block diagram of a coded excitation system, in which each channel has a transmitter able to transmit the desired code (which has a wide bandwidth and an increased pulse length), and a compression filter whose coefficients and length are strongly influenced by the code is placed after the receive beamformer so as to restore the axial resolution. The performance of pulse compression is generally characterized by the mainlobe width (related to the axial resolution) and the sidelobe level (related to the dynamic range and contrast resolution) of the compressed pulse, and the SNR improvement (i.e., the difference between the SNRs after and before pulse compression).

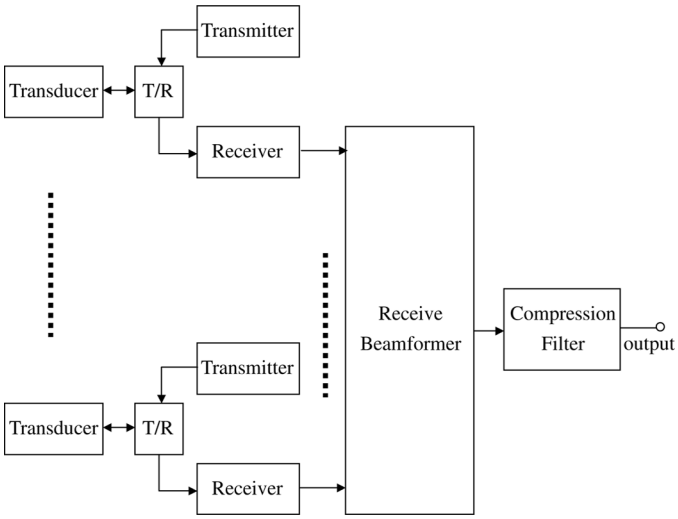

Fig. 1. Block diagram of a coded excitation system.

Codes can be classified according to the required transmitter type. A nonbinary code necessitates an arbitrary-waveform transmitter, and a binary code can be transmitted with a square-wave pulser. Although it is easy to design nonbinary codes with good compression performances, such codes have not been widely used in array systems mainly due to the increased hardware complexity and cost associated with the requirement for multiple arbitrary-waveform transmitters. Furthermore, the challenge of implementing an arbitrary-waveform transmitter increases with the center frequency of the transducer (or the code), and it may still be impractical to use codes other than binary ones for a high-frequency (e.g., 25 MHz) ultrasound system that images using an array of transducers. The difficulty of designing binary codes also increases with frequency due to the limited switching speed of square-wave pulsers and, consequently, the allowable sampling ratio decreases as the center frequency of the transducer increases (where the sampling ratio is the bit rate divided by the transducer center frequency).

Manuscript received February 23, 2006; accepted December 28, 2006. Partial support from the National Science Council of R.O.C. under Grant NSC 95-2218-E-002-036 and from the National Health Research Institutes of R.O.C. is gratefully acknowledged.

The authors are with the Department of Electrical Engineering, National Taiwan University, Taipei, Taiwan (e-mail: paichi@cc.ee.ntu.edu.tw).

Digital Object Identifier 10.1109/TUFFC.2007.340

In this paper, we focus on designing single-firing (or single-transmit) binary codes having a low sampling ratio (e.g., 2) and efficiently improving the SNR. Here a code improving SNR efficiently means that it provides a high ratio of SNR improvement to sidelobe duration after pulse compression. Given a certain code length (in units of time), using a lower sampling ratio is equivalent to having fewer tunable bits and fewer degrees of freedom in the code design, which results in worse performance. Note that in order to cover the full bandwidth of the transducer, the sampling ratio is generally at least 2.

In medical ultrasound, a typical approach to generating a binary radio-frequency (RF) code with a low sampling ratio is modulating an N_{C}-bit wideband sequence $c_{\mathrm{WB}}(n)$, $n = 0, 1, \ldots, N_{\mathrm{C}} - 1$, up to the transducer band using an N_{B}-bit base sequence $b(n)$, $n = 0, 1, \ldots, N_{\mathrm{B}} - 1$. Zeros are inserted into $c_{\mathrm{WB}}(n)$ to get:

$$c'_{\mathrm{WB}}(n) = \begin{cases} c_{\mathrm{WB}}(m) & \text{if } n = N_{\mathrm{B}}m \text{ for } m = 0, 1, \ldots, N_{\mathrm{C}} - 1 \\ 0 & \text{elsewhere} \end{cases}, \quad (1)$$

and then $c'_{\mathrm{WB}}(n)$ is convolved with $b(n)$ to form the final N-bit RF code $c_{\mathrm{RF}}(n)$, $n = 0, 1, \ldots, N - 1$, with $N = N_{\mathrm{C}}N_{\mathrm{B}}$ [2]–[4]. Explicitly:

$$\begin{aligned} c_{\mathrm{RF}}(p + qN_{\mathrm{B}}) &= b(p)c_{\mathrm{WB}}(q), \\ p &= 0, 1, \ldots, N_{\mathrm{B}} - 1, \\ q &= 0, 1, \ldots, N_{\mathrm{C}} - 1. \end{aligned} \quad (2)$$

The wideband sequence is chosen to have the desired properties such as enabling range sidelobe cancellation [2] or benefiting inverse filtering [3], [4], and the base sequence (together with the bit rate) is used to control the band of the RF code [2]–[4]. We call such an approach the modulation approach. Because it has at most $[(N_{\mathrm{C}}-1)+(N_{\mathrm{B}}-1)]$ adjustable bits, a major portion of N-bit codes is excluded as a candidate. This means that some codes with good compression performances are not considered in order to reduce the design effort. Therefore, not all single-firing codes designed using the approach provide a high SNR improvement together with a short sidelobe duration and a short near-field dead zone.

Although the exhaustive-search approach (checking all N-bit codes in order to find the best RF code) is unfeasible in general, there are feasible approaches that are better than the modulation approach. In this study, we developed an indicator-based, random-search approach to finding codes with good compression performance based on a genetic algorithm [5]. This indicator is easy to calculate, and a code with a high-indicator value usually has good compression performance. Hence, the adoption of the indicator makes the proposed approach feasible. As shown in Section IV, the compression performances of codes designed using this approach are superior to those designed using the modulation approach.

This paper is organized as follows. Section II describes the criterion for evaluating the codes that are used to improve the SNR. Section III details the indicator-based, random-search approach to binary code design. The genetic algorithm used for the code search also is presented. Section IV demonstrates the efficacy of the proposed approach and discusses its characteristics, and the paper concludes in Section V.

II. Criterion for Evaluating Codes

For single-firing codes, restoring the axial resolution by compressing the pulses is achieved by filtering. In order to clarify the criterion for evaluating codes, we must first describe how to design the compression filter used in this study.

A. Design of the Compression Filter

In general, a time-domain compression filter is preferable to a frequency-domain filter because the latter is vulnerable to the presence of incomplete echoes in the near field. In this study, we adopted a previously proposed method [6] providing direct control over the sidelobe level to design time-domain compression filters at baseband. If $h_{\mathrm{t}}(t)$ is the one-way impulse response of the transducer, the digitized echo signal corresponding to an N-bit code $c_{\mathrm{RF}}(n)$ from a point target can be modeled as:

$$e(n) = \left[c_{\mathrm{RF}}(t) \otimes h_{\mathrm{t}}(t) \otimes h_{\mathrm{t}}(t)\right]_{t=n/f_{\mathrm{s}}}, \quad (3)$$

where $\otimes$ denotes convolution,

$$c_{\mathrm{RF}}(t) = \sum_{n=0}^{N-1} c_{\mathrm{RF}}(n)\Pi\left(f_{\mathrm{b}}t - n + \frac{N}{2}\right), \quad (4)$$

f_{b} is the bit rate, f_{s} is the sampling rate of the analog-to-digital converter (ADC) at the receiver, and $\Pi(t) = 1$ if $0 \le t \le 1$ and 0 elsewhere. The $e(n)$ is demodulated into a baseband signal:

$$e_{\mathrm{b}}(n) = h_{\mathrm{L}}(n) \otimes \left[e(n) \cdot \exp(-j2\pi f_0 n/f_{\mathrm{s}})\right], \quad (5)$$

where f_0 is the center frequency of the transducer and $h_{\mathrm{L}}(n)$ is a low-pass filter. The $e_{\mathrm{b}}[n]$ then is downsampled by a factor of D to obtain $e_{\mathrm{d}}(n) = e_{\mathrm{b}}(Dn)$. Filtering $e_{\mathrm{d}}(n)$ with a compression filter $h_{\mathrm{o}}(n)$ restores the axial resolution in the output signal.

Given a filter length N_{f}, $h_{\mathrm{o}}(n)$ is designed to maximize the output SNR under the constraints on the mainlobe width and the sidelobe level. Let m denote the index of the peak position of $e_{\mathrm{d,c}}(n)$, I_{sl} denote the index set of the sidelobes, s specify the allowable peak sidelobe level, and $s_{\mathrm{dB}} = 20\log s$, then explicitly:

$$h_{\mathrm{o}}(n) = \arg\min_{h(n)} \sigma^2_{n_{\mathrm{d,c}}}(0) \text{ subject to } \begin{cases} e_{\mathrm{d,c}}(m) = 1 \\ \left|\mathrm{Re}\left\{e_{\mathrm{d,c}}(n)\right\}\right| \le s/\sqrt{2} \text{ for } n \in I_{\mathrm{sl}}, \\ \left|\mathrm{Im}\left\{e_{\mathrm{d,c}}(n)\right\}\right| \le s/\sqrt{2} \text{ for } n \in I_{\mathrm{sl}} \end{cases} \quad (6)$$

where $\sigma^2_{n_{\mathrm{d,c}}}$ denotes the power of the thermal noise $n_{\mathrm{d,c}}(n)$ after compression, $e_{\mathrm{d,c}}(n) = e_{\mathrm{d}}(n) \otimes h(n)$, $h(n)$ has a length of N_{f}, and $\mathrm{Re}\{\cdot\}$ and $\mathrm{Im}\{\cdot\}$ denote the real and imaginary parts, respectively. The details for solving (6) are available elsewhere [6].

B. Definition of Code Efficiency

The near-field dead zone of a coded excitation system using a code-filter combination $\{c_{\mathrm{RF}}(n;N),\, h_{\mathrm{o}}(n;N_{\mathrm{f}})\}$ is $(T_{\mathrm{c}}+T_{\mathrm{f}})/2$ larger than that of a pulsed excitation system, where $T_{\mathrm{c}} = N/f_{\mathrm{b}}$ and $T_{\mathrm{f}} = N_{\mathrm{f}}D/f_{\mathrm{s}}$ (both in units of time) are the code length and the filter length, respectively. In addition, the sidelobe of a point target spans a duration of $(T_{\mathrm{c}} + T_{\mathrm{f}})$ for this coded excitation system. Therefore, the value of $(T_{\mathrm{c}}+T_{\mathrm{f}})$ should be as small as possible, and a given code-filter combination is better than another if it provides the same SNR improvement and has a lower $(T_{\mathrm{c}} + T_{\mathrm{f}})$. Because the output SNR ideally should be proportional to both T_{c} and $(T_{\mathrm{c}} + T_{\mathrm{f}})$, it is reasonable to treat a code-filter combination as better if it has a higher code-filter efficiency:

$$E_{\mathrm{cf}}\left[c_{\mathrm{RF}}(n;N),\, h_{\mathrm{o}}(n;N_{\mathrm{f}})\right] \equiv \mathrm{SNR}_{\mathrm{dB}} - 10\log_{10}\left[(T_{\mathrm{c}}+T_{\mathrm{f}})/(T_0/2)\right], \quad (7)$$

where $\mathrm{SNR}_{\mathrm{dB}}$ is the output SNR in decibels, and $T_0 = f_0^{-1}$. We can use (7) to fairly compare two code-filter combinations even if they provide different SNR improvements.

Note that given a code $c_{\mathrm{RF}}(n;N)$, there is a one-to-one correspondence between N_{f} and $h_{\mathrm{o}}(n;N_{\mathrm{f}})$. That is:

$$E_{\mathrm{cf}}\left[c_{\mathrm{RF}}(n;N),\, h_{\mathrm{o}}(n;N_{\mathrm{f}})\right] = E_{\mathrm{cf}}\left[c_{\mathrm{RF}}(n;N),\, N_{\mathrm{f}}\right], \quad (8)$$

and there exists an N_{f} (or a T_{f}) that results in the maximal E_{cf} value for the code. Defining the efficiency E_{c} of a code $c_{\mathrm{RF}}(n;N)$ as:

$$E_{\mathrm{c}}\left[c_{\mathrm{RF}}(n;N)\right] \equiv \max_{N_{\mathrm{f}}}\left\{E_{\mathrm{cf}}\left[c_{\mathrm{RF}}(n;N),\, N_{\mathrm{f}}\right]\right\}, \quad (9)$$

means that a code which is easier to compress and/or improves the SNR to a greater extent will have a higher E_{c} value. Therefore, in this study a code is treated as more efficient at improving the SNR or having better compression performance if its E_{c} value is higher.

III. The Indicator-Based Search Approach to Binary Code Design

Genetic algorithms may be used to stochastically search a domain that is too large to be searched exhaustively [5]. A genetic algorithm previously was used to design binary codes suitable for being compressed with inverse filtering in the frequency domain [7]. In the present study, we developed a genetic algorithm to design binary codes with high efficiencies. Because given a code, for obtaining its efficiency, typically tens of compression filters corresponding to different N_{f}'s need to be designed [see (9)] and designing a compression filter means solving a quadratic programming problem [see (6)] [6], it is evident that directly calculating the efficiency of each code during the search process is computationally expensive. Therefore, in our algorithm the following indicator that is easier to calculate while being closely correlated with the code efficiency was used as the parameter to be optimized during the search process:

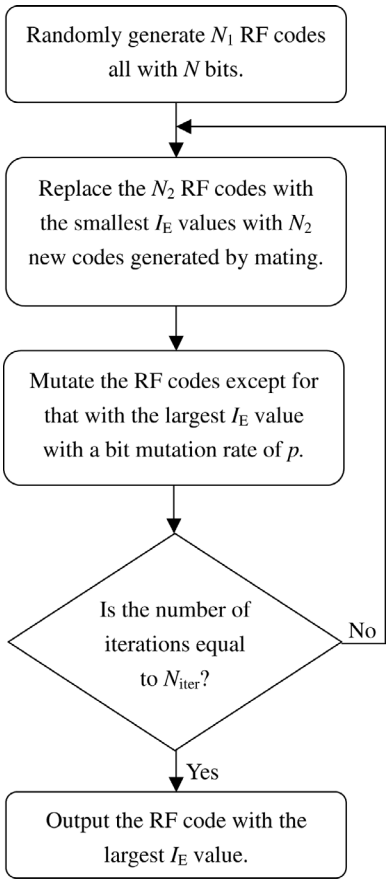

Fig. 2. Flow diagram of the genetic algorithm used in the proposed search approach.

$$I_{\mathrm{E}}\left[c_{\mathrm{RF}}(n;N)\right] \equiv \left\| \left\{ \frac{R_{c_{\mathrm{RF}}}(t)}{R_{c_{\mathrm{RF}}}(0)} - \frac{R_b(t)}{R_b(0)} \right\} \otimes h_{\mathrm{t}}(t) \right\|^{-1}, \quad (10)$$

where $R_a(t) = a(t) \otimes a^*(-t)$ denotes the autocorrelation function of the signal $a(t)$ [representing $c_{\mathrm{RF}}(t)$ or $b(t)$ here],

$$b(t) = \sum_{n=0}^{N_{\mathrm{B}}-1} b(n)\Pi\left(f_{\mathrm{b}}t - n + \frac{N_{\mathrm{B}}}{2}\right), \quad (11)$$

$R_{c_{\mathrm{RF}}}(0) = (N/f_{\mathrm{b}})$, and $R_b(0) = (N_{\mathrm{B}}/f_{\mathrm{b}})$. If the spectrum of an RF code in the transducer band is similar to that of the base sequence (in terms of the normalized amplitude), it will have a large I_{E} value. Because, in general, the base sequence (such as $\{1, -1\}$ or $\{1, -1, 1, -1\}$) has a smooth spectrum, RF codes with large I_{E} values tend to have a smooth spectrum. Therefore, they are easy to compress

TABLE I
HEXADECIMAL REPRESENTATIONS OF THE RF CODES DESIGNED USING THE SEARCH APPROACH (SECOND COLUMN) AND THE MODULATION APPROACH (FIFTH COLUMN) FOR $b(n) = (-1)^n$ AND $N_B = 4$.[1]

	Search approach		Modulation approach	
N	RF code	N_C	Wideband sequence	RF code
32	252A5551	8	1A	555AA5A5
36	75558AD4B	9	068	55AA5A555
40	4AD52AAAFB	10	0D0	55AA5A5555
44	5D554BA9529	11	065	5555AA55A5A
48	692952A15555	12	0CA	5555AA55A5A5
52	755552A952969	13	00CA	55555AA55A5A5
56	755556AB54A5A1	14	0195	55555AA55A5A5A
60	7555542A956A5AD	15	0EED	555AAA5AAA5AA5A
64	2D695AA550AAAABB	16	2833	55A5A55555AA55AA

[1]The wideband sequences [9] necessary for the modulation approach are listed in the fourth column. The transducer was assumed to have a Gaussian frequency response with a 60% fractional bandwidth, and the additive noise sampled by the ADC was assumed to be white.

and exhibit a high efficiency. That is, the base sequence is used to control the spectrum shape of the RF code in the proposed search approach, as is also the case for the modulation approach.

Fig. 2 shows the flow diagram of the genetic algorithm for RF code design. In the second step, the probability of a code being chosen as a parent code for mating is proportional to its I_E value. A pair of parent codes $\{c_{RF,1}(n), c_{RF,2}(n)\}$ generates two offspring codes $c'_{RF,1}(n)$ and $c'_{RF,2}(n)$ according to the following rule:

$$c'_{RF,k}(n) = \begin{cases} c_{RF,k}(n) & \text{if } u(n) \geq 0.5 \\ c_{RF,3-k}(n) & \text{otherwise} \end{cases}, \qquad (12)$$

where $u(n)$, $n = 0, 1, \ldots, N-1$, are random numbers generated with a uniform probability density within $[0, 1]$, and k equals to 1 or 2.

IV. Results and Discussion

A bit rate of 50 MHz was used in this study, except where stated otherwise. Given a fixed bit rate, the efficiency of a code relative to other codes is dominated by the transducer response and the noise characteristics, and it is less dependent on the parameters related to the design of the compression filter, including those of the filter $h_L(n)$, the sampling rate of the ADC ($f_s = 200$ MHz), the downsampling ratio ($D = 5$), the mainlobe width (defined as the central nine points of the compressed signal), and the allowable peak sidelobe level ($s = 0.01$ or $s_{dB} = -40$ dB). Here $h_L(n)$ was a Kaiser-windowed finite impulse response low-pass filter with filter length $(M + 1) = 19$, shape parameter $\beta = 3.7$, and -6 dB cutoff frequency $f_c = 0.1125$ [6], [8].

We designed RF codes using the search approach described in Section III and compared their efficiencies with those of the codes designed using the modulation approach. The additive noise sampled by the ADC was assumed to be a white noise. Furthermore, we assumed that the SNR defined as the ratio of the peak signal power to the average noise power at baseband was 1 when transmitting a single-bit signal. Section IV-A describes the RF codes corresponding to an assumed transducer response. Section IV-B presents the impulse response of a transducer and the consequent designs of the matching RF codes. The effects of quantizing filter coefficients on compression performance are discussed in Section IV-C.

A. Results for a Gaussian-Shaped Transducer Response

Codes were designed assuming that the transducer has a Gaussian frequency response with a center frequency f_0 of 25 MHz and a -6 dB bandwidth of 15 MHz. The parameters of the genetic algorithm were $N_1 = 200$, $N_2 = 100$, $p = 1/N$, and $N_{iter} = 1000$. Given a specific code length and a base sequence, we realized $N_3 = 200$ trials and calculated the efficiencies of the 10 RF codes with the largest I_E values, in which the code with the highest efficiency was chosen to be the final RF code. Twenty-six codes were designed in this way, nine of which correspond to $N = 32$ to 64 with a step size of 4 using a two-cycle square wave [i.e., $b(n) = (-1)^n$ and $N_B = 4$] as the base sequence (Table I), with the others corresponding to $N = 32$ to 64 with a step size of 2 using a one-cycle square wave [i.e., $b(n) = (-1)^n$ and $N_B = 2$] as the base sequence (Table II). Note that, before transforming a code into its hexadecimal representation, all the bits equal to -1 were replaced with 0. Tables I and II also list the codes designed using the modulation approach, which were used as the references. The wideband sequences for the modulation approach were the sequences minimizing the noise enhancement factor [9]. That is, the output SNR will be well maintained if inverse filtering is applied to compress such a sequence (or code) and the noise is white. Note that the above statement neglects the transducer frequency response; a base sequence is necessary for pulse shaping (i.e., controlling the band of the RF code) if the transducer is taken into account. RF codes have been designed [3], [4] using the modulation approach with previously listed sequences [9].

TABLE II
HEXADECIMAL REPRESENTATIONS OF THE RF CODES DESIGNED USING THE SEARCH APPROACH (SECOND COLUMN) AND THE MODULATION APPROACH (FIFTH COLUMN) FOR $b(n) = (-1)^n$ AND $N_B = 2$.[1]

	Search approach		Modulation approach	
N	RF code	N_C	Wideband sequence	RF code
32	3AAB5A4C	16	2833	59955A5A
34	03AAB5A4C	17	04C2B	165A5599A
36	3C96A5577	18	0B477	59A656A6A
38	1A56AA9B0C	19	17421	166A655956
40	25AD72AA0C	20	05D39	5566A65A96
42	1D755AB4F6C	21	07C452	16AA5656659
44	02494A95457	22	0F88A4	5AA95959965
46	0906B5AAAF04	23	00E6D5	1555A969A666
48	0E952AEADA4F	24	111E2D	565656A959A6
50	0C17455AA525B	25	073F536	16A5AAA665A69
52	6214A5556C24F	26	063F56D	5695AAA6669A6
54	0DED2B562ABA6C	27	0F1112D	15AA56565659A6
56	65DD5252A8567B	28	38FEA4D	5A95AAA99965A6
58	07641556AB4A53C	29	031FD5B2	15A56AAA6669A59
60	6964AD6AAAF04C0	30	09BF8EB5	5969AAA95A99A66
62	032CAAA456A521CC	31	1CEADBF0	16A5A999A69AAA55
64	06B56AD352EAAE80	32	00F2D533	5555AA59A6665A5A

[1]The wideband sequences [9] necessary for the modulation approach are listed in the fourth column. The transducer was assumed to have a Gaussian frequency response with a 60% fractional bandwidth, and the additive noise sampled by the ADC was assumed to be white.

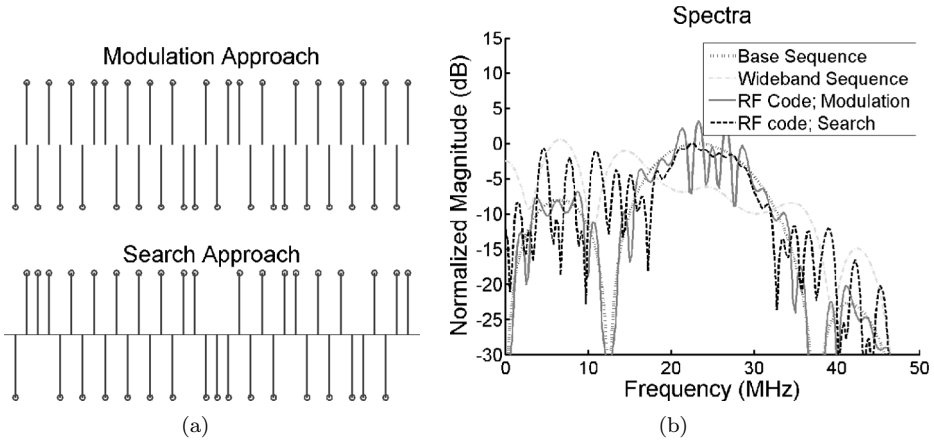

(a) (b)

Fig. 3. (a) 36-bit RF codes designed using the modulation and search approaches using a two-cycle square wave as the base sequence. (b) The normalized spectra of the base sequence, the wideband sequence for the modulation approach, and the RF codes.

As an example, the results from designing a 36-bit RF code using the modulation and search approaches with the two-cycle base sequence (i.e., $\{1, -1, 1, -1\}$) are shown in Fig. 3. Fig. 3(a) shows the RF codes designed using the two approaches, and Fig. 3(b) shows the normalized spectra of the base sequence, the wideband sequence for the modulation approach, and the RF codes. The spectrum in the transducer passband of the RF code designed using the search approach is smoother and thus easier to equalize than that designed using the modulation approach, resulting in a better compression performance and a higher efficiency. Note that Fig. 3(b) also illustrates that the base sequence controls the sampling ratio. If the base sequence $\{1, 1, -1, -1, 1, 1, -1, -1\}$ is used instead of $\{1, -1, 1, -1\}$, the sampling ratio will be 4 instead of 2. Given a code length T_c, N will increase by a factor of 2. Because there are more adjustable bits, the code designed using the search approach will have a higher efficiency traded with a higher bit rate. For example, the 72-bit code "1CE73988CCCCCDD936" operating at a bit rate of 100 MHz has an efficiency of 1.11 dB (resulting from an SNR of 21.31 dB at a filter length of 1.375 μs), which is 0.81 dB higher than that of its corresponding 36-bit code operating at 50 MHz.

Fig. 4(a) shows the efficiencies of codes as functions of their lengths. Each code designed using the search approach has a higher efficiency than its corresponding code designed using the modulation approach with the same base sequence, with the difference ranging between 1 and 6 dB. In addition, the efficiencies of codes designed using

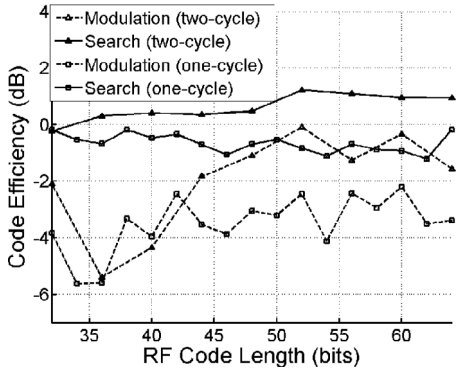

(a)

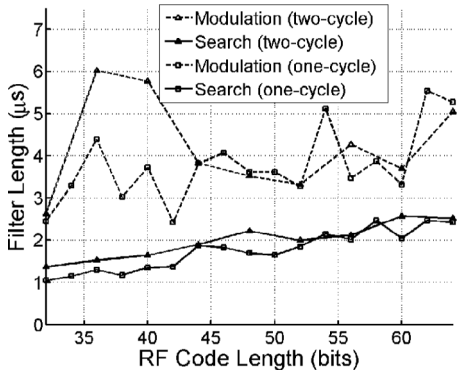

(b)

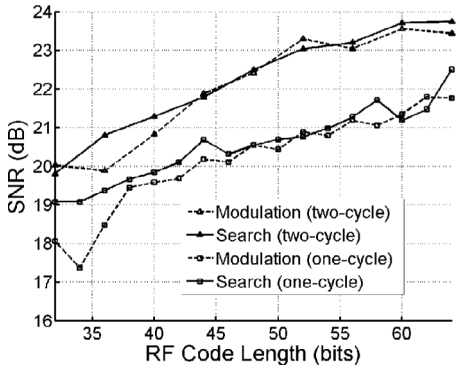

(c)

Fig. 4. Results for a Gaussian-shaped transducer response with a center frequency of 25 MHz and a −6 dB bandwidth of 15 MHz. (a) The efficiencies of codes as functions of their lengths. (b) The filter lengths that resulted in the maximal E_{cf} values equal to the code efficiencies. (c) The output SNRs corresponding to the filter lengths shown in (b).

the search approach are more independent of their lengths. Fig. 4(b) shows the filter lengths that resulted in the maximal E_{cf} values (i.e., the code efficiencies); the filter length is roughly proportional to the code length for the search approach. The ratios of the filter length to the code length range over [1.9, 2.3] and [1.5, 2.1] with the two- and one-cycle base sequences, respectively. In contrast, the filter length fluctuates markedly as the code length increases for the modulation approach; the ratios of the filter length to the code length range over [3.1, 8.4] and [2.8, 6.1] with the two- and one-cycle base sequences, respectively. Fig. 4(c) shows the output SNRs corresponding to the filter lengths

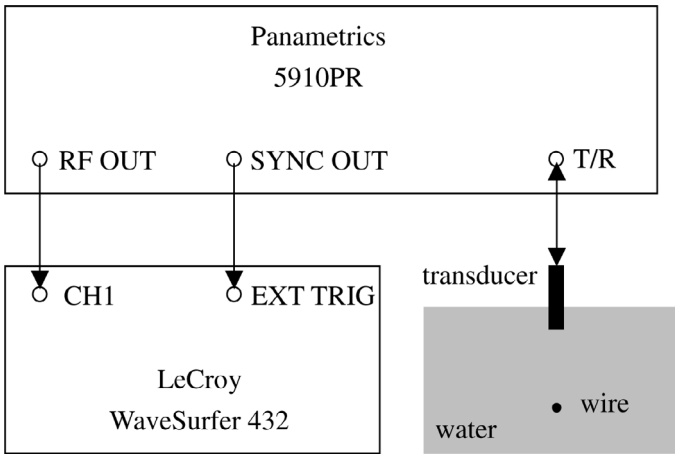

Fig. 5. Block diagram of the experimental setup used to measure the impulse response of a real transducer.

that resulted in the maximal E_{cf} values. Because the search approach tends to maximize the code efficiency instead of the SNR, some codes designed using this approach have SNRs that are lower than those of the corresponding codes designed using the modulation approach. In general, for a given code length, the SNR differs little between the codes designed using the two approaches; that is, the improvement in code efficiency using the search approach is mainly attributable to the reduction in the filter length. Furthermore, using a two-cycle square wave instead of a one-cycle square wave as the base sequence results in higher SNRs [Fig. 4(c)] due to the better match between the spectrum of the former base sequence and the transducer frequency response. This explains why the codes designed using the two-cycle base sequence have higher efficiencies, as shown in Fig. 4(a).

B. Results for a Measured Transducer Response

Fig. 5 shows the experimental setup used to measure the impulse response of a real transducer, which had a diameter of 6.35 mm and a focal length of 12.7 mm (V324, Panametrics, Waltham, MA). A pulser/receiver (5910PR, Panametrics) operating in pulse-echo mode was used to drive the transducer with a negative impulse, to receive and provide a noninverting 66 dB gain with −3 dB bandwidth between 5 and 400 MHz to the echo signal from a metal wire, and to synchronize an oscilloscope (WaveSurfer 432, LeCroy, Chestnut Ridge, NY) at a pulse repetition frequency of 200 Hz. The wire was measured to have a diameter of 32 μm and was placed 12.4 mm from the transducer. The amplified echo was digitized by the oscilloscope at a sampling rate of 2 GHz with an amplitude resolution of 8 bits.

Assuming that the effects of the finite bandwidths of the transmitted impulse and the amplifier in the receiver were negligible—although a thin wire was used instead of a small sphere—we treated the minus of the recorded echo e_{pulse} as a scaled approximation of the two-way impulse response of the transducer near the focus. Therefore, the

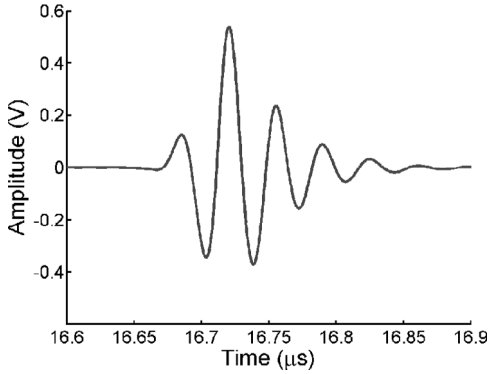

(a)

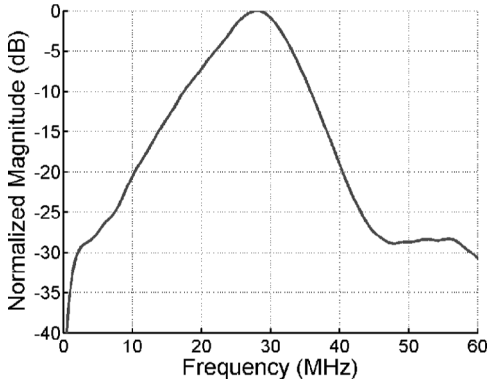

(b)

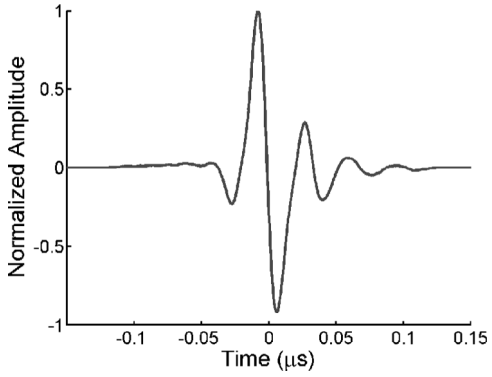

(c)

Fig. 6. (a) The averaged echo signal reflected from a wire. (b) The spectrum of the echo signal. (c) The one-way impulse response derived from the echo signal.

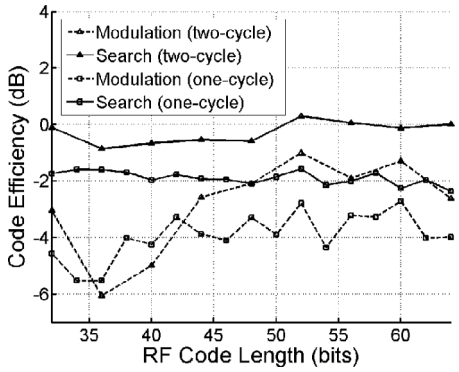

(a)

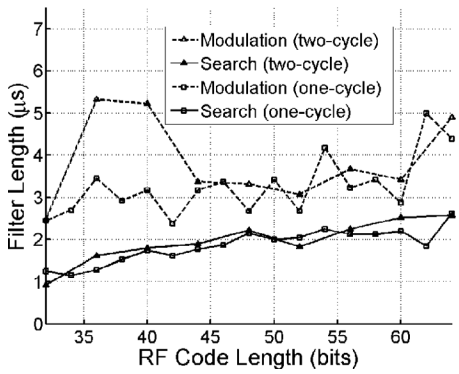

(b)

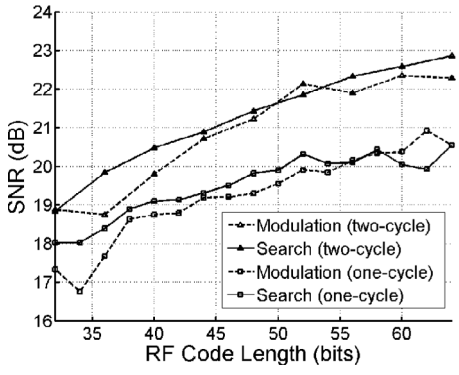

(c)

Fig. 7. Results for the measured transducer response shown in Fig. 6. (a) The efficiencies of codes as functions of their lengths. (b) The filter lengths that resulted in the maximal E_{cf} values equal to the code efficiencies. (c) The output SNRs corresponding to the filter lengths shown in (b).

normalized transducer response can be estimated using the following relation: $h_{\mathrm{t}}(t) \propto \mathbf{F}^{-1}\left\lfloor (\mathbf{F}\left[-e_{\mathrm{pulse}}(t)\right])^{1/2} \right\rfloor$, where $\mathbf{F}$ and $\mathbf{F}^{-1}$ denote forward and inverse Fourier transforms, respectively.

Figs. 6(a) and (b) show the echo signal e_{pulse} from the wire (which is the average of 2000 records) and its spectrum, respectively. The estimated center frequency and one-way −6 dB bandwidth were 26.4 and 20.7 MHz, respectively. The estimated transducer impulse response is shown in Fig. 6(c).

Twenty-six RF codes corresponding to the measured transducer response were designed using the search approach with the same parameters as used in Section IV-A for the genetic algorithm, nine of which correspond to $N = 32$ to 64 with a step size of 4 using a two-cycle square wave as the base sequence, with the others corresponding to $N = 32$ to 64 with a step size of 2 using a one-cycle square wave as the base sequence (Table III). Fig. 7(a) shows the efficiencies of codes as functions of their lengths, and Figs. 7(b) and (c) show the filter lengths that resulted in the maximal E_{cf} values (that equal the code efficiencies) and the corresponding output SNRs, respectively. These results are consistent with those given in Section IV-A. Each code designed using the search approach has a higher efficiency than its corresponding code designed using the modulation approach with the same base sequence, with the difference ranging between 0.5 and 5 dB. The higher

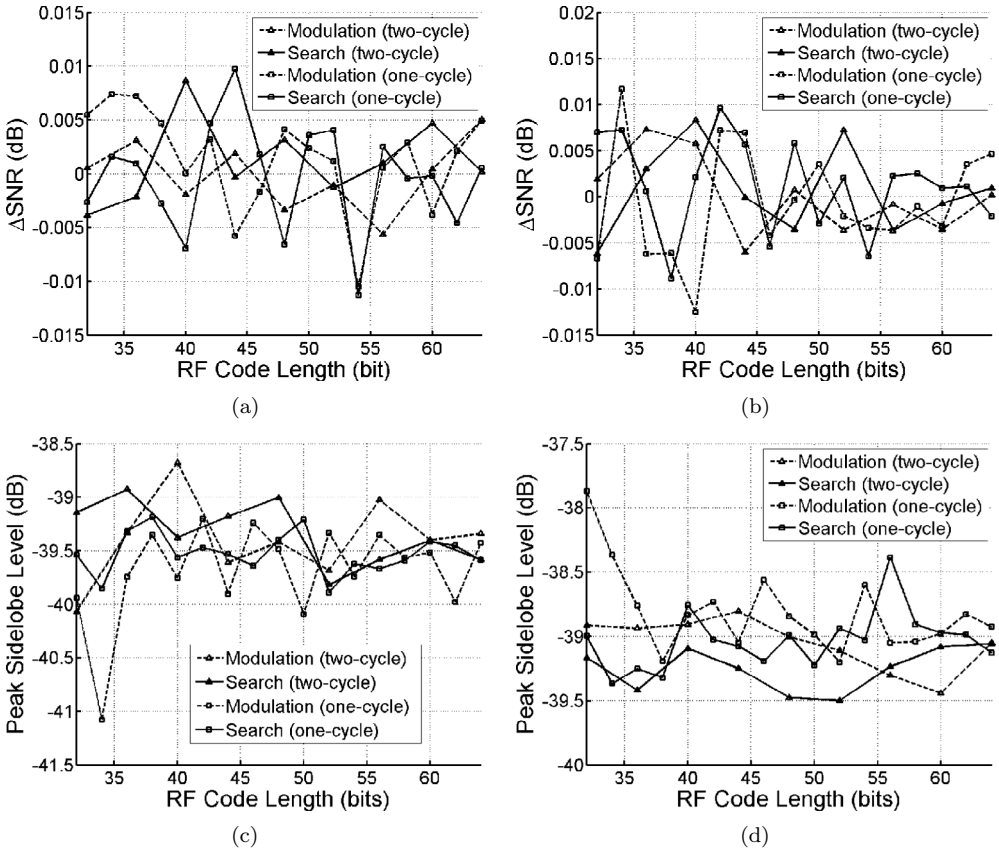

Fig. 8. Effects of amplitude quantization. (a) ΔSNRs (differences between SNR improvements with and without amplitude quantization) for the Gaussian-shaped transducer response. (b) ΔSNRs for the measured transducer response. (c) The peak sidelobe levels for the Gaussian-shaped transducer response. (d) The peak sidelobe levels for the measured transducer response.

TABLE III
HEXADECIMAL REPRESENTATIONS OF THE RF CODES DESIGNED USING THE SEARCH APPROACH FOR $b(n) = (-1)^n$ AND $N_B = 4$ (SECOND COLUMN), AND FOR $b(n) = (-1)^n$ AND $N_B = 2$ (THIRD COLUMN).[1]

N	Search approach	
	$N_B = 4$	$N_B = 2$
32	252A5551	0C96B557
34		03AAB5A4C
36	2D4A85551	7A52AAC93
38		096D2A55DD
40	5555AB52DB	3F555AD6C9
42		0DD55EA52DB
44	55552AD4B09	22AAD4A436C
46		027B5AB5574C
48	692952A15555	2484D554AD78
50		02254AA2A7B49
52	696B56AB55551	32E8AA950B4B4
54		18F5A9555B693F
56	755556AB54A5AD	09252B52AABB67
58		092127AAAB56B76
60	155556AB54AD2D6	212D4ABD4514D9F
62		1B68FB5556B57A73
64	0B5A56A955AAAAA8	0745145AAD4B4A67

[1]The transducer response measured with the setup shown in Fig. 5 is shown in Fig. 6, and the additive noise sampled by the ADC was assumed to be white.

code efficiency for the search approach relative to the modulation approach is mainly attributable to the reduction in filter length. With the two- and one-cycle base sequences, the ratios of the filter length to the code length range over [1.4, 2.3] and [1.5, 2.2] for the search approach, respectively, and over [2.9, 7.4] and [2.4, 4.8] for the modulation approach. Note that, in general, the code efficiencies are lower than those obtained in Section IV-A. This is due to the definition of SNR reference given at the beginning of this section. Because the transducer considered in the subsection has a wider bandwidth, a higher echo signal level will be obtained when a single-bit signal is transmitted. Therefore, setting the SNR corresponding to a single-bit firing signal to 1 equivalently assumes more noise. Also note that the codes designed using the modulation approach with the one-cycle base sequence adapt to the increased transducer bandwidth better than the other three groups of codes. Nonetheless, in terms of improving the SNR, those codes are worse than the others.

C. Quantization Effects

All the above results were obtained based on floating-point operations. In practical situations, filter coefficients may be quantized to fixed-point numbers. To evaluate the effects of amplitude quantization on pulse compression performance, for each code we quantized the real

and imaginary parts of the compression filter $h_o(n)$ to 8 bits, repeated the pulse compression procedure, and compared the resultant SNR, $SNR_{dB,q}$, with the SNR corresponding to the ideal filter, $SNR_{dB,i}$. Define ΔSNR as $SNR_{dB,q} - SNR_{dB,i}$. Figs. 8(a) and (b) show the ΔSNRs as functions of the code length for the Gaussian-shaped and measured transducer responses, respectively. All the ΔSNR values are small. Note that ΔSNR is equal to the difference between code efficiencies with and without amplitude quantization. Figs. 8(c) and (d) shows the peak sidelobe levels for the Gaussian-shaped and measured transducer responses, respectively. The results show that amplitude quantization only slightly degraded the pulse compression performance.

V. Conclusions

This paper proposes an approach to designing binary codes having a low sampling ratio and providing efficient SNR improvements. Unlike the conventional modulation approach in which a base sequence is used to modulate wideband sequences up to the transducer passband, which thereby excludes a major portion of the codes as possible RF codes, the proposed search approach uses a genetic algorithm to search all the codes that match the transducer passband; hence, the resultant codes can improve the SNR more efficiently. In the study, the bit rate was set to 50 MHz in order to keep the sampling ratios about 2, and two transducer responses were considered in order to demonstrate the adaptability of the proposed approach. Assuming that the transducer has an ideal Gaussian frequency response with a center frequency of 25 MHz and a −6 dB bandwidth of 15 MHz, the codes designed using the proposed approach outperformed those designed using the modulation approach by 1 to 6 dB in terms of code efficiency (i.e., in terms of the capacity for improving the SNR normalized by the total length of the code and the filter). When a real transducer with a center frequency of 26.4 MHz and a one-way −6 dB bandwidth of 20.7 MHz was considered, the codes designed using the proposed approach were superior by 0.5 to 5 dB. Our approach can be applied to designing binary codes with SNR improvements in high-frequency ultrasound systems, for which using arbitrary-waveform transmitters may be infeasible. A reasonable bit rate of 50 MHz will suffice if the ultrasonic center frequency is 25 MHz.

Acknowledgments

The authors would like to thank Dr. Matt O'Donnell for providing the equipment, including the pulser/receiver and the oscilloscope, necessary for measuring the transducer impulse response, and the reviewers for numerous helpful comments.

References

[1] M. O'Donnell, "Coded excitation system for improving the penetration of real-time phased-array imaging systems," *IEEE Trans. Ultrason., Ferroelect., Freq. Contr.*, vol. 39, no. 3, pp. 341–351, 1992.

[2] R. Y. Chiao and X. Hao, "Coded excitation for diagnostic ultrasound: A system developer's perspective," *IEEE Trans. Ultrason., Ferroelect., Freq. Contr.*, vol. 52, no. 2, pp. 160–170, 2005.

[3] M. O'Donnell and Y. Wang, "Coded excitation for synthetic aperture ultrasound imaging," *IEEE Trans. Ultrason., Ferroelect., Freq. Contr.*, vol. 52, no. 2, pp. 171–176, 2005.

[4] Y. Wang, K. Metzger, D. N. Stephens, G. Williams, S. Brownlie, and M. O'Donnell, "Coded excitation with spectrum inversion (CEXSI) for ultrasound array imaging," *IEEE Trans. Ultrason., Ferroelect., Freq. Contr.*, vol. 50, no. 7, pp. 805–823, 2003.

[5] R. L. Haupt and S. E. Haupt, *Practical Genetic Algorithms*. New York: Wiley, 1998.

[6] S.-W. Huang and P.-C. Li, "Arbitrary waveform coded excitation using bipolar square wave pulsers in medical ultrasound," *IEEE Trans. Ultrason., Ferroelect., Freq. Contr.*, vol. 53, no. 1, pp. 106–116, 2006.

[7] B. Haider, P. A. Lewin, and K. E. Thomenius, "Pulse elongation and deconvolution filtering for medical ultrasonic imaging," *IEEE Trans. Ultrason., Ferroelect., Freq. Contr.*, vol. 45, no. 1, pp. 98–113, 1998.

[8] A. V. Oppenheim and R. W. Schafer, *Discrete-Time Signal Processing*. Englewood Cliffs, NJ: Prentice-Hall, 1989.

[9] J. Ruprecht and M. Rupf, "On the search for good aperiodic binary invertible sequences," *IEEE Trans. Inform. Theory*, vol. 42, no. 5, pp. 1604–1612, 1996.

Sheng-Wen Huang was born in 1971 in Changhua, Taiwan, R.O.C. He received the B.S. and Ph.D. degrees from National Taiwan University, Taipei, Taiwan, R.O.C., in 1993 and 2004, respectively, both in electrical engineering. He worked as a postdoctoral researcher at National Taiwan University from 2004 to 2005, and is currently a postdoctoral researcher with the Department of Biomedical Engineering at the University of Michigan. His current research interests include thermal strain imaging, coded excitation, and optoacoustic imaging.

Pai-Chi Li (S'93–M'95–SM'01) received the B.S. degree in electrical engineering from National Taiwan University, Taipei, Taiwan, R.O.C., in 1987, and the M.S. and Ph.D. degrees from the University of Michigan, Ann Arbor, MI, in 1990 and 1994, respectively, both in electrical engineering: systems.

He was a research assistant with the Department of Electrical Engineering and Computer Science of the University of Michigan from 1990 to 1994. He joined Acuson Corporation, Mountain View, CA, as a member of the Technical Staff in June 1994. His work with Acuson was primarily in the areas of medical ultrasonic imaging system design for both cardiology and general imaging applications. In August 1997, he went back to the Department of Electrical Engineering at National Taiwan University, where he is currently Professor of Department of Electrical Engineering and Director of Institute of Biomedical Electronics and Bioinformatics. His current research interests include biomedical ultrasonic imaging and signal processing.

Dr. Li is a senior member of IEEE and Associate Editor of *IEEE Transactions on Ultrasonics, Ferroelectrics, and Frequency Control*. He is also on the Editorial Board of *Ultrasonic Imaging*. He received the 2005 Outstanding Electrical Engineering Professor Award, the Chinese Institute of Electrical Engineering, the 2004 Distinguished Research Award, National Science Council, the 2004 Distinguished Research Achievement Award, National Taiwan University, the 2003 Outstanding Researcher Award, National Taiwan University, the

2002 Dr. Wu Dayou Research Award from National Science Council, the 2002 Outstanding Young Electrical Engineer Award from Chinese Institute of Electrical Engineering and the Distinguished Industrial Collaboration Award of Ministry of Education. He was also the recipient of the Distinguished Achievement Award in Electrical Engineering: Systems in 1994 for his outstanding academic achievement at the University of Michigan.

Performance Evaluation of Coherence-Based Adaptive Imaging Using Clinical Breast Data

Shun-Li Wang, Chen-Han Chang, Hsin-Chia Yang, Yi-Hong Chou, and Pai-Chi Li, *Senior Member, IEEE*

***Abstract*—Sound-velocity inhomogeneities degrade both the spatial resolution and the contrast in diagnostic ultrasound. We previously proposed an adaptive imaging approach based on the coherence of the data received in the channels of a transducer array, and we tested it on phantom data. In this study, the approach was tested on clinical breast data and compared with a correlation-based method that has been widely reported in the literature. The main limitations of the correlation-based method in ultrasonic breast imaging are the use of a near-field, phase-screen model and the integration errors due to the lack of a two-dimensional (2-D) array. In contrast, the proposed coherence-based method adaptively weights each image pixel based on the coherence of the receive-channel data. It does not make any assumption about the source of the focusing errors and has been shown to be effective using 1-D arrays. This study tested its in vivo performance using clinical breast data acquired by a programmable system with a 5 MHz, 128-channel linear array. Twenty-five cases (6 fibroadenomas, 10 carcinomas, 6 cysts, and 3 abscesses) were investigated. Relative to nonweighted imaging, the average improvements in the contrast ratio and contrast-to-noise ratio for the coherence-based method were 8.57 dB and 23.2%, respectively. The corresponding improvements when using the correlation-based method were only 0.42 dB and 3.35%. In an investigated milk-of-calcium case, the improvement in the contrast was 4.47 dB and the axial and lateral dimensions of the object were reduced from 0.39 to 0.32 mm and from 0.51 to 0.43 mm, respectively. These results demonstrate the efficacy of the coherence-based method for clinical ultrasonic breast imaging using 1-D arrays.**

I. Introduction

A primary performance limitation of diagnostic ultrasound is the distortion introduced by sound-velocity inhomogeneities in human tissue. Because the sound velocity varies over a wide range (e.g., 1450 m/s in fat and 1665 m/s in collagen [1]), the use of a constant sound velocity when calculating focusing delays inevitably results in focusing errors. Such focusing errors also are termed phase aberrations, and they degrade both the spatial resolution and the contrast in the resultant images.

Manuscript received October 4, 2006; accepted March 2, 2007. Support from the National Science Council of Taiwan under grant no. NSC 95-2221-E-002-170 is gratefully acknowledged.

S.-L. Wang, C.-H. Chang, H.-C. Yang, and P.-C. Li are with the Department of Electrical Engineering, National Taiwan University, Taipei, Taiwan.

Y.-H. Chou is with the Department of Radiology, Taipei Veterans General Hospital, Taipei, Taiwan.

P.-C. Li also is with the Graduate Institute of Biomedical Electronics and Bioinformatics, National Taiwan University, Taipei, Taiwan (e-mail: paichi@cc.ee.ntu.edu.tw).

Digital Object Identifier 10.1109/TUFFC.2007.438

Several phase-aberration correction techniques have been proposed to adaptively reduce these errors and thereby improve the image quality [2]–[15]. Flax and O'Donnell [2] proposed a correlation-based method that modeled sound-velocity inhomogeneities as a near-field phase screen, which assumes that time-delay errors produce phase aberrations only at the surface of the transducer. The near-field phase screen can be estimated by finding the peak of the cross-correlation function of the signals from adjacent channels [2], [3], or using those from the individual channels to the beam sum [4] or partial beam sum [5]. Phase aberrations theoretically can be corrected by compensating for the time-delay errors, but several factors have limited the clinical applications of correlation-based methods. First, the near-field phase-screen model is often inadequate because sound-velocity inhomogeneities result in not only time-delay errors but also energy-level fluctuations and waveform distortion. This led to a displaced phase-screen model that accounts for phase aberrations as a phase screen positioned some distance from the transducer surface [6]. However, its performance in ultrasonic breast imaging is still insufficient because the sound-velocity variations in breast are more distributed. The other reason for the inadequate performance of correlation-based methods is the three-dimensional (3-D) nature of sound-velocity inhomogeneities. Preventing aberrator integration errors in time-delay estimation requires the use of a 1.5-D or 2-D array [7], [16]. However, these are not yet in widespread use in clinics due to the significantly increased system complexity and cost.

Adaptive sidelobe-reduction techniques also can be used to reduce focusing imperfections [8]–[15], one example of which is the parallel adaptive receive-compensation algorithm (PARCA) [8]–[11]. At each image point, the PARCA removes unwanted sidelobe contributions and maintains the mainlobe signal intensity by estimating the on-axis and off-axis signal components. However, a significant drawback of PARCA is its computational complexity.

Another adaptive sidelobe-reduction method is based on the use of the coherence factor (CF) of the receive-channel data [12]–[14], which represents a focusing-quality index:

$$\mathrm{CF} = \frac{\left|\sum_{i=0}^{N-1} S(i,t)\right|^2}{N\sum_{i=0}^{N-1} |S(i,t)|^2}. \quad (1)$$

where N denotes the total number of array channels, $S(i)$ is the signal received at channel i, and t denotes the time corresponding to the depth of the image point. In other words, the CF is defined as the ratio between the energy of the coherent sum to the total incoherent energy (i.e., N times the incoherent sum). Therefore, an image point with a high CF value possesses good focusing quality, and its amplitude should be maintained, whereas the amplitude of an image point with a low CF value possesses poor focusing quality and its amplitude should be suppressed. Thus, this method is effectively an adaptive weighting technique in which the amplitude of each image pixel is weighted by the corresponding CF such that the unwanted sidelobes are effectively reduced. The CF also has been modified to the generalized CF (GCF) to accommodate the coherence properties of speckle-generating objects [15]. The efficacy of the GCF-weighting method has been demonstrated for phantom data [15]. The main purpose of the present study was to test the feasibility of applying the GCF to clinical breast data. Specifically, the method was applied to different types of breast lesions: cyst, fibroadenoma, carcinoma, and abscess.

This paper explores the contrast and other general characteristics of the GCF technique. It is organized as follows. In Section II, the basic principles and experimental methods for the GCF-weighting method are described. Section III presents the experimental results. The results then are discussed in Section IV. The paper concludes in Section V.

II. Imaging Principles and Research Methods

A. Generalized Coherence Factor

The GCF is calculated using the Fourier spectrum of the aperture-domain data, which are the data received in individual array channels after the application of focusing delays but prior to beam summation. The corresponding Fourier spectrum is obtained by performing a discrete Fourier transform across the array at each time (i.e., depth):

$$S(i,t) \xrightarrow{\text{FT}} p(k,t), \tag{2}$$

where $p(k,t)$ is the Fourier spectrum with spatial frequency index k and time variable t. As described in [11], the spectrum can be viewed as an approximation of multiple parallel receive beams centered at the transmit beam direction. The definition of the CF described in (1) also can be expressed as follows:

$$\text{CF} = \frac{|p(0,t)|^2}{\sum_{k=-N/2}^{N/2-1} |p(k,t)|^2}. \tag{3}$$

The numerator of (3) is the energy of the dc component of the spectrum, and the denominator is the total spectral energy. The dc component represents the signals received from the transmit beam direction (i.e., on-axis component). The other components represent the signals from other angles (i.e., off-axis components).

Adaptive weighting using CF is feasible for point-like targets. However, for diffuse scatterers (i.e., speckle-generating objects), part of the mainlobe signal appears within the low-frequency region. Therefore, using the ratio of the dc energy to the total energy as a weighting factor underestimates the coherence. The GCF was proposed to take this into account [15], and it thus is defined as the ratio of the energy within a certain low-frequency region to the total energy:

$$\text{GCF} = \frac{\sum_{k=-M_0}^{M_0} |p(k,t)|^2}{\sum_{k=-N/2}^{N/2-1} |p(k,t)|^2}, \tag{4}$$

where M_0 denotes the prespecified cut-off frequency in the spatial-frequency domain. Note that the CF is the special case of the GCF with $M_0 = 0$.

B. Signal Processing Procedures

The signal processing procedures we used are shown schematically in Fig. 1. After the echo signal is received and digitized by the A/D converter, the received RF data are demodulated down to baseband, and the baseband beamformer applies geometric focusing delays and phase rotations to the baseband data. The B-mode image then is obtained by performing beam summation across the array with prespecified apodization. Note that the geometric delays are adjusted for every depth on receive to achieve dynamic focusing. However, as previously mentioned, the focusing delays applied in a beamformer are derived by assuming a constant sound velocity without considering the sound velocity variations in soft tissues. Therefore, it is the purpose of the proposed GCF method to estimate and suppress such focusing errors. Because the carrier frequency needs to be removed when calculating the coherence factor, baseband beamformers are preferred. The GCF is calculated for the specific configuration using the delayed baseband data across the aperture at all ranges prior to beam summation. The amplitude of the beam sum then simply is multiplied by the corresponding GCF:

$$x_{\text{weighted}} = \text{GCF} \cdot x, \tag{5}$$

where x denotes the original amplitude of the beam-sum data, and x_{weighted} denotes the amplitude of the beam sum weighted by the GCF. The weighted beam-sum data then are stored in a buffer for further signal processing, scan conversion, and display.

C. Clinical Data Acquisition

Experiments were performed to evaluate the efficacy of the proposed method in clinical breast imaging. Clinical

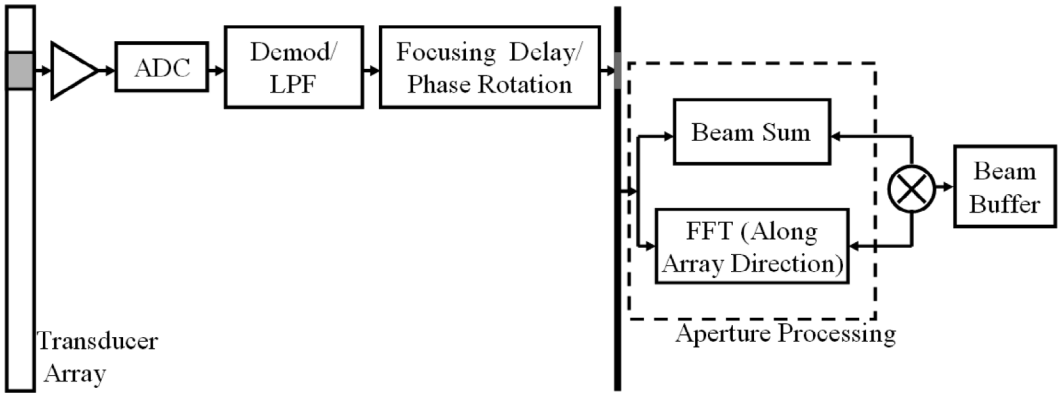

Fig. 1. Signal processing procedures of the proposed GCF-weighting technique.

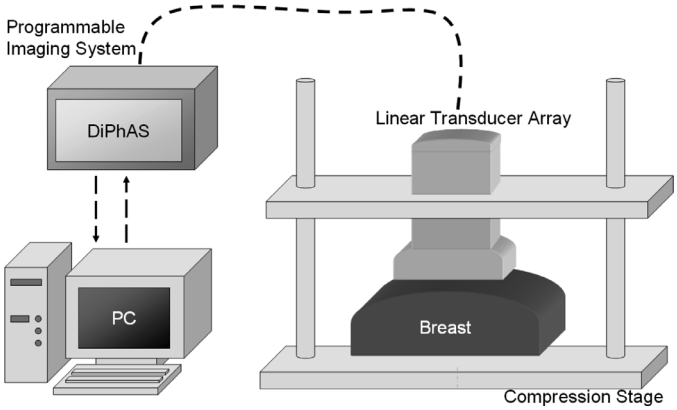

Fig. 2. Clinical data-acquisition apparatus.

data of the female breast were collected in the ultrasonic consulting room of the Taipei Veterans General Hospital by one of the authors (Y.-H. Chou) after patients had provided informed consent. A total of 25 patients aged from 23 to 89 years were included. Among them, there were 6 fibroadenomas, 10 carcinomas, 6 cysts, and 3 abscesses. A schematic of the experimental apparatus is shown in Fig. 2, which included a mechanical compression stage similar to that used in X-ray mammography to stabilize the breast during data acquisition. A programmable imaging system with 64 system channels (DiPhAS, IBMT, Fraunhofer Institutes, St. Ingbert, Germany) was used to acquire the aperture-domain data (i.e., the receive-channel data prior to beam summation). The linear transducer array had a center frequency of 5 MHz, a −6 dB bandwidth of 4.1 MHz and 128 channels (L6/128, Sound Technology, State College, PA) at a pitch of 0.3 mm. A complete data set was obtained from each patient (i.e., 128×128 RF A-mode scans recorded from the 128-element array, for which each A-mode scan represents the echo signal of a particular transmit/receive combination) at a sampling rate of 20 MHz. Each complete data set took approximately 3 s to acquire. The acquired data sets were used to reconstruct the aperture-domain data with full dynamic focus on both transmit and receive. In order to evaluate tissue motion, B-mode images were acquired and stored before and after full data set acquisition. The two images then were compared to make sure that no noticeable tissue motion was present. An f-number of 1 was applied for aperture control. All images displayed here are in linear gray scale mapping with a dynamic range of 60 dB and are shown in a linear scan format. The step size for the linear scan was 0.15 mm (i.e., half the pitch of the transducers). B-mode images are formed by applying transmit and receive focusing delays before beam summation, and multiple imaging methods can be compared with one another using the same data set.

III. Experimental Results

A. Cut-off Frequency M_0

In the GCF technique, cut-off frequency M_0 should be specified so as to achieve optimal performance. Both the contrast ratio (CR) and contrast-to-noise ratio (CNR) were used in the experiments to evaluate the effects of varying M_0. The CR is defined as the ratio between the mean value in a background region to that in a region of interest (ROI) [3]. The CNR is defined as the ratio between the CR and the standard deviation of the image intensity in a background region [4]. Fig. 3(a) shows an original image without application of the GCF-weighting method, and Figs. 3(b)–(f) show the GCF-weighted images with M_0 ranging from 0 to 4. Note that $M_0 = 0$ represents the case of using the CF. The background region and ROI used to calculate CRs and CNRs are indicated in Fig. 3(a) by the black and white boxes, respectively. The ROI in this case is a cyst. Note that in all cases the contrast is clearly improved, and the background noise is suppressed. Figs. 4(a) and (b) show the CR and CNR after GCF weighting as functions of M_0, respectively. Fig. 4(a) shows that the CR was improved in all cases, decreasing as M_0 increased. When the background-intensity variations are taken into account, Fig. 4(b) shows that the CNR was not improved when $M_0 = 0$. Nevertheless, with $M_0 \geq 1$, CNR improvement is again demonstrated. Specifically, the optimal CNR was achieved at $M_0 = 3$ in this case. The results indicate that using CF as a weighting index can

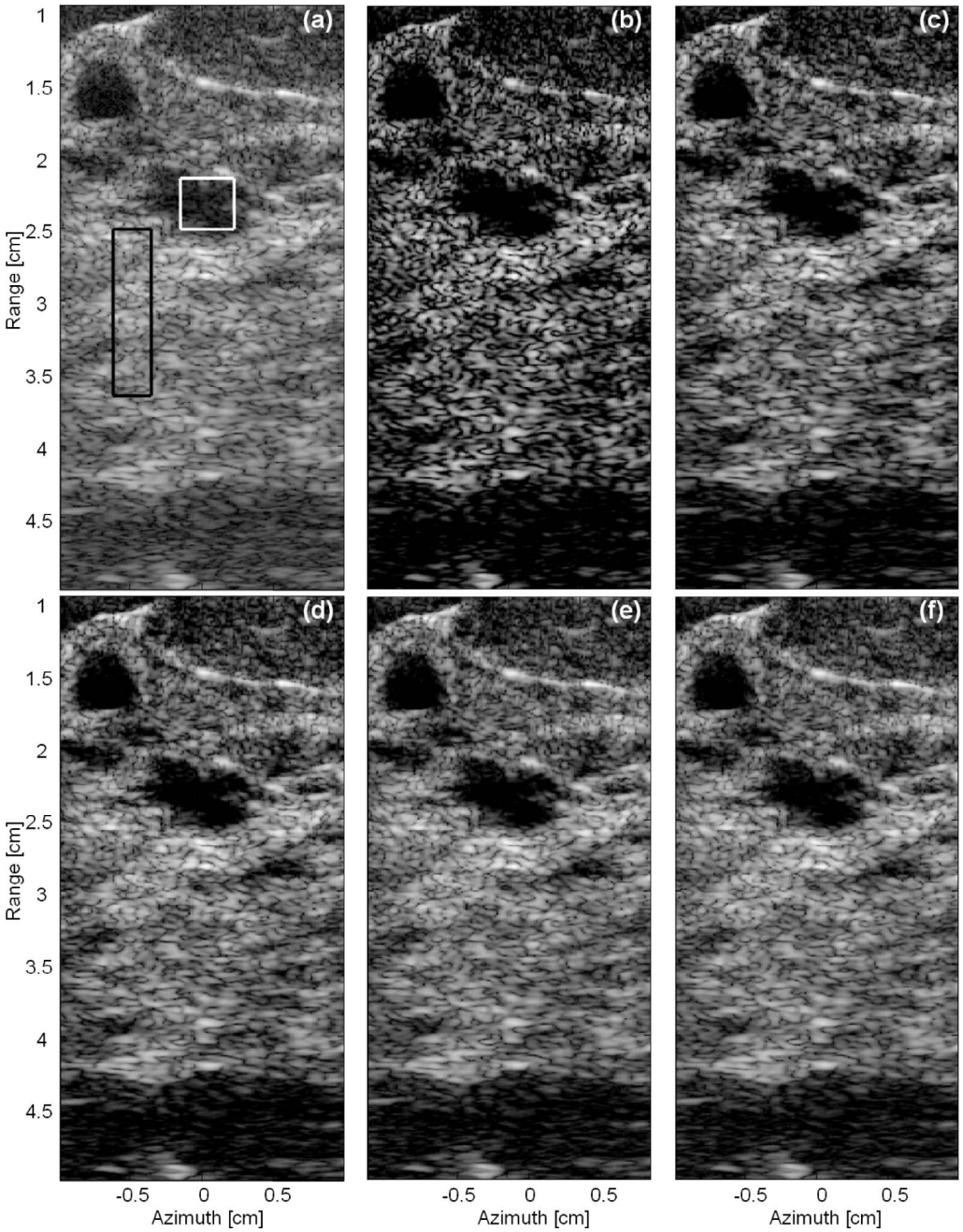

Fig. 3. Effects of cut-off frequency M_0 on the images of a a cyst, displayed with a dynamic range of 60 dB. (a) Original image. Black box indicates background region. White box indicates ROI. (b)–(f) GCF-corrected images for M_0 values of 0 (b), 1 (c), 2 (d), 3 (e), and 4 (f).

effectively increase the CR. However, CF also gives rise to strong intensity variations and degrades the CNR. This also is illustrated in Fig. 3(b) in which the CF-weighting technique introduced artifactual black holes in the background region, which in turn affect the detection of an ROI. Based on these results, $M_0 = 3$ was used in the subsequent investigations (which are described below).

B. Cyst

The sonogram needs to be interpreted accurately in order to avoid unnecessary biopsies and to differentiate a cyst from a solid mass. Fig. 5 shows images of a cyst in a 66-year-old female patient. The background and the ROI regions used in the CR and CNR calculations are indicated in Fig. 5(a) by the black and white boxes, respectively. Fig. 5(a) shows the original image, Fig. 5(b) shows the image obtained using the correlation-based method (as a reference) [2], [3], and Fig. 5(c) is the image obtained with adaptive compensation using GCF weighting. For the correlation-based method, time delay between adjacent channels was calculated by finding the peak position of the cross-correlation function of the signals received by the two channels. An infinite isoplanatic patch size (i.e., single aberration profile applied throughout the image) was used in this study without smoothing the aber-

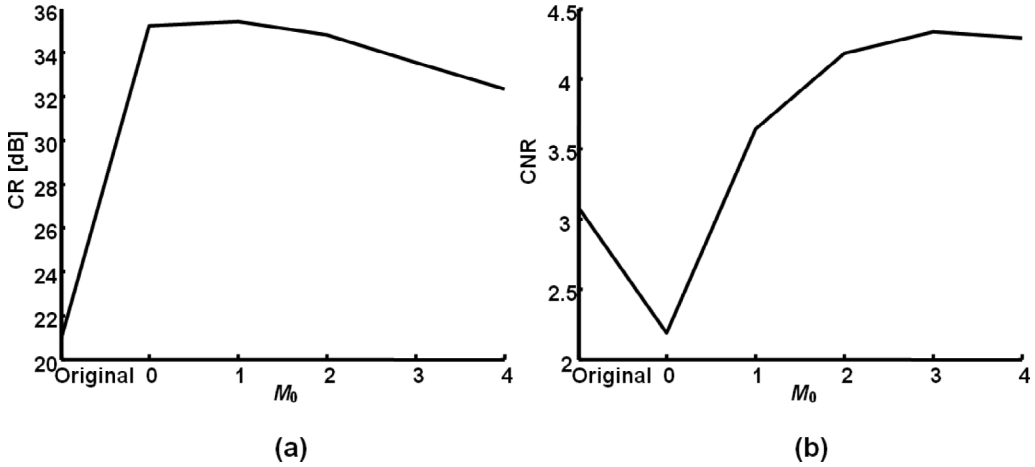

Fig. 4. Values of CR (a) and CNR (b) for the specimen shown in Fig. 3 as functions of M_0.

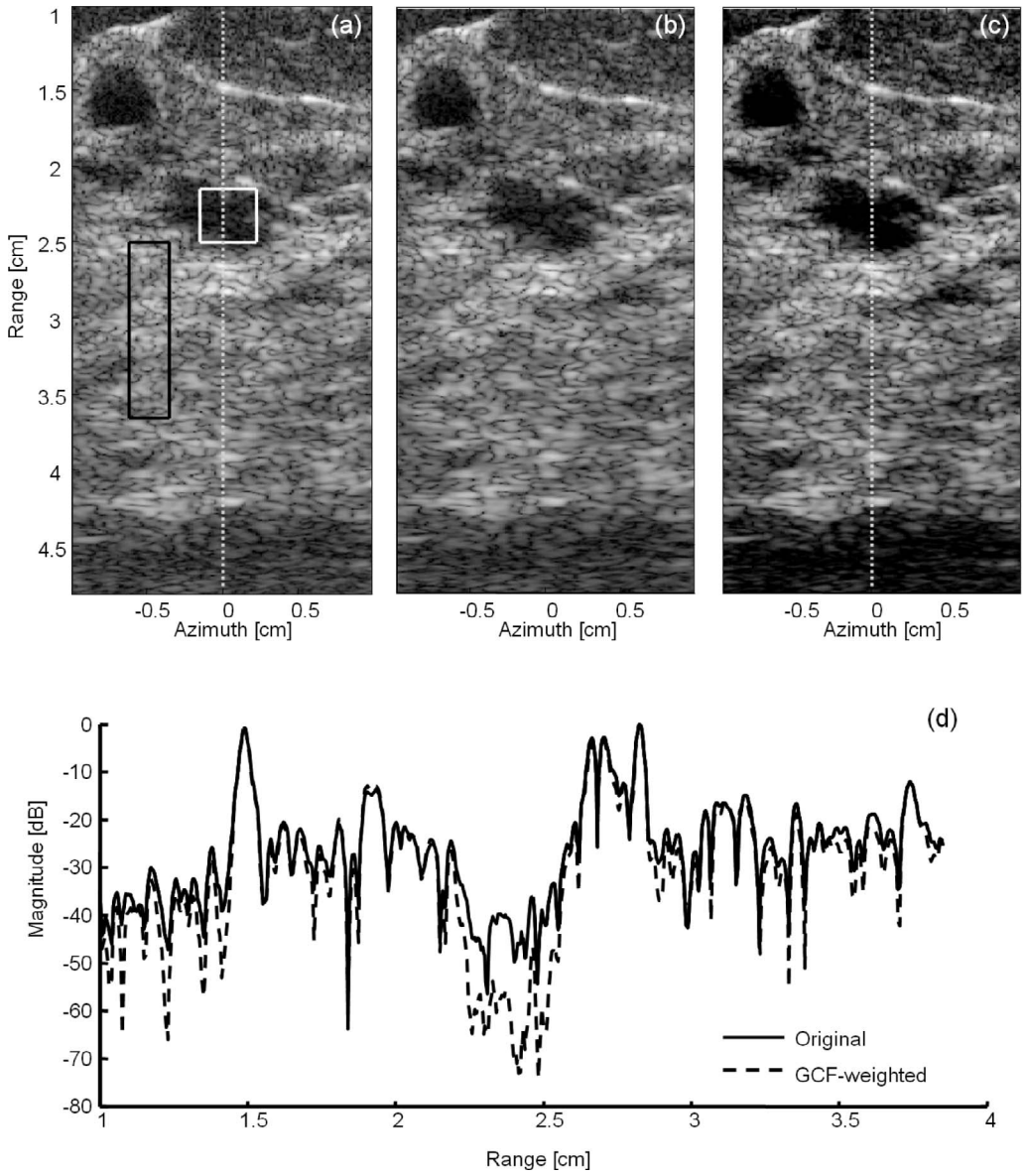

Fig. 5. Images of a cyst in a 66-year-old woman, displayed with a dynamic range of 60 dB: original B-mode image (a), and images obtained using the correlation-based method (b) and the GCF-weighting method (c). The black box in (a) indicates the background image. The white box indicates the ROI. (d) Intensities of the scan-line data along the gray dotted lines shown in (a) and (c) using solid and dashed lines, respectively.

ration profile. The aberration profile is applied after the linear components were removed. The CRs and CNRs were 20.97 dB and 3.07 for the original image, 20.52 dB and 2.95 for the correlation-based method, and 33.53 dB and 4.33 for the GCF-weighting method. With the correlation-based method, the CR and CNR were slightly degraded, by 0.44 dB and 3.85%, respectively. This may be due to the phase aberrations in the breast being more distributed, and aberrator integration errors may be present with the 1-D array. In contrast, the improvements in the CR and CNR using the GCF-weighting method were 12.56 dB and 40.97%, respectively. The original image shows an indistinct internal echo within the cystic mass. The GCF-weighted image shows that the signal within the cystic mass was effectively suppressed and that the CR was enhanced. The solid line in Fig. 5(d) shows the intensity along the scan line shown as the dotted vertical line in Fig. 5(a). With the proposed method, the intensity along this line [i.e., the vertical dotted line in Fig. 5(c)] is shown as the dashed line in Fig. 5(d). Note that image intensities between 1–1.4 cm and 2.2–2.5 cm are similar in the original image [Fig. 5(a)]. With the application of the proposed method; however, image intensities resulting from unwanted sidelobes in the cyst region (2.2–2.5 cm) are effectively reduced. The image intensities in the tissue region (1–1.4 cm) are less affected. Therefore, effective sidelobe reduction is demonstrated, and it is clear that the method is not just a simple "reject" control. The margin of the cyst was more distinct than that in the original image. These results illustrate the significant improvement in contrast and boundary definition in this case.

C. Fibroadenoma

Fig. 6 shows images of a fibroadenoma lesion in a 42-year-old female patient. The background and the ROI regions used in the calculation of the CR and CNR are indicated in Fig. 6(a) by the black and white boxes, respectively. Fig. 6(a) shows the original image, and Figs. 6(b) and (c) show the corrected images obtained using the correlation-based method and the GCF-weighting method, respectively. The CRs and CNRs were 16.92 dB and 2.76 for the original image, 17.51 dB and 2.82 for the correlation-based method, and 25.73 dB and 3.67 for the GCF-weighting method. The CR and CNR improved by 0.58 dB and 2.36% with the correlation-based method and by 8.81 dB and 33.07% with the GCF-weighting method. The original image shows poor boundary definition. However, with the application of the correlation-based method, no noticeable change was observed, and the method was not able to improve the image. But, the use of the GCF-weighting method noticeably improves the contrast and boundary definition in this case. In spite of these improvements, the suppression of the echo signal in the ROI region reduces the delineation of the interior echo, resulting in possible confusion when differentiating a fibroadenoma (solid) from a cyst (liquid). This requires further investigation. Nonetheless, in this case the lesion is determined as a fibroadenoma without ambiguity based on the boundary echogenicity. Typically, a cyst has brighter echoes at the boundary, and those of a fibroadenoma are not as strong.

D. Carcinoma

Fig. 7 shows images of a carcinoma lesion in a 63-year-old female patient. The background and the ROI used in the calculation of the CR and CNR are indicated in Fig. 7(a) by the black and white boxes, respectively. Fig. 7(a) shows the original image, and Figs. 7(b) and (c) show the corrected images obtained using the correlation-based method and the GCF-weighting method, respectively. The CRs and CNRs were 13.63 dB and 2.19 for the original image, 13.80 dB and 2.23 for the correlation-based method, and 21.52 dB and 2.87 for the GCF-weighting method. The CR and CNR improved by 0.16 dB and 1.59% with the correlation-based method and by 7.89 dB and 30.75% with the GCF-weighting method, respectively. Again, the original image shows an indistinct lesion margin. The internal echo and several echogenic foci indicating microcalcifications within the breast parenchyma also are not clearly evident. However, with the application of the correlation-based method, no noticeable change was observed, and the method was not able to improve the image. The GCF-weighted image shows better characterization of the margin, enhanced delineation of the internal architecture, and enhanced conspicuity of microcalcifications within the breast parenchyma due to improved spatial resolution and contrast.

E. Abscess

Fig. 8 shows images of an abscess lesion in a 31-year-old female patient. The background and the ROI used in the calculation of the CR and CNR are indicated in Fig. 8(a) by the black and white boxes, respectively. Fig. 8(a) shows the original image, and Figs. 8(b) and (c) show the corrected images obtained using the correlation-based method and the GCF-weighting method, respectively. The CRs and CNRs were 22.20 dB and 3.73 for the original image, 22.85 dB and 3.80 for the correlation-based method, and 32.11 dB and 4.59 for the GCF-weighting method. The CR and CNR improved by 0.65 dB and 1.83% with the correlation-based method and by 9.91 dB and 23.10% with the GCF-weighting method, respectively. The original image shows a well-circumscribed hypoechoic mass with internal echogenic debris, a slight posterior acoustic enhancement, and indistinct calcification. However, with the application of the correlation-based method, no noticeable change was observed, and the method was not able to improve the image. The GCF-weighted image shows a clearer lesion margin and enhanced delineation of the internal architecture due to improvement of the contrast.

F. Milk of Calcium

Fig. 9 shows images of a milk of calcium in a cyst lesion in a 25-year-old female patient. Fig. 9(a) shows the original image, and Figs. 9(b) and (c) show the corrected

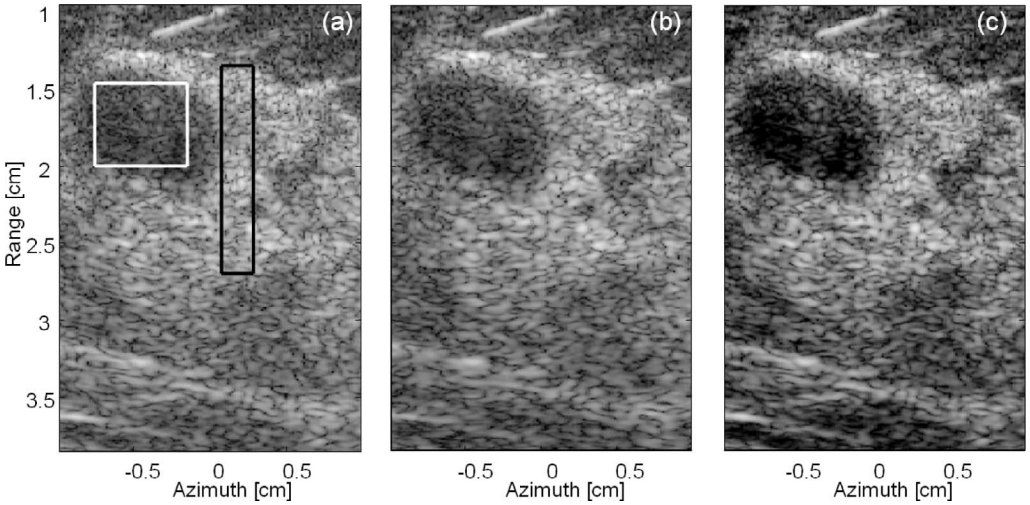

Fig. 6. Images of a fibroadenoma in a 42-year-old woman, displayed with a dynamic range of 60 dB: original B-mode image (a), and images obtained using the correlation-based method (b) and the GCF-weighting method (c). The black box in (a) indicates the background region. The white box indicates the ROI.

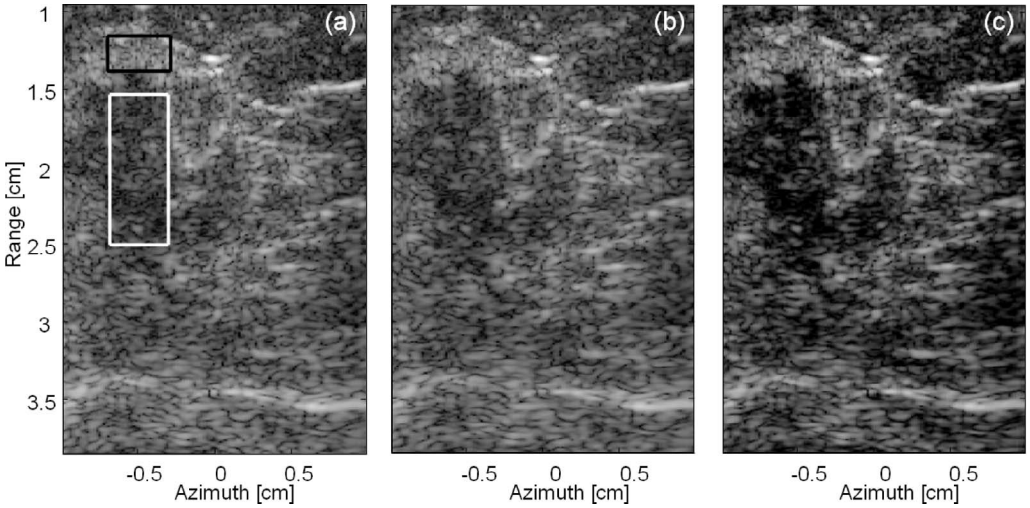

Fig. 7. Images of a carcinoma in a 63-year-old woman, displayed with a dynamic range of 60 dB: original B-mode image (a), and images obtained using the correlation-based method (b) and the GCF-weighting method (c). The black box in (a) indicates the background region. The white box indicates the ROI.

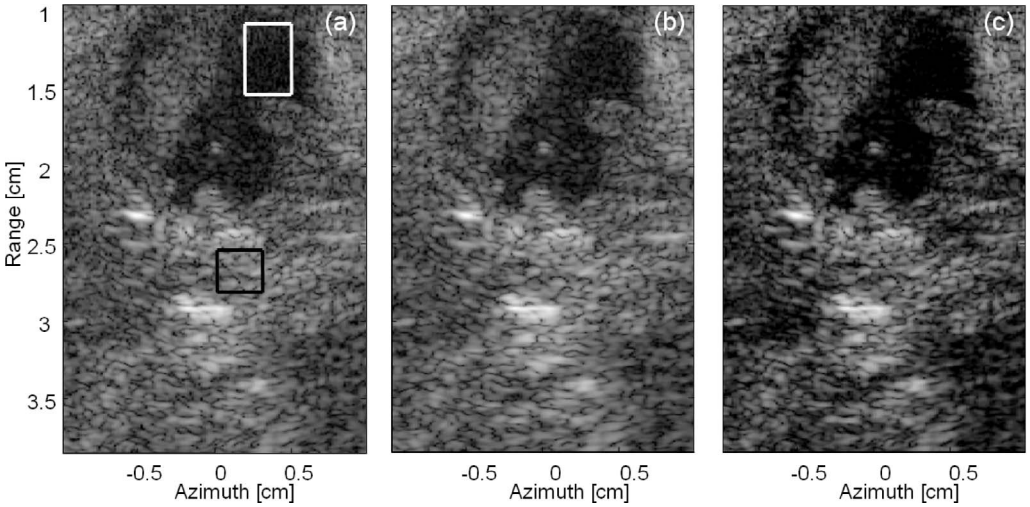

Fig. 8. Images of an abscess in a 31-year-old woman, displayed with a dynamic range of 60 dB: original B-mode image (a), and images obtained using the correlation-based method (b) and the GCF-weighting method (c). The black box in (a) indicates the background region. The white box indicates the ROI.

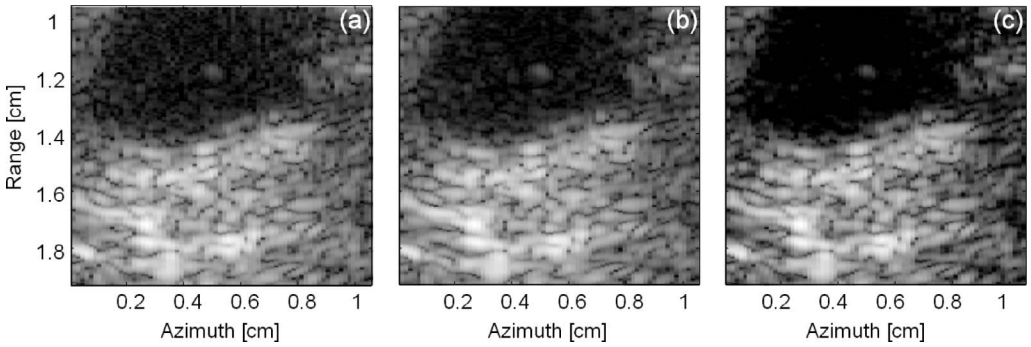

Fig. 9. Images of a milk of calcium in a cyst in a 25-year-old woman, displayed with a dynamic range of 60 dB: original B-mode image (a), and images obtained using the correlation-based method (b) and the GCF-weighting method (c).

TABLE I
SUMMARY OF THE CR AND CNR VALUES.

Patient no.	Age (years)	Lesion type[1]	CR			CNR			CR improvement (dB)		CNR improvement (%)		Subjective score
			Original	Corr.[1] based	GCF	Original	CF	GCF	Corr. based	GCF	Corr. based	GCF	GCF
1	53	Cyst	38.84	38.51	53.19	5.84	5.82	6.96	−0.33	14.34	−0.28	19.18	2+
2	49	Cyst	42.00	41.58	57.05	6.09	6.37	7.08	−0.41	15.04	4.51	16.19	2+
3	59	CA	26.00	26.53	36.70	4.03	3.99	4.73	0.52	10.69	−0.88	17.43	1+
4	28	FA	16.88	17.16	23.48	3.05	2.97	3.77	0.28	6.59	−2.73	23.37	1+
5	63	CA	13.63	13.80	21.11	2.19	2.23	2.85	0.16	7.47	1.59	28.09	2+
6	79	CA	10.39	11.05	19.57	1.53	1.59	2.46	0.65	9.17	3.85	60.94	2+
7	66	Cyst	20.97	20.52	33.53	3.07	2.95	4.33	−0.44	12.56	−3.85	40.97	2+
8	43	CA	4.35	4.84	7.67	0.66	0.73	0.96	0.49	3.32	11.65	45.41	1+
9	33	Abscess	14.11	14.57	20.05	2.16	2.23	2.59	0.46	5.93	2.96	19.58	1+
10	59	CA	16.37	17.94	24.87	2.58	2.79	3.29	1.56	8.50	7.92	27.24	2+
11	63	FA	15.32	15.28	20.59	2.67	2.65	2.99	−0.03	5.27	−0.90	12.05	1+
12	46	FA	15.74	16.12	20.94	2.47	2.53	2.89	0.38	5.20	2.30	16.94	1+
13	63	Abscess	12.99	13.05	20.68	2.20	2.15	3.05	0.06	7.68	2.60	38.29	2+
14	89	CA	12.22	12.26	19.43	1.70	1.73	2.04	0.03	7.20	1.90	20.04	1+
15	23	FA	14.19	14.07	18.40	2.54	2.65	2.92	−0.11	4.20	4.28	14.94	1+
16	50	CA	21.07	22.07	30.27	3.55	3.69	4.21	0.99	9.19	3.86	18.36	1+
17	42	FA	16.36	16.91	24.12	2.67	2.73	3.44	0.54	7.75	2.23	28.97	2+
18	25	Cyst	15.45	19.61	27.09	2.56	3.12	3.18	4.16	11.63	22.09	24.50	2+
19	45	CA	21.56	21.18	29.26	3.55	3.29	3.92	−0.37	7.70	−7.26	10.29	1+
20	45	CA	15.85	16.06	21.33	2.98	3.07	3.46	0.21	5.48	3.17	16.17	1+
21	47	Cyst	23.10	23.83	34.91	3.53	3.74	4.08	0.73	11.81	6.02	15.62	1+
22	55	FA	24.18	24.33	33.58	3.80	3.86	4.31	0.14	9.39	1.52	13.30	1+
23	58	Cyst	24.43	24.20	35.70	3.45	3.83	4.32	−0.22	11.26	11.07	25.18	1+
24	31	Abscess	22.20	22.85	30.98	3.73	3.80	4.37	0.65	8.78	1.83	17.12	1+
25	57	CA	26.51	26.92	34.83	4.14	4.33	4.56	0.40	8.31	4.51	10.02	2+

[1]CA = carcinoma, FA = fibroadenoma, Corr. = Correlation.

images obtained using the correlation-based method and the GCF-weighting method, respectively. The contrast between the milk of calcium and the tissue improved by 0.05 dB for the correlation-based method and by 4.47 dB for the GCF-weighting method. The lateral and axial −6-dB widths of the milk of calcium object were 0.51 and 0.39 mm in the original image, 0.55 and 0.41 mm in the correlation-based image, and 0.43 and 0.32 mm in the GCF-weighted image, respectively. The GCF-weighting method improved both the spatial resolution and the contrast in this case, which in turn helped in the detection of calcification.

IV. Discussion

The CR and CNR values obtained with the correlation-based and GCF-weighting methods are listed in Table I. The mean values for the CR and CNR improvements were 0.42 dB and 3.4% for the correlation-based method and 8.57 dB and 23.20% for the GCF-weighting method. It should be noted that, although the CR and CNR are widely reported as performance indices in the literature and are directly related to fundamental characteristics of an image, their exact values may change with the selected ROI and may not be directly related to diagnostic out-

comes. Therefore, these images also were evaluated by an experienced clinician (Y.-H. Chou) using the following scoring system: 2+, significant improvement; 1+, moderate improvement; 0, no noticeable effects; 1−, slight degradation; and 2−, significant degradation. In general, application of the GCF-weighting method improved the image quality in all the cases assessed in this study. The improvement in the contrast was more significant for a liquid lesion (e.g., a cyst) than for a solid lesion (e.g., a fibroadenoma), and the improvement in the boundary definition makes it easier to detect a malignant tumor (e.g., a carcinoma).

The proposed method requires only the use of individual channel data for each firing. Nonetheless, complete data sets were acquired in this study. With the complete data set, dynamic, two-way focusing can be realized. Therefore, the problem associated with reduced coherence at positions away from the fixed transmit focus can be avoided. However, acquisition of a complete data set suffers from lower signal-to-noise ratios and potential motion artifacts. In clinical situations, a reasonable compromise is to use multizone focusing on transmit.

Although the correlation-based method is one of the most popular adaptive imaging methods reported in the literature, several problems were encountered when we applied this to breast imaging in this study. The estimated time delays were affected by several factors, including the cumulative error along the array direction, the signal-to-noise ratio, the correlation between adjacent channels, the kernel size, and the aberrator integration errors of a 1-D array [17]–[19]. In addition to the above problems, the distributed sound-velocity inhomogeneities also represent a uniquely difficult problem in adaptive breast imaging, as illustrated in Fig. 10. The image shown in Fig. 10(a) is displayed without any aberration correction. Fig. 10(b) plots the estimated time-delay errors as a function of the channel index at the image points corresponding to the boxes marked in Fig. 10(a), which are located along the same beam and are spaced by 7.7 mm. The time delays were estimated according to previously described principles [3]. Significant variations in the estimated time delays are clearly evident, and these limit the performance of the correlation-based method. The depth dependency of the estimated time delay may result from breast tissue comprising a heterogeneous mixture of fatty, fibrotic, connective, and glandular tissues.

The arrival time and energy level reportedly vary with breast sample thickness [20], and the correlation length of the aberration profile in breast tissue varies with age and body type [20]–[22]. Therefore, it is to be expected that the near-field, phase-screen model is inaccurate, resulting in poor breast imaging when using the correlation-based method. It also has been reported that waveform distortion is severe and sidelobes are high for breast tissue, primarily because it is a highly refracting and heterogeneous medium [20], [23]–[25]. Therefore, adaptive sidelobe-reduction techniques, such as the GCF-weighting method investigated in the study, are of particular interest because they do not make any assumptions regarding the origin of the sidelobes. As shown in this paper, application of the GCF-weighting method significantly improves the contrast and boundary definition for cyst and solid masses. We also have demonstrated that the GCF-weighting method is more effective than correlation-based methods in improving the quality of images obtained from ultrasonic breast imaging without the use of a 2-D (or 1.5-D) array.

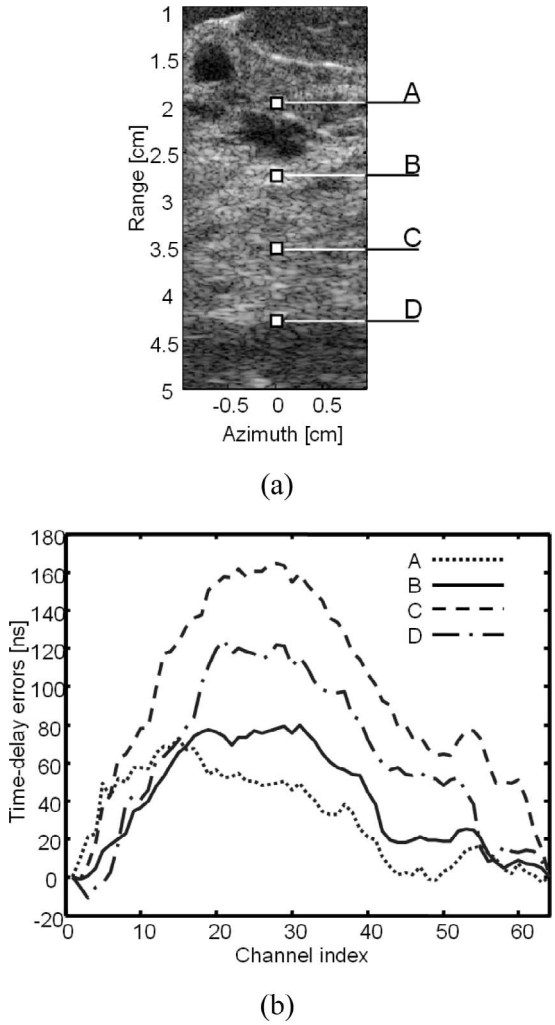

Fig. 10. Estimated time-delay errors. (a) Clinical image displayed with a dynamic range of 60 dB. (b) Corresponding estimated time-delay errors as functions of channel index at the imaging points indicated in (a).

This paper illustrates efficacy in sidelobe reduction of the proposed method using 1-D arrays. Nonetheless, the proposed method also can be extended to imaging with 1.5-D/2-D arrays. In particular, because the aperture also is sampled along the elevational direction, the proposed method can be applied to improve elevational focusing quality. Signal processing required for elevational GCF weighting with 1.5-D/2-D arrays will be similar to that for lateral GCF weighting with 1-D arrays.

V. Conclusions

In this paper, we have experimentally evaluated an adaptive imaging approach for reducing focusing errors

in ultrasonic imaging. This method is based on coherence and corrects focusing errors by suppressing unwanted sidelobes. The experimental results demonstrate that the image quality was noticeably improved in all of the cases investigated using a 1-D array.

Acknowledgment

Support from the National Science Council of Taiwan under grant no. NSC 95-2221-E-002-170 is gratefully acknowledged.

References

[1] S. A. Goss, R. L. Johnston, and F. Dunn, "Comprehensive compilation of empirical ultrasonic properties of mammalian tissues," *J. Acoust. Soc. Amer.*, vol. 64, pp. 423–457, 1978.

[2] S. W. Flax and M. O'Donnell, "Phase-aberration correction using signals from point reflectors and diffuse scatterers: Basic principles," *IEEE Trans. Ultrason., Ferroelect., Freq. Contr.*, vol. 35, no. 6, pp. 758–767, 1988.

[3] M. O'Donnell and S. W. Flax, "Phase-aberration correction using signals from point reflectors and diffuse scatterers: Measurements," *IEEE Trans. Ultrason., Ferroelect., Freq. Contr.*, vol. 35, no. 6, pp. 768–774, 1988.

[4] S. Krishnan, K. W. Rigby, and M. O'Donnell, "Improved estimation of phase aberration profile," *IEEE Trans. Ultrason., Ferroelect., Freq. Contr.*, vol. 44, no. 3, pp. 701–713, 1997.

[5] G. C. Ng, S. S. Worrell, P. D. Freiburger, and G. E. Trahey, "A comparative evaluation of several algorithms for phase aberration correction," *IEEE Trans. Ultrason., Ferroelect., Freq. Contr.*, vol. 41, no. 5, pp. 631–643, 1994.

[6] D. L. Liu and R. C. Waag, "Correction of ultrasonic wavefront distortion using backpropagation and a reference waveform method for time-shift compensation," *J. Acoust. Soc. Amer.*, vol. 96, no. 2, pp. 649–660, 1994.

[7] P.-C. Li and M. O'Donnell, "Phase aberration correction on two-dimensional conformal arrays," *IEEE Trans. Ultrason., Ferroelect., Freq. Contr.*, vol. 42, no. 1, pp. 73–82, 1995.

[8] P.-C. Li, S. W. Flax, E. S. Ebbini, and M. O'Donnell, "Blocked element compensation in phased array imaging," *IEEE Trans. Ultrason., Ferroelect., Freq. Contr.*, vol. 40, no. 4, pp. 283–292, 1993.

[9] P.-C. Li and M. O'Donnell, "Improved detectability with blocked element compensation," *Ultrason. Imag.*, vol. 16, no. 1, pp. 1–18, 1994.

[10] S. Krishnan, P.-C. Li, and M. O'Donnell, "Adaptive compensation of phase and magnitude aberrations," *IEEE Trans. Ultrason., Ferroelect., Freq. Contr.*, vol. 43, no. 1, pp. 44–55, 1996.

[11] S. Krishnan, K. W. Rigby, and M. O'Donnell, "Efficient parallel adaptive aberration correction," *IEEE Trans. Ultrason., Ferroelect., Freq. Contr.*, vol. 45, no. 3, pp. 691–703, 1998.

[12] K. W. Hollman, K. W. Rigby, and M. O'Donnell, "Coherence factor of speckle from a multi-row probe," in *Proc. IEEE Ultrason. Symp.*, 1999, pp. 1257–1260.

[13] R. Mallart and M. Fink, "Adaptive focusing in scattering media through sound-speed inhomogeneities: The van Cittert Zernike approach and focusing criterion," *J. Acoust. Soc. Amer.*, vol. 96, no. 6, pp. 3721–3732, 1994.

[14] S. D. Silverstein, "Ultrasound scattering model: 2-D cross-correlation and focusing criteria—theory, simulations, and experiments," *IEEE Trans. Ultrason., Ferroelect., Freq. Contr.*, vol. 48, no. 4, pp. 1023–1030, 2001.

[15] P.-C. Li and M.-L. Li, "Adaptive imaging using the generalized coherence factor," *IEEE Trans. Ultrason., Ferroelect., Freq. Contr.*, vol. 50, no. 2, pp. 128–141, 2003.

[16] W. F. Walker and G. E. Trahey, "Aberrator integration error in adaptive imaging," *IEEE Trans. Ultrason., Ferroelect., Freq. Contr.*, vol. 44, no. 4, pp. 780–791, 1997.

[17] G. C. Ng, S. S. Worrell, P. D. Freiburger, and G. E. Trahey, "A comparative evaluation of several algorithms for phase aberration correction," *IEEE Trans. Ultrason., Ferroelect., Freq. Contr.*, vol. 41, no. 5, pp. 631–643, 1994.

[18] W. F. Walker and G. E. Trahey, "A fundamental limit on the performance of correlation based phase correction and flow estimation techniques," *IEEE Trans. Ultrason., Ferroelect., Freq. Contr.*, vol. 41, no. 5, pp. 644–654, 1994.

[19] F. Viola and W. F. Walker, "A comparison of the performance of time-delay estimators in medical ultrasound," *IEEE Trans. Ultrason., Ferroelect., Freq. Contr.*, vol. 50, no. 4, pp. 392–401, 2003.

[20] L. M. Hinkelman, D.-L. Liu, R. C. Waag, Q. Zhu, and B. D. Steinberg, "Measurements and correction of ultrasonic pulse distortion produced by human breast," *J. Acoust. Soc. Amer.*, vol. 97, no. 3, pp. 1958–1969, 1995.

[21] R. C. Gauss, G. E. Trahey, and M. S. Soo, "Adaptive imaging in the breast," in *Proc. IEEE Ultrason. Symp.*, 1999, pp. 1563–1569.

[22] G. E. Trahey, P. D. Freiburger, L. F. Nock, and D. C. Sullivan, "In vivo measurements of ultrasonic beam distortion in the breast," *Ultrason. Imag.*, vol. 13, pp. 71–90, 1991.

[23] D.-L. Liu and R. C. Waag, "Time-shift compensation of ultrasonic pulse focus degradation using least-mean-square error estimates of arrival time," *J. Acoust. Soc. Amer.*, vol. 95, no. 1, pp. 542–555, 1994.

[24] Q. Zhu and B. D. Steinberg, "Wavefront amplitude distortion and image sidelobe levels. I. Theory and computer simulations," *IEEE Trans. Ultrason., Ferroelect., Freq. Contr.*, vol. 40, no. 6, pp. 747–753, 1993.

[25] Q. Zhu, B. D. Steinberg, and R. L. Arenson, "Wavefront amplitude distortion and image sidelobe levels. II. In vivo experiments," *IEEE Trans. Ultrason., Ferroelect., Freq. Contr.*, vol. 40, no. 6, pp. 754–762, 1993.

Shun-Li Wang was born in 1981 in Taipei, Taiwan, R.O.C. He received the B.S. degree in electrical engineering from National Taiwan University, Taiwan, R.O.C. in 2003. He is currently working toward the Ph.D. degree in electrical engineering at National Taiwan University. His current research interests include biomedical ultrasonic imaging, especially for flow velocity estimation and adaptive imaging.

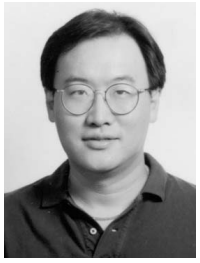

Pai-Chi Li (S'93–M'95–SM'01) received the B.S. degree in electrical engineering from National Taiwan University, Taipei, Taiwan, R.O.C., in 1987, and the M.S. and Ph.D. degrees from the University of Michigan, Ann Arbor in 1990 and 1994, respectively, both in electrical engineering: systems.

He was a research assistant with the Department of Electrical Engineering and Computer Science of the University of Michigan from 1990 to 1994. He joined Acuson Corporation, Mountain View, CA, as a member of the Technical Staff in June 1994. His work in Acuson was primarily in the areas of medical ultrasonic imaging system design for both cardiology and general imaging applications. In August 1997, he went back to the Department of Electrical Engineering at National Taiwan University, where he is currently Professor of Department of Electrical Engineering and Director of Institute of Biomedical Electronics and Bioinformatics. His current research interests include biomedical ultrasonic imaging and signal processing.

Dr. Li is a senior member of IEEE and Associate Editor of IEEE Transactions on Ultrasonics, Ferroelectrics, and Frequency Control. He is also on the Editorial Board of Ultrasonic Imaging. He received the 2005 Outstanding Electrical Engineering Professor Award, the

Chinese Institute of Electrical Engineering, the 2004 Distinguished Research Award, National Science Council, the 2004 Distinguished Research Achievement Award, National Taiwan University, the 2003 Outstanding Researcher Award, National Taiwan University, the 2002 Dr. Wu Dayou Research Award from National Science Council, the 2002 Outstanding Young Electrical Engineer Award from Chinese Institute of Electrical Engineering and the Distinguished Industrial Collaboration Award of Ministry of Education. He was also the recipient of the Distinguished Achievement Award in Electrical Engineering: Systems in 1994 for his outstanding academic achievement at the University of Michigan.

Ultrasound in Med. & Biol., Vol. 33, No. 11, pp. 1681–1687, 2007

0301-5629/07/$–see front matter

ELSEVIER

doi:10.1016/j.ultrasmedbio.2007.05.012

● *Original Contribution*

RECONSTRUCTION OF ULTRASONIC SOUND VELOCITY AND ATTENUATION COEFFICIENT USING LINEAR ARRAYS: CLINICAL ASSESSMENT

CHEN-HAN CHANG,* SHENG-WEN HUANG,* HSIN-CHIA YANG,* YI-HONG CHOU,† AND PAI-CHI LI*‡

*Department of Electrical Engineering, National Taiwan University; †Department of Radiology, Taipei Veterans General Hospital and National Yang Ming University School of Medicine; and ‡Graduate Institute of Biomedical Electronics and Bioinformatics, National Taiwan University, Taipei, Taiwan

(*Received* 2 *November* 2006, *revised* 11 *May* 2007, *in final form* 16 *May* 2007)

Abstract—The aim of this study was to determine the efficacy of using sound velocity and tissue attenuation to clinically discriminate breast cancer from healthy tissues. The methods for reconstructing the sound-velocity and attenuation-coefficient distributions were previously proposed and tested on tissue-mimicking phantoms. The methods require only raw channel data acquired by a linear transducer array and can therefore be implemented on existing clinical systems. In this paper, these methods are tested on clinical data. A total of 19 biopsy-proven cases, consisting of five carcinomas (CAs), seven fibroadenomas (FAs), six adipose tissue (fat) and one oil cyst, were evaluated. A single imaging setup consisting of a 5-MHz, 128-channel linear array was used to simultaneously obtain B-mode image data, time-of-flight data and attenuation data. The sound velocity and attenuation coefficient can be reconstructed inside and outside a region of interest manually selected in the B-mode image. To reduce distortion caused by tissue inhomogeneities, an optimal filter derived from pulse-echo data—with water replacing the breast tissue—is applied. We found that the sound velocities in CA, FA and fat tissues relative to those in the surrounding tissues were 49.8 ± 35.2, 2.6 ± 27.3 and −25.1 ± 44.9 m/s (mean ± SD), respectively, whereas the relative attenuation coefficients were 0.21 ± 0.58, 0.27 ± 0.62 and −0.02 ± 0.59 dB/cm/MHz. These results indicate that CA can be discriminated from FA and fat by choosing an appropriate threshold for the relative sound velocity (*i.e.*, 18.5 m/s). However, the large variations in the attenuation within the same type of tissue make simple thresholding ineffective. Nevertheless, the method described in this paper has the potential to reduce negative biopsies and to improve the accuracy of breast cancer detection in clinics. (E-mail: paichi@cc.ee.ntu.edu.tw)

Key Words: **Time-of-flight, Attenuation, Region-of-interest, Sound velocity, Attenuation coefficient.**

INTRODUCTION

Breast cancer is a leading cause of death from cancer in females, indicating the importance of its early detection. Mammography is considered the best noninvasive screening method because it can detect nonpalpable and small tumors. Nevertheless, mammography exposes the subject to ionizing radiation and the mammograms of young women with dense breasts are hard to interpret (Lanfranchi 2000). Ultrasonic imaging has become an effective adjunct to mammography (Telger 1996), but the use of conventional ultrasonic pulse-echo B-mode imaging to find breast tumors is also often limited by the image distortion caused by sound-velocity inhomogeneities in the breast tissue (Gauss et al. 1997). With ultrasound, it is also possible to detect breast cancer by reconstructing distributions of the sound velocity and attenuation coefficient. For example, it has been reported that the sound velocity is faster in cancerous tissue than in fat (Goss et al. 1978) and that the attenuation coefficient is higher in cancerous tissue than in a cyst (Goss et al. 1980; Madsen et al. 1982, 1988). However, these reconstructions typically require a tomographic setup to acquire data from a large number of projections, and such setups are rarely used in clinical situations. Another approach to the tomographic reconstructions of sound velocity and attenuation coefficient is limited-angle tomography using linear arrays (Huang and Li 2004a, 2004b, 2005; Krueger et al. 1998). This uses the same

Address correspondence to: Pai-Chi Li, Department of Electrical Engineering, National Taiwan University, No. 1, Sec. 4, Roosevelt Road, Taipei 106, Taiwan. E-mail: paichi@cc.ee.ntu.edu.tw

imaging setup as that used for conventional B-mode imaging and, thus, both imaging methods can be used. In addition, a plate reflector is placed under the breast, and the breast is under compression during data acquisition. This approach also requires the selection of a region-of-interest (ROI) to alleviate the difficulties caused by the limited angles of tomographic data acquisition, and it has yielded good results on tissue-mimicking phantoms (Huang and Li 2004b, 2005). In the present study we applied the approach to clinical data, and we also modified the original method to accommodate tissue inhomogeneities that are present in breast tissue (which were not present in the phantoms used previously). Because a critical step in this approach is preselecting an ROI, the effects of variations in the ROI selection on the performance of the method were also determined.

METHODS

This section first introduces the method for reconstructing the distributions of sound velocity and attenuation coefficient, and then describes the experimental setup for acquiring clinical data from individual array channels. We then list the procedures of ROI selection and the implementation of a least-squares (LS) filter used to reduce distortion from tissue inhomogeneities and then, finally, we describe the patients.

Reconstruction of sound velocity and attenuation coefficient

Based on our previous studies (Huang and Li 2004a, 2004b, 2005) and Kossoff et al. (1973), water was used as a reference, whereby for each clinical dataset, a corresponding dataset acquired with water replacing breast tissue was also acquired without changing the setup. The sound velocity of water (c_0) was assumed to be 1496 m/s (Bilaniuk and Wong 1993) and the attenuation coefficient of water (α_0) was specified as 0 dB/cm/MHz at room temperature, 25°C. As described below, the known properties of water were used to estimate the properties of the breast. Let $c_1(x,y)$ denote the sound velocity at the position (x,y) in the B-mode image. As shown in Fig. 1, if the ultrasonic signal has round-trip times-of-flight t_0 and t_1 in water and breast, respectively, then

$$t_0 = \int_L \frac{1}{c_0} dl = \int_L s_0 dl, \tag{1}$$

$$t_1 = \int_L \frac{1}{c_1(x,y)} dl = \int_L s_1(x,y) dl, \tag{2}$$

where L is the signal path length and $s_1(x,y)$ is defined as the slowness. The difference between t_0 and t_1 is

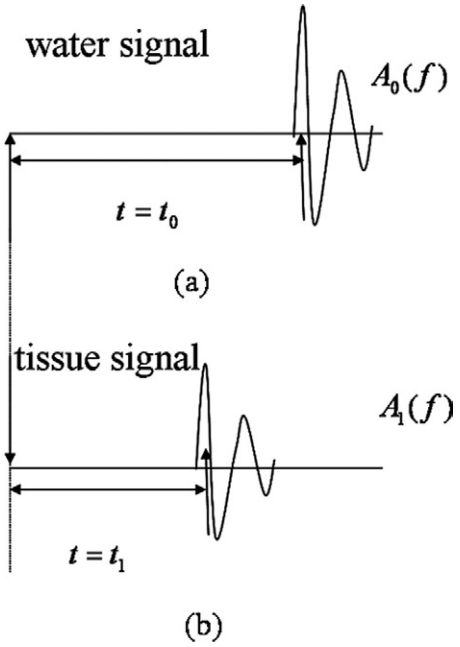

Fig. 1. Illustration of the time-of-flight and tissue attenuation of the water signal (top) and the breast signal (bottom).

$$\Delta t = t_1 - t_0 = \int_L [s_1(x,y) - s_0] dl = \int_L \Delta s(x,y) dl. \tag{3}$$

The attenuation coefficient is linearly proportional to frequency in the frequency ROI and represented by $\alpha(x,y)$. Let $A_0(f)$ and $A_1(f)$ denote the echo spectra for water and breast as the propagating media, respectively, then

$$\Delta A(f) = 20 \log_{10}(A_0(f)) - 20 \log_{10}(A_1(f)) \quad \text{(dB)}, \tag{4}$$

$$\Delta A' = \int_L \alpha(x,y) dl \quad \text{(dB/MHz)}, \tag{5}$$

where $\Delta A'$ is also the slope of a first-order polynomial fit to $\Delta A(f)$.

The integral equations previously mentioned (*i.e.*, eqns (3) and (5)) can be written in the following discrete forms:

$$\Delta t_{ij} = \sum_{n=1}^{N} \sum_{m=1}^{M} \Delta s(m,n) l_{ij}(m,n), \tag{6}$$

$$\Delta A'_{ij} = \sum_{n=1}^{N} \sum_{m=1}^{M} \alpha(m,n) l_{ij}(m,n), \tag{7}$$

where the B-mode image is divided into $N \times M$ pixels, and the index ij represents the transmit–receive channel

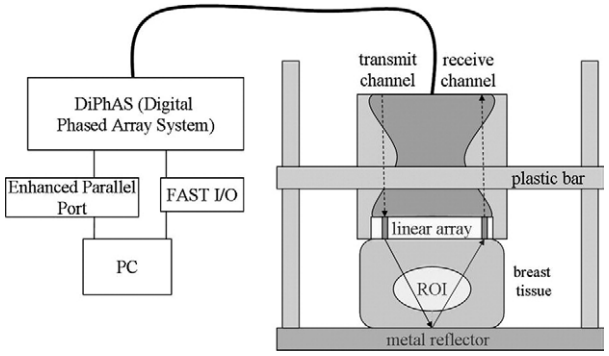

Fig. 2. Schematic of the setup for acquiring clinical data. The plastic bar was used to hold the transducer. The setup was used to compress the breast, similar to X-ray mammography.

combination (*i.e.*, transmit from the i^{th} channel and receive on the j^{th} channel). Furthermore, eqns (6) and (7) can be written in matrix form as

$$L\Delta \boldsymbol{s} = \Delta t, \tag{8}$$

$$L\alpha = \Delta A'. \tag{9}$$

Note that the dimensions of the matrices and vectors in eqns (8) and (9) can be reduced by discarding data containing apparent errors. For example, if the time-of-flight difference is outside a prespecified reasonable range, it is discarded. The reasonable range for the time-of-flight is determined by assuming the sound velocity to be within the range 1400 to 1600 m/s, because the sound velocities of cyst and fat are about 1570 m/s and 1470 m/s, respectively. The details of this approach are available elsewhere (Huang and Li 2004a, 2004b, 2005).

Data acquisition

Figure 2 shows a schematic of the experimental setup used to acquire clinical data. The plastic bar was used to hold the transducer. The setup was used to compress the breast, similar to X-ray mammography. A programmable digital phased-array system capable of acquiring radiofrequency channel data (DiPhAS, Fraunhofer IBMT, St. Ingbert, Germany) was used (Lemor et al. 2003). The full dataset includes radiofrequency pulse-echo data from all individual channels with all transmit-receive combinations. The linear array transducer (L6/128, STI, State College, PA, USA) had 128 channels with a pitch of 0.3 mm, an elevation width of 5 mm, an elevation focus of 25 mm, a center frequency of 5.57 MHz and a −6-dB bandwidth of 4.10 MHz. The transmitted pulse is a five-cycle square wave at 5 MHz, and all data were sampled at 20 MHz, with a vertical resolution of 12 bits. The collected channel data were acquired at a sampling rate of 20 MHz using a digital I/O card (PCI-7300A, ADLINK, Taipei, Taiwan) housed in a personal computer. Furthermore, a stainless plate was placed at the bottom as a reflector so that limited-angle tomographic data could be acquired. The total data acquisition time was around 4 s, during which the patients were asked to hold their breath to reduce motion artifacts.

After acquiring a full dataset, the first step was to extract from the data to estimate the difference in time-of-flights t_0 and t_1 based on eqns (1) through (3). The second step was to estimate attenuation based on eqns (4) and (5). As mentioned in "Reconstruction of Sound Velocity and Attenuation Coefficient" section, following eqns (6) and (7), the final matrix forms of time-of-flight data and attenuation data were produced.

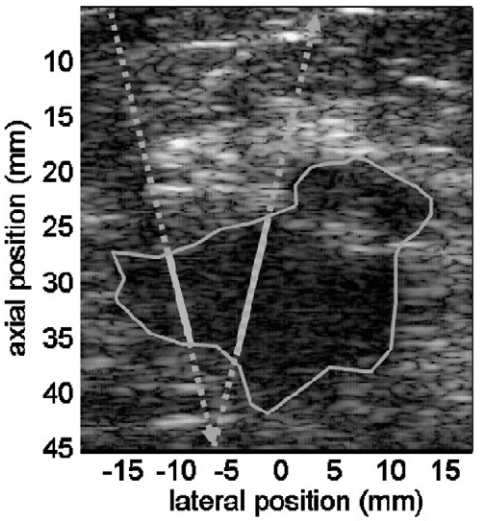

(a)

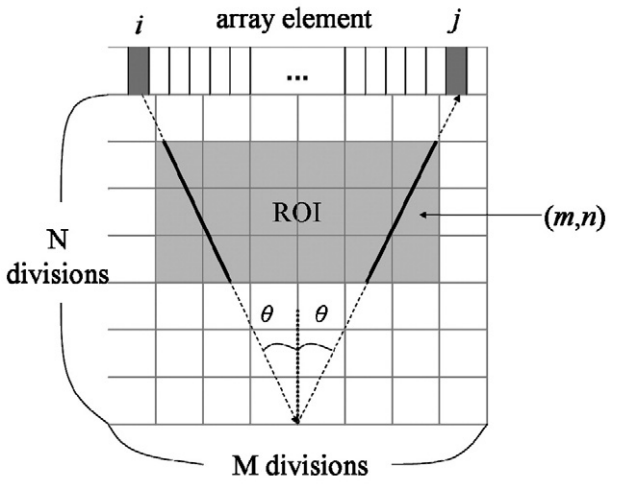

(b)

Fig. 3. An example of (a) ROI selection and (b) the schematic of signal path of one transmit-receive combination.

Region of interest selection

For each dataset, an ROI such as the one shown in Fig. 3a was preselected manually using a graphical user interface. According to Chiang et al. (2001), some contour features, such as spiculation and angular margin, have been recognized as characteristics of malignancy. The clinician chose the ROIs according to the primary features associated malignancy such as echogenicity, size, shape and the border of the tumors. Some additional contour features, such as spiculation and angular margin, have also been used. The purpose of ROI selection is to provide reconstruction constraints by forcing both the sound velocity and attenuation coefficient values to be uniform inside and outside the ROI (Huang and Li 2005). The assumption of uniformity can be seen as the average for that region. A technique for measuring the *in-vivo* average velocity of ultrasound in the female breasts was developed in Kossoff et al. (1973). In Fig. 3a and b, the thick solid line represents the ROI path, whereas the dashed line is for the background path. In Fig. 3b, it shows that the signal is transmitted from the i^{th} channel and received by the j^{th} channel. Based on the aforementioned constraints, eqns (6) and (7) can be reduced to

$$\Delta t_{ij} = \Delta S_{ROI} \sum_{n=1}^{N} \sum_{m=1}^{M} l_{ij,ROI}(m,n) + \Delta s_{back} \sum_{n=1}^{N} \sum_{m=1}^{M} l_{ij,back}(m,n) = l_{ij,ROI} \Delta s_{ROI} + l_{ij,back} \Delta s_{back}, \quad (10)$$

$$\Delta A'_{ij} = \alpha_{ROI} \sum_{n=1}^{N} \sum_{m=1}^{M} l_{ij,ROI}(m,n) + \alpha_{back} \sum_{n=1}^{N} \sum_{m=1}^{M} l_{ij,back}(m,n) = l_{ij,ROI} \alpha_{ROI} + l_{ij,back} \alpha_{back}. \quad (11)$$

where (m,n) corresponds to one pixel in the B-mode image. When i is not equal to j, θ is not equal to zero degree. Also, eqns (8) and (9) are modified to

$$[l_{ROI} \quad l_{back}] \begin{bmatrix} \Delta s_{ROI} \\ \Delta s_{back} \end{bmatrix} = \Delta t, \quad (12)$$

$$[l_{ROI} \quad l_{back}] \begin{bmatrix} \alpha_{ROI} \\ \alpha_{back} \end{bmatrix} = \Delta A', \quad (13)$$

where l_{ROI}, l_{back}, Δt and $\Delta A'$ are column vectors, with each element therein representing a valid transmission–reception combination. l_{ROI} is the total length of the ROI path and l_{back} is the total length of the background path, Δs is the difference in slowness, α is the attenuation coefficient, Δt is the estimated difference in the times-of-flight and $\Delta A'$ is the estimated attenuation at the center frequency of 5 MHz.

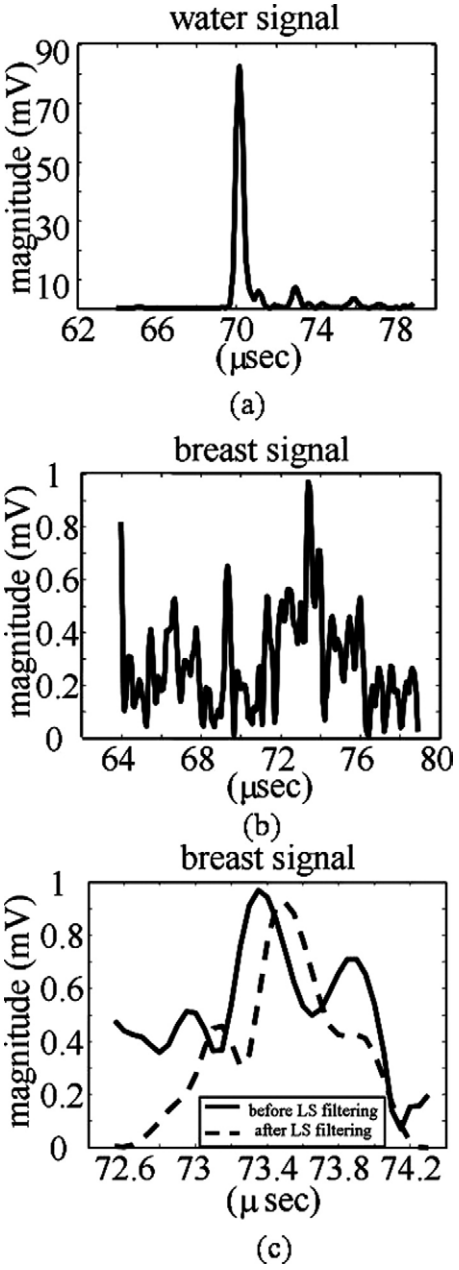

Fig. 4. Envelopes of the received signals, which are the first echo reflected from metal reflector: (a) water, (b) breast and (c) breast before (thick solid line) and after LS filtering (dashed line). The distortion from the breast tissue is clearly shown as the peak position is shifted, waveform is changed and the clutter signal is higher.

Least-squares filter for distortion reduction

Due to the inhomogeneities present in breast tissue, the received signal is often severely distorted in both amplitude and phase compared with those of a water signal (Lewin and O'Brien 1996; Zhu and Steinberg 1992, 1994, 1996, 1997). A typical example is shown in Fig. 4a (envelope of water signal with no distortion) and

Fig. 4b (envelope of breast signal with distortion). Figure 4a and b show the first echo reflected from the metal plate through water and breast tissue, respectively. Compared with the water signal (Fig. 4a), the distortion from the breast tissue is clearly shown as the peak position is shifted, waveform is changed and the clutter signal is higher. Such distortion significantly affects the estimation results, and an LS filter was used to reduce potential errors. For each transmit-receive combination, the filter was designed by using the breast signal as the input and the corresponding water signal as the desired output. In addition, the DC gain of the filter was normalized to unity to not introduce errors into the attenuation estimation. Likewise, the linear component of the phase in the frequency domain was also removed to not introduce additional time delays that would affect the time-of-flight.

Letting b denote the breast signal vector, whose envelope is as shown in Fig. 4c (the thick solid line), w denotes the water signal, f denotes the filter, we have

$$b \otimes f = w, \tag{14}$$

where $\otimes$ is the convolution operator. Equation (14) is further simplified into a multiplication form as

$$B \cdot f = w, \tag{15}$$

where B is the convolution matrix of b (Li et al. 1992). According to the LS error method, f can be obtained from

$$f = (B'B)^{-1}B'w. \tag{16}$$

Note that the above equations are based on the baseband signal representation. As mentioned previously, filter f was modified to not introduce estimation errors: it was first normalized to its DC gain and then the first-order (*i.e.*, linear) component of the phase in the frequency domain was removed.

Figure 4c shows the filtered version (the dashed line) of the breast signal (the thick solid line), which indicates that the filtering allows the time-of-flight and attenuation coefficient to be estimated more accurately. From Waag et al. (1989), the received signal can be represented by a convolution of an undistorted beam and a distortion function. Therefore, the correlation coefficient can represent the extent of distortion. The efficacy of the LS filter is further illustrated by the correlation coefficients between the breast signal (with and without filtering) and the water signal as shown in Fig. 5. It shows that these correlation coefficients are generally higher than 0.7 after filtering, whereas before filtering some of the correlation coefficients are low and the estimation results are not reliable.

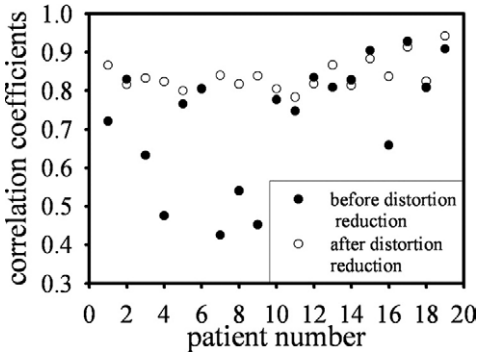

Fig. 5. Correlation coefficients before and after distortion reduction. The correlation coefficients of case 6 were virtually indistinguishable.

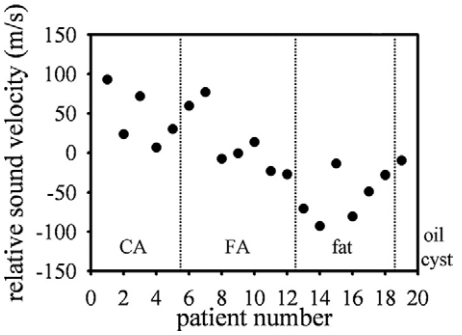

Fig. 6. Relative sound–velocity results.

Patients

Nineteen biopsy-proven cases, consisting of five carcinomas (CAs), seven fibroadenomas (FAs), six adipose tissue (fat) and one oil cyst, were evaluated. The clinical data were collected in the ultrasonic consulting room at Taipei Veterans General Hospital by one of the authors after patients had provided informed consent. During data acquisition, the patients (in a sitting position) were asked to hold their breath and their breasts were compressed by the device shown in Fig. 2.

RESULTS AND DISCUSSION

In the following, the relative values (*i.e.*, difference between the ROI and the background) were used.

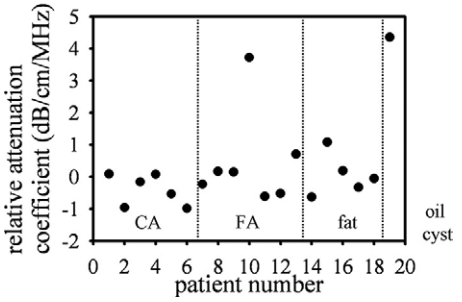

Fig. 7. Relative attenuation–coefficient results.

Table 1. Average sound velocity and attenuation coefficient with SD

	Sound velocity (m/s)	Attenuation coefficient (dB/cm/MHz)
CA	1530.9 ± 36.2	0.66 ± 0.52
FA	1499.8 ± 26.8	0.68 ± 0.66
Fat	1464.8 ± 45.1	0.63 ± 0.61

The relative sound velocities are shown in Fig. 6 and were 49.8 ± 35.2 m/s (mean ± SD), 2.6 ± 27.3 m/s and −25.1 ± 44.9 m/s for CA, FA and fat, respectively. The relative sound velocity for the single case of an oil cyst was −9.4 m/s. According to Fig. 6, it is possible to correctly distinguish 14 of 18 cases (excluding the oil cyst) using thresholds of 18.5 m/s and −28.3 m/s. The relative attenuation coefficients are shown in Fig. 7 and were 0.21 ± 0.58, 0.27 ± 0.62 and −0.02 ± 0.59 dB/cm/MHz for CA, FA and fat, respectively. It demonstrates that, unlike sound velocity, it is not feasible to use the relative attenuation coefficient to distinguish different types of objects. On the other hand, the average results of sound velocity and attenuation coefficients were put in Table 1.

Effects of different reference sound velocity were also investigated. As shown in Table 2, using 1522 m/s as the sound velocity in water, the relative sound velocities are 44.9 ± 35.9 m/s (mean ± SD), 13.0 ± 40.5 m/s and −55.9 ± 30.9 m/s for CA, FA and fat, respectively. The sound velocity thresholds can be set at 17.6 m/s and −39.3 m/s, respectively. Similarly, the relative attenuation coefficients using 1522 m/s as the sound velocity in water, as shown in Table 3, are −0.30 ± 0.45, 0.24 ± 1.59 and 0.16 ± 0.64 dB/cm/MHz for CA, FA and fat, respectively.

From the tables, we found that the relative sound velocities changed by −4.9 m/s, −10.4 m/s and +30.8 m/s for CA, FA and fat, respectively. Nonetheless, 14 of 18 cases can be distinguished in both cases by choosing threshold individually. Also, it showed that the temperature control during data acquisition is critical.

Because the ROI was selected manually, the impact of ROI selection on the estimation results was also evaluated. Figure 8a and b show, respectively, the sound-velocity and attenuation-coefficient results for patients 1, 7 and 9 as examples. The estimation results for the background generally do not change with ROI areas in the range 10 to 140 mm^2. However, the attenuation coefficient of ROI for patient 7 is an exception. This may indicate that the assumption that the attenuation coefficient is uniform inside the ROI is invalid in this case.

As shown in Table 1, the sound-velocity and attenuation-coefficient results reported in this paper differ from those reported in the literature. In Duck (1990), the sound velocities for CA and FA were 1550 ± 32 m/s and 1584 ± 27 m/s, and in Landini et al. (1985), the attenuation coefficients for CA, FA and fat were in the range 0.08 to 0.16 dB/cm/MHz. In Huang and Li 2005, for each transmit-receive combination, data corresponding

Table 2. Relative sound velocity at different reference sound velocities

Relative sound velocity (m/s)	CA	FA	Fat
I. c_0 = 1496 m/s	49.8 ± 35.2	2.6 ± 27.3	−25.1 ± 44.9
II. c_0 = 1522 m/s	44.9 ± 35.9	13.0 ± 40.5	−55.9 ± 30.9

Table 3. Relative attenuation coefficient at two reference sound velocities

Relative attenuation coefficient (dB/cm/MHz)	CA	FA	Fat
I. c_0 = 1496 m/s	0.21 ± 0.58	0.27 ± 0.62	−0.02 ± 0.59
II. c_0 = 1522 m/s	−0.30 ± 0.45	0.24 ± 1.59	0.16 ± 0.64

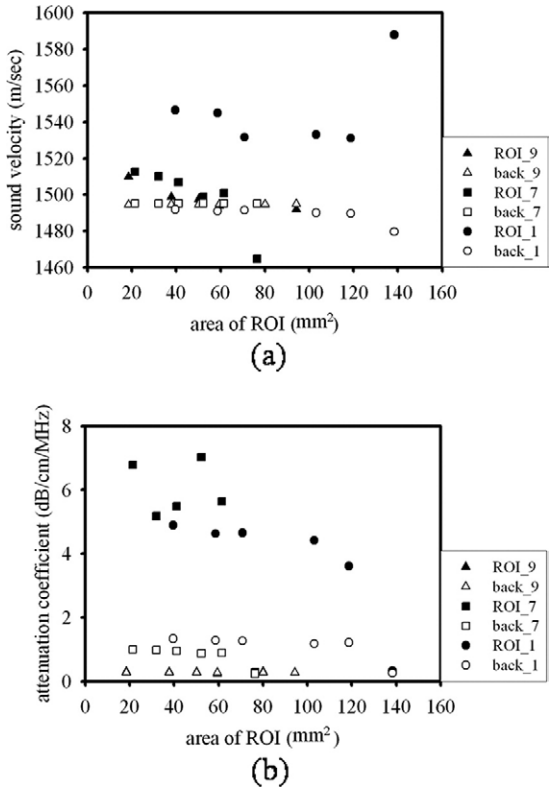

Fig. 8. (a) Estimated sound velocity and (b) attenuation coefficient as functions of the ROI area for patients 1, 7 and 9.

to 16 consecutive firings were averaged off-line to increase the signal-to-noise ratio. However, considering the duration of patients' holding their breath, no averaging was performed in the data acquisition. Low signal-to-noise ratio might lead to estimation errors. Besides, in Landini et al. (1985), each one-way measurement was obtained through 1-cm-thick tissue specimens to estimate the attenuation coefficient. Particularly, the mean value was obtained among a series of 20 measurements. In contrast, the tissue thickness under our experimental setup is usually between 7 cm and 10 cm (round trip). The standard deviations of attenuation coefficient in four groups from Landini et al. (1985) were 0.04, 0.06, 0.06 and 0.10 dB/cm/MHz, respectively. On the other hand, as shown in Table 1, the standard deviations of the attenuation coefficient were from 0.52–0.66 dB/cm/MHz in our study. The poor signal-to-noise ratio because of lack of signal averaging and large propagation distance are expected to be a major factor in the large estimation errors. More patient data need to be collected and *in-vivo* measurements are needed to understand such differences.

The limited angle tomography use in this study is a trade-off between full-view (*i.e.*, full 360°) tomography and direct reflection mode (*i.e.*, only at 0°) data acquisition. Compared with full-view tomography, limited-angle tomography has loss of angular information. However, one advantage is that such a setup can be implemented easily using an existing B-mode imaging system with a linear array. To overcome the loss of information because of limited angular extent, the reconstruction method proposed in our previous studies (Huang and Li 2004a, 2004b, 2005) was adopted.

CONCLUSIONS

This study has demonstrated the feasibility of using clinical data to reconstruct the sound velocity and attenuation coefficient using a linear array system. The setup is similar to that of X-ray mammography, with the breast being compressed and LS filtering used to reduce distortion. We also evaluated the effects of changing the ROI area. Our results show that the sound velocity can be used to distinguish different lesion types, whereas the attenuation coefficient varies over a wide range and hence is not yet useful for tissue characterization. The method proposed in this study has the potential to aid breast cancer detection and decrease the percentage of negative biopsies performed in clinics.

Acknowledgments—This study was financially supported by the National Science Council of Taiwan under grant no. NSC-93-2213-E-002-063.

REFERENCES

Bilaniuk N, Wong GSK. Speed of sound in pure water as a function of temperature. J Acoust Soc Am 1993;93(3):1609–1612.

Chiang HK, Tiu CM, Hung GS, Wu SC, Chang TY, Chou YH. Stepwise logistic regression analysis of tumor contour features for breast ultrasound diagnosis. IEEE Ultrason Sympos 2001;2:1303–1306.

Duck FA. Physical properties of tissue. London: Academic Press, 1990.

Gauss RC, Soo MS, Trahey GE. Wavefront distortion measurements in the human breast. IEEE Ultrason Sympos 1997;2:1547–1551.

Goss SA, Johnston RL, Dunn F. Comprehensive compilation of empirical ultrasonic properties of mammalian tissues. J Acoust Soc Am 1978;64(2):423–457.

Goss SA, Johnston RL, Dunn F. Compilation of empirical ultrasonic properties of mammalian tissues. II. J Acoust Soc Am 1980;68(1):93–108.

Huang SW, Li PC. Computed tomography sound velocity reconstruction using incomplete data. IEEE Trans Ultrason Ferroelectr Freq Control 2004a;51(3):329–342.

Huang SW, Li PC. Experimental investigation of computed tomography sound velocity reconstruction using incomplete data. IEEE Trans Ultrason Ferroelectr Freq Control 2004b;51(9):1072–1081.

Huang SW, Li PC. Ultrasonic computed tomography reconstruction of the attenuation coefficient using a linear array. IEEE Trans Ultrason Ferroelectr Freq Control 2005;52(11):2011–2022.

Kossoff G, Kelly-Fry E, Jellins J. Avergae Velocity of Ultrasound in the Human Female Breast. J Acoust Soc Am 1973;53(6):1730–1736.

Krueger M, Burow V, Hiltawsky KM, Ermert H. Limited angle ultrasonic transmission tomography of the compressed female breast. IEEE Ultrason Sympos 1998;2:1345–1348.

Landini L, Sarnelli R, Squartini F. Frequency-dependent attenuation in breast tissue characterization. Ultrasound Med Biol 1985;11(4):599–603.

Lanfranchi ME. Breast ultrasound. 2nd ed. New York: Marban Books, 2000.

Lemor RM, Weber PK, Fonfara PK, Guenther C, Welsch JH, Hoss ML. A new combined open research platform for ultrasound radio frequency signal processing. IEEE Ultrason Sympos 2003;1:33–37.

Li PC, Ebbini E, O'Donnell M. A new filter design technique for coded excitation systems. IEEE Trans Ultrason Ferroelectr Freq Control 1992;39(6):693–699.

Lewin T, O'Brien WD Jr. Tissue-induced ultrasonic wavefront distortion. IEEE Ultrason Sympos 1996;2:1415–1418.

Madsen EL, Zagzebski JA, Frank GR, Greenleaf JF, Carson PL. Anthropomorphic breast phantoms for assessing ultrasonic imaging system performance and for training ultrasonographers: Part I. J Clin Ultrasound 1982;10(2):67–75.

Madsen EL, Kelly-Fry E, Frank GR. Anthropomorphic phantoms for assessing systems used in ultrasound imaging of the compressed breast. Ultrasound Med Biol 1988;14(suppl 1):183–201.

Telger TC. Teaching atlas of breast ultrasound. New York: Thieme Medical Publishers, 1996.

Waag RC, Smith JF 3rd, Sumino Y. Wavefront distortion in ultrasonic imaging. Proc 11th Annu Int Conf IEEE Engineering in Med and Biol Soc 1989;395–396.

Zhu Q, Steinberg BD. Large-transducer measurements of wavefront distortion in the female breasts. Ultrason Imaging 1992;14(3):276–299.

Zhu Q, Steinberg BD. Modeling, measurement and correction of wavefront distortion produced by breast specimens. IEEE Ultrason Sympos 1994;3:1613–1617.

Zhu Q, Steinberg BD. A toward inverse filtering approach for ultrasonic wavefront compensation. IEEE Ultrason Sympos 1996;2:1357–1361.

Zhu Q, Steinberg BD. Modeling and correction of incoherent wavefront distortion. Int J Imag Syst Technol 1997;8(3):322–335.

出席國際學術會議心得報告

計畫編號	NSC95-2221-E-002-169
計畫名稱	新參數超音波乳房影像技術(3/3)
出國人員姓名 服務機關及職稱	李百祺/台灣大學電機系/台灣大學生醫電子與資訊學研究所
會議時間地點	2007/10/28-2007/10/31 New York, USA
會議名稱	IEEE Ultrasonics Symposium
發表論文題目	六篇論文附錄於成果報告

一、參加會議經過

此 IEEE 國際超音波研討會(IEEE Ultrasonics Symposium)，今年在美國紐約(New York, USA)舉行。此會議每年舉辦一次，主要是提供世界各地從事超音波相關領域的專家學者一個發表研究成果及討論交換心得的機會，自 2007/10/28 到 2007/10/31 共四天，於美國紐約之 Hilton New York 舉行。本人參加之重點為生物醫學超音波之相關議程。如同往年，此次研討會參與程度相當踴躍，發表論文亦有一定水準，相信與會者皆感到不虛此行。

二、與會心得

此研討會分為工業超音波及生醫超音波兩大部分，由議程看來，今年度會議在生醫超音波的重點在於新成像技術(beamformation) 、高頻探頭製作、光聲影像(Photoacoustic Imaging)及分子影像（Molecular Imaging）等。本人之報告共計六篇，整體來說屬於全球相關領域產出較多的實驗室之一，所發表的題目分別為” In vitro blood flow mean velocity estimation using a fast photoacoustic imaging system”、”Identification of hepatocellular carcinomas with contrast enhanced 40 MHz ultrasound in hepatitis B Virus X protein transgenic mice”、”Breast ultrasound computer-aided diagnosis using both acoustic and image features” 、 ”Error analysis of autocorrelation-based velocity vector estimation in the aperture domain”、“Coded excitation and nonlinear pulse compression in pulse inversion fundamental imaging ”、“Fabrication and Assembly of A Monolithic 3D CMUT Array for Imaging Applications ”。其中第一篇為新穎之光聲影像系統，是關於血流速度之量測。第二篇為使用高頻超音波對比增強影像應用於肝腫瘤之辨識。第三篇為利用聲學與影像特徵之乳房超音波電腦輔助診斷。第四篇為基於自相關的速度向量

估計之誤差分析。第五篇為編碼波形與非線性脈衝波之壓縮於反向脈衝波之基波成像。第六篇為用於影像應用之三維微型電容式超音波換能器陣列之製程。以上成果相當具有學術價值，因此在會場上得到不錯之反應，在會中亦與各國學者有許多交流。

整個研討會過程，能與在場的專家學者一起討論，觀摩其他實驗室的研究成果及研究方向，讓本人獲益良多。所發表之六篇論文請參考附件。